

i

VACUUM BOILING OF WATER IN A STEAM JET REFRIGERATION SYSTEM

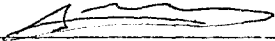
Stephen Ronald Mitchley

A dissertation submitted to the Faculty of Engineering, University of the Witwatersrand, Johannesburg, in fulfilment of the requirements for the degree of Master of Science in Engineering

Johannesburg, 1998

DECLARATION

I declare that this dissertation is my own, unaided work. It is being submitted for the Degree of Master of Science in Engineering in the University of the Witwatersrand, Johannesburg. It has not been submitted before for any degree or examination in any other University.



Stephen Ronald Mitchley

27 day of December 1998

ABSTRACT

This experimental project aims to describe the influencing factors in the vacuum boiling of water in water vapour refrigeration systems. Testing was conducted using a 2 kW three-stage steam jet ejector system, with barometric condensers, as the compression device. Three direct-contact evaporators were used to investigate the boiling phenomena. These were : a through-flow evaporator where heat and mass transfer rates were established for boiling mechanisms at various positions within the evaporator; a vertical cylinder where small quantities of water were subjected to rapid decompression and the effects measured, and a simple channel for photographic studies of the process.

Boiling in direct-contact water vapour systems is described herein. The vacuum boiling process was found to be controlled by a combination of the water surface temperature and the hydrostatic pressure gradient, these being governed by the water vapour flow geometry between the water surface and ejector suction and convective heat transfer below the boiling region. The contributions of the various boiling regimes to the total heat transfer are discussed. Heat and mass transfer coefficients and their applicability to evaporator design are presented.

ACKNOWLEDGEMENTS

ABSTRACT

This experimental project aims to describe the influencing factors in the vacuum boiling of water in water vapour refrigeration systems. Testing was conducted using a 2 kW three-stage steam jet ejector system, with barometric condensers, as the compression device. Three direct-contact evaporators were used to investigate the boiling phenomena. These were: a through-flow evaporator where heat and mass transfer rates were established for boiling mechanisms at various positions within the evaporator; a vertical cylinder where small quantities of water were subjected to rapid decompression and the effects measured; and a simple channel for photographic studies of the process.

Boiling in direct-contact water vapour systems is described herein. The vacuum boiling process was found to be controlled by a combination of the water surface temperature and the hydrostatic pressure gradient, these being governed by the water vapour flow geometry between the water surface and ejector suction and convective heat transfer below the boiling region. The contributions of the various boiling regimes to the total heat transfer are discussed. Heat and mass transfer coefficients and their applicability to evaporator design are presented.

ACKNOWLEDGEMENTS

The Author wishes to thank the following people and organisations for their assistance in the compilation of this dissertation:

DeBeers for granting permission to undertake this project.

The University of the Witwatersrand for its financial assistance.

Foundation for Research and Development for its financial assistance.

Professor Sheer and Doctor Jawurek for their advice and guidance.

CONTENTS	Page
DECLARATION	ii
ABSTRACT	iii
ACKNOWLEDGEMENTS	iv
CONTENTS	v
LIST OF FIGURES	vi
LIST OF TABLES	xi
LIST OF SYMBOLS	xii
1 INTRODUCTION	1
1.1 Steam Jet Refrigeration	2
1.2 Heat Transfer Processes in the System	6
1.2.1 The Evaporator	6
1.2.2 The Condensers	6
1.3 Behaviour of Water in a Vacuum	8
1.4 Project Objectives	9
1.5 Dissertation Structure	10
2 LITERATURE SURVEY	12
2.1 Review of Steam Jet Refrigeration	12
2.2 Review of Boiling Theory	17
2.3.1 Introduction and Overview	17
2.3.2 Nucleate Boiling	21
2.3.3 Sub-atmospheric Boiling	26
2.3.4 Flashing	29
3 THEORETICAL ANALYSIS	40
3.1 Evaporator Modelling	40
3.1.1 Basic model	41
3.1.2 Ideal ejector	49
3.1.3 Mass transfer coefficient	51
3.1.4 Coefficients to be investigated	54
3.2 Vacuum Boiling in a Vertical Column	56
3.2.1 Introduction	56
3.2.2 Heat transfer coefficient	60
3.3 Options for the Design of Steam Jet Ejector Systems	61

4	DESIGN OF EXPERIMENTAL SYSTEM AND EXPERIMENTAL PROCEDURE	62
4.1	Design of the Steam Jet Ejector System	62
4.1.1	Ejector design	63
4.1.2	Condenser design	65
4.1.3	Commissioning tests	67
4.2	Evaporator Design	71
4.2.1	Through-flow evaporator design	71
4.2.2	Design of evaporator for the photographic study	75
4.2.3	Vertical cylinder design	77
4.3	Layout of Test Equipment	79
4.3.1	Through-flow evaporator	79
4.3.2	Photographic study	82
4.3.3	Vertical cylinder	83
4.4	Commissioning Tests	84
4.4.1	Through-flow evaporator	84
4.4.2	Vertical Cylinder	86
5	EXPERIMENTAL RESULTS AND OBSERVATIONS	87
5.1	Through-Flow Evaporator	88
5.1.1	Evaporator pressure	88
5.1.2	Temperature gradients	90
5.1.3	Rate of heat transfer	92
5.1.4	Mass transfer coefficients	94
5.2	Photographic Study	101
5.3	Vertical Cylinder	109
5.3.1	Evaporator pressure	114
5.3.2	Temperature distribution	115
5.3.3	Cooling rate	117
5.3.4	Mass transfer	121
5.3.5	Mass transfer coefficient	124
5.3.6	Heat transfer coefficient	127
6	DISCUSSION	130
6.1	Through-Flow Evaporator	130
6.1.1	Evaporator Pressure	130
6.1.2	Temperature distribution	130
6.1.3	Boiling regimes	132
6.1.4	Mass transfer coefficients	132
6.1.5	Evaporator design	133

6.2	Photographic Study	135
6.3	Vertical Cylinder	138
6.3.1	The vacuum boiling process	138
6.3.2	Non-equilibrium fraction	146
6.3.3	Evaporator design	149
6.4	Project Shortcomings	150
6.4.1	Project focus	150
6.4.2	Evaporator design	150
6.4.3	Temperature measurement	150
7	CONCLUSIONS AND RECOMMENDATIONS	151
7.1	Conclusions	151
7.1.1	Through-flow evaporator	151
7.1.2	Photographic study	152
7.1.3	Vertical cylinder	153
7.2	Recommendations	154
APPENDIX A	Assumptions made for the design of Steam Jet Ejectors	
APPENDIX B	EES Equation Listings	
APPENDIX C	Design Options for Steam Jet Ejector Systems	
APPENDIX D	Design Drawings	
APPENDIX E	Instrumentation Calibration Data	
APPENDIX F	Results	
APPENDIX G	Paper : Vacuum Boiling in a Water Vapour Refrigeration System	
REFERENCES		

LIST OF FIGURES

Figure	Page
1.1 : Schematic of a steam jet refrigeration cycle.	3
1.2 : Thermodynamics of a steam jet refrigeration cycle, modified from Tyrer & Meyer [5].	4
1.3 : Pressure enthalpy diagram for steam jet cycle.	5
1.4 : Typical refrigeration system with barometric condenser.	7
2.1 : Typical performance curves.	14
2.2 : Steam jet refrigeration system COP map.	15
2.3 : Variation of Coefficient of Injection with Coefficient of expansion.	16
2.4 : Boiling curve.	18
2.5 : Nucleate boiling.	19
2.6 : Transition boiling.	20
2.7 : Film boiling.	20
2.8 : Sketches of vapour structures in pool boiling.	22
2.9 : Boiling curve for nucleate boiling of water.	23
2.10 : Verification of bulk boiling theory.	25
2.11 : Boiling curve for water at 50 mm Hg.	27
2.12 : Boiling curve for water at 200 mm Hg.	27
2.13 : Schematic of Pressure-Enthalpy diagram during flashing.	29
2.14 : Pressure-time traces showing undershoot.	31
2.15 : Pressure undershoot for varying initial temperature and decompression rates.	32
2.16 : Variation in pressure in the tank (a) and the velocity of steam at the surface of the water layer (b) upon decompression.	34
2.17 : Variation of the saturation and the water temperature during slow depressurization.	35
2.18 : Reaction of water drops to superheat.	35
2.19 : Variation of pressure in the flash chamber with time.	36
2.20 : Variation of nonequilibrium fraction with time.	37
2.21 : Heat transfer dependence on liquid level.	38
3.1 : Evaporator sketch with boundary.	41
3.2 : EES program algorithm.	44
3.3 : Evaporator pressure as a function of water flow rate.	45
3.4 : Evaporator ratio of heat transfer as a function of water flow rate.	46
3.5 : Evaporator pressure as a function of inlet temperature.	47
3.6 : Evaporator heat exchange rate as a function of inlet temperature.	47
3.7 : Combined effect of inlet temperature and water flow rate on evaporator pressure.	48

3.8	: Combined effect of inlet temperature and water flow rate on heat transfer rate.	48
3.9	: Idealised ejector.	49
3.10	: Cooling capacity as a function of water flow rate for varying temperatures, idealised ejector.	50
3.11	: Evaporator pressure for an idealised system.	51
3.12	: Variation of saturation pressure with temperature.	56
3.13	: Saturation Temperatures for increasing pressure and various levels of water.	57
3.14	: Boiling penetration depths, extracted from Miyatake[40].	58
4.1	: Steam Jet Refrigeration rig.	63
4.2	: Photograph of completed steam jet refrigeration system.	66
4.3	: Temperature distribution in the system, compared to previous	67
	10	
4.4	: Surface boiling of a pool of water.	68
4.5	: Ice layer at the surface.	69
4.6	: Through-flow evaporator sketch.	74
4.7	: Evaporator used for Photographic study.	76
4.8	: Evaporator used for Vertical cylinder test.	78
4.9	: Photograph of the direct contact evaporator during testing.	79
4.10	: Piping layout for through flow evaporator.	80
4.11	: Layout of instrumentation used for the flow-through direct contact evaporator.	81
4.12	: A photograph of the decompressing valve.	82
4.13	: Layout of instrumentation used in vertical cylinder testing.	83
5.1	: Evaporator pressure as a function of inlet temperature, mean flow rate = 0.0245 kg/s.	89
5.2	: Evaporator pressure as a function of inlet temperature, mean flow rate = 0.0671 kg/s.	89
5.3	: Temperature distribution within the through-flow evaporator, mean flow rate = 0.0671 kg/s.	90
5.4	: Temperature distribution within the direct contact evaporator, mean flow rate = 0.0584 kg/s.	90
5.5	: Temperature distribution within the through flow evaporator, mean flow rate = 0.0245 kg/s.	91
5.6	: Percentage contribution to total heat transfer by the flashing boiling regime, mean flow rate = 0.0671 kg/s.	92
5.7	: Percentage contribution to total heat transfer by the flashing boiling regime, mean flow rate = 0.0584 kg/s.	93
5.8	: Percentage contribution to total heat transfer by flashing boiling regime, mean flow rate = 0.0245 kg/s.	93
5.9	: Bulk mass transfer, mean flow rate 0.0671 kg/s.	94
5.10	: Bulk mass transfer, mean flow rate 0.0584 kg/s.	95
5.11	: Bulk mass transfer, mean flow rate 0.0244 kg/s.	95
5.13	: Flashing mass transfer, mean flow rate 0.0671 kg/s.	96

5.14 : Flashing mass transfer, mean flow rate 0.0588 kg/s.	97
5.15 : Flashing mass transfer, mean flow rate 0.0244 kg/s.	97
5.16 : Non-dimensional bulk mass transfer as a function of superheat, eqns. 5.1	99
5.17 : Non-dimensional flashing mass transfer as a function of superheat, eqns 5.2.	99
5.20 : Initial still pool of water, $t=0.0$ s.	102
5.21 : Valve opened, boiling initiation, $t=1.6$ s.	103
5.22 : Flashing in bulk of the liquid, $t= 6.1$ s.	103
5.23 : Flashing decreasing in lower regions, $t=9.1$ s.	104
5.24 : Boiling at liquid surface, $t=16.4$ s.	105
5.25 : Water surface calm, $t=19.0$ s.	105
5.26 : Secondary surface boiling, $t=21.4$ s.	105
5.27 : Secondary surface boiling, $t=24.3$ s.	106
5.28 : Secondary surface boiling, $t=27.5$ s.	106
5.29 : Water surface calm, $t=37.9$ s.	107
5.30 : Initiation of third surface boiling, $t=40.7$ s.	108
5.31 : Temperature measured by LM-35 compared to the temperature measured by a thermocouple.	110
5.32 : Temperature at various depths below water surface as a function of time.	111
5.33 : Temperature as a function of time, preheated cylinder.	112
5.34 : Temperature distributions. 13°C input, not heated.	113
5.35 : Evaporator pressure as a function of time.	114
5.36 : Evaporator pressure as a function of time.	115
5.37 : Temperature distribution with time, 15cm height, 19°C initial temperature.	115
5.38 : Temperature distribution with time, 40°C initial temperature.	116
5.39 : Cooling rates for varying input temperatures.	117
5.40 : Superimposed results of cooling rates.	118
5.41 : Rate of change of temperature as a function of bulk temperature for various initial water temperatures.	119
5.42 : Rate of change of temperature as a function of surface temperature.	120
5.43 : Mass transfer and change in temperature as a function of time	121
5.44 : Mass transfer rate and evaporator pressure as a function of time, 19°C input temperature, 15 cm height.	122
5.45 : Mass transfer rate and evaporator pressure as a function of time, 19°C input temperature, 15 cm height.	122
5.46 : Mass transfer rate for various initial temperatures for 15 cm column of water.	123
5.47 : Mass transfer coefficient based on surface temperature saturation pressure.	124
5.48 : Maximum mass transfer rate, 15 cm liquid height.	125
5.49 : Mass transfer rates for 12 cm liquid height.	125
5.50 : Non-dimensional mass transfer rate as a function of surface temperature.	126

5.14 : Flashing mass transfer, mean flow rate 0.0588 kg/s.	97
5.15 : Flashing mass transfer, mean flow rate 0.0244 kg/s.	97
5.16 : Non-dimensional bulk mass transfer as a function of superheat, eqns. 5.1.	99
5.17 : Non-dimensional flashing mass transfer as a function of superheat, eqns 5.2.	99
5.20 : Initial still pool of water, t=0.0 s.	102
5.21 : Valve opened, boiling initiation, t=1.6 s.	103
5.22 : Flashing in bulk of the liquid, t= 6.1 s.	103
5.23 : Flashing decreasing in lower regions, t= 9.1 s.	104
5.24 : Boiling at liquid surface, t=16.4 s.	105
5.25 : Water surface calm, t=19.0 s.	105
5.26 : Secondary surface boiling, t=21.4 s.	105
5.27 : Secondary surface boiling, t= 24.3 s.	106
5.28 : Secondary surface boiling, t=27.5 s.	106
5.29 : Water surface calm, t=37.9 s.	107
5.30 : Initiation of third surface boiling, t= 40.7 s.	108
5.31 : Temperature measured by LM-35 compared to the temperature measured by a thermocouple.	110
5.32 : Temperature at various depths below water surface as a function of time.	111
5.33 : Temperature as a function of time, preheated cylinder.	112
5.34 : Temperature distributions, 13°C input, not heated.	113
5.35 : Evaporator pressure as a function of time.	114
5.36 : Evaporator pressure as a function of time.	115
5.37 : Temperature distribution with time, 15cm height, 19°C initial temperature.	115
5.38 : Temperature distribution with time, 40°C initial temperature.	116
5.39 : Cooling rates for varying input temperatures.	117
5.40 : Superimposed results of cooling rates.	118
5.41 : Rate of change of temperature as a function of bulk temperature for various initial water temperatures.	119
5.42 : Rate of change of temperature as a function of surface temperature.	120
5.43 : Mass transfer and change in temperature as a function of time	121
5.44 : Mass transfer rate and evaporator pressure as a function of time, 19°C input temperature, 15 cm height.	122
5.45 : Mass transfer rate and evaporator pressure as a function of time, 19°C input temperature, 15 cm height.	122
5.46 : Mass transfer rate for various initial temperatures for 15 cm column of water.	123
5.47 : Mass transfer coefficient based on surface temperature saturation pressure.	124
5.48 : Maximum mass transfer rate, 15 cm liquid height.	125
5.49 : Mass transfer rates for 12 cm liquid height.	125
5.50 : Non-dimensional mass transfer rate as a function of surface temperature.	126

5.51 : Variation of vapour mass transfer rate over liquid flow rate with temperature.	127
5.52 : Heat transfer coefficient 5 °C input temperature and 15 cm height.	128
5.53 : Heat transfer coefficient 13 °C input temperature.	128
5.54 : Heat transfer coefficient 19 °C input temperature.	129
6.1 : Pressure distribution 15 cm below liquid surface.	139
6.2 : Pressure distribution 12 cm below liquid surface.	139
6.3 : Pressure distribution 9 cm below liquid surface.	140
6.4 : Pressure distribution 6 cm below liquid surface.	140
6.5 : Sub-cooled pressure distribution for convection.	141
6.6 : Pressure lines for 9 cm height, at 3 cm, 5 °C input.	142
6.7 : Pressure lines, 13 °C input.	143
6.8 : Pressure lines, 19 °C initial water temperature.	143
6.9 : Pressure lines, 40 °C initial temperature 9 cm height, at 6 cm.	144
6.10 : Pressure lines for 40 °C input and 9 cm height, at 3 cm.	145
6.11 : NEF as a function of time, 40 °C initial temperature 15 cm liquid height.	146
6.11 : NEF as a function of time, 40 °C initial temperature 12 cm liquid height.	147
6.11 : NEF as a function of time, 40 °C initial temperature 9 cm liquid height.	147
6.14 : NEF as a function of time, 40 °C initial temperature 6 cm liquid height.	148
6.11 : NEF as a function of time, 40 °C initial temperature 3 cm liquid height.	148

LIST OF TABLES

4.1 : Ejector design sizes.	63
4.2 : Resized ejector specifications.	65
4.3 : Leakage test results.	86
5.1 : Through-flow evaporator test conditions	88
5.2 : Test conditions	101
5.3 : Times of specific photographs	101
5.4 : Time span of specific regimes	108
5.4 : Vertical cylinder test conditions	109

NOMENCLATURE

A	Surface area	m^2
C_p	Specific heat	kJ/kgK
d	Diameter	m
e	Specific energy associated with a elementary mass dm	kJ/kg
E	Youngs modulus	Gpa
E_c	Total specific energy of a control volume	kJ
g	Gravitational constant	m/s^2
h	Enthalpy	kJ/kg
h _j	Heat transfer coefficient at point j	kW/m^2
j	Mass flux	$kg/s/unit\ area$
K_m	Mass transfer coefficient	$kg/s\ m^2\ kPa$
KM_{bulk}	Bulk mass transfer coefficient	$kg/kg\ K$
KM_{flash}	Flashing mass transfer coefficient	$kg/kg\ K$
m	Mass	kg
M	Molecular weight	18.015 $kg/kmol$
$M_{L(OUT)}$	Liquid mass flow rate	kg/s
M_j	Liquid mass at point j	kg
m_{vapor}	Vapour mass flow rate	kg/s
p	Pressure	kPa
P_e	Evaporator pressure	kPa abs.
ΔP	Difference between evaporator and atmospheric pressure	kPa
Q	Heat transfer	kW
R	Universal gas constant	8.314 $kJ/kmol\ K$
<i>l</i>	Thickness	m
T	Temperature	K
T_{inlet}	Flow through evaporator inlet water temperature	$^{\circ}C$
T_{out}	Flow through evaporator outlet water temperature	$^{\circ}C$
T_{evap}	Saturation temperature corresponding to evaporator press.	$^{\circ}C$
T_l	Liquid temperature	K
T_v	Vapour temperature	K
u	Internal energy	kJ/kg
V	Velocity	m/s
v	Specific volume	m^3/kg
z	Elevation	m

For the work of *Han et al* [22] & [23]

Ra	Rayleigh number.
Nu	Nusselt number.
h	Heat transfer coefficient
D	Area of the heating surface
C_p	Specific heat of the liquid.
α	Thermal diffusivity of the fluid.
γ	Liquid volumetric thermal expansion coefficient
ρ	Density of the liquid.
ν	Viscosity of the liquid
g	Gravitational constant.
T_w	Wire temperature.
T_∞	Bulk water temperature

For the work of *Belyayev and Artemenko* [41]

Nu	Thermal nusselt number
Nu_{D_1}	Diffusion Nusselt number.
Ri	Richman number.
Gu	Guchman number
ζ	Evaporation rate.
α	Heat transfer coefficient.
l	Characteristic length.
B	Mass transfer coefficient.
λ	Thermal conductivity.
D	Diffusion coefficient for water.
T_{am}	Ambient temperature
T_{loc}	Water surface temperature.

For the work of *Miyatake* [40], [47] & [48]

NEF (t)	Non equilibrium fraction.
$T_b(t)$	Bulk liquid temperature at time t.
T_{b0}	Initial bulk liquid temperature
T_{sat}	Saturation temperature corresponding to the evaporator pressure
K	Flashing coefficient and has the units $\text{kg mole}^{-1}(\text{m}^3 \cdot \text{hr atm})$

CHAPTER 1

INTRODUCTION

This chapter briefly introduces the topic of water vapour refrigeration, explains the need for research in this field and states the specific aims and objectives of this investigation.

Due to the alarming rate of ozone depletion in the stratosphere, the international community introduced the Montreal Protocol to phase out the production and use of chlorofluorocarbon (CFC) based refrigerants and propellants [1].

As a result, there is a global need for the development of replacement refrigerants or means of refrigeration, to ensure no future pollution or environmentally harmful repercussions. One such means of refrigeration is water vapour refrigeration, i.e. the use of water as the sole fluid in a refrigeration cycle. In such systems water evaporates at low pressures and so provides cooling. The method used to provide the vacuum could be any compression device able to compress high volumetric flow rates of water vapour over large pressure ratios. This requirement is due to cooling taking place at low pressures where the specific volume of water is very high. A device well suited for this task is the steam jet ejector. In a steam jet refrigeration system water is used both as the refrigerant and as the means of providing the vacuum. The use of compression devices other than steam jet ejectors is not considered in this dissertation as this would form a study in its own right.

1.1 Steam Jet Refrigeration

Steam-jet vacuum refrigeration systems were first investigated prior to 1901 by *Leblanc* and *Parsons* [2]. Although the primitive nature of thermo-compressors and ejector design limited their application for cooling in the early part of this century, by 1948 the use of steam jet refrigeration encompassed a wide range of industrial applications, reportedly even being used for air conditioning on the British vessels Queen Mary, Queen Elizabeth and the Empress of Britain[3]. Typical uses of the systems by 1969 included : gas absorption, comfort air conditioning, beverage cooling, chilling of leafy vegetables, crystallisation of chemicals and foods and the dehydration of pharmaceutical products such as antibiotics [4]. Although the refrigerating temperatures in such systems are typically limited to the freezing point of water, in many instances where conventional refrigerants are used, water is used as a transfer medium restricting temperatures to above freezing..

A typical steam jet refrigeration cycle (Figure 1.1) is similar to conventional refrigeration cycles, consisting of an evaporator, a compression device, a condenser, an expansion device and a refrigerant. The mechanical compressor is however replaced by a steam jet ejector. The cooling effect is produced by the continuous vaporization of part of the water in the evaporator at a low absolute pressure. The enthalpy of vaporization for the evaporated water is furnished by the remaining water, thereby cooling it. The temperature achieved is dependent on the vacuum that is maintained, which in turn depends on the energy that is supplied to the ejector-condenser system.

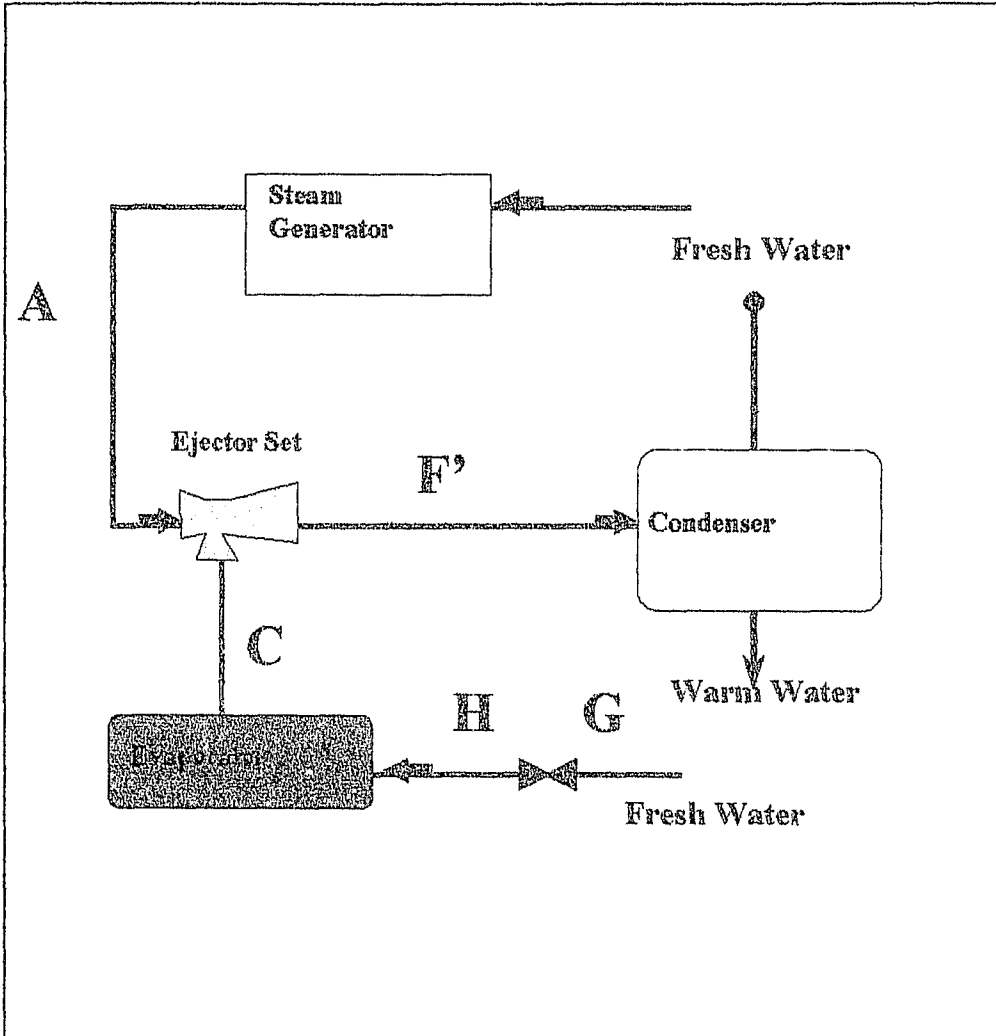


Figure 1.1: Schematic of a steam jet refrigeration cycle.

The thermodynamic cycle is depicted by Figure 1.2 [5]. The motive steam leaving the generator is represented by point **A**. Ideally, the steam would expand isentropically through the ejector nozzle to the evaporator temperature (point **B**). Due to inefficiencies in the expansion process the expansion is irreversible to point **B'**. Further losses occur as the steam transfers kinetic energy to the flash vapour, leading to steam conditions **D** before mixing.

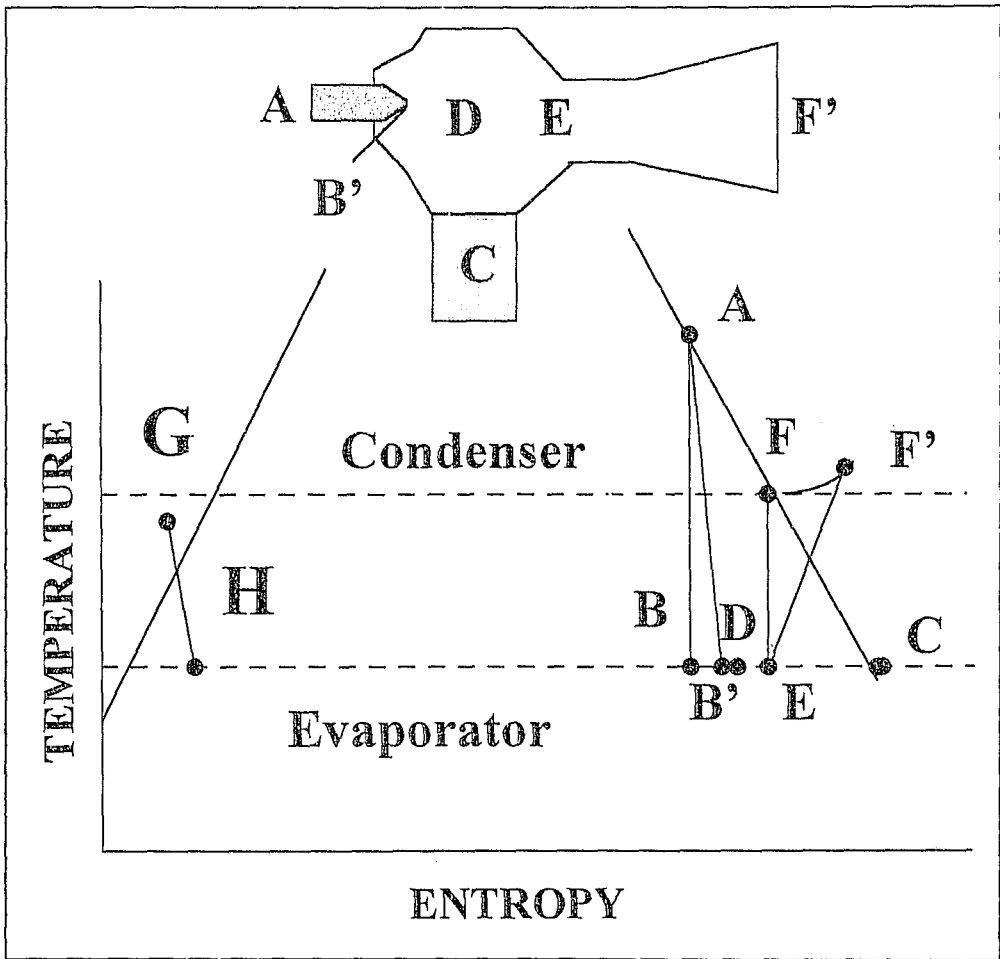


Figure 1.2: Thermodynamics of a steam jet refrigeration cycle, modified from Tyrer [5].

Water enters the evaporator at point **G**, expanding to point **H**. The vapour produced in the evaporator is assumed to be in thermal equilibrium with the water, and is represented by the saturation point **C** of the evaporator temperature. Water vapour is entrained in the mixing section and combines with the motive steam (point **D**) to give the resulting condition at point **E** before compression. Inefficiencies in the diffuser lead to an irreversible compression to point **F'** on the isobar of the condenser pressure, deviating from the ideal isentropic compression, point **F**.

The pressure-enthalpy diagram for the cycle is shown in figure 1.3[6]. The cycle shown includes feed-back or make-up water, expanding isenthalpically along 1-8.

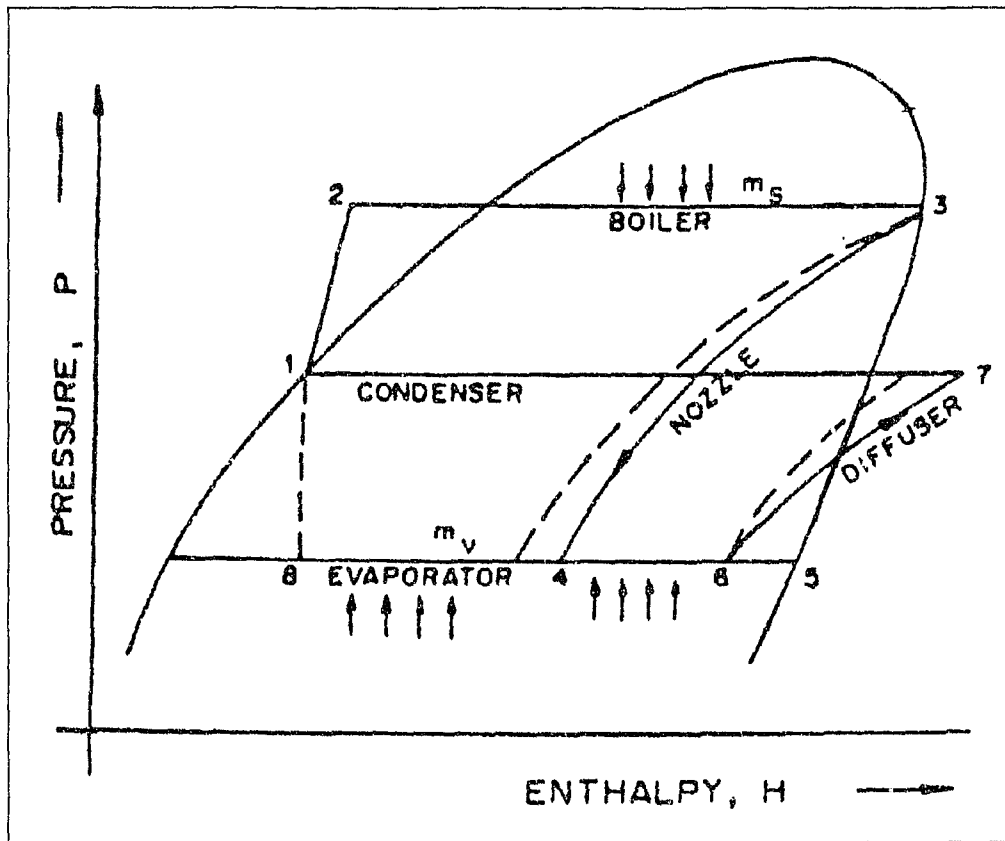


Figure 1.3: Pressure enthalpy diagram for steam jet cycle[6]

1.2 Heat Transfer Processes in the System

1.2.1 The Evaporator

The evaporator is typically a vessel which provides a large water surface area for efficient evaporative cooling action[7]. Two common means of maximising water surface are cascades and water sprays. The evaporator should be of sufficient size to allow the vapour to freely separate from the liquid. Spray systems are susceptible to water carry-over into the ejectors. Evaporators can be divided into two types: those for *Open* and *Closed Chilled Water Systems*. In open chilled water systems the refrigerant water in the evaporator is circulated directly to the cooling load, while in closed systems the refrigerant water is recirculated within the evaporator over a coiling coil. The open system has the advantage of having one less stage of heat transfer. The evaporator temperature need therefore not be as low as in a closed system. Furthermore it will later be shown that the heat transfer coefficients on the coils in such systems decrease with decreasing pressure.

1.2.2 The Condensers

The ejectors compress the water vapour and discharge into condensers. The condensers condense the water vapour and steam. Non-condensibles in the condenser are removed by the next stage of compression. Condensers can be one of three basic types : surface condensers, evaporative condenser or barometric condensers.

1.2 Heat Transfer Processes in the System

1.2.1 The Evaporator

The evaporator is typically a vessel which provides a large water surface area for efficient evaporative cooling action [7]. Two common means of maximising water surface are cascades and water sprays. The evaporator should be of sufficient size to allow the vapour to freely separate from the liquid. Spray systems are susceptible to water carry-over into the ejectors. Evaporators can be divided into two types: those for *Open* and *Closed Chilled Water Systems*. In open chilled water systems the refrigerant water in the evaporator is circulated directly to the cooling load, while in closed systems the refrigerant water is recirculated within the evaporator over a coiling coil. The open system has the advantage of having one less stage of heat transfer. The evaporator temperature need therefore not be as low as in a closed system. Furthermore it will later be shown that the heat transfer coefficients on the coils in such systems decrease with decreasing pressure.

1.2.2 The Condensers

The ejectors compress the water vapour and discharge into condensers. The condensers condense the water vapour and steam. Non-condensibles in the condenser are removed by the next stage of compression. Condensers can be one of three basic types: surface condensers, evaporative condenser or barometric condensers.

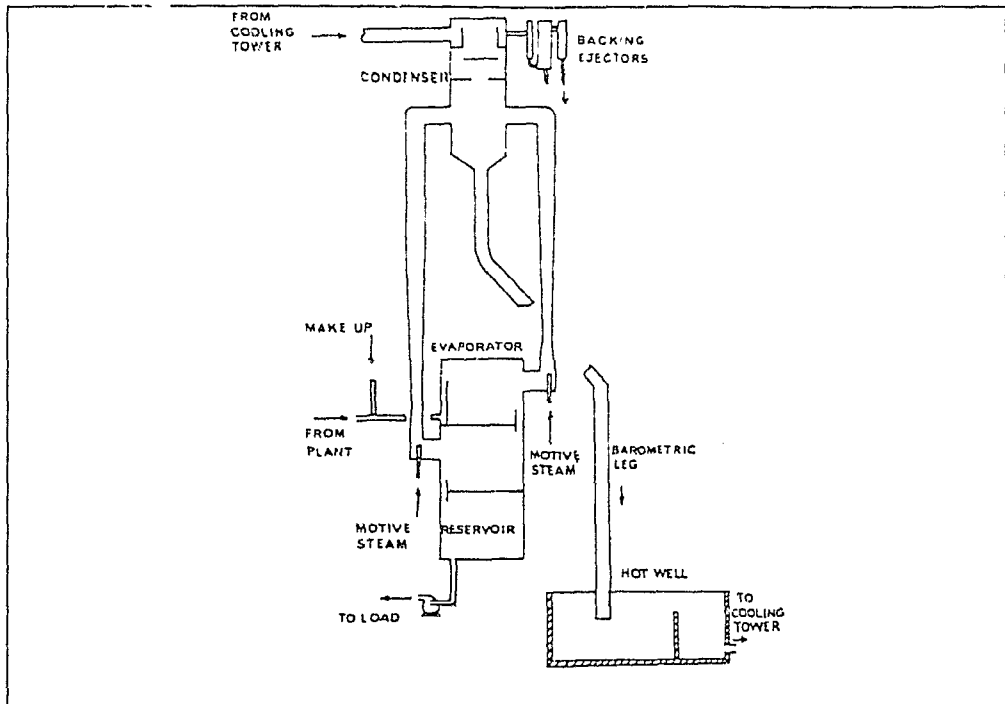


Figure 1.4: Typical refrigeration system with barometric condenser [8]

Barometric condensers find application where there are no space limitations and low initial cost is a criterion. They have the advantages of simple design and construction and are less susceptible to fouling. They have a high efficiency in systems where the condensibles need not be recovered. A typical system using a barometric condenser is shown in figure 1.4[8]. The tail pipe at the bottom of the condenser ('barometric leg') is used to balance a column of water between the condenser pressure and atmospheric pressure. Various methods are used in condensing the vapour pumped into the condenser. Of these, direct contact counterflow systems provide greater cooling, allowing more of the condensibles to be removed. Spray nozzles or baffle plates are used to provide adequate mixing of the vapour and the cooling water. Baffle plates tend to increase the pressure load on the second and third ejectors. Spray nozzles achieve a high interfacial surface area, leading to very efficient liquid-vapour contact for heat and mass transfer[9].

1.3 Behaviour of Water in a Vacuum

Although the thermophysical properties of water are well documented, the actual boiling process under vacuum within the evaporator has not been the subject of much research. Most boiling research has centred around heat transport from heated surfaces, with attempts being made to relate the heat transfer rates to conditions such as superheat of the plate, liquid height and ambient pressure, and physical phenomena such as bubble departure size, frequency of bubble generation and rise velocity. The effects that various geometrical and physical characteristics of the plate have on the boiling process have also been investigated. Some of this research has focused on sub-atmospheric boiling or vacuum boiling of pool water off a heated plate. (See Chapter 2 for a review of the pertinent literature.) In a direct-contact water vapour refrigeration system there is no heat transfer surface as such, as the bulk of the water is the primary heat source. Conventional boiling theory does not adequately describe this form of boiling.

In order to design an efficient evaporator the criteria for sizing need to be established. The manner in which the water boils and the contributions of the boiling mechanisms to the cooling process also need to be quantified, as do the cooling rates involved. An investigation of the vacuum boiling of water in a water vapour refrigeration system would therefore aid the development of this form of refrigeration.

1.4 Project Objectives

The specific objectives of this project are as follows :

- 1) To identify and quantify the contribution to the heat transfer process of the boiling mechanisms in a direct contact vacuum evaporator.
- 2) To conduct a basic photographic study of the vacuum boiling process with the aim of visualising the boiling mechanisms.
- 3) To investigate the effect of varying inlet water flow rates and temperatures on the heat transfer of a vacuum evaporator.
- 4) To investigate the boiling and heat transfer mechanisms associated with the vacuum boiling of a body of water in a closed container, with the aim of establishing the effect of initial temperature on heat and mass transfer rates during decompression.
- 5) To derive a "mass transfer coefficient" and judge its applicability in the design of direct contact vacuum evaporators.
- 6) To relate results to those of previous researchers.

1.5 Dissertation Structure

The chapters included in this dissertation are as follows:

Chapter 1 : INTRODUCTION

Chapter One introduces the subject of water vapour refrigeration and motivates and states the project objectives.

Chapter 2 : LITERATURE SURVEY

Chapter Two reviews literature pertinent to the vacuum boiling of water in an evaporator and to some other aspects of steam jet refrigeration.

Chapter 3 : THEORY AND MODELLING

Chapter Three considers the thermodynamics and modelling of the vacuum boiling of water in a through flow evaporator and in a vertical column evaporator.

Chapter 4 : DESIGN OF EXPERIMENTAL SYSTEM AND EXPERIMENTAL PROCEDURE

In chapter Four the design and development of the experimental equipment is presented. Preliminary tests are discussed, as are the selection and calibration of the instrumentation. The equipment layout, initial testing and experimental procedure for the various tests conducted are presented in this chapter.

Chapter 5 : RESULTS AND OBSERVATIONS

The results and observations of the three test methods are presented in this chapter. Photographs obtained in the photographic study are included.

Chapter 6 : DISCUSSION

Chapter Six is a discussion of the results and observations presented in Chapter Six. Results obtained are compared with theory presented in Chapter Three

Chapter 7 : CONCLUSION AND RECOMMENDATIONS

Conclusions drawn in Chapter Six are presented in Chapter Seven. These are related to the project objectives and recommendations for further work are made.

CHAPTER 2

LITERATURE SURVEY

The literature surveyed in this chapter covers steam jet refrigeration, steam jet ejectors and boiling phenomena, with the aim of presenting a broad review of these topics, as well as highlighting any information which has a direct bearing on the heat transfer processes occurring in the evaporator of any water-vapour refrigeration system.

2.1 Review of Steam Jet Refrigeration

Spencer[10] proposed a modified steam jet cycle, with conventional water-cooled condensers being replaced by evaporative condensers. Substantial reductions in steam and water consumption were reported. It was noted that barometric condensers had the advantage of having no heat exchange surfaces and are not susceptible to fouling.

Munday and *Bagster*[11] developed ejector theory with particular reference to steam jet refrigeration performance. They recommended that systems be designed for the most severe conditions in order to maximize efficiency. Further work by *Munday* and *Bagster*[12] led to the

development of a new theory of ejector behaviour. Agreement between the theory and plant scale tests was achieved. It was reported that the water in the evaporator is in equilibrium with its vapour and that the saturation pressure of the chilled water can be taken as the pressure of the evaporator. The recommendation was made that once the required condenser pressure is established, it is necessary to assume a difference between the exit condenser water temperature and the saturation temperature corresponding to the condenser pressure. This value may be kept fairly low in a barometric condenser as compared with surface condensers. Design graphs were plotted of system cooling capacity versus condenser pressure for varying evaporator pressure. Performance could be seen to increase greatly with decrease in condenser pressure and hence cooling water temperature (see figure 2.1). The ejector was described as a constant capacity device. An increase in motive steam pressure was found not to increase the ejector's capacity beyond a maximum. It was noted that less motive steam is required in the cooler months when cooler condenser water is available. The efficiency of the ejectors was shown to be dependent on whether the evaporator reached design conditions. It was concluded that systems should be designed for the most often prevailing conditions rather than the most severe, as previously stated.

An investigation into the use of water-vapour refrigeration, in order to cool mine service water, was conducted by *Shone*[13]. A comparison between the coefficients of performance of steam jet and mechanical compression systems was made and it was concluded that, although the steam jet system could chill water to its freezing point, its low coefficient of performance prevented an economic advantage over conventional CFC or ammonia vapour compression systems. It was further concluded that the use of multiple ejectors was essential in improving system energy efficiency.

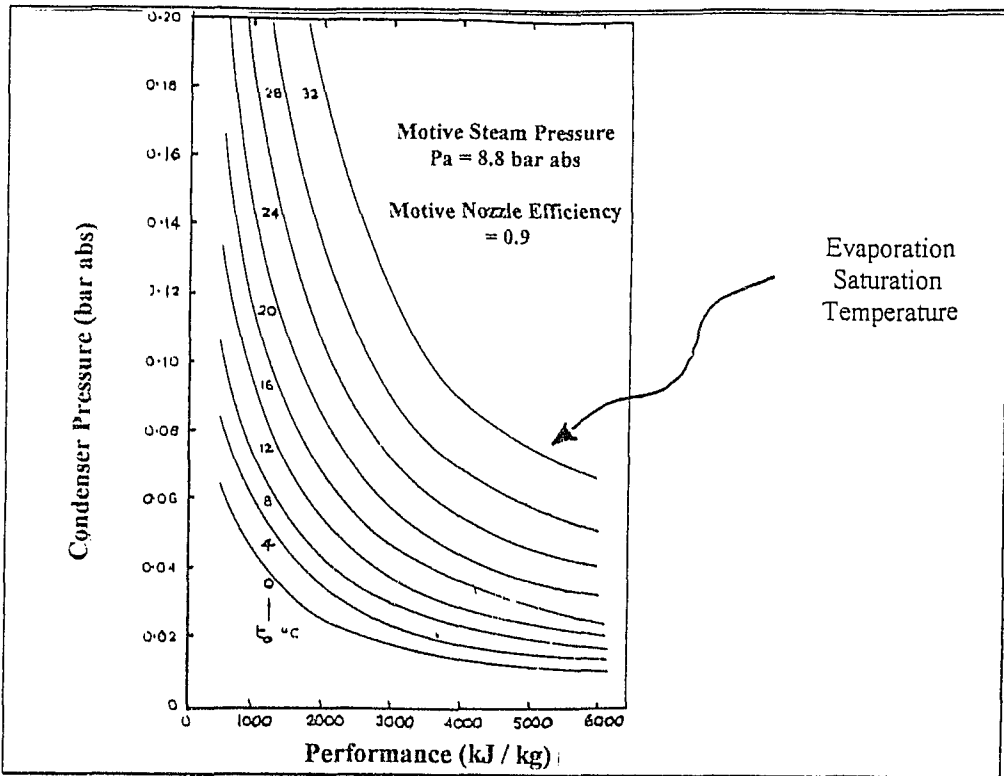


Figure 2.1 : Typical performance curves [12]

Huang et al [14] presented a design analysis of steam jet refrigeration systems. Various simulations were carried out yielding performance maps of system coefficients of performance (COP). A typical map relating condenser temperature to that of generator and evaporator temperatures is shown in figure 2.2. Of particular interest is the strong dependence, in both Figure 2.1 and 2.2, of the cooling capacity on both evaporator temperature and condenser temperature.

Abdel-Aal et al [15] described other options of mass and energy input for steam jet refrigeration systems. The system used a solar collector for steam generation. Various relationships were provided for determining ejector dimensions and for determining the effect of motive steam rate, chilled water temperature and condenser pressure on the system's performance.

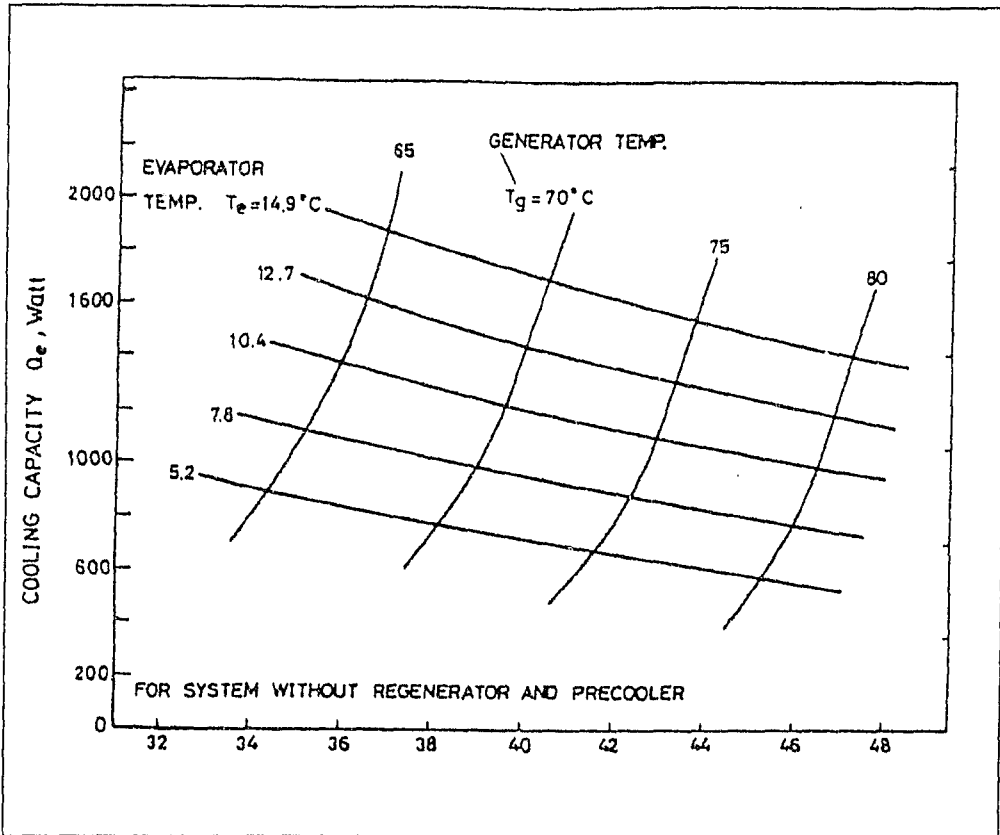


Figure 2.2: Steam jet refrigeration system COP map [14]

Vil'der[16] presented a paper on a simplified method of calculating steam-jet ejector vacuum pumps. The method was claimed to permit the rapid and precise calculation of multistage steam jet ejector pumps. The method of calculation and the underlying assumptions are summarised in appendix A. Using Vil'der's data it is possible to optimise the steam consumption for a required overall compression ratio. Figure 2.3 shows the variation of coefficient of injection (ratio of the mass of the medium to be pumped to that of the working steam) with degree of expansion (ratio of working steam pressure to pre-ejector pressure) for varying compression ratios (the discharge pressure divided by the ejector suction pressure). Utilizing two ejectors with two stages of evaporation, as opposed to a single ejector with a high compression ratio, can be shown to affect

be shown to affect considerable savings in steam consumption. This would only apply where the condenser pressure is high due to the temperature of the condenser cooling water being a limiting factor (particularly in warmer areas). This chart was used in the design of the ejector set used for this investigation.

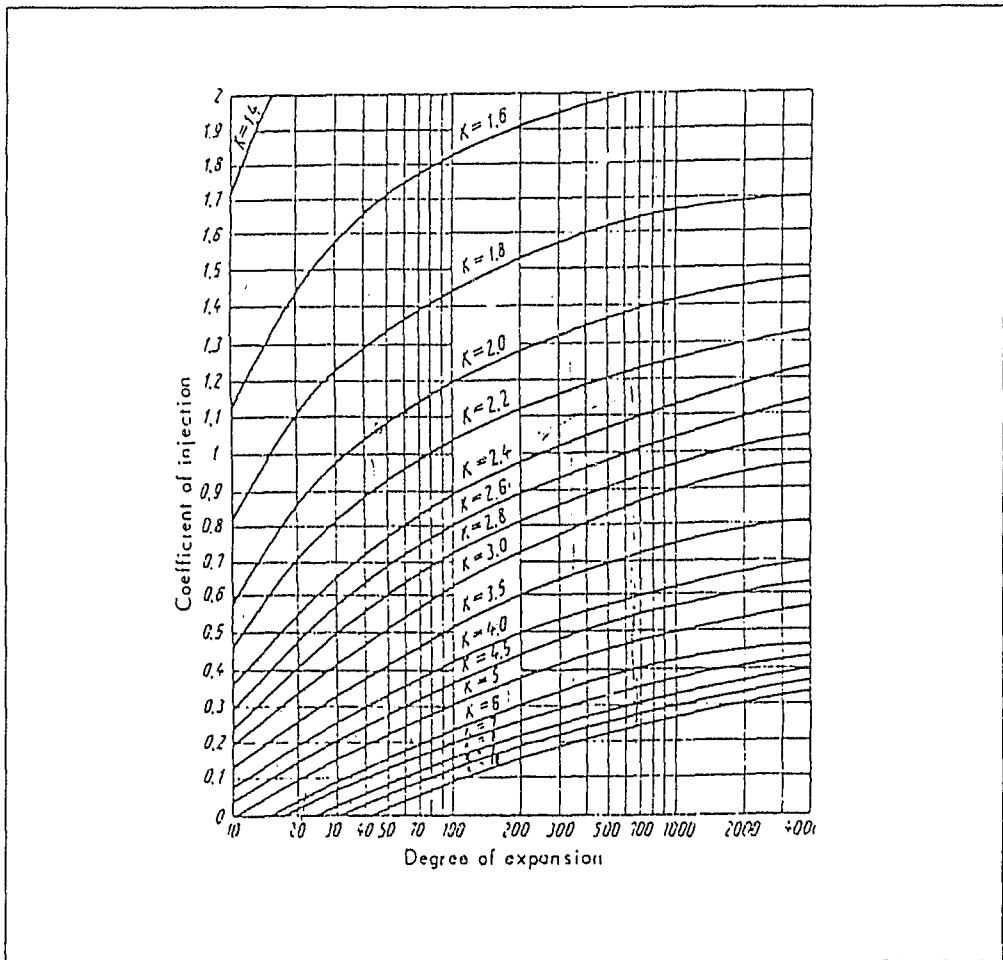


Figure 2.3 : Variation of Coefficient of Injection with Coefficient of expansion [16].

2.2 : A Brief Review of Boiling Heat Transfer

There are two basic types of boiling, namely *pool* and *flow* boiling. Pool boiling occurs when a heating surface is submerged in a pool of initially quiescent liquid. Flow boiling constitutes the boiling of fluid in a flowing stream. The survey of literature here focuses primarily on pool boiling and boiling at sub-atmospheric pressures as it is felt that the vacuum boiling of water will be related most closely to these aspects.

2.3.1 Introduction and Overview

The various regimes of pool boiling can be explained from the typical boiling curve in figure 2.4[17]. The region depicted between *O-P* is the region where heat transmission occurs only by convection. *A-Q* represents *nucleate boiling*, where superheated liquid near the wall evaporates, forming bubbles at nucleation sites such as tiny pits or scratches. The bubbles nucleate from a pre-existing gas phase which is trapped and stabilized in the nucleation sites. The bubbles move to the liquid surface and increase the convective heat transfer by agitating the liquid near the surface. This region is typified by high rate of heat transfer for a small temperature difference between heating surface and liquid. There are two sub-regimes of nucleate boiling, namely *local* and *bulk boiling*. Local boiling occurs when a heated surface is submerged in a sub-cooled liquid and bubbles condense locally (*P-A*). Bulk boiling is common in saturated liquid where bubbles do not collapse.

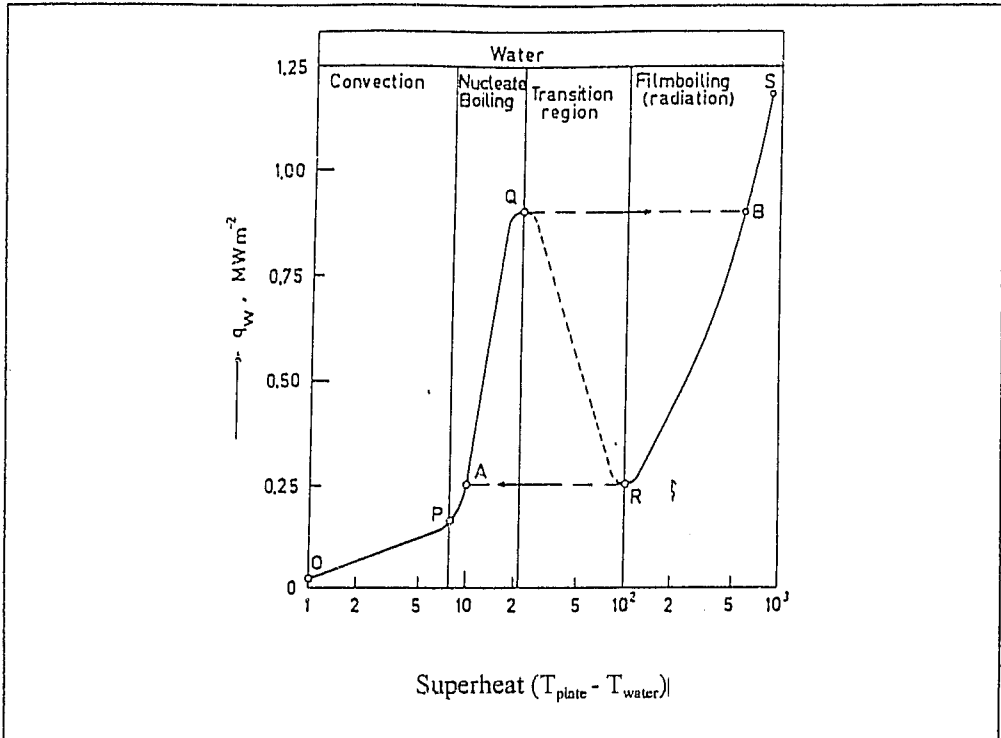


Figure 2.4 : Boiling Curve [17]

The generation of vapour bubbles causes a periodic disturbance of the superheated thermal boundary layer, by displacing liquid into the cooler bulk liquid, followed by a flow of cold liquid to the heating surface which results in a high rate of heat transfer. When the population of bubbles becomes too high, at some heat flux point Q , the out-going bubbles obstruct the incoming liquid and an insulating vapour layer is formed on the heating surface. This results in a lower heat flux and an increase in heating surface wall temperature. This phenomenon is generally termed *boiling crisis* or *burn out*. In the region Q - R *transition boiling* occurs, where the heating surface is alternatively covered by a vapour blanket and a liquid layer, resulting in an oscillating surface temperature. R - S represents the region of *stable film boiling* where a stable vapour layer is formed on the heating surface.

The range of the boiling curve of interest for most practical applications is that of nucleate boiling where high heat transfer rates can be achieved at relatively low surface temperatures. Figures 2.5-2.7 illustrate the various boiling regimes. It can be seen that by examining the nature of the bubbles generated one can, in principle, estimate the relative magnitude of the heat transfer at a given stage in the boiling process.

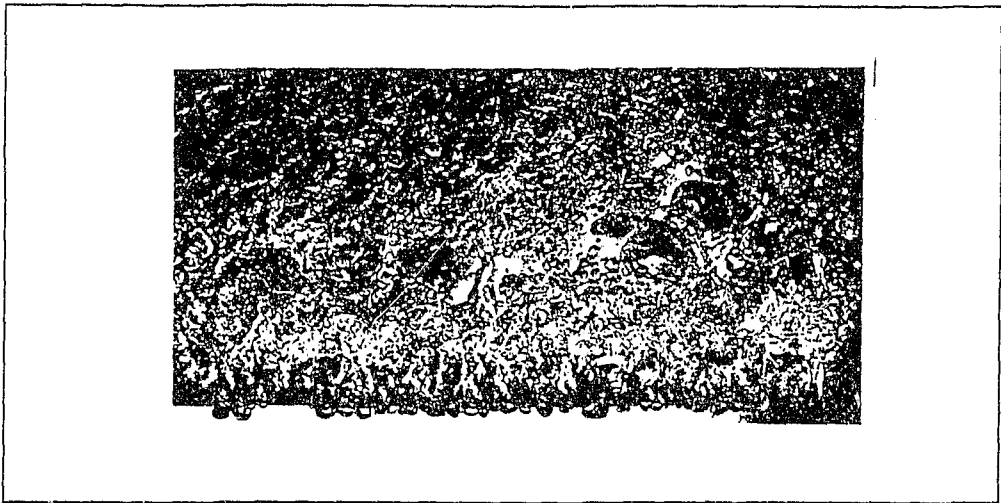


Figure 2.5 : Nucleate boiling [25]



Figure 2.6 : Transition boiling [25]



Figure 2.7 : Film boiling [25]

2.3.2 Nucleate Boiling

Gaertner[18] produced a photographic study of nucleate pool boiling. A metal surface was electrically heated in a glass vessel. The vapour produced was condensed in a tube and shell heat exchanger and was heated to saturation temperature before being returned to the boiler. The roughness of various heating surfaces was measured. Thermocouples were located in various parts of the apparatus to measure average temperature profiles and the saturation temperature of the liquid was measured with a thermocouple suspended above the heat-transfer surface. High speed motion pictures of boiling were taken. The nucleate boiling regime was found to be comprised four regions.

The first region was that of discrete bubble growth, where nearly spherical or slightly tear drop shaped bubbles left the surface. Immediately above the surface, the bottom of the bubbles advanced upward causing them to become bell shaped, folding over themselves as they rose. Bubbles initiated closely on the surface tended to separate as they rose. As the temperature of the surface was raised, so the population density of nucleation sites was observed to increase. The relation between active site population and heat flux was established.

As the heat flux increased, the boiling mechanism moved into the second sub-regime: *The first transition region*. Vertical columns of vapour, consisting of up to four coalesced bubbles, were seen to appear at few nucleation sites where discrete bubbles had previously been generated.

A further increase in heat flux saw an increase in the number of vapour columns formed. The bubbles were seen to not only coalesce at the same activation site but also between two or more neighbouring active sites, leading to the formation of "vapour mushrooms". When these mushrooms grew large enough for the buoyancy force to overcome the surface tension force holding it to the surface, they broke away at the stems and rose from the surface. Vapour mushrooms passing over vapour columns led to coalescence, with the column becoming another stem feeding the mushroom.

The last sub-regime observed was the *second transition region* where stems of vapour mushrooms became hydrodynamically unstable. Stems collapsed, causing local vapour patches to form on the heat-transfer surface, decreasing the number of active sites and reducing the rate of heat transfer.

The findings of *Gaertner* are graphically summarised by figure 2.8.

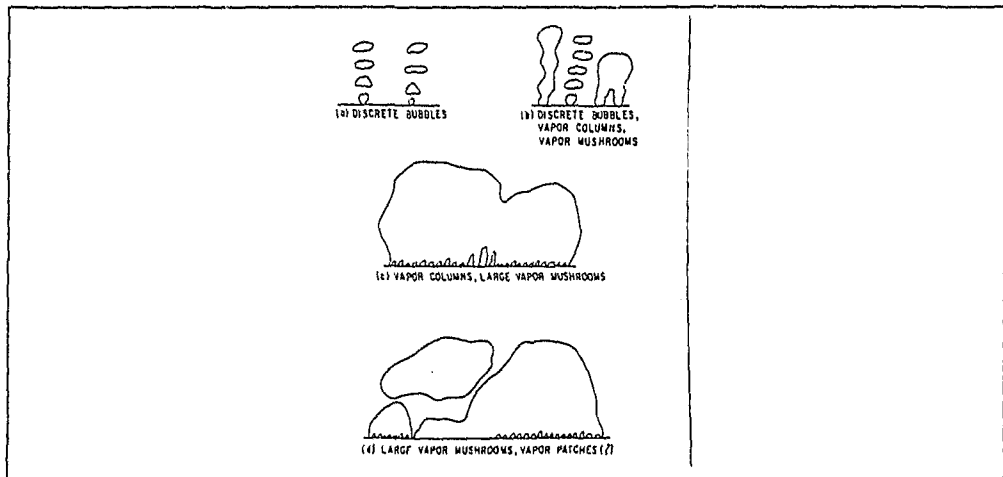


Figure 2.8 : Sketches of vapour structures in pool boiling [18]

The boiling curve developed through testing shows the range over which the regions were seen to occur (Figure 2.9). Of particular interest is the faster increase in the rate of heat transfer at boiling initiation and the slower increase in the rate of heat transfer during the second transition region.

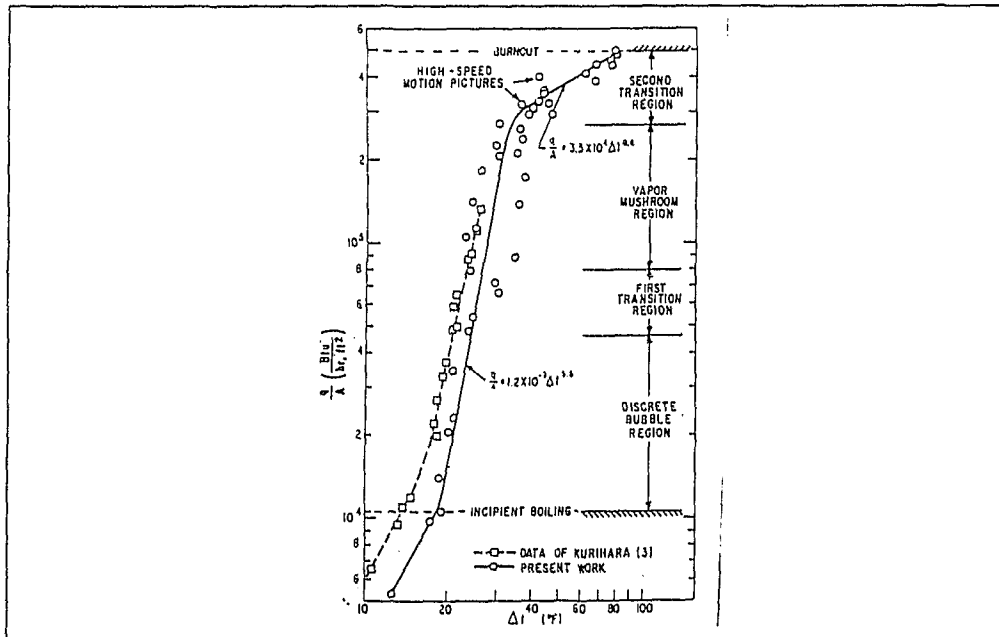


Figure 2.9 : Boiling curve for nucleate boiling of water [18]

Madejski[19] proposed a three-component boiling theory, postulating that the components of heat transfer are:

- latent heat transport rate
- turbulent convection to the liquid
- molecular conduction rate.

These components were said to be functions of the frequency of bubble emission, the number of bubble columns per unit area, the departure bubble diameter and the latent heat of vaporisation.

Numerous studies on nucleate boiling have been done by various authors, including *Van Stralen* [20] & [21] and *Han et al* [22] & [23]. Various detailed relationships were presented encompassing a broad range of topics related to nucleate boiling. *Han et al* presented the following relationships for natural pool boiling based on the Nusselt number and the Rayleigh number. For the laminar range :

$$\begin{aligned} 10^5 < Ra < 2 \times 10^7 \\ Nu = 0.54 Ra^{\frac{1}{4}} \end{aligned} \quad (2.1)$$

For the turbulent range :

$$\begin{aligned} 2 \times 10^7 < Ra < 3 \times 10^{10} \\ Nu = 0.14 Ra^{\frac{1}{3}} \end{aligned} \quad (2.2)$$

Where $Nu = \frac{hD}{\rho C_p \alpha}$, and $Ra = \frac{\gamma g (T_w - T_s) D}{\alpha \nu}$

Reasonable agreement between this theory and experimentation was achieved, as shown in figure 2.10

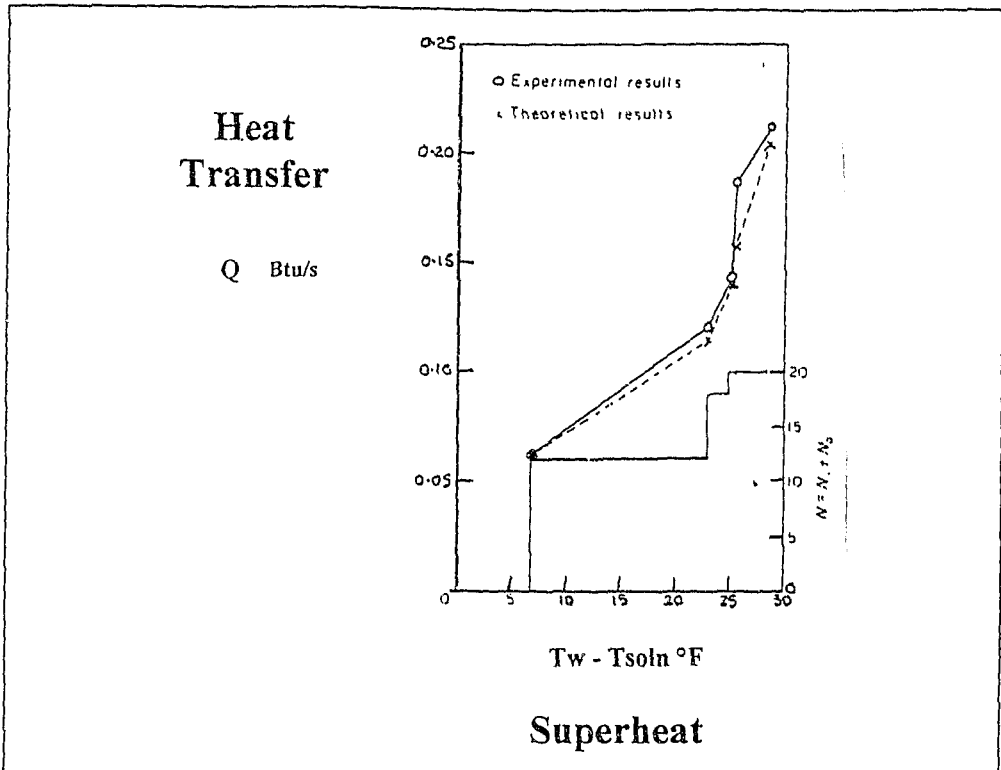


Figure 2.10 : Verification of bulk convection theory [23].

Tong[24] suggests that the life of a single bubble can be divided into five distinct stages: *nucleation, initial growth, intermediate growth, asymptotic growth* and *possible collapse*. The primary requirement for nucleation to occur is that the liquid should be locally superheated. Nuclei can be formed in a pure liquid, where it can be either a high energy molecular group resulting from thermal fluctuations of liquid molecules, or a cavity resulting from a local pressure reduction. Another form of nucleus is that formed on a foreign body such as a heating surface or suspended foreign material. Tong states that nucleation occurs preferentially at cavities on a heating surface and that bulk nucleation only occurs in special cases, such as a liquid heated in a smooth glass container. In these cases bubble growth is said to be extremely rapid, due to high superheat.

This phenomenon of bulk boiling was also observed by *Westwater* (1956)[25] .

Various authors including *Mikic et al*[26] , *McFadden et al*[27] , *Akiyama*[28] , *Cooper*[29] , *Kiper* [31] , *Van Ouwerkerk*[32] , *Saini et al*[33] , *Van Stralen et al*[34] and *Torikai*[35] investigated bubble growth rates and bubble dynamics but it is felt that their results are not directly relevant within the scope of this project.

2.3.3 Sub-Atmospheric Boiling

The heat transfer during saturated nucleate boiling of water at low pressure was investigated by *Raben et al*[36] . The transfer of energy from the heating surface was assumed to be accomplished by free convection, vapour-liquid exchange and latent heat transport, and a relation was developed for the heat transfer during discrete bubble nucleation. High speed films were taken of de-gassed, distilled water, boiling over a range of pressures. Although the system pressure did not appear explicitly in the heat transfer equation, various relations were pressure dependent. The mechanisms of energy transport in nucleate boiling were found to become less effective with reduced pressure, primarily due to a decrease in the number of bubbles on the surface, reduced contribution of convective transport and reduced vapour density. A discontinuity was observed in the transition between convective heat transfer and the nucleate boiling heat transfer regime. The magnitude of this discontinuity decreased with increasing temperature. This is illustrated in figures 2.11 and 2.12 . It can be seen (Figure 2.11) that at lower pressure, a lower heat transfer rate for the same super heat is achieved.

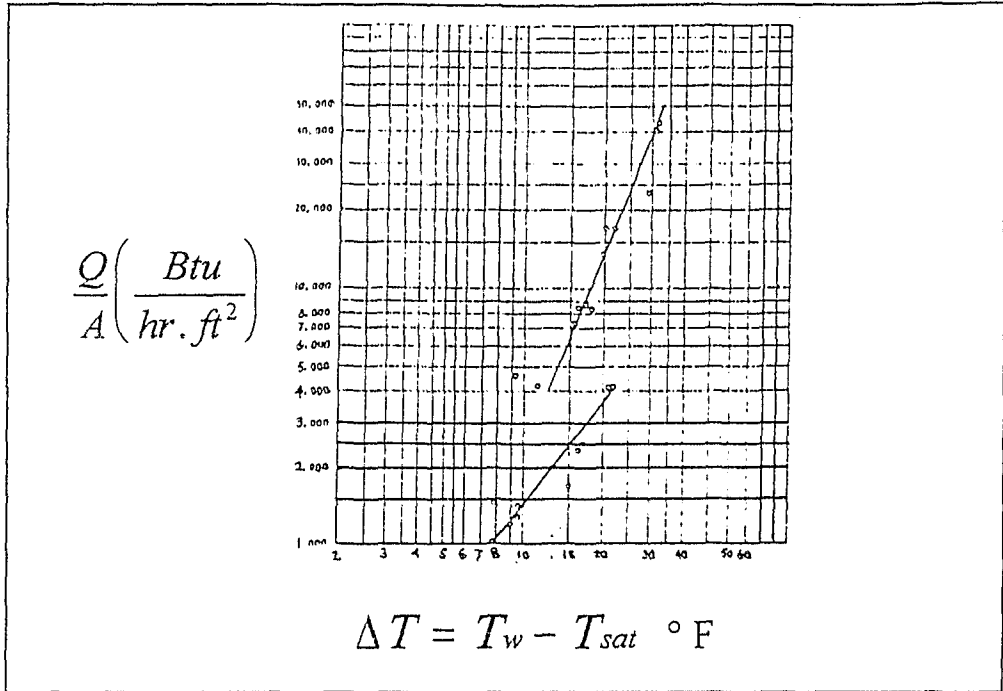


Figure 2.11 : Boiling curve for water at 50 mm Hg [36]

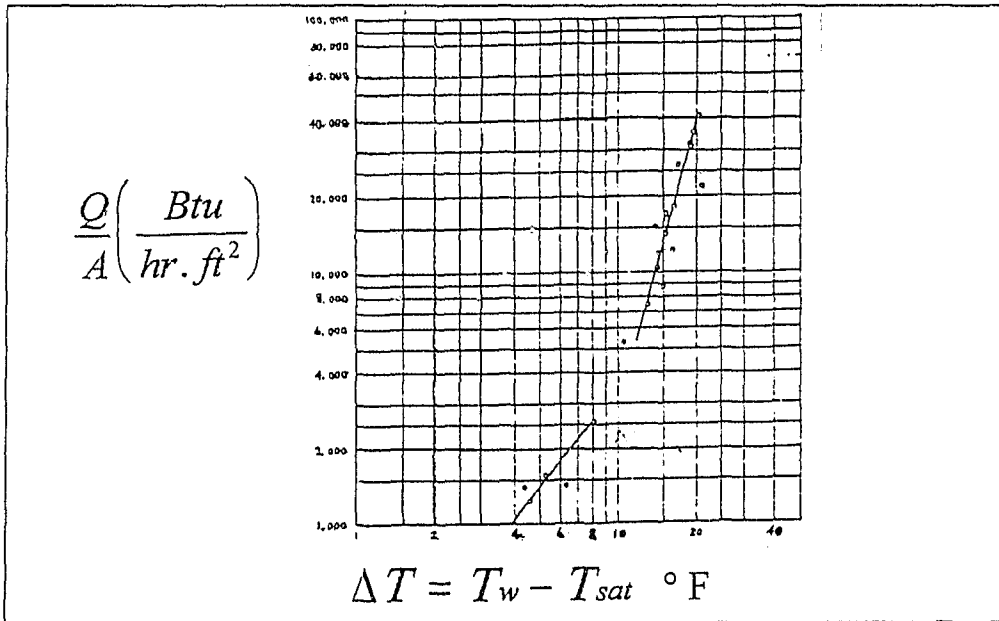


Figure 2.12 : Boiling curve for water at 200 mm Hg [36]

The effect of pressure on bubble growth was studied over a wide range of pressure, by *Akiyama et al*[37]. A test vessel containing degassed liquid and having an electrically heated test piece was connected to a vacuum pump, and bubble dynamics were recorded by a high speed camera. It was observed that as the pressure was reduced, the density of the nucleation sites became small and violent ebullition took place accompanied by the appearance of large bubbles. Increasing the pressure decreased the bubble size. The flatness of bubbles in the early growth stage was seen to be increased with pressure decrease. This was attributed to the increased growth rate under reduced pressure, resulting in greater inertia force acting on the bubble.

Van Stralen et al[38] studied bubble growth rates in nucleate boiling at subatmospheric pressures in the range of 26.7 kPa to 2.0 kPa. It was found that bubble frequency decreases substantially with decreasing pressure.

Dobrzanski et al[39] investigated the vapour generation in nucleate boiling of water on horizontal tubes, under a vacuum. The tubes were heated by internal electric heaters. The pressure range was taken between 5 kPa and 100 kPa. It was found that a decrease in pressure led to an increase in bubble diameter and a decrease in generation frequency. It was stated that the amount of superheat required to produce boiling increased with decrease in pressure.

The effect of pressure on bubble growth was studied over a wide range of pressure, by *Akiyama et al*[37]. A test vessel containing degassed liquid and having an electrically heated test piece was connected to a vacuum pump, and bubble dynamics were recorded by a high speed camera. It was observed that as the pressure was reduced, the density of the nucleation sites became small and violent ebullition took place accompanied by the appearance of large bubbles. Increasing the pressure decreased the bubble size. The flatness of bubbles in the early growth stage was seen to be increased with pressure decrease. This was attributed to the increased growth rate under reduced pressure, resulting in greater inertia force acting on the bubble.

Van Stralen et al[38] studied bubble growth rates in nucleate boiling at subatmospheric pressures in the range of 26.7 kPa to 2.0 kPa. It was found that bubble frequency decreases substantially with decreasing pressure.

Dobrzanskiy et al[39] investigated the vapour generation in nucleate boiling of water on horizontal tubes, under a vacuum. The tubes were heated by internal electric heaters. The pressure range was taken between 5 kPa and 100 kPa. It was found that a decrease in pressure led to an increase in bubble diameter and a decrease in generation frequency. It was stated that the amount of superheat required to produce boiling increased with decrease in pressure.

2.3.4 Flashing

When a liquid undergoes a sudden pressure decrease below the saturation pressure corresponding to its temperature, all the heat is unable to be contained as sensible heat and the surplus heat changes to enthalpy of vaporization[40]. This causes vapour to be generated in the bulk of the liquid, with this momentary boiling being known as flashing.

The process can be visualised on a Pressure-Enthalpy diagram, as shown in figure 2.13. If a liquid (at point A) expands isenthalpically into a low pressure region and the constant enthalpy line crosses the saturation line(at point B), vapour is produced. That the rate of vapour production is linked to the rate of depressurization.

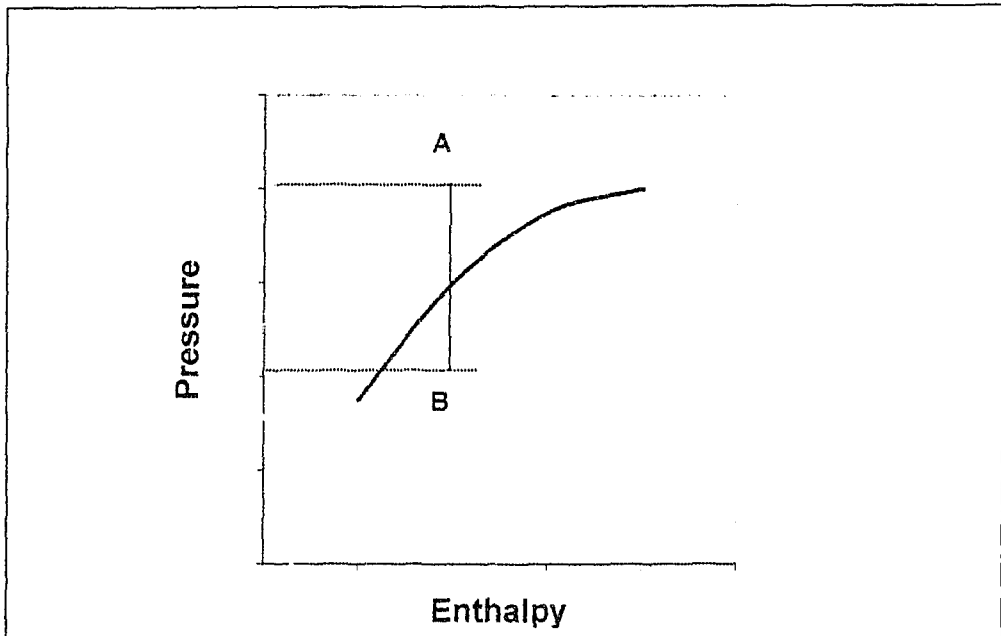


Figure 2.13 : Schematic of Pressure- Enthalpy diagram during flashing.

Belyayev and Artemenko[41] presented data for rates of evaporation of water at temperatures of 293-323 K and pressures of 100 - 760 mm Hg. Various parameters such as vapour pressure and temperature, bulk liquid temperature, liquid surface temperature and evaporator pressure were measured with respect to time. It was stated that the evaporation rate increased with decreasing evaporator pressure. The rate of heat transfer from the evaporation surface was seen either to increase or decrease with reduction in pressure, depending on the relationship between water surface temperature and the ambient temperature. Two relations were developed for dimensionless heat and mass transfer coefficients respectively, being valid for cases where the liquid temperature is lower than the ambient temperature.

$$\begin{aligned} Nu &= 0.229 Ri Gu^{-1.5} \\ Nu_D &= 0.436 Ri Gu^{-1.25} \end{aligned} \quad (2.3)$$

$$\begin{aligned} Nu &= \frac{\alpha l}{\lambda} & Nu_D &= \frac{\beta l}{D} \\ Ri &= \frac{\zeta l}{\eta} & Gu &= \frac{T_{am} - T_{loc}}{T_{am}} \end{aligned} \quad (2.4)$$

The Diffusion Nusselt number is known in western literature as the Sherwood number.

Alamgir and Lienhard[42] investigated the rapid depressurization of hot water. It was found that the initiation of depressurization is accompanied by the generation of a rarefaction wave into the higher pressure liquid. Rapid depressurization is either halted or attenuated by bubble nucleation. The pressure was found to fall below the liquid saturation pressure, this difference being called the *pressure undershoot*. Following this undershoot, bubble growth causes the pressure to recover to the saturation pressure. Typical results are shown in figure 2 14.

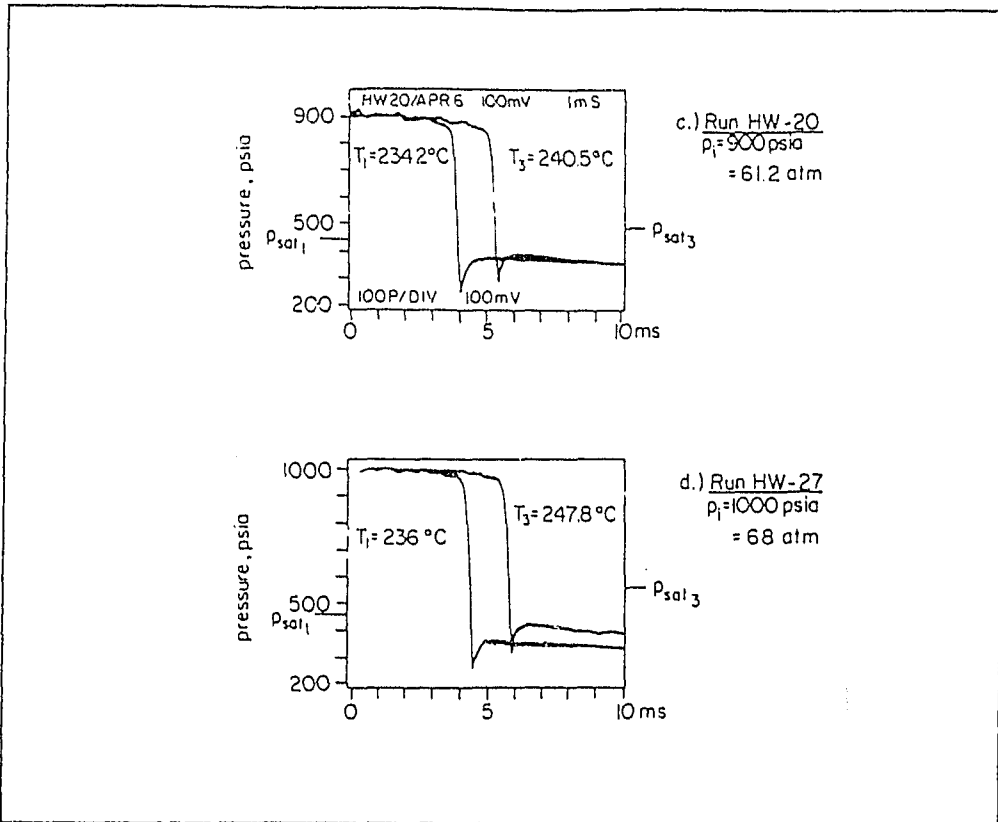


Figure 2.14 : Pressure-time traces showing undershoot [42]

It was also shown that the recovery pressure was less than the saturation pressure corresponding to the initial water temperature. This recovery pressure was shown to be related to the recovery temperature (the initial water temperature being cooled by vapour generation).

Further work by *Alamgir* and *Lienhard*[43] quantified the effect of depressurization rate on the aforementioned pressure undershoot. It was stated that the faster the depressurization rate, the more violent the flashing.(figure 2.15)

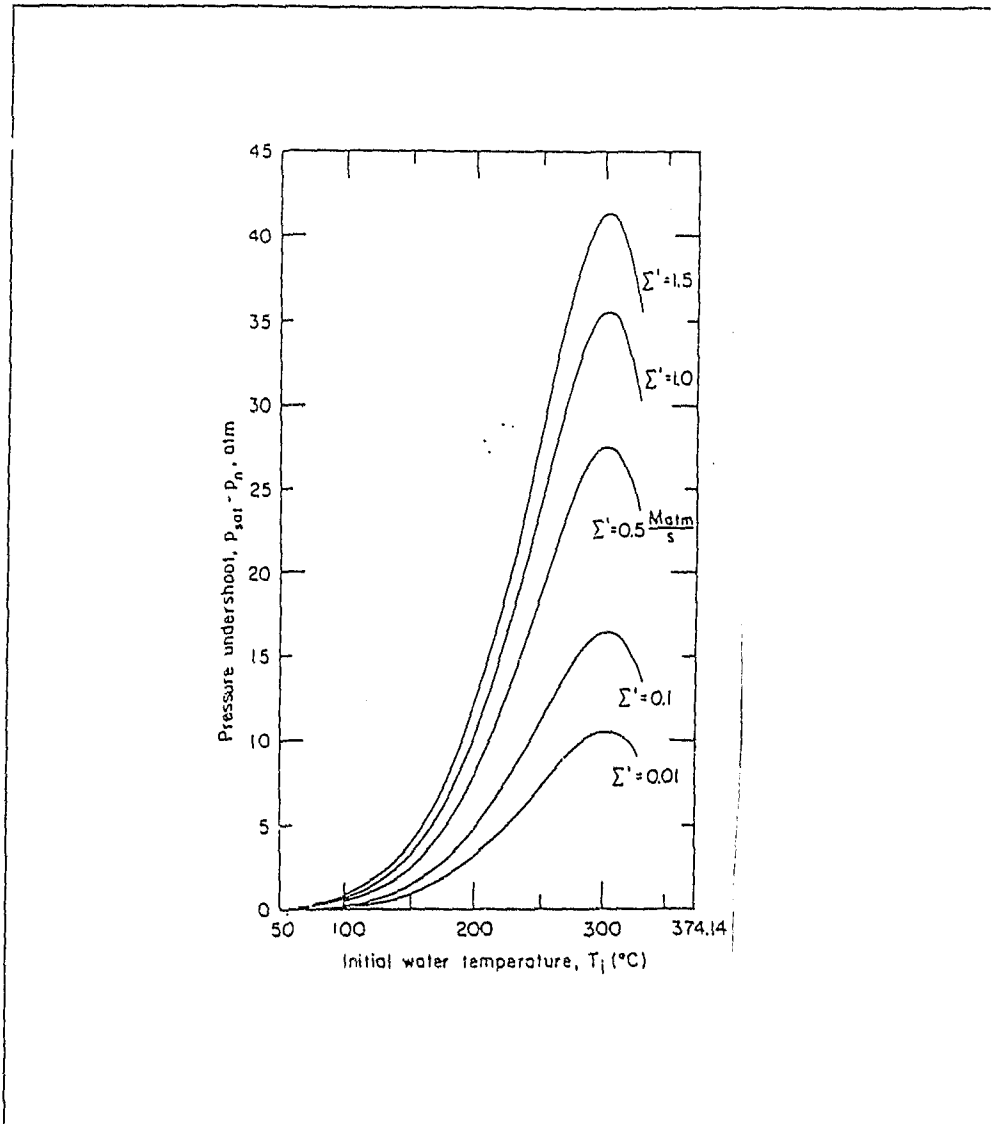


Figure 2.15 : Pressure undershoot for varying initial temperature and decompression rates [43]

Yefimochkin [44] investigated the flashing of hot water upon decompression. A tank was rapidly depressurized from initial pressures ranging from 0.02 to 0.1 Mpa. The tank had a surface area of 0.2 m². It was found that increasing the depressurization port diameter or increasing the initial pressure, increased the rate of flashing of the water and the depth of the water layer in which flashing occurs. The change in tank pressure with time is shown in figure 2.16. The curve was divided into three characteristic segments:

- 1-2 Discharge of dry steam from the space above the water layer
- 2-3 Partial pressure recovery, discharge of variable liquid content steam flow. The pressure fluctuations are induced by fluctuations in the layer of emulsion of liquid and vapour in the lower part of the tank. These fluctuations are damped out when the rates of generated and ejected steam are equal.
- 3-4 The ejected and generated steam rates are equal.

The flashing delay time during depressurization of drops of saturated water was investigated by **Kendoush**[45]. The delay time was taken as the time from when liquid passes through the saturation state up to the first appearance of detectable bubbles. This is illustrated in figure 2.17. The depressurization process was assumed to be isentropic. The delay time was found to depend on the superheat and the decompression rate.

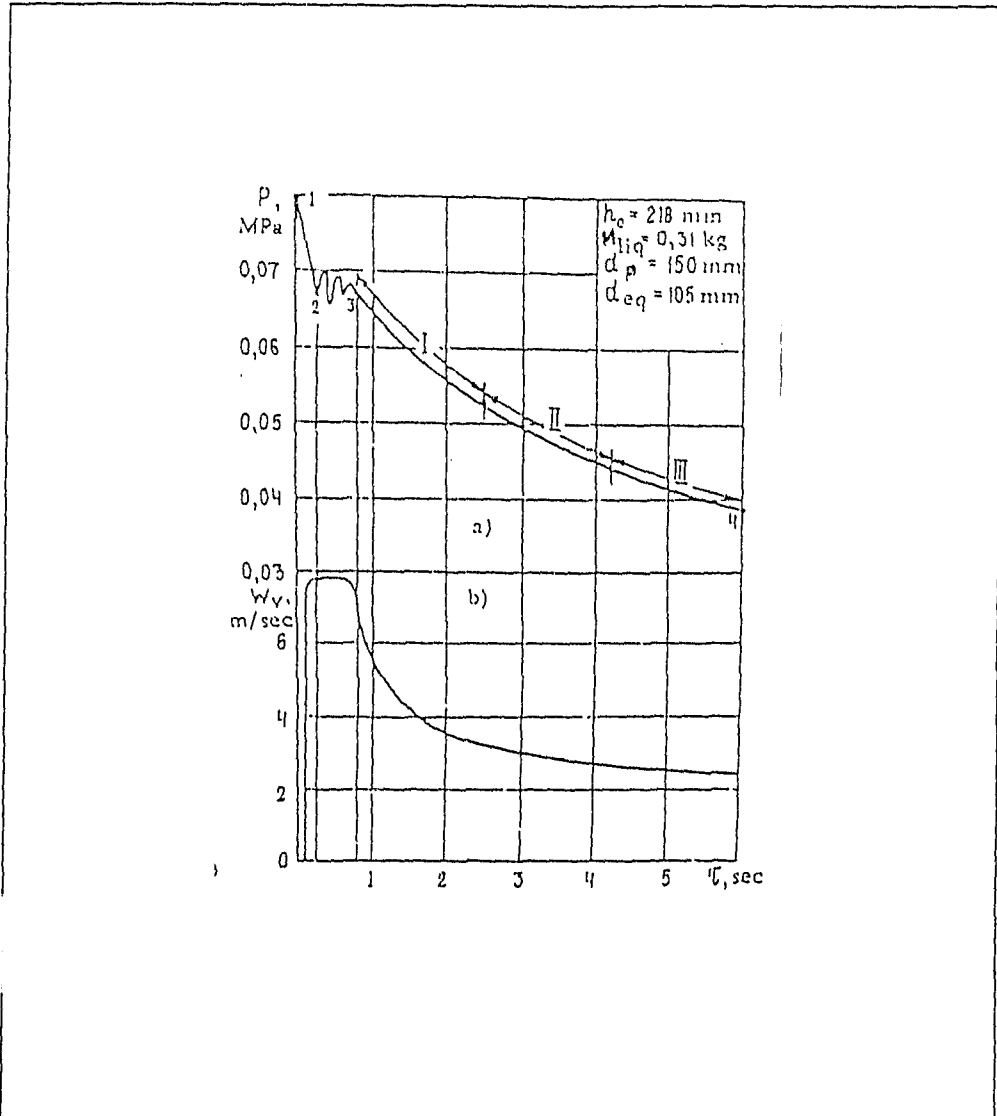


Figure 2.16 : Variation in the pressure in the tank (a) and the velocity of steam at the surface of the water layer (b) upon decompression[44]

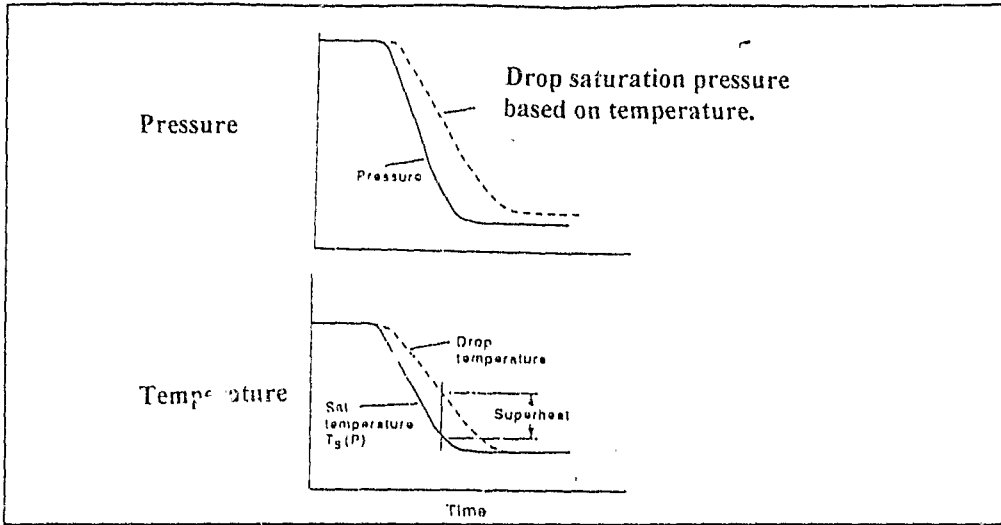


Figure 2.17 : Variation of the saturation and the water temperature during slow depressurization[45]

Owen and Jalil[46] considered the flashing of water drops. It was found that the boiling depends not only on the amount of superheat but also on the drop diameter. Figure 2.18 shows the boiling regimes noted.

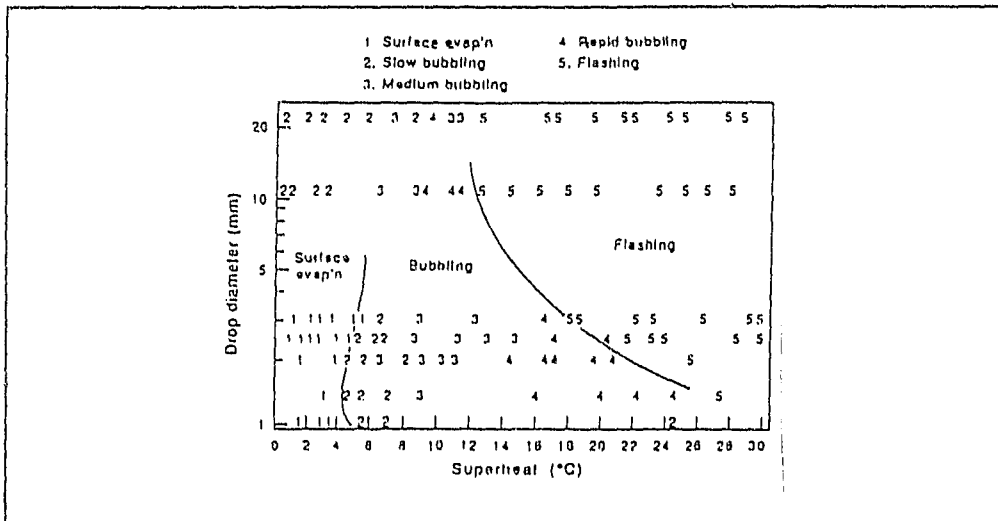


Figure 2.18 : Reaction of water drops to superheat [46]

Fundamental experiments with flash evaporation were carried out by *Miyatake et al*[47]. Water at 40, 60 and 80°C was lowered to pressures corresponding to superheats of 3°C and 5°C. The flashing of the water and hence cooling rate was shown to strongly depend on the initial temperature. The pressure in the evaporator was seen to increase shortly after depressurization, due to the vapour, generated by flashing, expanding into the flash chamber at a greater rate than the vacuum pump could remove it. This effect is shown in figure 2.19.

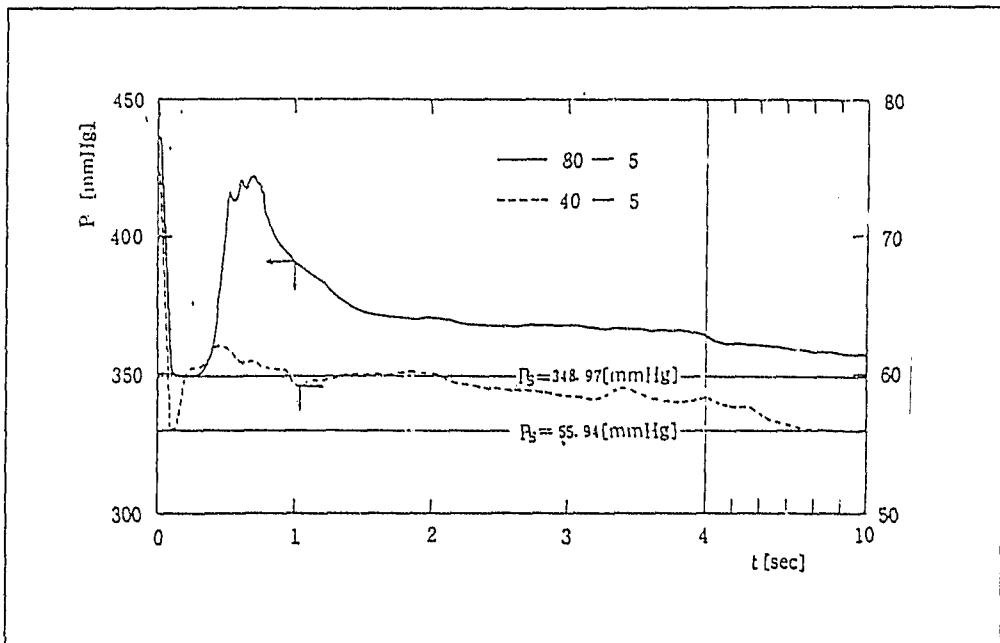


Figure 2.19 : Variation of pressure in the flash chamber with time [47]

A non-dimensionalised bulk temperature, the non equilibrium fraction, was defined as:

$$NEF(t) = \frac{T_b(t) - T_{evap}}{T_{b0} - T_{evap}} \quad (2.5)$$

Figure 2.21 shows NEF(t) plotted as a function of time. The traces show two distinct regimes: a rapid decrease in bulk temperature followed by a gradual decrease in bulk temperature.

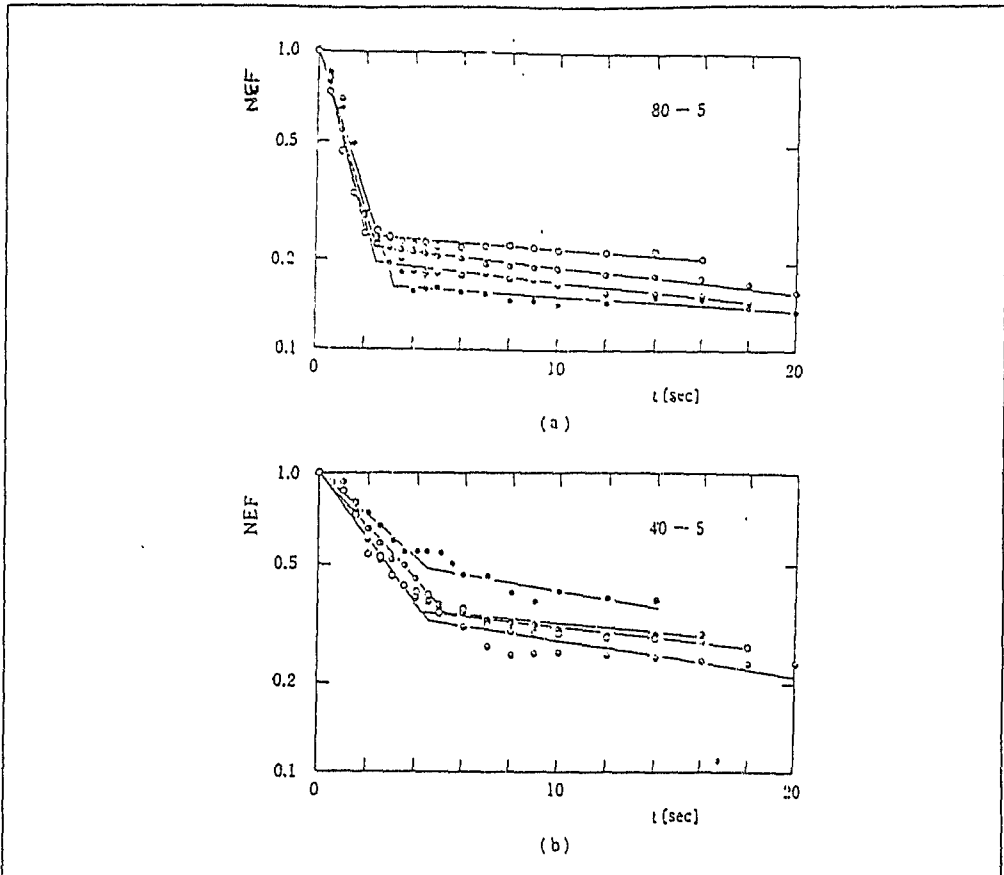


Figure 2.20 : Variation of nonequilibrium fraction with time [48]

Typical results obtained during the tests are shown in figure 2.20. A general coefficient of flash evaporation was determined and found to follow :

$$K = 3.25 * 10^4 T_{evap}^{-0.6} \quad (2.6)$$

A correlation was also developed for the cooling in flash evaporators, taking into account mean liquid height and mean residence time.

Miyatake et al(1977)[48] extended previous work to incorporate varying liquid height. Flash evaporation was found to undergo two exponentially decaying processes.

Nishikawa et al(1966)[49] investigated nucleate boiling at low liquid levels. It was found that boiling heat transfer rate increases with decreasing liquid level. Typical results are shown in figure 2.21.

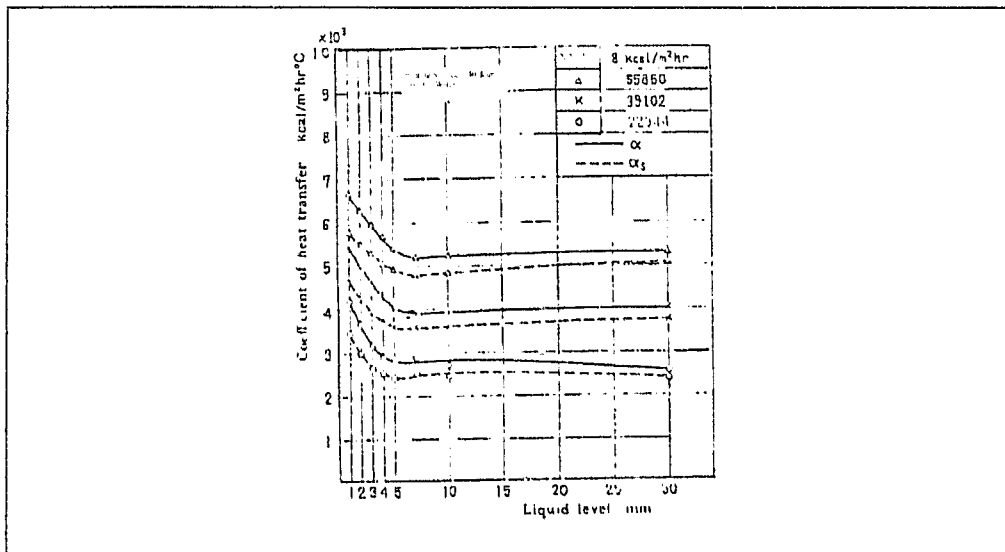


Figure 2.21 : Heat transfer dependence on liquid level. [49]

Considering figure 2.21, the phenomenon observed may be explained as follows. The initial decrease in heat transfer with increase in liquid height could well be the result of local superheat at the heating element being lowered due to increasing hydrostatic pressure. At a critical height (5mm for the given conditions) this decrease tapers off and it would appear that there is a distinct change in boiling regime. The heat transfer coefficient is not affected by further increases in liquid height, except in the case of low heat input where heat transfer can be seen to decrease with increasing height.

It is suggested that the superheat at the surface is sufficient to initiate bubbles but that due to the height of the liquid some of these bubbles are able to coalesce back into the bulk of the water, thus reducing mass transfer at the liquid surface.

Forest and Ward(1977)[50] investigated the effect of a dissolved gas on the homogeneous nucleation pressure of a liquid during an isothermal decompression. It was found that the presence of dissolved gas raises the pressure at which nucleation occurs, thus reducing the superheat necessary for the formation of the gaseous phase.

CHAPTER 3

THEORETICAL ANALYSIS

This chapter contains an analytical consideration of the vacuum boiling of water, from two perspectives: in a through-flow evaporator and in a fixed control volume. The analysis of the evaporator is based on the assumption that once the evaporator is in operation, inlet and outlet conditions are at steady state. Once the theory is developed the characteristics of an idealised ejector are combined with the evaporator model. This is done to predict expected evaporator performance due to using steam-jet ejectors, in an attempt to view the boiling process initially in isolation from the performance characteristics of the compression device. Consideration is also given to the concept of a generalised "mass transfer coefficient" for design of direct contact evaporators. The second part of the analysis considers the decompression of small fixed masses of water and attempts to explain the nature of the consequent boiling and predict factors which would limit or enhance cooling rates.

3.1 Evaporator Modelling

Based on the literature surveyed, it seems reasonable to expect to be able to design with some confidence the various components of a steam jet water vapour refrigeration system. Certainly, the design of the ejector set poses no problem, with the primary ejector compression ratio being constrained primarily by the available condenser temperature. The design and sizing of the evaporator however does pose a problem as there are no design guidelines or readily available sizing factors.

3.1.1 Basic Model

The basic principle of operation of the direct contact evaporator is that water at approximately ambient temperature (typically 10-20°C) is drawn into an evaporator held at a pressure corresponding to the saturation temperature of the required cooled water. The surplus heat in the water is released as enthalpy of vaporization and the water is cooled. The processes involved include flashing, various boiling regimes and steady surface evaporation. From the literature surveyed, factors which influence the time frame over which these processes take place include surface area, liquid height, the degree of superheat, flow regimes etc. Thus to establish the expected performance of a general evaporator of arbitrary geometry at steady state conditions, consider an energy balance on the evaporator shown in figure 3.1.

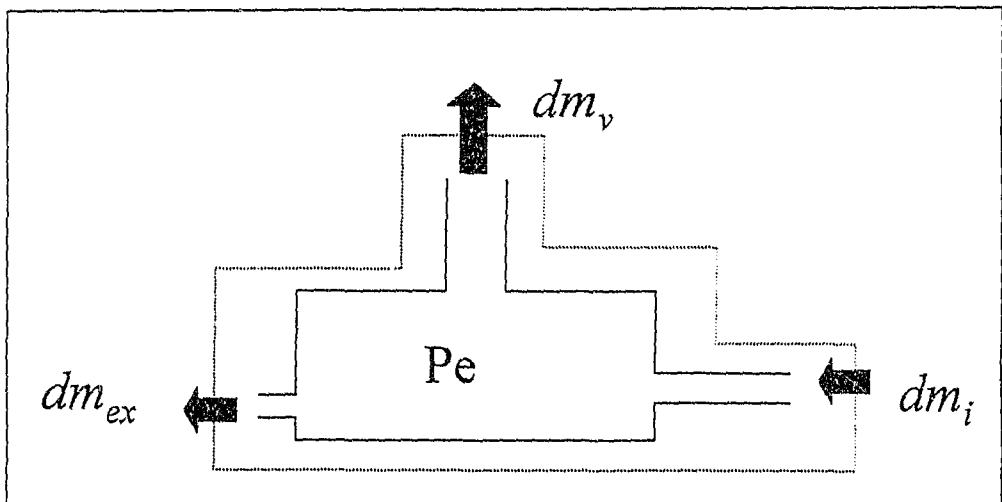


Figure 3.1: Evaporator sketch with boundary

The following assumptions are made :

- 1) $dW=0$.
- 2) Heat gains are negligible.
- 3) No pressure gradients exist in the evaporator itself.
- 4) There are no leaks or dissolved gases in the water.
- 5) The outlet temperature is assumed to be the saturation temperature corresponding to the evaporator pressure.
- 6) Due to the low mass flow rates (both water and vapour) the velocity terms are negligible. Changes in height are negligible.

From the steady flow energy equation [55] :

$$(e + pv)_i dm_i = dh'_c + (e - pv)_{ex} dm_{ex} + (e + pv)_v dm_v \quad (3.1)$$

By definition :

$$e + pv = u + pv + \frac{V^2}{2} + gz$$

$$h = u + pv$$

From whence

$$\left(h + \frac{V^2}{2} + gz\right)_i dm_i = dh'_c + \left(h + \frac{V^2}{2} + gz\right)_{ex} dm_{ex} + \left(h + \frac{V^2}{2} + gz\right)_v dm_v \quad (3.2)$$

From assumption 6)

$$h_i dm_i = dh'_c + h_{ex} dm_{ex} + h_v dm_v \quad (3.3)$$

Further there is no significant change in stored kinetic, potential or internal energies at steady state conditions :

$$\begin{aligned}
 d(M_c E_c) &= dM_c * h_c + dh_c * M_c \\
 &= M_c * (C_p * dT + \frac{\delta h}{\delta P} dP)_c \\
 &= 0
 \end{aligned}
 \tag{3.4}$$

From a mass balance :

$$\begin{aligned}
 dm_i &= dm_{ex} + dm_v \\
 \therefore dm_{ex} &= dm_i - dm_v
 \end{aligned}
 \tag{3.5}$$

thus :

$$\begin{aligned}
 (h_i)_i dm_i &= (h_f)_{ex} (dm_i - dm_v) + (h_g)_v dm_v \\
 \therefore (h_i - h_f) dm_i &= h_{fgv} * dm_v
 \end{aligned}
 \tag{3.6}$$

Thus, assuming p exit corresponds to p evap :

$$-C_p * dm_i * dT = h_{fg} * dm_v
 \tag{3.7}$$

Using the equation 3.7 one can begin to model the processes involved in the evaporator. It will initially be assumed that the compressing device can maintain a constant mass flow rate over a range of pressures. (The performance of an ideal ejector will be added in at a later stage.) The following algorithm was implemented in the Engineering Equation Solver (EES) [56] package. The source code of the models presented is shown in appendix B.

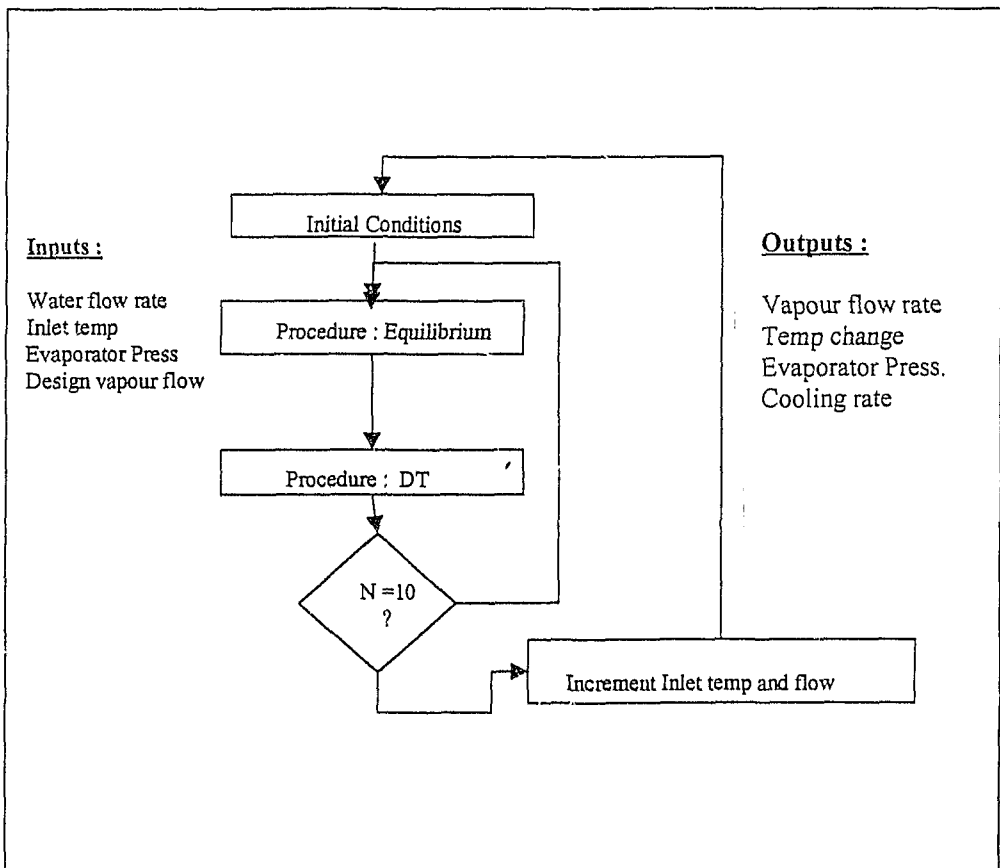


Figure 3.2: EES program algorithm

Dependence of pressure on Flow Rate

As can be seen from figure 3.3, if a constant vapour mass flow rate were to be maintained by the compressor, the evaporator pressure would have to rise for increasing water flow rate, above the designed value. For flows below the designed flow rate it is assumed that the compressor will not drive the pressure below its design pressure (hence the discontinuity in the graph). Inlet temperature is constant at 27°C and evaporator volume 0.01 m³.

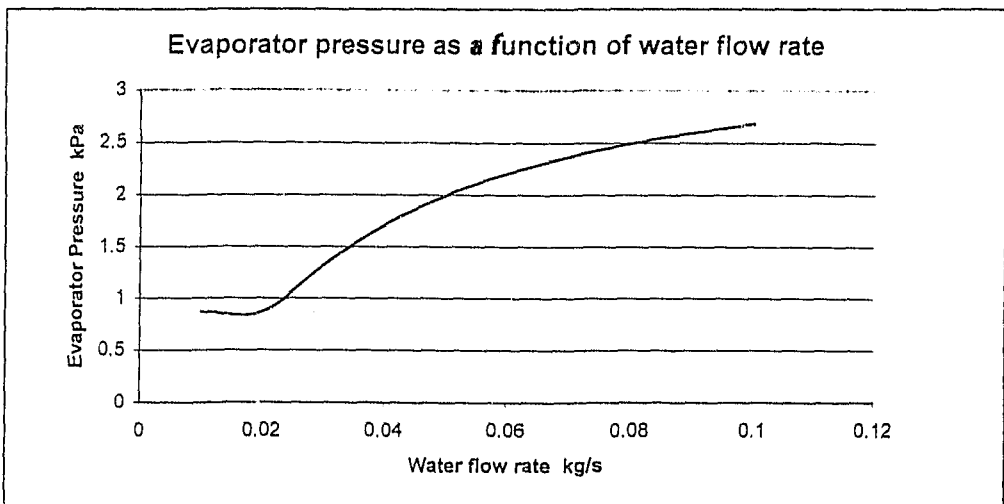


Figure 3.3 : Evaporator pressure as a function of water flow rate.

Dependence of Rate of Heat Transfer on Flow Rate

Water flow rate has less of an effect on the rate of heat exchange than on the evaporator pressure, as seen in figure 3.4. At water flow rates above design, there is a slight drop off in rate of heat exchange. At below-design flow rates there is a significant decrease in rate, ascribed to the fact that the evaporator pressure was assumed to have a lower limit. Thus at low flow rates the water can not be cooled further and the heat exchange rate decreases. At the triple point this would no longer be true as freezing would take place.

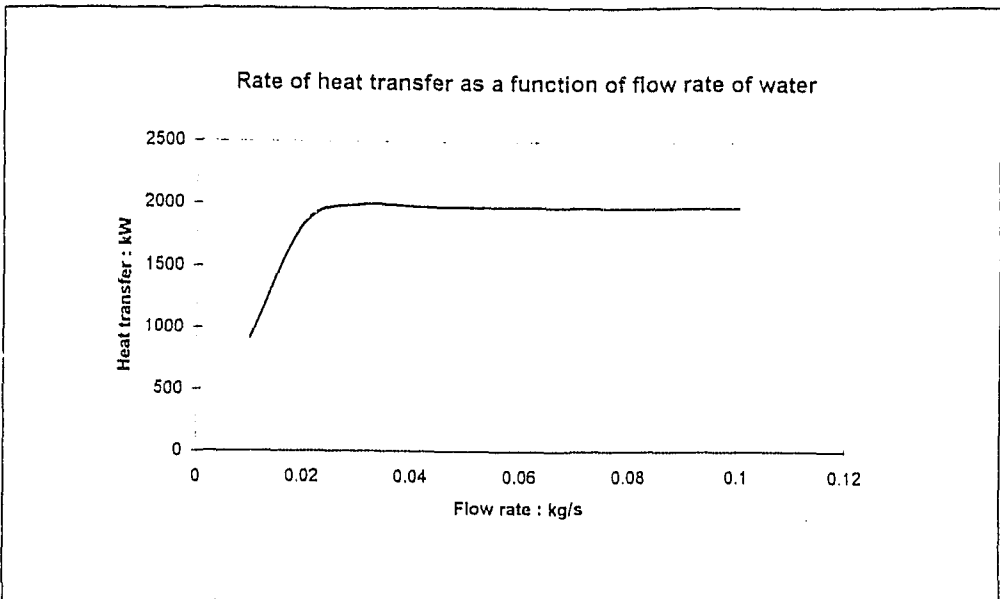


Figure 3.4 : Evaporator rate of heat transfer as a function of water flow rate.

Again inlet temperature is 27°C and evaporator Volume is 0.01m^3 . Evaporator pressure is not allowed to fall below 0.8719 kPa abs .

Dependence of Pressure on Inlet Temperature

In the same way that varying the flow rate of water through the evaporator will affect the evaporator pressure, so too will varying the inlet temperature. From figure 3.5 it can be seen that the evaporator pressure is strongly dependent on the inlet temperature, increasing asymptotically with increasing inlet temperature. The water flow rate and vapour flow rate are constant at 0.0477 kg/s and 0.00821 kg/s respectively. Evaporator pressure is not allowed to fall below 0.8719 kPa .

Dependence of Cooling Capacity on Inlet Temperature

Figure 3.6 shows the effect that the inlet temperature has on the evaporator performance. As in 3.5, the water flow rate and vapour flow rate are constant at 0.0477 kg/s and 0.00821 kg/s .

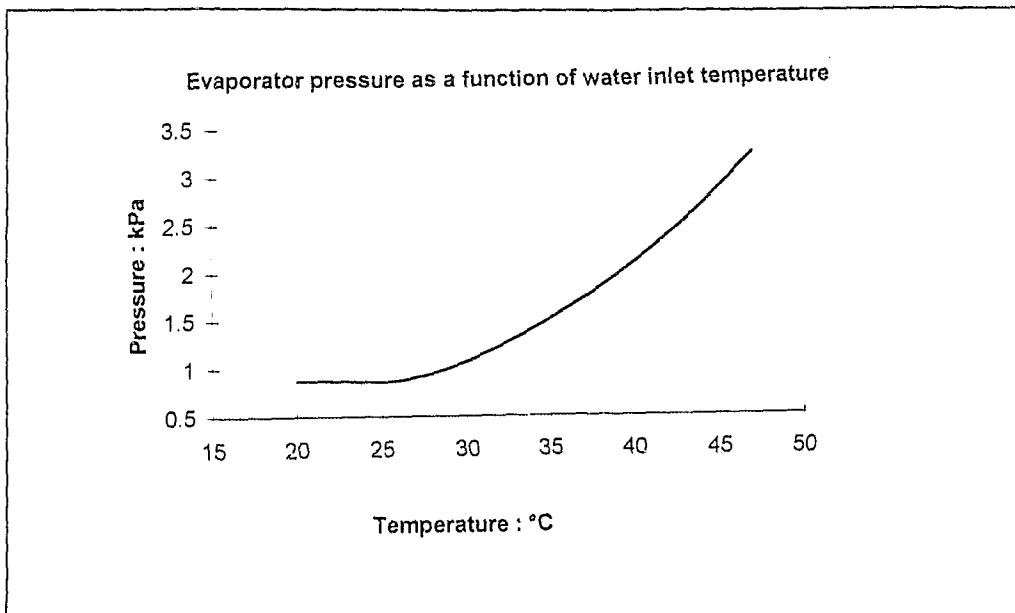


Figure 3.5 : Evaporator pressure as a function of inlet temperature

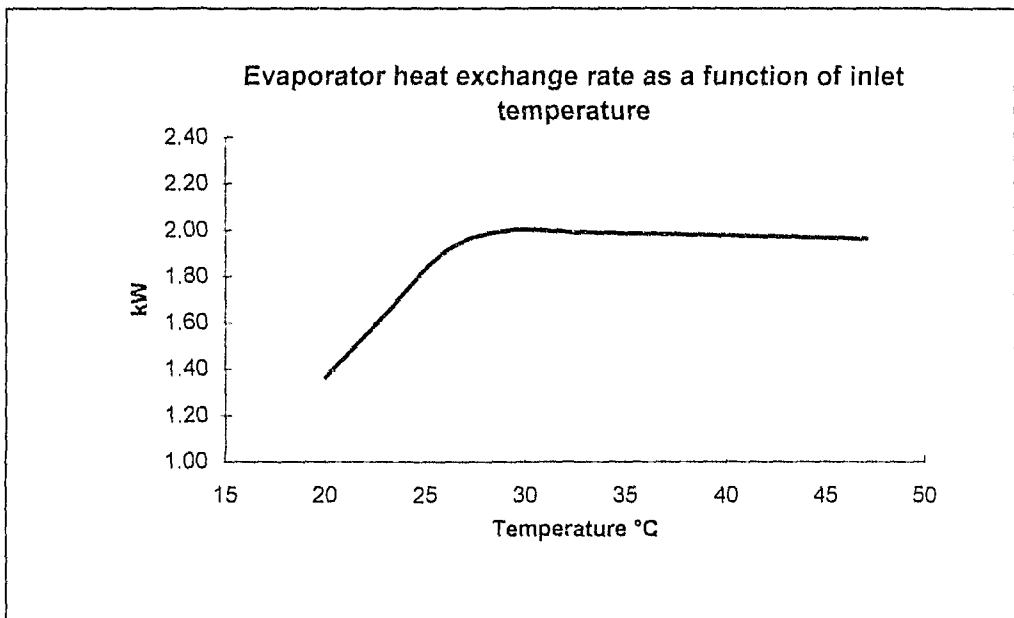


Figure 3.6 : Evaporator heat exchange rate as a function of inlet temperature

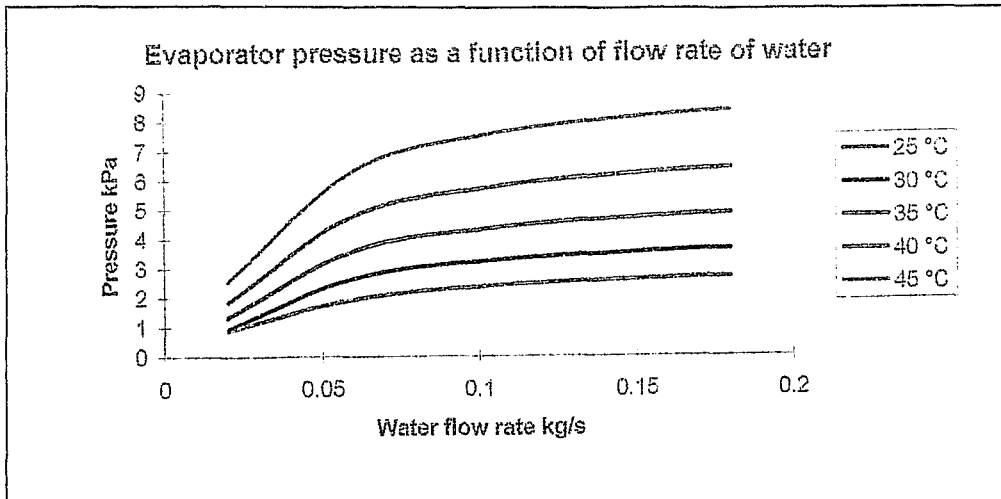


Figure 3.7 : Combined effect of inlet temperature and water flow rate on evaporator pressure

The combined effects of flow rate and inlet water temperature on evaporator pressure and cooling capacity are shown in figures 3.7 and 3.8 respectively. Vapour flow rate is held constant at 0.00821 kg/s, evaporator volume is 0.01 m³.

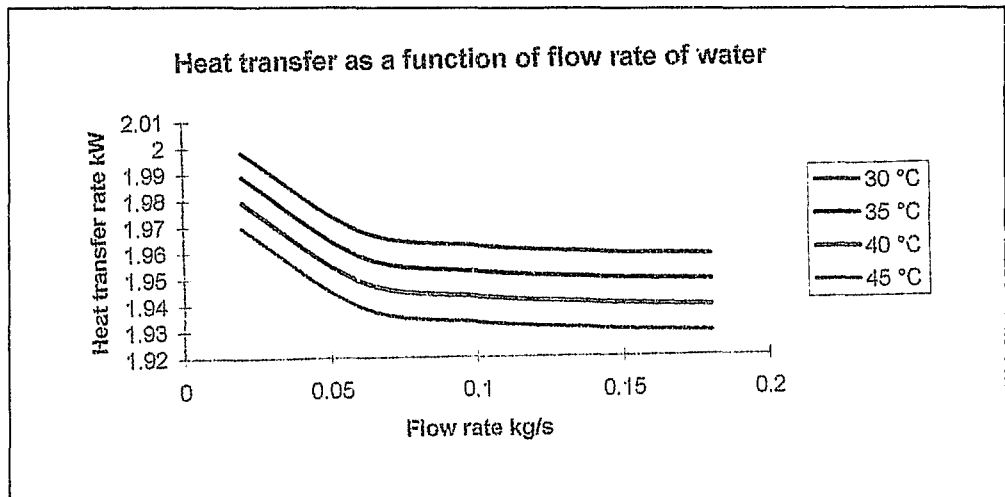


Figure 3.8 : Combined effect of inlet temperature and water flow rate on heat transfer rate.

It is interesting to note that the evaporator pressure and cooling capacity do not depend on the heat load into the evaporator, but on the particular inlet temperature and flow rate. As previously mentioned, in the above simulations it was assumed that the vapour mass flow rate was constant. This is unlikely to occur in an actual system. It is thus worth considering the effect of an ideal ejector set on the evaporator performance .

3.1.2 Ideal Ejector

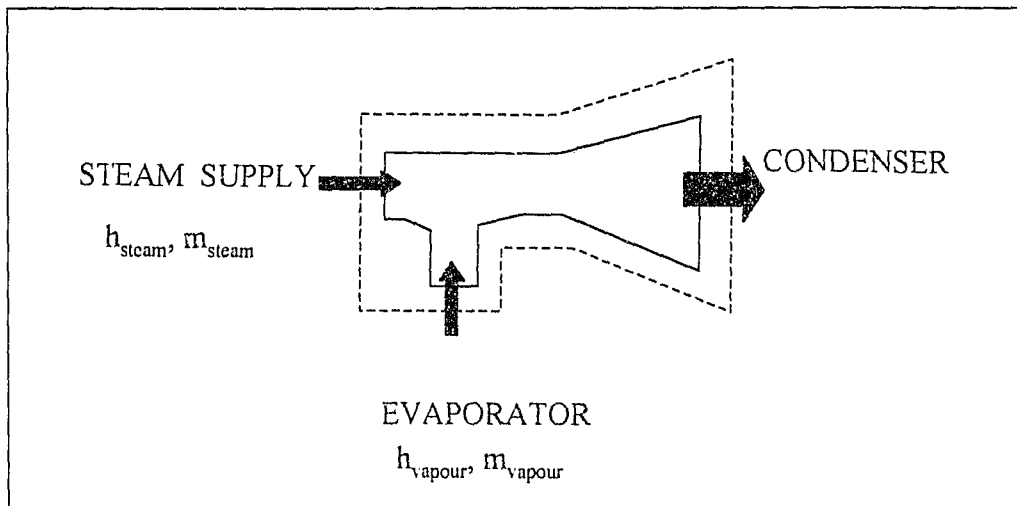


Figure 3.9 : Idealised ejector

Consider the ejector in figure 3.9. From an energy balance on the ejector it can be shown that:

$$h_{\text{steam}} * m_{\text{steam}} + h_{\text{vapour}} * m_{\text{vapour}} = h_{\text{condenser}} * (m_{\text{steam}} + m_{\text{vapour}}) \quad (3.8)$$

From whence :

$$m_{\text{vapour}} = \frac{m_{\text{steam}} * (h_{\text{steam}} - h_{\text{condenser}})}{h_{\text{condenser}} - h_{\text{vapour}}} \quad (3.9)$$

The above equation was included in the EES program and the results obtained are shown in figure 3.10. For an ideal ejector, there is a marked increase in heat transfer rate with increasing water inlet temperature. The rate of heat transfer can be seen to increase with increasing water flow rate. That the rate of heat transfer (cooling capacity) is predicted to increase so dramatically is ascribed to the fact that as the evaporator pressure rises, so the lift to the condenser pressure decreases. The enthalpy of the water vapour is thus closer to that of the condenser which means that a higher vapour mass flow rate can be achieved.

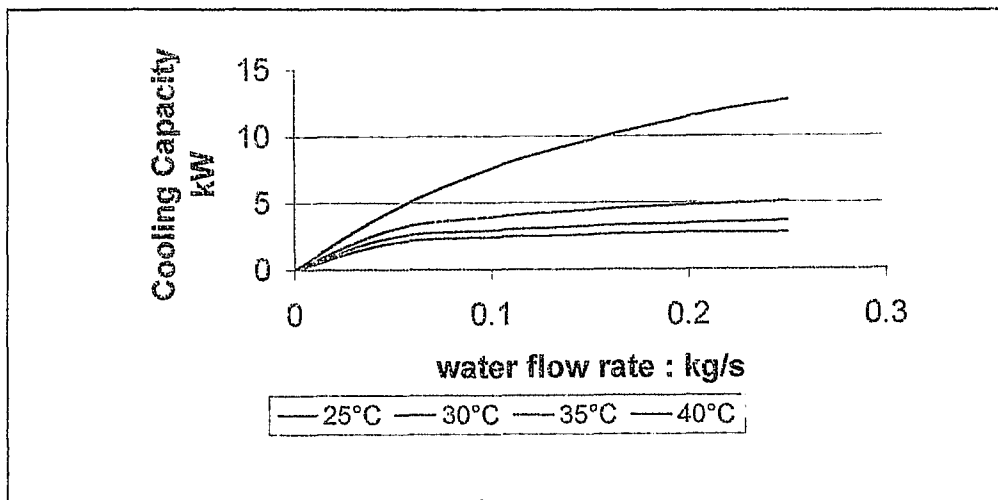


Figure 3.10 : Cooling capacity as a function of water flow rate for varying inlet water temperatures, idealised ejector.

In figure 3.10, the motive steam pressure is 590 kPa and condensing pressure 6 kPa. Evaporator volume is 0.01 m³. Figure 3.11 shows the effect of the conditions modelled on the evaporator pressure. In the model the evaporator pressure was allowed to drop to 60% of the design value of 0.8719 kpa.

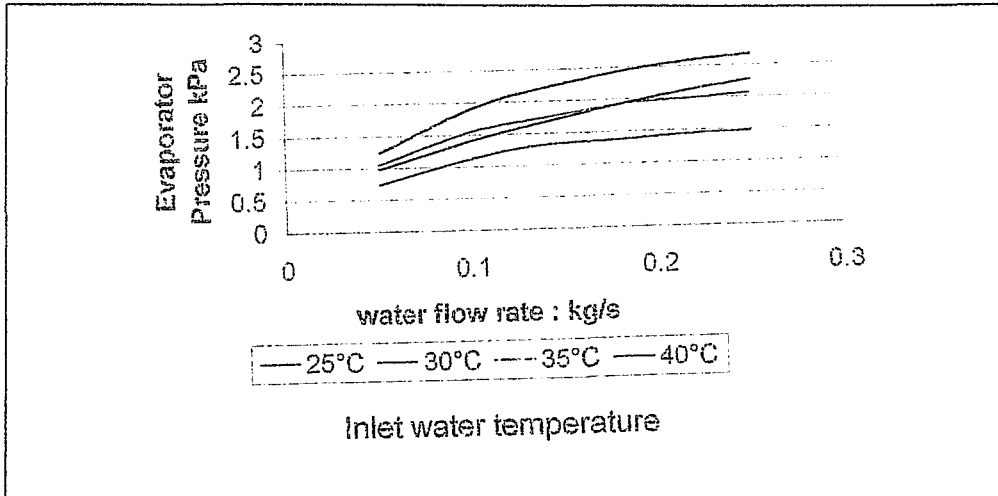


Figure 3.11 : Evaporator pressure for an idealised system.

It is notable that the equations developed are independent of area or any geometric factors, thus giving no indication as to what size the evaporator should be. Furthermore the equations give no indication of the boiling mechanisms involved or of the time scale involved. This is due to the "black box" approach used. To model the process more accurately, it becomes necessary to either introduce flashing and mass transfer coefficients or to model the flow of both the liquid and the evaporated vapour, and to establish the pressure gradients in the evaporator.

3.1.3 Mass Transfer Coefficient

In heat transfer problems the surface area of a heat transfer surface can be estimated by establishing the flow regime, the heat transfer rate required and the temperature difference between two media :

$$A = \frac{Q}{\Delta T \cdot h} \quad (3.10)$$

Where : A is the surface area
 Q is the heat transferred
 \bar{h} is the heat transfer coefficient

In the same way, the aim of a mass transfer coefficient would be to predict the mass transfer (indirectly the amount of cooling) or vapour generation for a given "driving potential". This driving potential could be based on the amount of "superheat" or the difference between the evaporator pressure and the saturation pressure corresponding to the given initial water temperature. Such a coefficient would be specific to a host of parameters such as:

- flow geometry within the evaporator
- liquid height
- water conditions
- depressurization rate

Measured mass transfer coefficients for a given system geometry could have little or no applicability to a similar system with a different compression device or different operating conditions. If a generalised mass transfer coefficient did exist, for a specific flow geometry, it could be possible to use it to size an evaporator of similar geometry.

The greatest problem that this concept poses is that if the water does not cool sufficiently, due to insufficient mass transfer then it would leave the evaporator in a superheated state relative to the prevailing evaporator pressure. This implies that a pressure gradient would exist within the evaporator which contradicts the definition of a driving potential.

Consider two evaporators at the same pressure, flow rate and suction rate. Evaporator A is sized correctly and evaporator B is half the size of evaporator A :

For both :

T_{inlet} = inlet temperature

T_{out} = outlet temperature

P_e is the evaporator pressure

Q is the flow rate

A is the surface area

m_{vapour} is the vapour flow rate

$$\begin{aligned} m_{vapour,A} &= K_m * A * \Delta P \\ m_{vapour,B} &= K_m * \frac{A}{2} * \Delta P \end{aligned} \quad (3.12)$$

Then :

$$\begin{aligned} -(T_{out} - T_{inlet})_A &= \frac{K_m * A * \Delta P * h_{fg}}{Q * C_p} \\ -(T_{out} - T_{inlet})_B &= \frac{K_m * A * \Delta P * h_{fg}}{2 * Q * C_p} \end{aligned} \quad (3.13)$$

From which :

$$T_{out,B} = T_{out,A} + \frac{K_m * A * \Delta P * h_{fg}}{2 * Q * C_p} \quad (3.14)$$

Thus $T_{\text{out}B}$ would exceed the saturation temperature corresponding to the evaporator pressure. This however implies that the water leaving evaporator B would have to be at a higher pressure than that of the water leaving evaporator A. This would be true if the evaporator pressure is raised or if a pressure difference exists through the height of the evaporator.

In the first case the driving potential is lowered, and thus a different K_m would be defined. In the second case a small pressure difference in the evaporator could be supported by the high mass flow rate of water vapour, depending on the given geometry.

It would thus seem that a mass transfer coefficient would only be useful in cases where very tight restrictions are placed on evaporator geometry and operating conditions or where the coefficient is either specific to a given driving potential and operating conditions, or is used with scaling for sizing geometrically similar. It does not seem possible to have a general mass transfer based purely on driving potential, even in geometrically similar evaporators.

3.1.4 Coefficients to be Investigated

A mass transfer coefficient would typically be defined based on a convenient driving potential and would incorporate the evaporating area. For the tests conducted the driving potential was taken as the difference between the evaporator pressure and the saturation pressure at the water inlet temperature after the expansion device (flashing temperature). This is likely to be substantially cooler than the water entering the expansion device due to flashing occurring as the water undergoes a change in pressure. This inlet temperature thus also needs to be

established before the driving potential for the mass transfer coefficient – and hence the size of an evaporator, can be established.

As the inlet water undergoes a drop in pressure an amount of flashing can be expected. It seems viable to measure the amount of cooling due to flashing and to define a flashing coefficient. Here the driving potential used could be either the difference between the temperature, or corresponding saturation pressure, of the water entering the system and either the evaporator temperature or the flashing temperature.

Due to the non-linear dependence of water saturation pressure on temperature (as shown in figure 3.12), the driving potential chosen is temperature.

The bulk mass transfer coefficient is defined as :

$$KM_{BULK} = \frac{m_{EVAPORATED}}{M_{H_2O} * (T_{INLET} - T_{EVAP})} \quad (3.15)$$

and the flashing coefficient as:

$$KM_{Flash} = \frac{m_{EVAPORATED}}{M_{H_2O} * (T_{INLET} - T_{FLASH})} \quad (3.16)$$

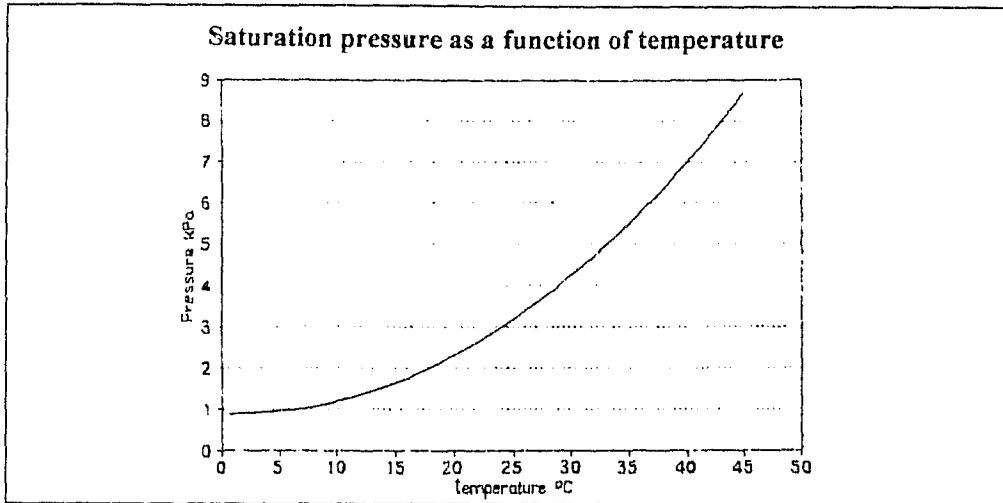


Figure 3.12 : Variation of saturation pressure with temperature.

3.2 Vacuum Boiling in a Vertical Column

3.3.1 Introduction

As indicated by the literature survey, much work has been done in the field of boiling of water in heat transfer applications. Most of this work has concentrated on the boiling of water off a heated surface, with many correlations having been developed for heat transfer coefficients for given pressure and temperature conditions. Substantially less work has been done on the phenomena of "bulk boiling" and boiling due to rapid decompression (flashing). In this case the water is not locally superheated at a given surface, but the bulk of the water is superheated.

In the tests conducted by Miyatake[41&49], the superheat is defined as the amount by which the bulk liquid temperature exceeds the saturation temperature of water, corresponding to the evaporator pressure. Due to the increase in hydrostatic pressure with liquid depth, the actual superheat at the base of the evaporator is lower than that at the water surface. This difference increases as the evaporator pressure decreases, as shown in figure 3.13.

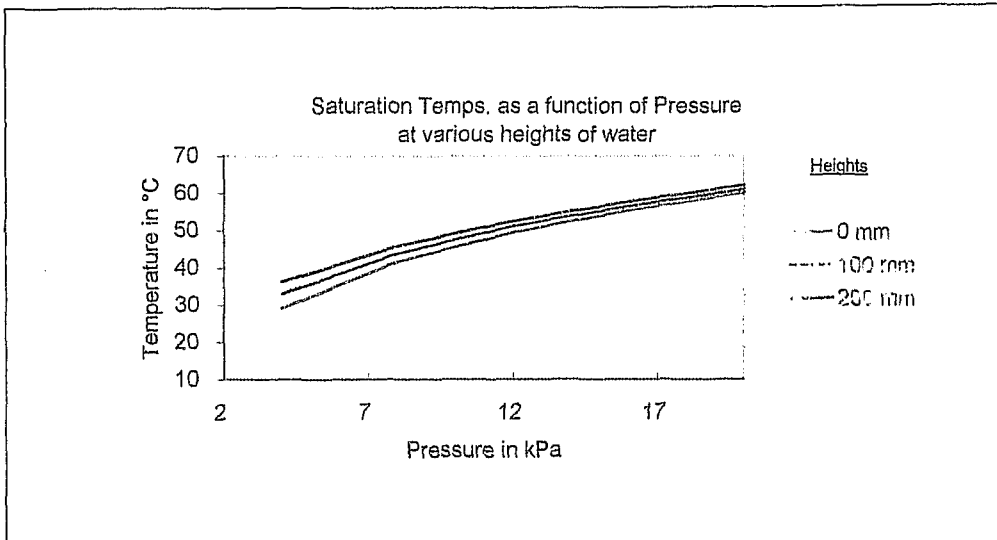


Figure 3.13 : Saturation Temperatures for increasing pressure and various levels of water.

It can be suggested that upon decompression the water would flash to local saturation temperatures, setting up a temperature gradient between the surface of the water and the base of the water column. Incorporating this concept into Miyatake's work goes some way toward explaining some of the phenomena that were noticed.

Penetration depth

Miyatake investigated the depth of penetration of sizeable vapour bubbles into the bulk of the liquid. These values were substantially less than the depth at which the liquid would no longer be superheated, as can be seen in figure 3.14.

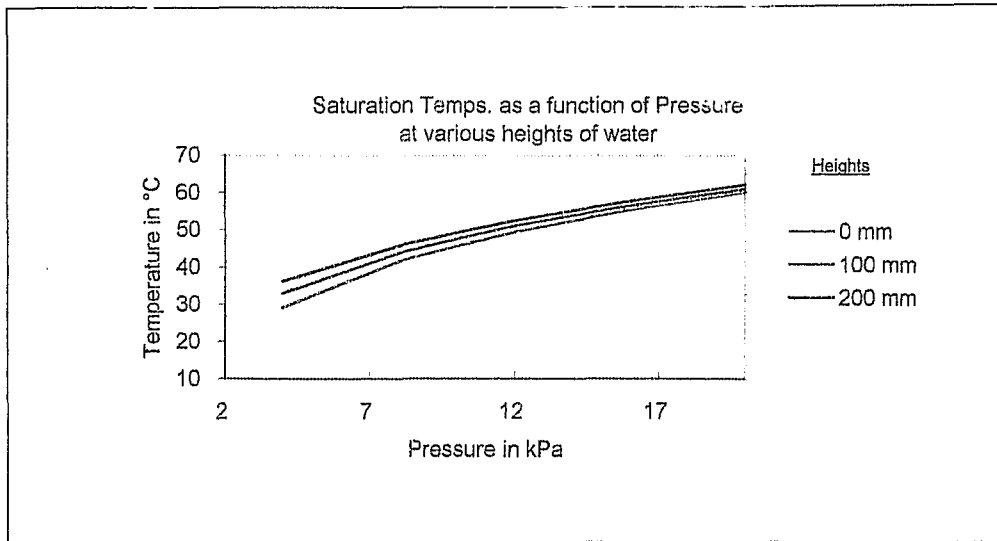


Figure 3.13 : Saturation Temperatures for increasing pressure and various levels of water.

It can be suggested that upon decompression the water would flash to local saturation temperatures, setting up a temperature gradient between the surface of the water and the base of the water column. Incorporating this concept into Miyatake's work goes some way toward explaining some of the phenomena that were noticed.

Penetration depth

Miyatake investigated the depth of penetration of sizeable vapour bubbles into the bulk of the liquid. These values were substantially less than the depth at which the liquid would no longer be superheated, as can be seen in figure 3.14.

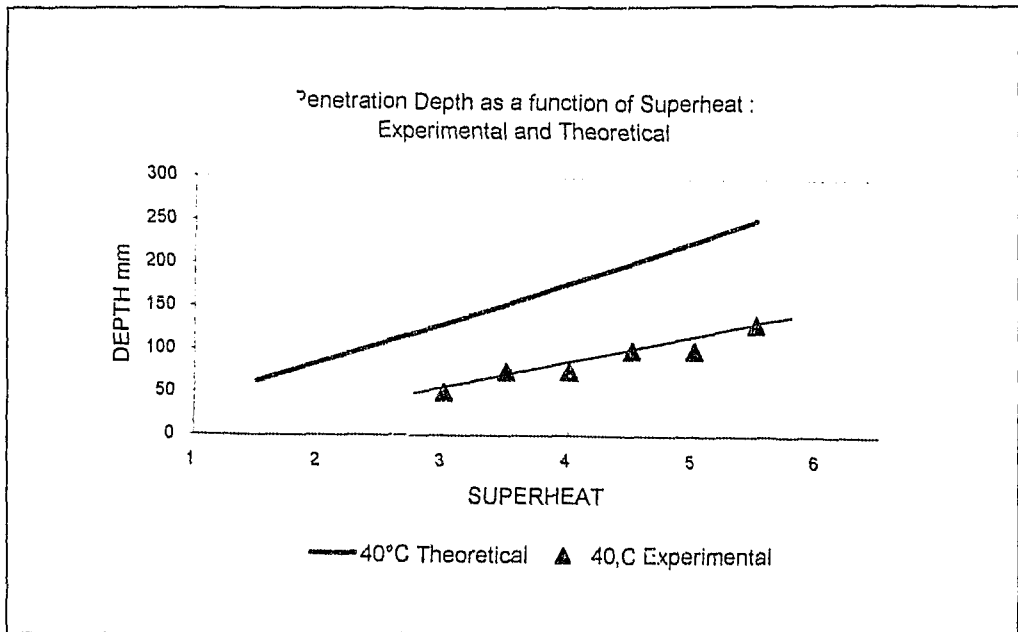


Figure 3.14 : Boiling penetration depths, extracted from Miyatake[49].

The reason for this could be three-fold:

- rise in evaporator pressure would further reduce local superheat
- From nucleate boiling theory there is the concept of a minimum superheat, for given conditions, which would initiate boiling. Below this superheat convection prevails.
- For water at any point in the column to flash to vapour and cooling to a temperature greater than the saturation temperature corresponding to the evaporator pressure, would require a pressure difference between this point and the evaporator pressure. This could be due to the instantaneous vapour extraction rate (caused by the compressor suction) being less than the local vapour production rate (caused by flashing). The result would be the pressure below this point being raised as well, thus reducing the local driving potential at lower levels..

These possibilities are considered hereunder.

Rise in evaporator pressure

Due to the high mass flux associated with flash evaporation the compressor may be unable to remove all the vapour generated. The excess vapour would cause the evaporator pressure to rise. The extent of this rise would depend on the size of the vacuum chamber above the cylinder being evaporated and on the quantity of water vapour being evacuated.

Minimum superheat

As mentioned previously, there exists a minimum superheat which marks the onset of nucleate boiling. As shown in figure 2.4, up to this temperature, convection takes place off a heated plate. The water in contact with the plate does form vapour but any small bubbles formed coalesce back into the layers of water above the plate. The greater the superheat, the greater and more frequent the vapour generation. A point is reached where vapour is produced in sufficient quantity not to condense into the bulk of the water and evaporation occurs at the surface. The situation is almost reversed in vacuum boiling. There is no heated surface and the upper layers of water have greater local superheat than the lower ones. Thus a bubble generated at any point can not be condensed by the water above it as it becomes more superheated as it approaches the surface. The reason for there being a minimum superheat can thus not follow the same arguments. This sort of effect was also noted by Kendoush[46], where drop centre temperature was seen to lag the surrounding pressure.

Pressure gradients

An explanation for the observed reduced "penetration depth", is that the generation of vapour may be accompanied by a local rise in pressure as discussed. Certainly from figure 2.19 it can be seen that the pressure of the evaporator is raised during vapour generation. It is thus plausible that the pressure at a given point in the liquid could be raised due to the rate of vapour generation exceeding the rate of vapour being extracted from the evaporator. This would result in the superheat of the water below this point being decreased even further. Vapour generation at lower levels would thus be arrested.

Large temperature gradients

As will be seen in chapter 4 there is a large temperature gradient with increasing depth. This is further shown in the two phases of flashing proposed by Miyatake[49]. Taking hydrostatic pressure and local pressure elevation into account, the initial stage can be seen as flashing of higher water layers and the second stage as heat transfer to the surface due to the temperature gradients set up by the flashing process.

3.2.2 Heat transfer coefficient

The lack of "penetration depth" observed indicates that temperature gradients would be set up within the water column. The lower liquid levels would be thus cooled by convective heat transfer to the higher, cooler levels. Using this concept it is possible to determine the heat transfer coefficient at a given level. For a control volume at a given height j , the rate of heat transfer from the volume to a higher level would be equal to the rate of cooling of the volume plus the rate of heat transfer from a lower level.

This can be written as follows:

$$h_j = \frac{M_j c_p \left(\frac{dT_j}{dt} \right) h_j (T_{j,2} - T_{j,1})}{T_{j,2} - T_{j,1}} \quad (3.17)$$

By measuring the temperature of a liquid column at various heights in the column the local heat transfer can be determined.

3.3 Options for the Design of Steam Jet Ejector Systems

It would be difficult to justify producing steam for a system with a typical coefficient of performance (COP) of around 0.5 compared with that of approximately 4 of vapour compression units (where COP here refers to the ratio of cooling attained to energy input). On an economic scale this gap may be narrowed somewhat by the fact that steam may be produced locally and the cost of having an electricity supplier is removed, furthermore a water vapour system can produce clear water and direct contact evaporators offer a reduction in heat transfer resistance. Even taking this into account, producing steam solely for refrigeration purposes does not usually prove economically viable [13].

In order to make steam jet refrigeration systems viable there is an obvious need to considerably reduce the steam consumption. Two methods of achieving such savings are presented in appendix C. These options were not implemented due to the focus of this project being on the vacuum boiling of water and not steam jet refrigeration design optimization.

CHAPTER 4

DESIGN OF EXPERIMENTAL SYSTEM AND EXPERIMENTAL PROCEDURE

This chapter describes the experimental steam jet ejector refrigeration plant, its commissioning and the design of the evaporators used during testing. The instrumentation used is also discussed. The chapter also describes the experimental procedure followed. Some attention is given to initial testing that was required.

4.1 Design of the Steam Jet Ejector System

In 1992 a laboratory scale steam jet refrigerator was designed and constructed in the Mechanical Engineering Laboratory by S Meyer and D Tyrer as a fourth year design project in fulfilment of the requirements of a BSc in Mechanical Engineering[5].

The design cooling capacity of the steam jet refrigeration unit was 2 kW. The evaporator pressure was designed to be 1.2 kPa (corresponding to a temperature of 10°C). The system comprised a three stage ejector set with two inter-stage direct contact barometric condensers.

A schematic diagram of the system is shown in figure 4.1.

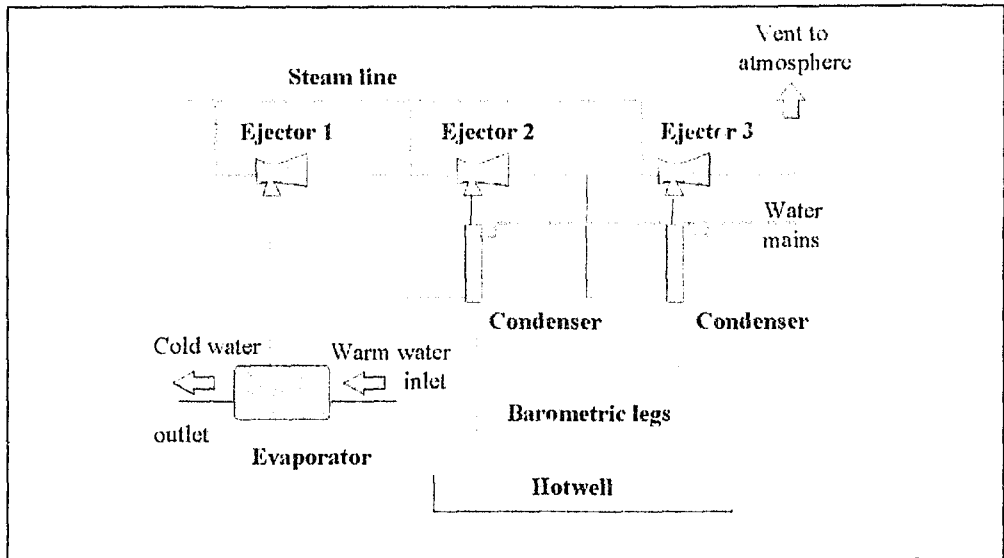


Figure 4.1 : Steam Jet Refrigeration rig.

4.1.1 Ejector Design

The ejectors were sized using the method laid out by Vil'der[51] , and made by the company Scientific Design (Pty) Ltd. The specifications of the ejectors were as follows :

TABLE 4.1 : EJECTOR DESIGN SIZES

Ejector	1	2	3
Compression Ratio	5	5	2.75
Entrainment Ratio	0.46	0.3	0.42
Nozzle Throat D	1.8 mm	1.4 mm	1.2 mm
Nozzle Discharge D	13.2 mm	5.2 mm	2.4 mm
Diffuser Throat D	21.4 mm	6.8 mm	3.8 mm

During tests conducted during October 1992 by Meyer and Tyrer the plant could not reach design operating conditions, despite extensive checking for leaks. Further work on the steam jet refrigeration system was carried out by S.Meyer in November and December of 1992. The objective of this work was to ensure system safety when a positive pressure is applied to the system and to achieve design pressure distribution. Three separate tests were conducted, namely a safety test, a leakage test and a performance test. (The safety test entailed pressurising the system with water.) The leakage into the system was calculated as 0.023 kg of air per hour. The performance of the system was found to depend on the supply steam pressure. The design pressure distribution could only be obtained if the supply pressure was above 680 kPa. This pressure could only be maintained for short period of time. It was recommended that the ejectors be resized for a motive steam pressure of 580 kPa because of limitations of the steam generator in the laboratory.

Before consideration could be given to the evaporation process the steam jet refrigeration unit first had to be made operational. The ejectors were resized as recommended by Tyrer, this work being done by the Mechanical Engineering Workshop after consultation with J.Kirsch of Scientific Design. During the re-boring of the ejectors it was discovered that the third ejector was undersized by 1 mm, which could have had an effect on its performance. While the ejectors were being re-bored the entire unit was resealed, with clamps being tightened and where necessary being replaced and new vacuum grease being applied to joints. After the ejector resizing was completed the ejectors were replaced and initial tests conducted. The objectives of these initial tests were to gain familiarity with the system operation and to achieve the design pressure distribution.

The specifications of the modified ejectors were as follows :

TABLE 4.2 : RESIZED EJECTOR SPECIFICATIONS

Ejector	1	2	3
Compression Ratio	5	5	2.75
Entrainment Ratio	0.46	0.3	0.42
Nozzle Throat D	2.0 mm	1.56 mm	1.41 mm
Nozzle Discharge D	13.72 mm	5.45 mm	2.49 mm
Diffuser Throat D	21.7 mm	7.03 mm	3.89 mm

4.1.2 : Condenser Design

The direct contact condensers were designed using empirical methods outlined in Vil'der and How's articles[52] . The height of the barometric legs was established simply as :

$$H = \frac{P_{atm} - P_{cond}}{\rho * g} \quad (4.1)$$

The barometric legs had been designed purely on hydrostatic pressure. It was felt that taking pipe friction into account would increase the leg's performance. The primary condenser operating pressure is 5.1 kPa, which requires a head of 77.9 kPa (approximately 8 metres). The available height from the ejector system base to the sump was 7.3 m and the condenser was 0.8 m above the floor, giving a total of 8.1 m..

Applying the equation for pipe friction :

$$h_f = \frac{8fLQ^2}{\pi^2 d^5 g} \quad (4.2)$$

Where : f is the pipe friction factor = 2.017×10^{-2} for a Re number of 58626 at 15°C

L is the pipe length and unknown

Q is the volumetric flow rate = 0.42 l/s

d is the internal pipe diameter = 0.025 m

This gives a head loss of 0.24 m at full operation. The system was thus raised by 30 cm . This was achieved by placing the plant frame on trestles. The inlet steam line was lengthened, as were all the exhaust pipes and tubes and water inlet pipes. Figure 4.2 shows a photo of the completed steam jet refrigeration rig.

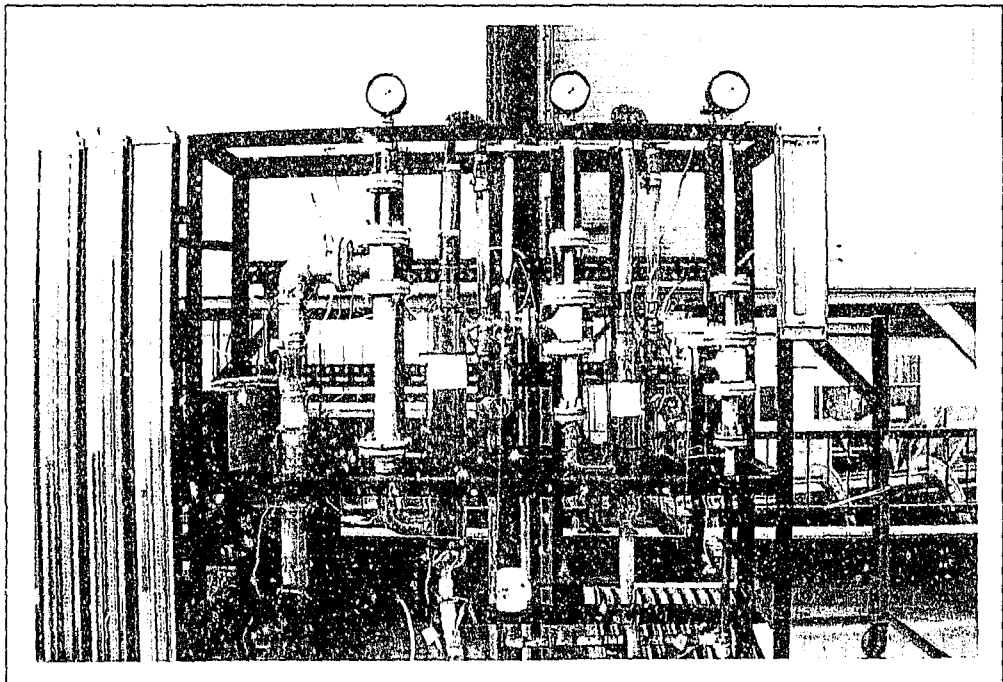


Figure 4.2 : Photograph of completed steam jet refrigeration system.

4.1.3 : Commissioning Tests

Various commissioning tests were conducted. The steam jet system was connected to a glass evaporator. Minor modifications were made to the rig including the insertion of in-line filters in the ejectors, replacement of worn steam supply valves and cleaning of the manometers. Sealing the rig and leak detection was also done. The results are compared graphically, in figure 4.3, with those obtained by Meyer and Tyrer.

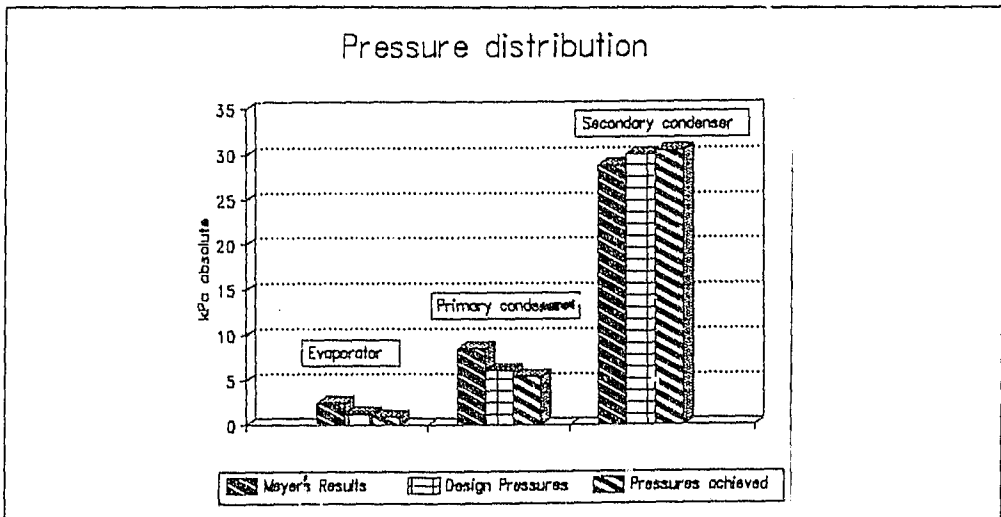


Figure 4.3 : Pressure distribution in the system, compared to previous results.

The evaporator temperature was measured 13.2 cm below the surface of the water; it was found that it decreased with time. The water surface eventually froze. Photographs of the glass evaporator were taken and are presented below.

Figure 4.4 shows the violent boiling of the water in the evaporator during the test. It is interesting to note the absence of significant vapour bubbles in the water, with no set nucleation sites being observed below the water surface. The bubbles on the surface were large in size (about 1.5cm diameter).

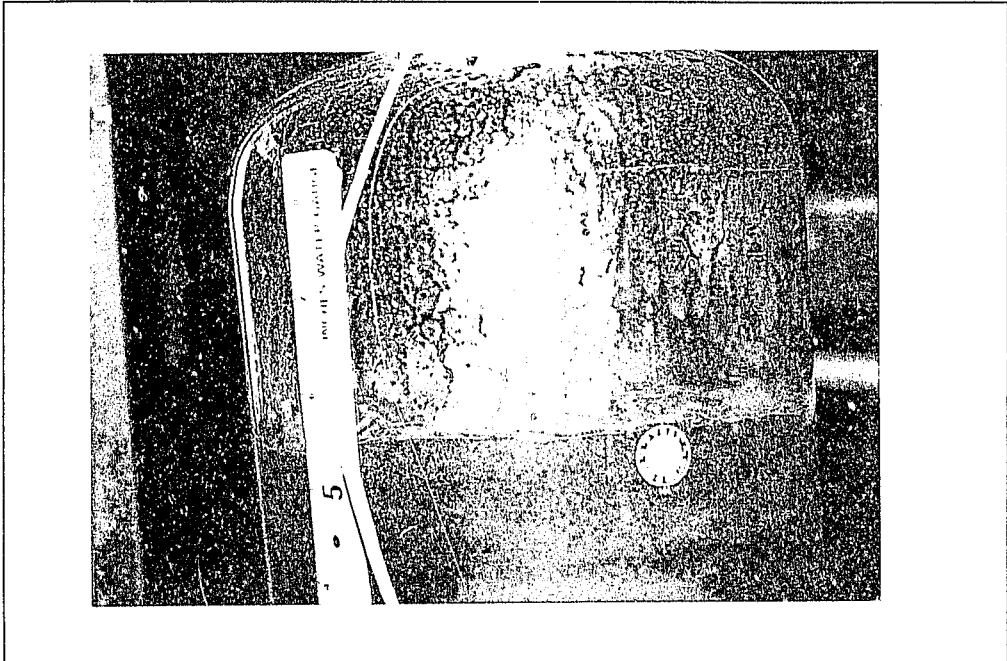


Figure 4.4 : Surface boiling of a pool of water

As the bulk water temperature decreased so the boiling at the surface died down, with sporadic high energy "explosions" occurring at the surface. At this stage a thin layer of ice formed on the water surface. This layer was repeatedly broken by the ferocity of the isolated bursts on the water surface, but eventually became thick enough to form a crust below which small vapour bubbles appeared, shown in figure 4.5.

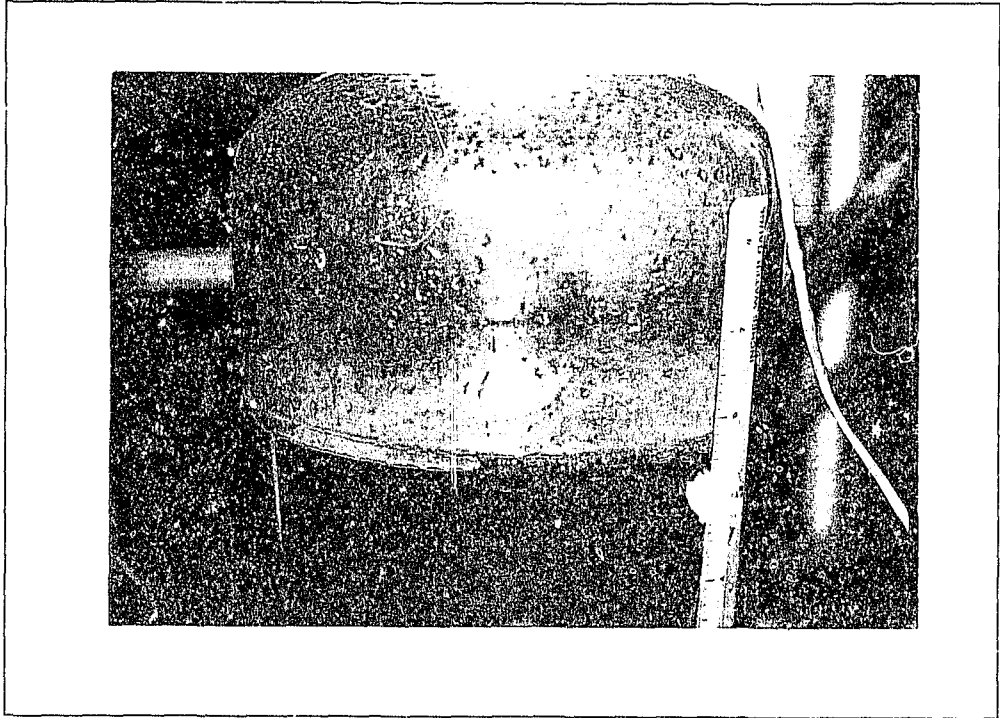


Figure 4.5 : Ice layer at the surface.

A large number of bubbles was observed in the flow-meters. This was initially ascribed to leaks but the bubbles disappeared once the flow stopped. It is thought that these bubbles consisted of dissolved gases in the supply water coming out of solution as the water passed from the supply pressure to the condenser pressure.

The flow rate in the condensers could only reach 40 % of its maximum design flow of 0.42 l/s. Flow rates below 35 % resulted in boiling ceasing. The low condenser flow rates indicated that the barometric legs were not providing sufficient head and required redesign.

A high temperature gradient between the surface of the water and the thermocouple measurement point was attributed to the hydrostatic pressure difference between these two points. A water height of 13.2 cm corresponds to a hydrostatic pressure of 1.3 kPa. As the evaporator is at a pressure of 0.61 kPa or lower this means that the pressure at the temperature measurement point was likely to be in the region of 1.7 to 1.9 kPa, which corresponds to a saturation temperature of 15°C to 16.7°C. The temperature gradient of 3.7°C between the evaporator base and the water surface can thus be supported.

The modifications to the ejectors appeared to have had the desired effect and enabled the system to reach a vacuum corresponding to the triple point of water. It could be concluded that, due to this increase in compression ratio with the same available motive steam pressure, the system cooling capacity is likely to be below the 2 kW designed for. The evaporators could then be designed and the vacuum boiling of water investigated.

4.2 Evaporator Design

In accordance with the project objectives listed in Chapter 1, three types of studies were conducted. These were a photographic study to visualize the boiling process; a study of a fixed volume of water subjected to rapid decompression to identify the nature of, and mechanisms involved in, boiling under vacuum conditions; and a study of an evaporator under flow-through conditions. This required three types of evaporators: an evaporator for the photographic study, a vertical cylinder and a flow-through direct contact evaporator. The need for and design of each of these is discussed separately below.

4.2.1 Through-Flow Evaporator Design

In order to cool a flow of water it is necessary to pass it through the evaporator. ASHRAE recommends[7] an evaporator with spray nozzles, where the evaporator surface area is such that droplets cannot be entrained into the ejectors, but no indication of the vertical height required is given. For this investigation it was decided to have water flowing through the evaporator over a flat plate and then being removed via a pump and barometric leg. It was felt that the boiling process could be more clearly observed with flow over a plate than as a spray. It was further hoped that the validity of using a mass transfer coefficient for sizing the evaporator could more readily be established by considering the flow over a two dimensional surface, whereas in spray nozzles the total surface area depends not only on mean droplet size but also on the number of droplets, which would be difficult to establish.

The basic requirements for the evaporator were ease of access into the evaporator, that the evaporator would not corrode and interfere with the boiling process and that it be easy to make visual inspections of the processes occurring inside the evaporator. Aluminium and PVC were considered and PVC was chosen over aluminium for reasons of ease of construction. In order to be able to view the flat plate, windows were placed in either side of the evaporator and the plate was made of perspex with transparent side walls. Detachable plates at the base and top of the evaporator ensured that the evaporator could be easily opened. A recess around the base with an O-ring provided sealing, the plate being secured by a clamp with 5mm diameter bolts screwed into the base. An inlet ramp ensured that the flow was evenly distributed over the plate.

Sizing the evaporator proved difficult due to the lack of design guidelines. An order of magnitude approach was thus taken. The mass rate of flow at a liquid-vapour interface is given as [53] :

$$j = \left(\frac{M}{2\pi R} \right)^{0.5} \left[\frac{p_g}{T_g^{0.5}} - \frac{p_f}{T_f^{0.5}} \right] \quad (4.3)$$

Where j is the mass flux (kg/s/ unit area)

M is the molecular weight = 18.015 kg/kmol

R is the universal gas constant = 8.314 KJ/kmol K

T_f was taken as 278 K

T_g was taken as 293 K

p_f was taken as 0.8712 kPa

p_g was taken as 2.337 kPa

This yielded a mass flow rate of 1.565 kg/s/m^2 . The design vapour flow rate was $8.3 \cdot 10^{-4} \text{ kg/s}$ to provide 2 kW of cooling. This gave an area of $5.3 \cdot 10^{-4} \text{ m}^2$ or 530 mm^2 . If the water flashed rapidly as it entered the evaporator, say to 6°C , then j would decrease to $2.95 \cdot 10^{-2} \text{ kg/s/m}^2$ and the required area increases to $28\,000 \text{ mm}^2$. An evaporator outer base area of 300 by 150 mm was selected with a flow base plate size of 230 by 100mm, giving $23\,000 \text{ mm}^2$ of area available for evaporation. An evaporator height of 150 mm was chosen.

The wall thickness was calculated by calculating the thickness for a circular plate of equivalent surface area to the maximum surface area of the evaporator side and with similar pressure gradient across it, thus [54] :

$$t^3 = \frac{p^3 P A^4}{64 E d} \quad (4.4)$$

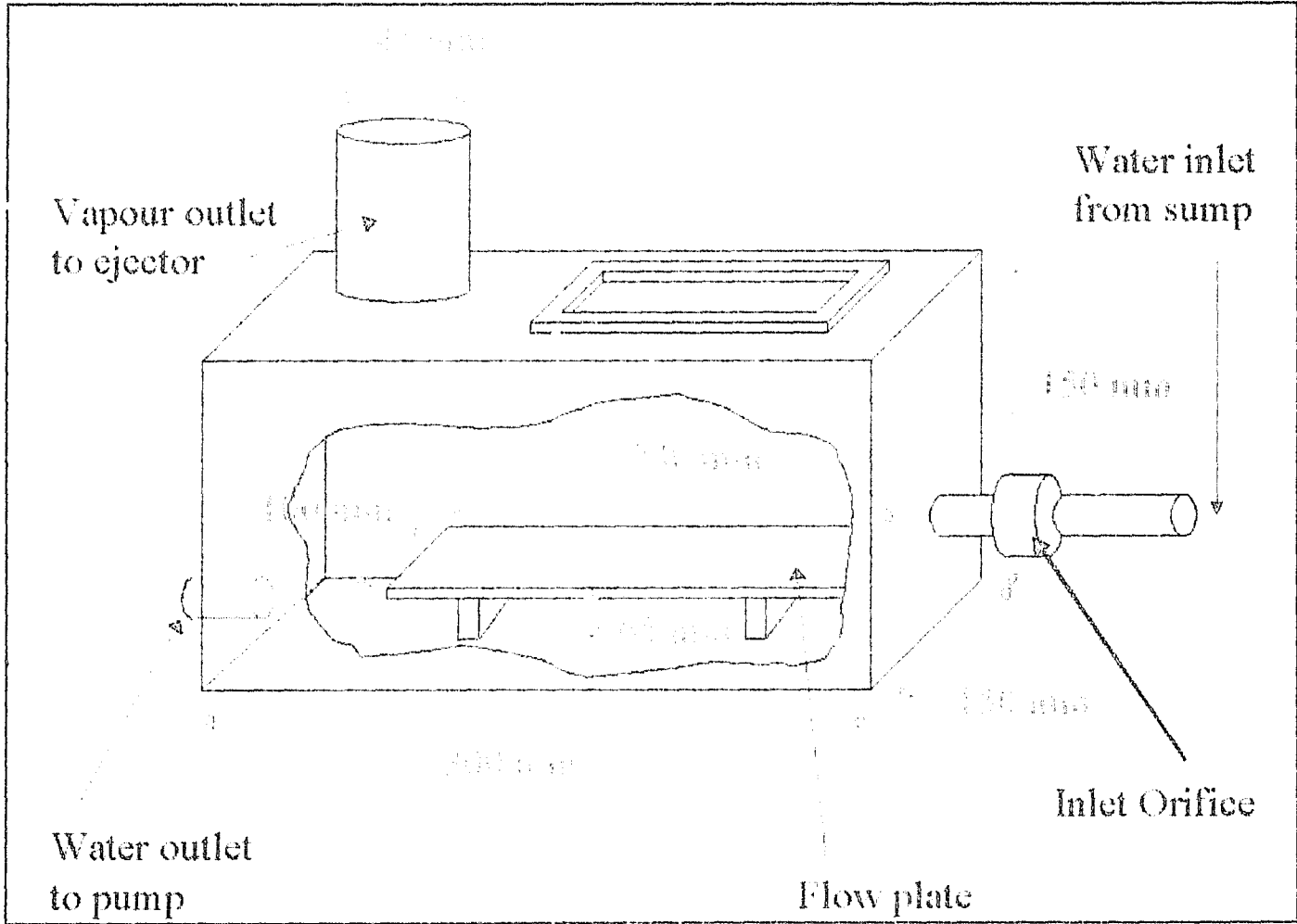
Where t is the thickness required

P is the difference between evaporator and atmospheric pressure in kpa

A is the equivalent radius = $3.78 \cdot 10^{-2} \text{ m}^2$

Maximum deflection was restricted to 0.2 mm giving a thickness of 10 mm for PVC. The design and assembly drawings of the evaporator are given in appendix D. Figure 4.6 is a dimensioned sketch of the through-flow evaporator.

Figure 4.6 : Through-flow evaporator sketch

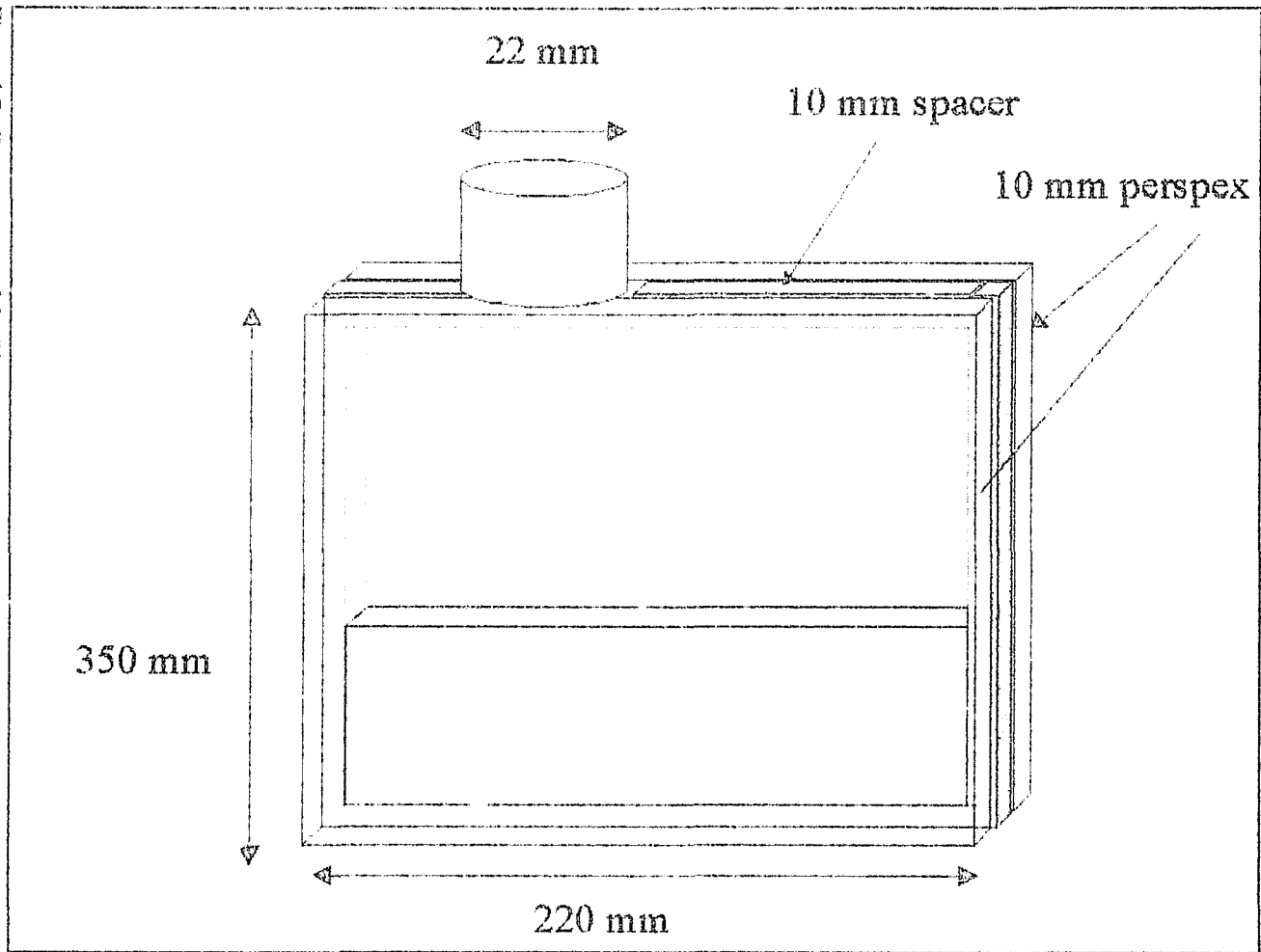


The inlet water was at atmospheric pressure and was drawn into the evaporator through a barometric leg from a 50 litre basin. This gave a minimum capacity of 26 minutes at the design conditions. The barometric leg length from the evaporator to this basin was 8.4 m in length, which meant a shortfall in required hydrostatic pressure of 11.1 kPa. It was thus decided to place an orifice plate along the barometric leg, at the entrance to the evaporator. Flow could then be controlled with a ball valve. The orifice plate was designed according to BS 1042, and is shown in appendix D.

4.2.2 Design of Evaporator for the Photographic Study

In order to adequately describe the vacuum boiling of water, it was deemed necessary to conduct a photographic study of the process. To this end a simple evaporator was built, consisting of two sheets of perspex separated by a 10 mm PVC spacer, in which the boiling of a pool of water, undergoing decompression, could be viewed. This evaporator was fitted to the direct contact evaporator circuit. The evaporator used is shown in figure 4.7.

Figure 4.7 : Evaporator used for Photographic study



4.2.3 : Vertical Cylinder Design

Miyatake's [41&49] work suggested flashing coefficients of the order of $0.03 \text{ kg}/(\text{s m}^2 \text{ mmHg})$. Thus for an evaporator pressure of 0.611 kPa with inlet temperatures ranging from 10 to 40°C , ie a maximum pressure difference of 50.7 mm Hg , mass flow rates of 1.22 kg/s m^2 could be expected using similar equipment. Naturally whether this value is sustained would depend on the evacuation rate of the compressor system and the volume of the vacuum chamber. Using the design value of $8.3 \cdot 10^{-4} \text{ kg/s}$ would mean that a maximum area of $5.452 \cdot 10^{-4} \text{ m}^2$ could be used, ie a diameter of 26.34 mm . 22 mm internal diameter PVC pipe was the closest diameter available. A vertical cylinder of 30 cm length was made, with a union at one end. This could be attached to a union connected to a ball valve which was connected to the pipe leading to the ejector. A loop made of a PVC 90° elbow was fitted before the ball valve to prevent water running down into the cylinder from the ejector. The pressure transmitter was placed above this valve to reduce shock loading. Figure 4.8 is a diagram of the vertical cylinder and decompressing valve.

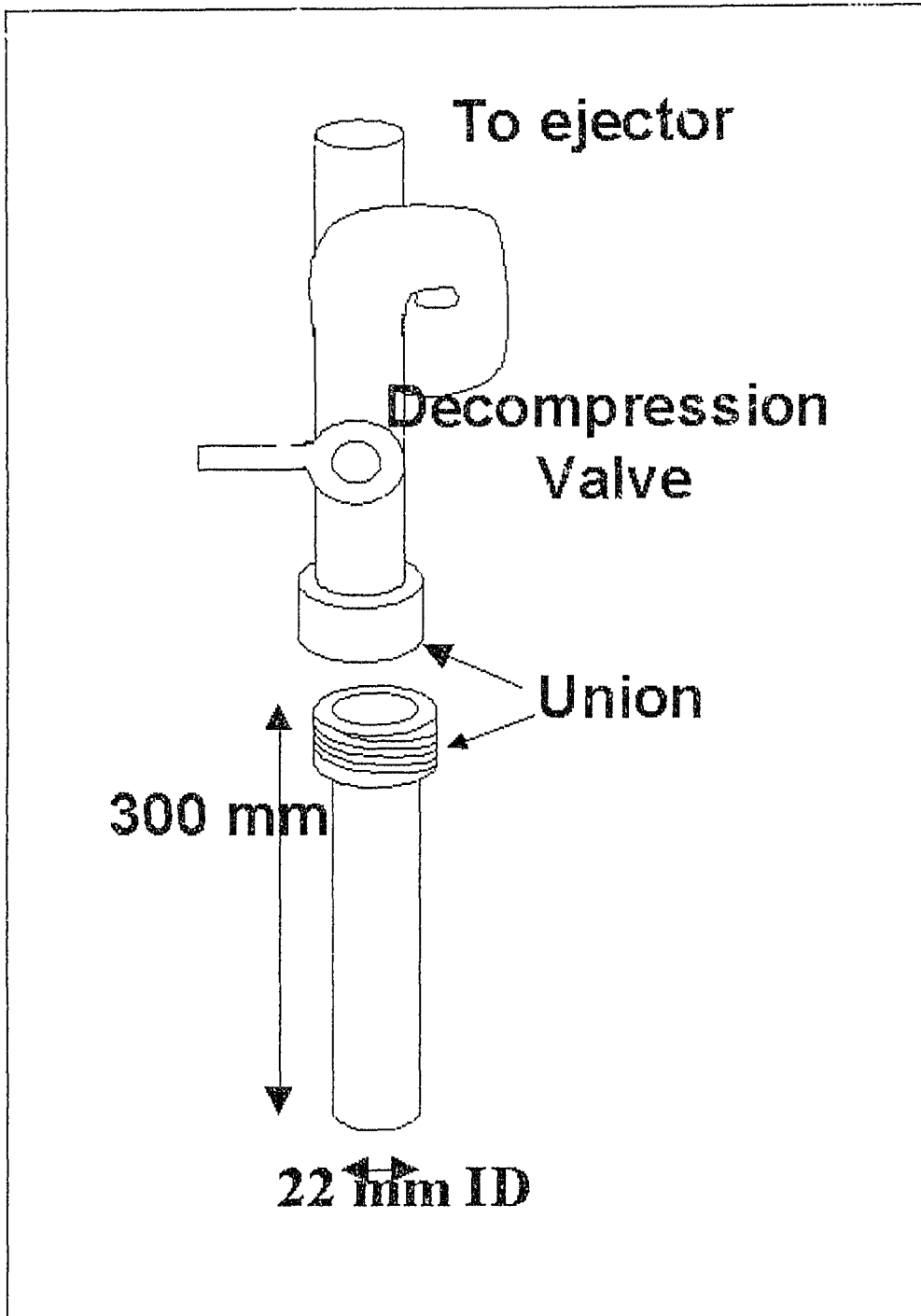


Figure 4.8 : Evaporator used for Vertical cylinder test

1967, Vol. 5, No. 1, pp. 1-10

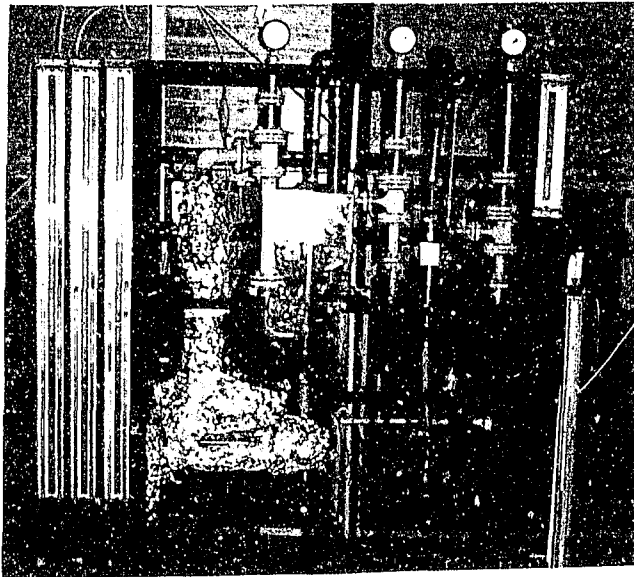


Figure 1. Photograph of the high-pressure cell during the reaction.

The reaction was carried out in a high-pressure cell of the type described by Bridgman.¹² The cell was filled with a mixture of the monomer and the initiator, and the reaction was initiated by the application of a high pressure. The reaction was allowed to proceed for a certain period of time, and the reaction mixture was then cooled and the reaction was stopped. The reaction mixture was then analyzed by the method described above. The results of the analysis are shown in Table I. It can be seen from the table that the reaction proceeds quantitatively, and that the reaction is first order with respect to the monomer and first order with respect to the initiator. The rate constant of the reaction is 1.5×10^4 l./mole-sec. at 100°C. and 10,000 atm. The activation energy of the reaction is 15.5 kcal./mole.

The primary flow rate measurement was to come from measuring change in volume in the vessels connected to the legs. The orifice plate could not be calibrated as under operating conditions the flow would contain two phases of water.

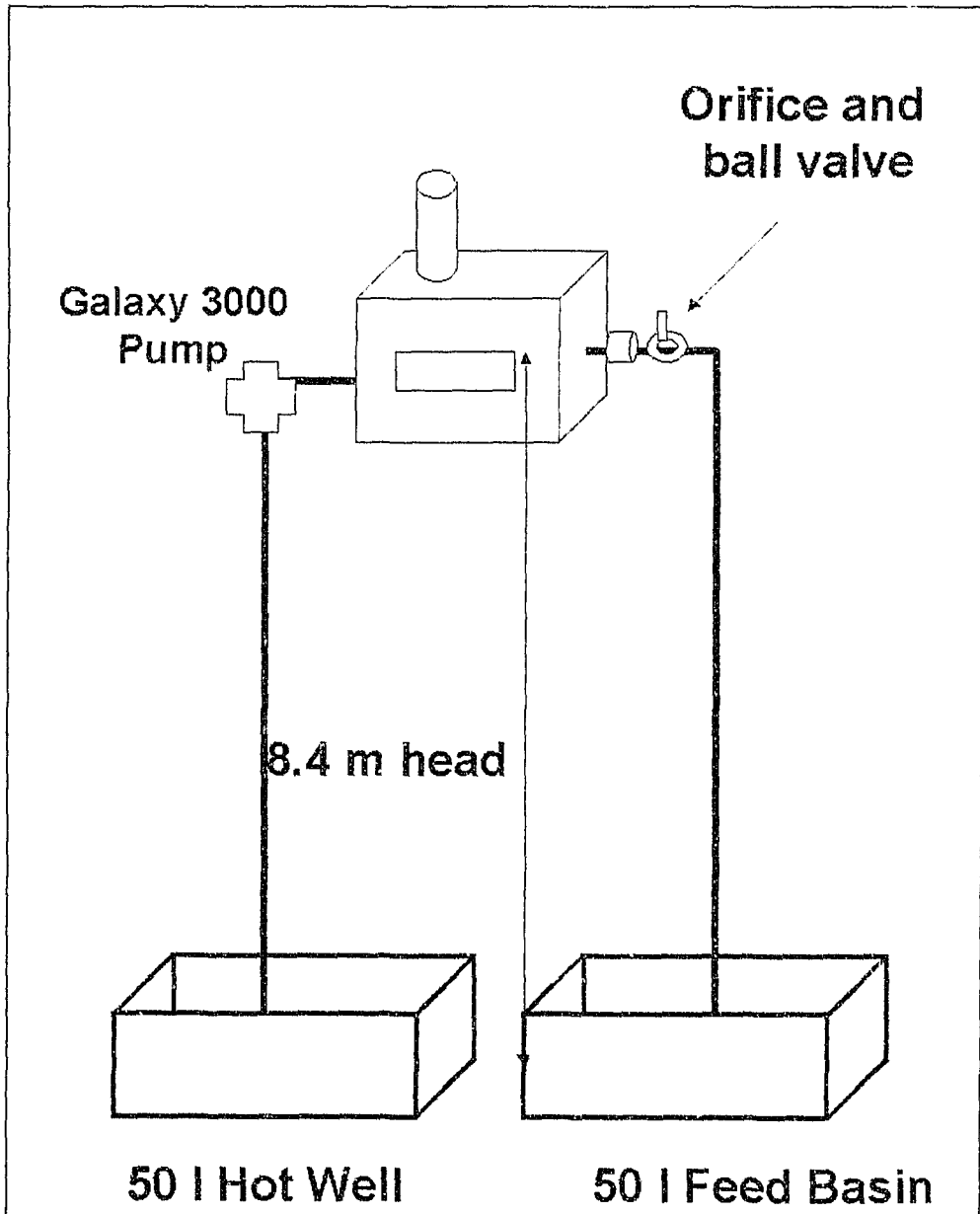


Figure 4.10 : Piping layout for through flow evaporator testing.

Though the through-flow evaporator was fitted with perspex windows, photographs of the boiling process could not be taken as excessive splashing occurred on these surfaces during testing. Figure 4.11 is a schematic diagram of the layout of the instrumentation used.

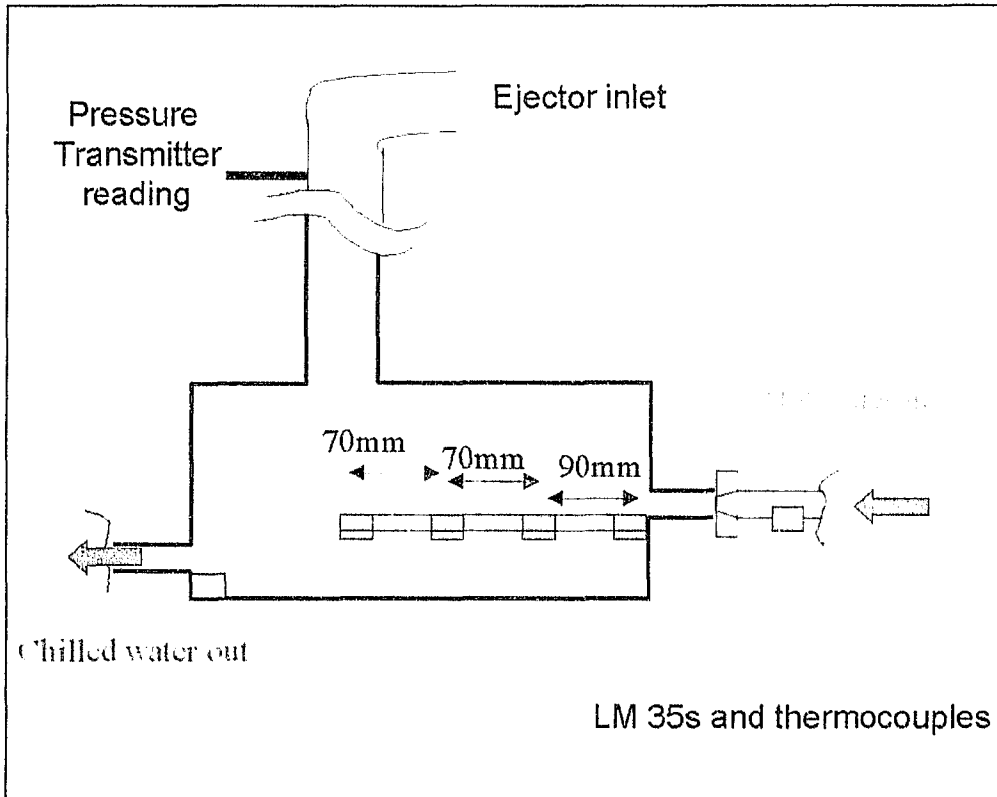


Figure 4.11 : Layout of instrumentation used for the flow-through direct contact evaporator

Water was drawn at constant velocity into the evaporator. The height of the inlet tank was measured against time. A heater was placed in the inlet tank to vary inlet temperature. The temperatures at inlet sump, evaporator inlet after the orifice, along the flat plate and evaporator outlet were measured using type T thermocouples and LM35 temperature sensors. The evaporator pressure was also recorded. These signals were logged by a "Computerscope" data logger.

4.3.2 Photographic Study

A hand held video recorder was used in conjunction with a 35 mm camera to perform a photographic study of the boiling process under a vacuum. The video material was used to establish the time scales involved. The photographic study evaporator was connected to the steam jet unit and the water circuit (figure 4.10). The process with the water flowing through the evaporator was then photographed using the video recorder. The water was observed to boil violently as it passed through the evaporator, with flashing occurring mainly at the water surface. Not much could be concluded regarding the boiling process. Only when the inlet and outlet valves were closed did this boiling die down. It was thus decided to film the depressurisation process without water flowing through the evaporator. Depressurising the evaporator was achieved through the use of a ball valve. A water trap was installed above the ball valve to prevent any leakage into the evaporator from the section of pipe leading to the primary ejector. A photograph of the decompression valve arrangement is shown in figure 4.12.

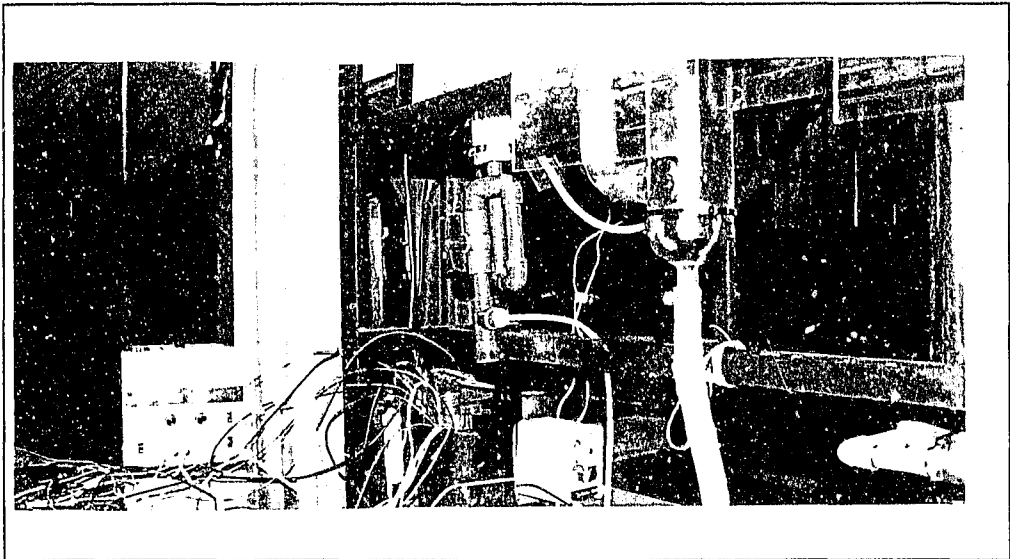


Figure 4.12 : A photograph of the decompression valve.

4.3.3 Vertical Cylinder

In order to view the boiling process, it was decided to measure temperatures at various heights in the vertical cylinder. LM-35 temperature sensors and type T thermocouples were fitted at heights of 0, 3, 6, 9, 15 and 21 cm. The pressure transmitter was fitted above the depressurisation valve to reduce shock loading of the transmitter. Additional readings that were taken were pre-primary nozzle pressure, pre-secondary nozzle pressure, steam pressure and temperature.

Figure 4.13 is a schematic diagram of the layout of instrumentation used during this study.

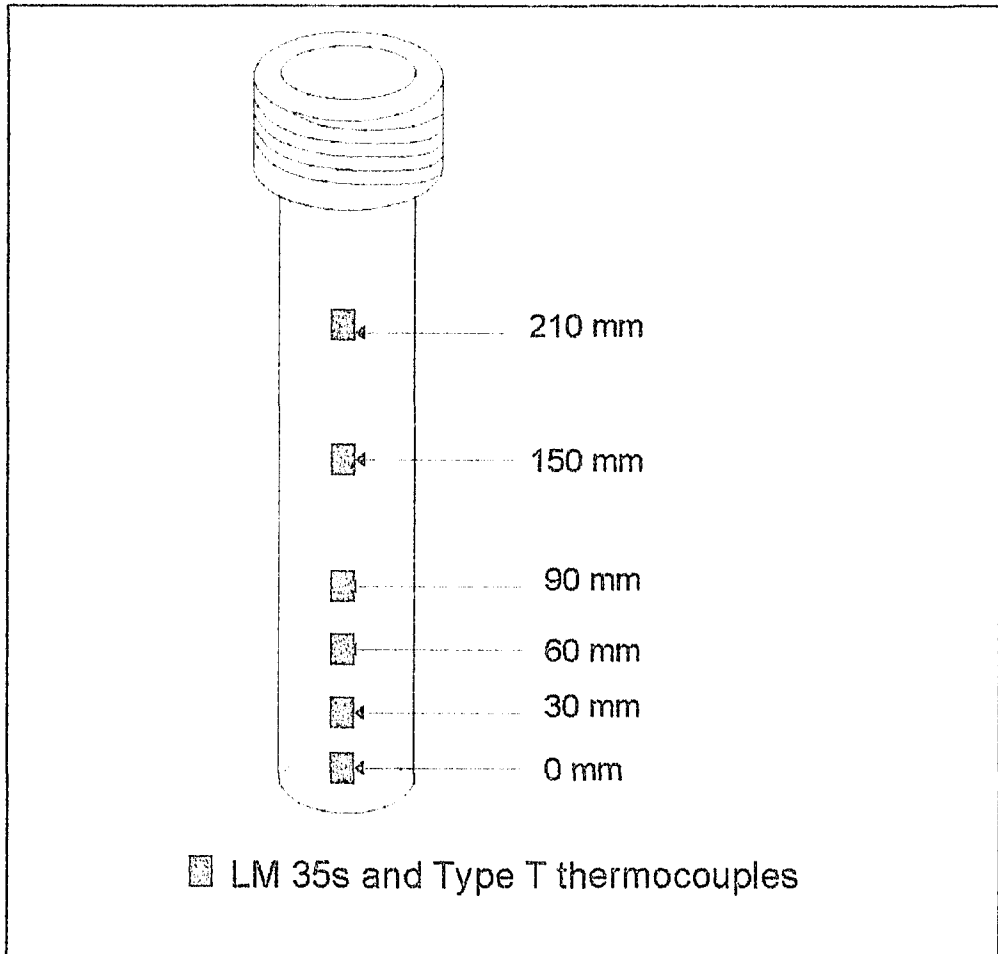


Figure 4.13 : Layout of instrumentation used in the vertical cylinder testing.

4.4 COMMISSIONING TESTS

4.4.1 Though-Flow Evaporator

Test Procedure

Two vessels were used to supply and receive water from the evaporator. These were filled with distilled water and the inlet temperature and dissolved oxygen content were recorded. The steam lines were opened and the pressures allowed to settle. The valves on the inlet and outlet barometric legs were opened and the change in liquid height in the vessels measured periodically. Steam pressure, system pressures and condenser water flow rates were noted.

Results and Observations

The output of the LM-35 temperature sensors and of the pressure transmitter were recorded using a "Computerscope" data logger computer scope. These data were then calibrated using a spreadsheet. In addition to this the changes in inlet vessel liquid height were converted to flow rates for each of the tests. Calibration details are presented in Appendix E. Sample calculations are presented in Appendix F.

The most notable observation made during the testing was noise and shuddering that was induced in the throttling orifice at the evaporator inlet. The pressure read off the manometer prior to the nozzle oscillated violently, while the pressure after the nozzle varied little.

Bubbles could be seen to rise from the positions where the thermocouples entered the evaporator, despite various attempts at sealing these points. It was found that the best sealing that could be achieved was using an epoxy coated with a silicone sealer.

Discussion

The temperatures at the measuring points along the plate were found to be highly oscillatory. Intuitively one would expect the temperatures to be fairly steady. Given the oscillation in the orifice pressure and the shuddering observed it was deduced that the flow over the plate was inconsistent and the plate was not level in spite of the evaporator being level. The inconsistency in the flow rate can be explained giving consideration to the physical process involved in drawing water through the barometric leg and into the evaporator. As the water flows through the restricting orifice plate to a pressure lower than its saturation pressure, flashing occurs. Due to this flashing there is a local increase of pressure and the barometric liquid height can not be supported. Water is thus drawn back down into the leg. As the vapour is extracted the evaporator pressure drops, the water is drawn back into the evaporator and the process repeats itself.

The evaporator pressure was generally higher than the saturation pressure corresponding to the mean evaporating temperature. This can be ascribed to two possible causes : an error in calibration, or a leak at the point of measurement. The connections on the pressure transmitter were resealed and the transmitter re-calibrated against a Macleod gauge (Appendix E).

Modifications

The barometric leg on the inlet side of the evaporator was replaced by a short (1 m) leg with a valve and the PVC orifice plate. It was hoped that this would eliminate the oscillation previously discussed.

4.4.2 : Vertical Cylinder

Before testing the leakage of the cylinder needed to be established . The cylinder was evacuated using a vacuum pump and its pressure measured over a period of time. The results of this test are listed below.

TABLE 4.3 : LEAKAGE TEST RESULTS

Change in Pressure (mm Hg)	TIME (Min)
182	42
24	10
56	25
30	14

The maximum leakage was $8.48 \cdot 10^{-5}$ kg/hour which is well below the 0.3 kg/hour designed for.

CHAPTER 5

EXPERIMENTAL RESULTS AND OBSERVATIONS

This chapter presents the results obtained and observations made during the tests. The chapter is divided into three main sections, these being the three tests conducted: the through-flow evaporator, the photographic study and the vertical cylinder evaporator. This chapter is accordingly divided into three main sections, which focus on the aforementioned tests respectively. In each section the objectives of the test is restated, the range of conditions over which the tests were conducted listed and the results and observations presented.

5.1 Through-Flow Evaporator

The objectives of the through-flow evaporator tests were to examine the heat transfer processes in a through-flow evaporator, to investigate the effect of varying inlet water flow rates and temperatures on these processes and on the evaporator's operating conditions, and to derive a mass transfer coefficient for the design of such evaporators. The range of conditions under which the evaporator was tested is listed below.

TABLE 5.1 : Through-flow evaporator test conditions

Flow rate kg/s	Inlet temperature °C
0.0671	12, 14, 16, 21, 24
0.0588	8, 10, 14, 15, 17, 19
0.0245	12, 16, 18, 20, 24 - 34

Each test consisted of the average of 64 samples at 500 ms intervals. The samples were averaged and the processed results were grouped into the three flow rates listed in the table above and are presented in full in appendix F.

5.1.1 Evaporator Pressure

As modelled in Chapter 3 (Figures 3.3 and 3.11), the evaporator pressure was observed to increase with increasing inlet temperature, shown in figures 5.1 and 5.2.

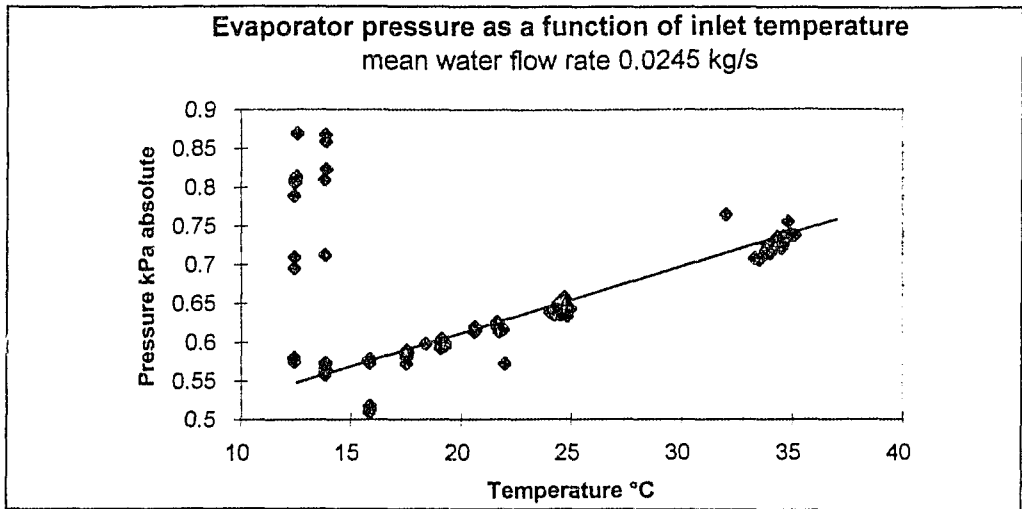


Figure 5.1 : Evaporator pressure as a function of inlet temperature,

mean flow rate = 0.0245 kg/s.

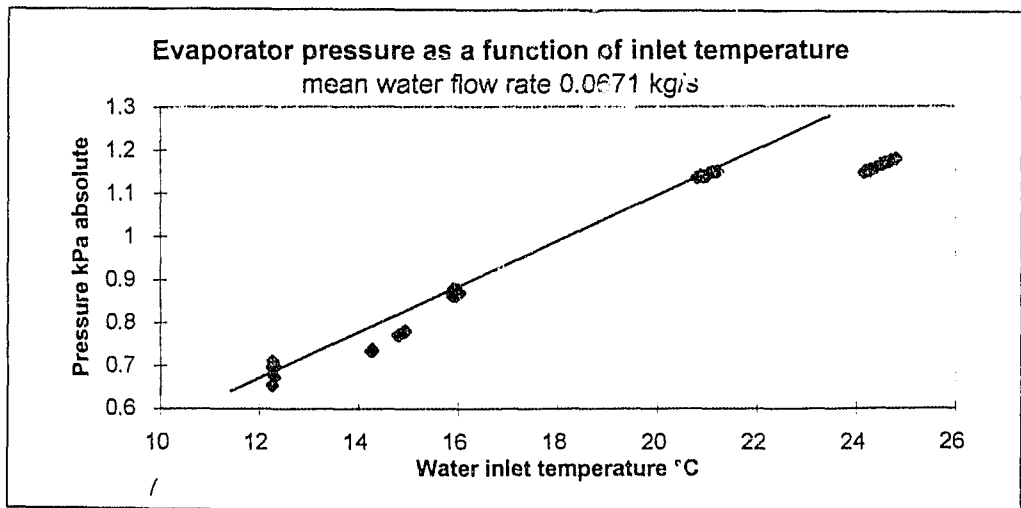


Figure 5.2 : Evaporator pressure as a function of inlet temperature,

mean flow rate = 0.0671 kg/s.

5.1.2 Temperature Gradients

It was hoped that an evaporator mass transfer coefficient could be determined based on the temperature distribution on the plate. No consistent temperature gradient along the length of the plate could be established. A mean difference in temperature could however be noted between inlet, plate end and evaporator exit. (Figures 5.3 - 5.5)

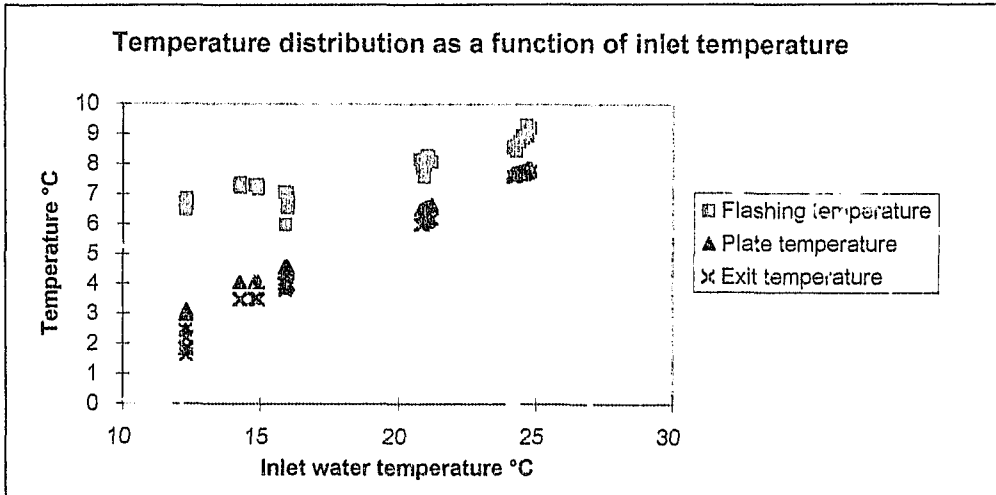


Figure 5.3 : Temperature distribution within the through-flow evaporator,

mean flow rate = 0.0671 kg/s.

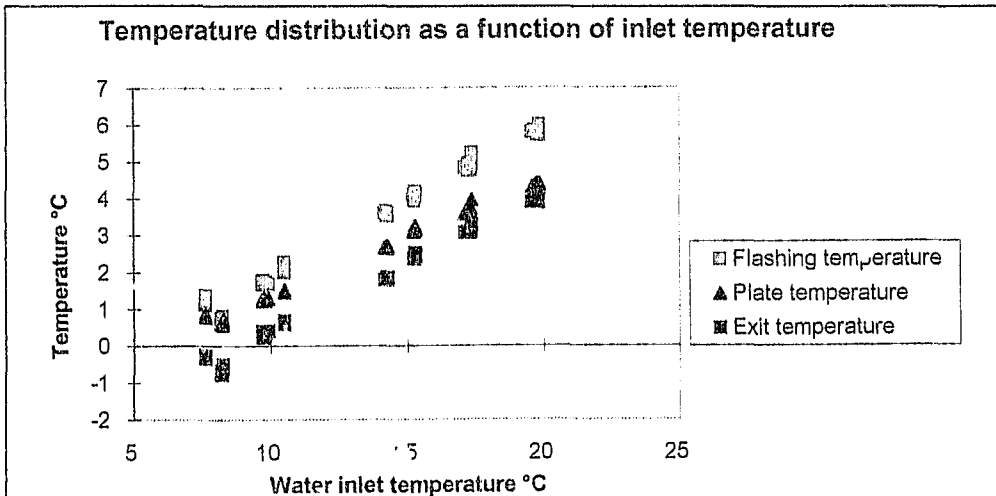


Figure 5.4 : Temperature distribution within the direct contact evaporator,

mean flow rate = 0.0584 kg/s.

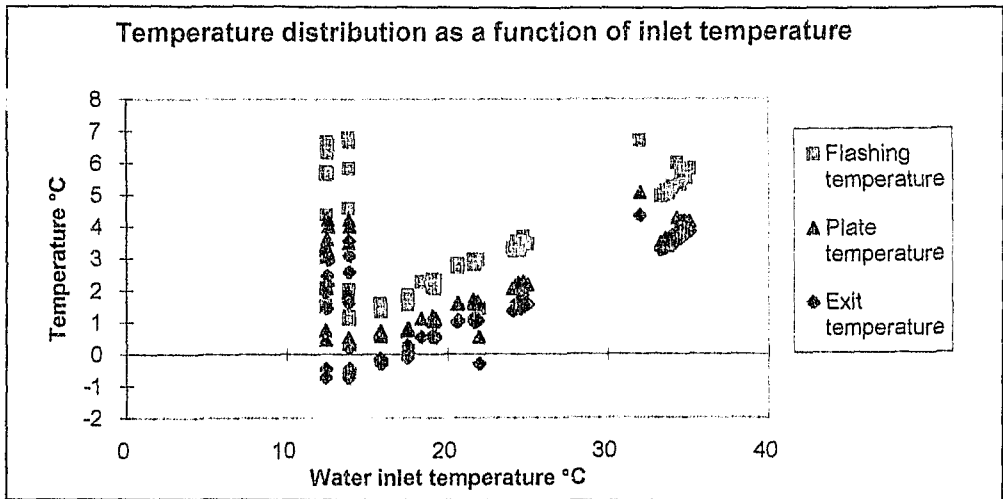


Figure 5.5 : Temperature distribution within the through flow evaporator,

mean flow rate = 0.0245 kg/s.

From these plots, the flashing temperature (ie temperature measured after isenthalpic expansion) is observed to increase with increasing flow rate at given inlet temperatures. The difference between inlet and exit temperature is observed to increase with increasing inlet temperature, ie the heat transfer process in the evaporator becomes more efficient with increasing driving potential. The difference between the flashing temperature and the exit temperature decreased with increasing input temperature. At lower input temperature there is a greater difference between the plate temperature and the exit temperature.

The temperature distribution in the evaporator was used to establish the contributions of the various boiling regimes to the cooling of the bulk of the water. The regimes identified were :

- Flashing across the orifice.
- Surface evaporation along the plate.
- Agitated evaporation after the plate.

5.1.3 Heat Transfer

From the temperatures measured within the evaporator, rates of heat transfer were established between the measured points. As the evaporator temperatures were measured immediately after flashing through the nozzle, after surface evaporation across the plate, and prior to the water being pumped out, the rates of heat transfer as the water flowed through the evaporator could be calculated. The contribution of flashing to the overall heat transfer rate was found to be significantly higher than that of surface or agitated evaporation. Figures 5.6 - 5.8 show the percentage contribution that flashing across the nozzle made in the cooling process. To negate variations in leakage or ejector performance, the contributions to cooling were plotted against the inlet temperature, as a percentage of the total rate of heat transfer across the evaporator.

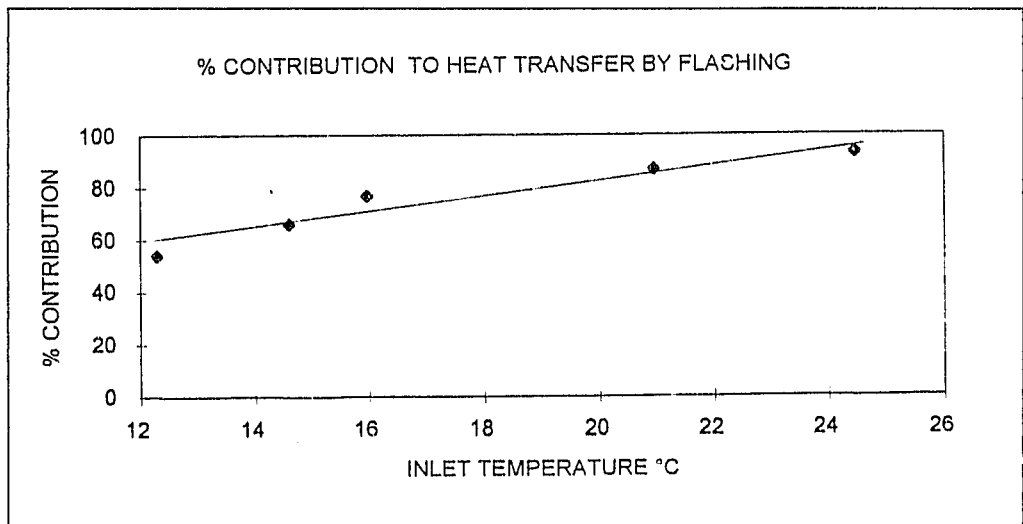


Figure 5.6 : Percentage contribution to total heat transfer by the flashing boiling regime, mean

flow rate = 0.0671 kg/s.

The contribution of flashing to the cooling process can be observed to increase with increasing inlet temperature. The percentage contribution of flashing is fairly consistent at given driving potentials for the three flow rates.

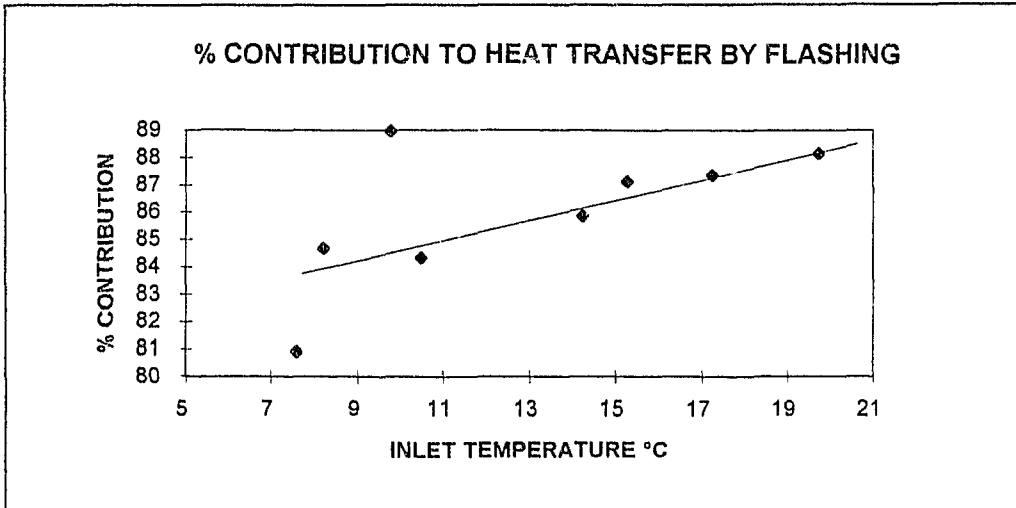


Figure 5.7 : Percentage contribution to total heat transfer by the flashing boiling regime,
mean flow rate = 0.0584 *kg/s.

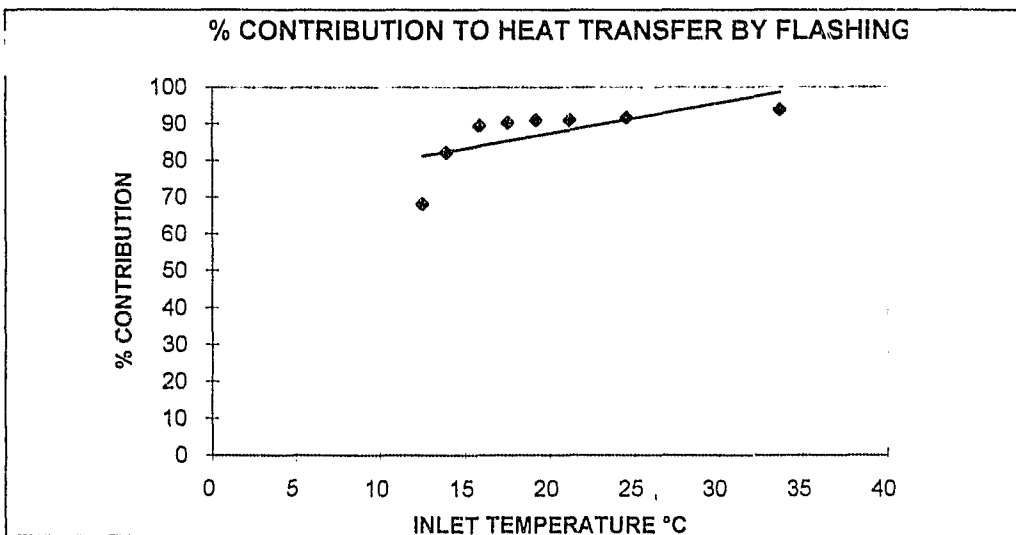


Figure 5.8 : Percentage contribution to total heat transfer by flashing boiling regime,
mean flow rate = 0.0245 kg/s.

5.1.4 Mass Transfer Coefficients

From the heat transfer rates, rates of mass transfer were established. From Chapter 3, equation 3.15 a bulk mass transfer coefficient was defined as:

$$KM_{BULK} = \frac{m_{VAPOURTOTAL}}{V_{LIQ} * (T_{INLET} - T_{EVAP})} \quad (3.15)$$

For a specific rate of mass transfer, as the driving potential decreases, so KM would have to increase rapidly due to division by small values. It was thus decided to remove the driving potential term from the equation. The non-dimensional coefficient thus established would be the slope of the ratio of Vapour flow rate to Liquid flow rate, plotted against the driving potential. In the absence of a minimum superheat to initiate heat transfer, a best fit line for these graphs would pass through the origin.

Figures 5.9 to 5.11 show non-dimensional bulk mass transfer as a function of driving potential.

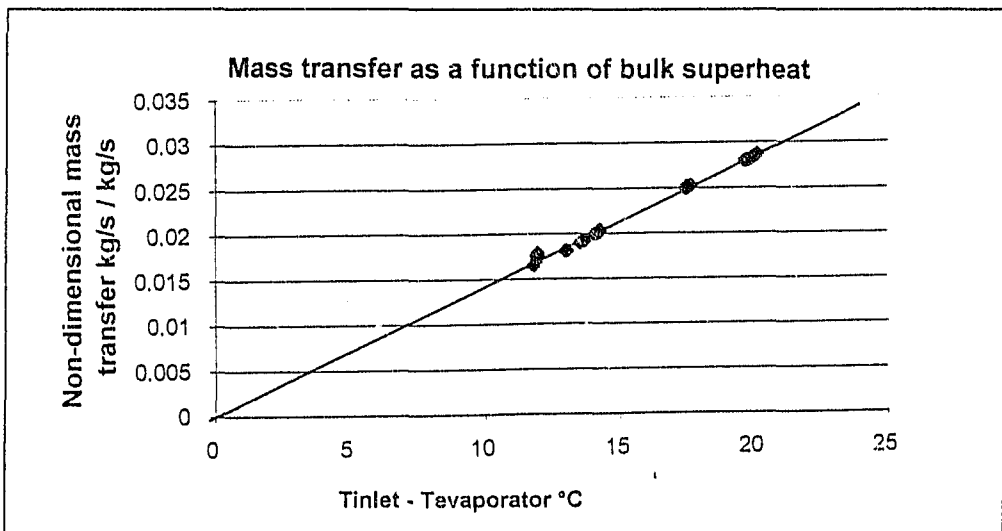


Figure 5.9 : Bulk mass transfer , mean flow rate 0.0671 kg/s

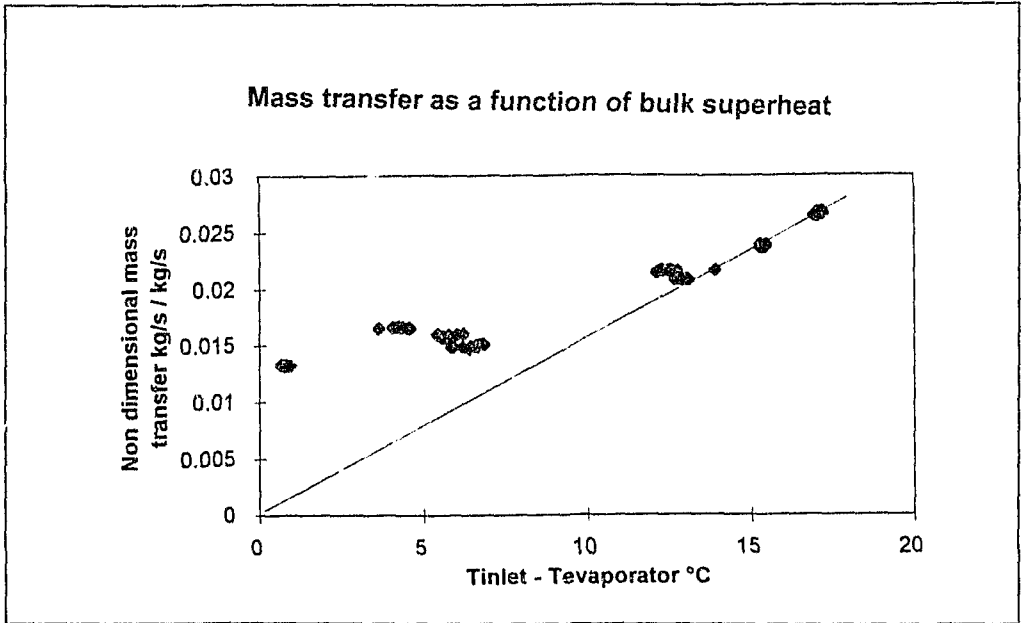


Figure 5.10 : Bulk mass transfer, mean flow rate 0.0584 kg/s

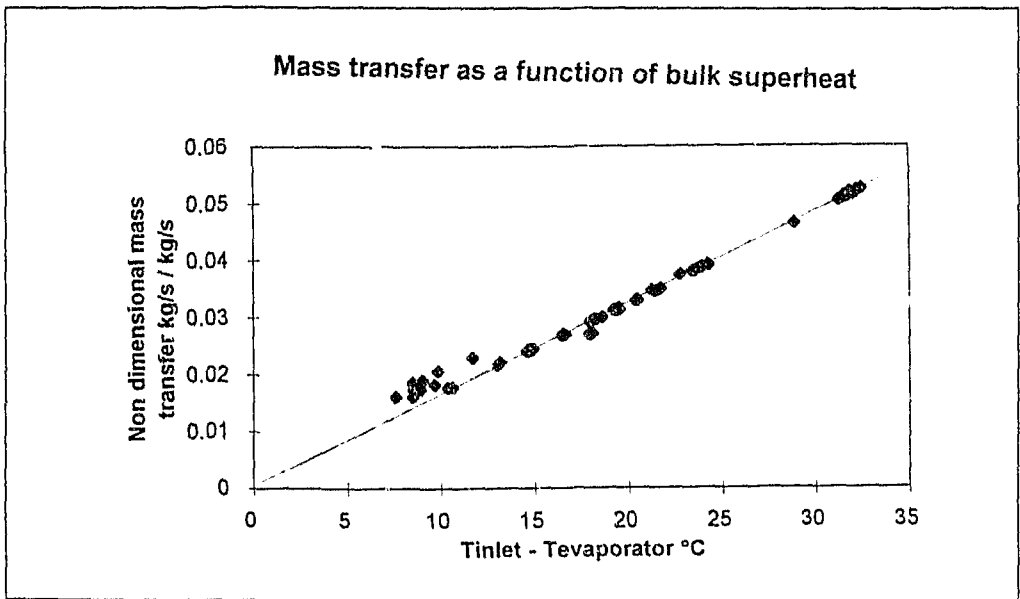


Figure 5.11 : Bulk mass transfer, mean flow rate 0.0244 kg/s

A similar approach was used in attempting to establish a flashing mass transfer coefficient, which was defined as (equation 3.16)

$$KM_{Flash} = \frac{m_{VAPOUR FLASHED}}{M_{LIQUID} * (T_{INLET} - T_{EVAP})} \quad (3.16)$$

Where $m_{VAPOUR FLASHED}$ determined by calculating the vapour generated to effect the measured change in water temperature across the orifice plate.

The flashing mass transfer for the flow rate ranges are shown in figures 5.13 to 5.15.

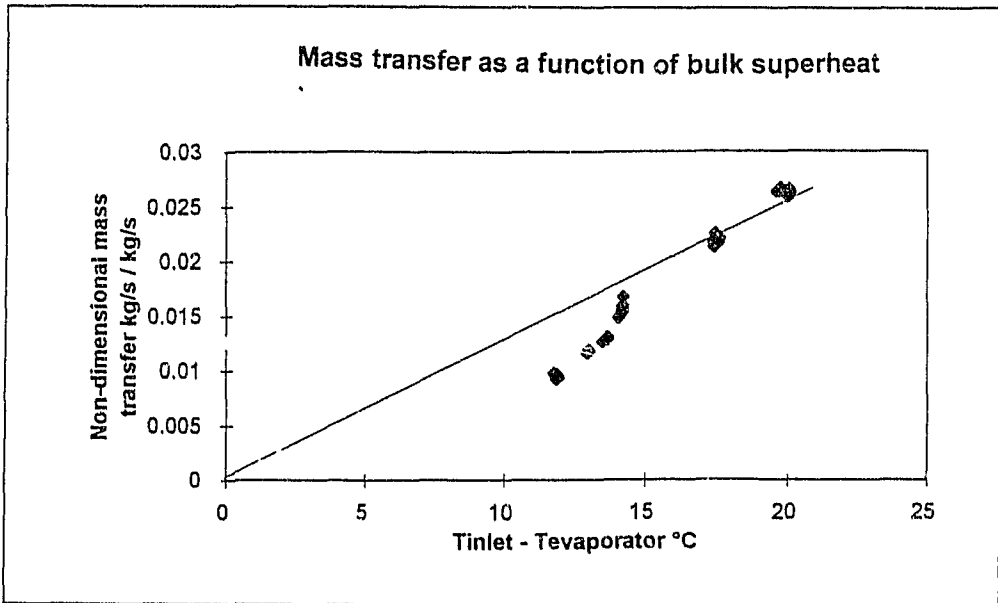


Figure 5.13 : Flashing mass transfer, mean flow rate 0.0671 kg/s

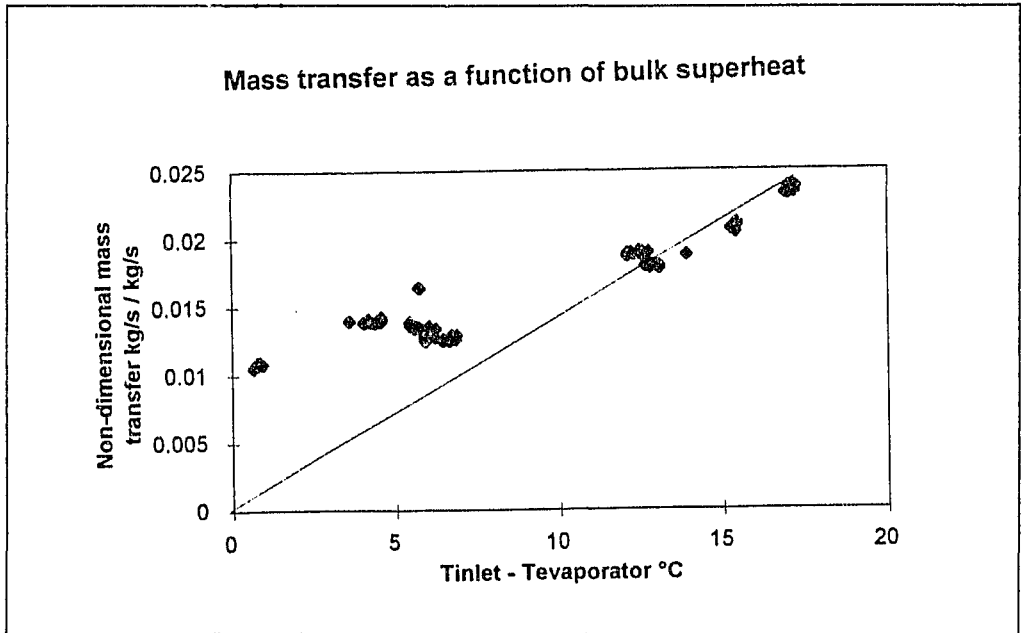


Figure 5.14 : Flashing mass transfer, mean flow rate 0.0588 kg/s

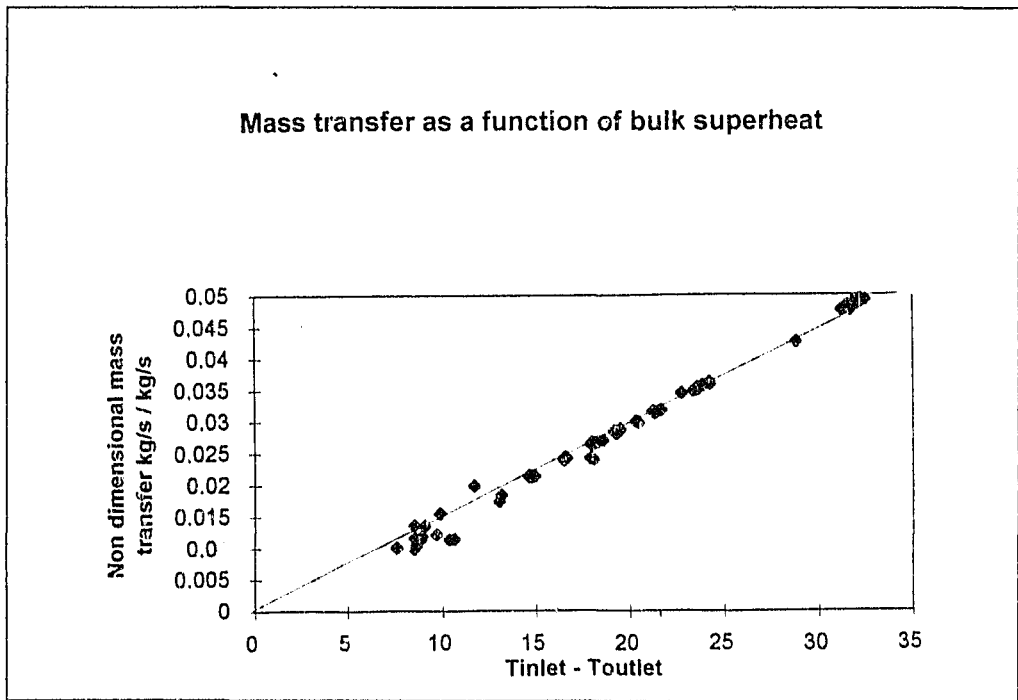


Figure 5.15 : Flashing mass transfer, mean flow rate 0.0244 kg/s

The tests conducted at 0.0671 kg/s and 0.0244 kg/s show a strongly linear relationship between bulk non-dimensional mass transfer and driving potential. The 0.0584 kg/s tests show a linear behaviour above 10°C temperature difference between inlet water and evaporator saturation temperature. Below 10°C driving potential, the mass transfer appears fairly constant. The tests at 0.0244 kg/s may appear to show the same trend.

This strongly linear relationship was not repeated for the non-dimensional flashing mass transfer plots. Results were however found to be of the same order of magnitude, for the different flow rate tests.

Straight line fits through each of the graphs, passing through the origin yielding the following coefficients:

$$\begin{aligned}
 \text{KM bulk} &= 0.001616 \text{ (kg/s / kg/s) / K} & \text{Flow rate } 2.45 \cdot 10^{-5} \text{ m}^3/\text{s} \\
 \text{KM bulk} &= 0.001667 \text{ (kg/s / kg/s) / K} & \text{Flow rate } 5.88 \cdot 10^{-5} \text{ m}^3/\text{s} \\
 \text{KM bulk} &= 0.001429 \text{ (kg/s / kg/s) / K} & \text{Flow rate } 6.71 \cdot 10^{-5} \text{ m}^3/\text{s} \quad (5.1)
 \end{aligned}$$

$$\begin{aligned}
 \text{KM flash} &= 0.00152 \text{ (kg/s / kg/s) / K} & \text{Flow rate } 2.45 \cdot 10^{-5} \text{ m}^3/\text{s} \\
 \text{KM flash} &= 0.001444 \text{ (kg/s / kg/s) / K} & \text{Flow rate } 5.88 \cdot 10^{-5} \text{ m}^3/\text{s} \\
 \text{KM flash} &= 0.001293 \text{ (kg/s / kg/s) / K} & \text{Flow rate } 6.71 \cdot 10^{-5} \text{ m}^3/\text{s} \quad (5.2)
 \end{aligned}$$

The above coefficients are represented graphically in figures 5.16 & 5.17.

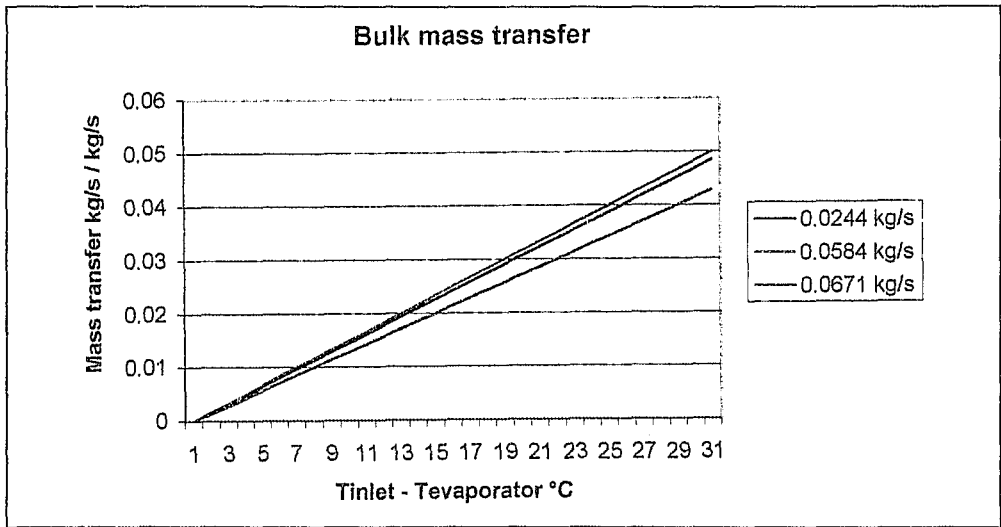


Figure 5.16 : Non-dimensional bulk mass transfer as a function of superheat, eqns. 5.1.

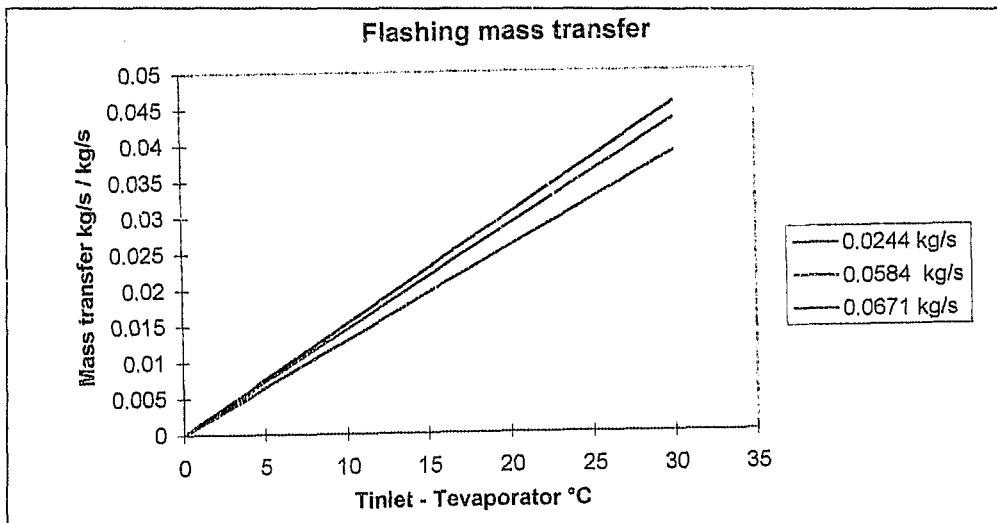


Figure 5.17 : Non-dimensional flashing mass transfer as a function of super-heat, eqns 5.2.

It is particularly interesting to note that the slopes of the curves follow the same trends as those of the evaporator pressure. This implies that for a given system geometry, if the performance of the compression device can be accurately modelled then the flashing coefficient can be established. It was not possible to incorporate an area or geometry term into the above expressions. Further testing with evaporators of varying geometry could achieve this. It can be seen that averaging the predicted coefficients to give a general term would have an associated maximum error of approximately 25 %.

5.2 Photographic Study

The objective of the photographic study was to view the boiling process. The test procedure is described in Chapter Four. The results obtained are presented in the observations as a series of photographs with the relevant times. The conditions during the test were as follows :

TABLE 5.2 : Test Conditions

P steam	585 kPa	M initial	200 ml
		T initial	19.5 °C

The times of the photographs were obtained by timing the soundtrack of the video recorder.

These are presented in the following table.

TABLE 5.3 : TIMES OF SPECIFIC PHOTOGRAPHS

Figure	Mean time	Figure	Mean time	Figure	Mean Time
5.21	1.6 s	5.26	21.4 s	5.31	37.9 s
5.22	6.1 s	5.27	24.3 s	5.32	40.7 s
5.23	9.1 s	5.28	27.5 s	5.33	43.9 s
5.24	16.4 s	5.29	30.5 s	5.34	41.2 s
5.25	19.0 s	5.30	33.6 s	5.35	55.8 s

The following series of photographs show the processes involved in the vacuum boiling of water and are discussed sequentially. In all these photos the bottom of the container corresponds to the bottom of the photo.

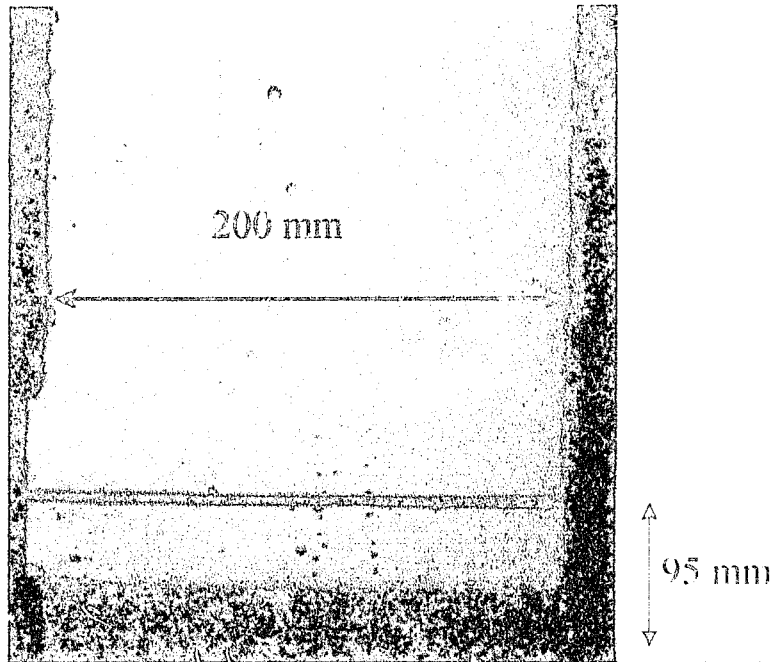


Figure 5.20 : Initial still pool of water, $\Gamma=0.0s$

Figure 5.20 shows the evaporator in its initial state, before depressurisation. The bubbles visible are droplets on the surface of the perspex. The valve was opened and although bubbles were immediately formed, it is interesting to note that the flashing of the bulk of the liquid did not start immediately. There was a delay of 4.5 s before bulk boiling occurred. The evaporator pressure during this period was seen to rise, presumably due to the fact the flow rate of air coming out of suspension exceeded the rate that could be removed by the ejectors

As the pressure recovered bubble activity increased, mainly at the water surface. Figure 5.21 shows the initiation of boiling. Comparing figures 5.20 and 5.21, fine bubbles can be observed near the water surface in figure 5.21 with occasional larger bubbles throughout the liquid height.

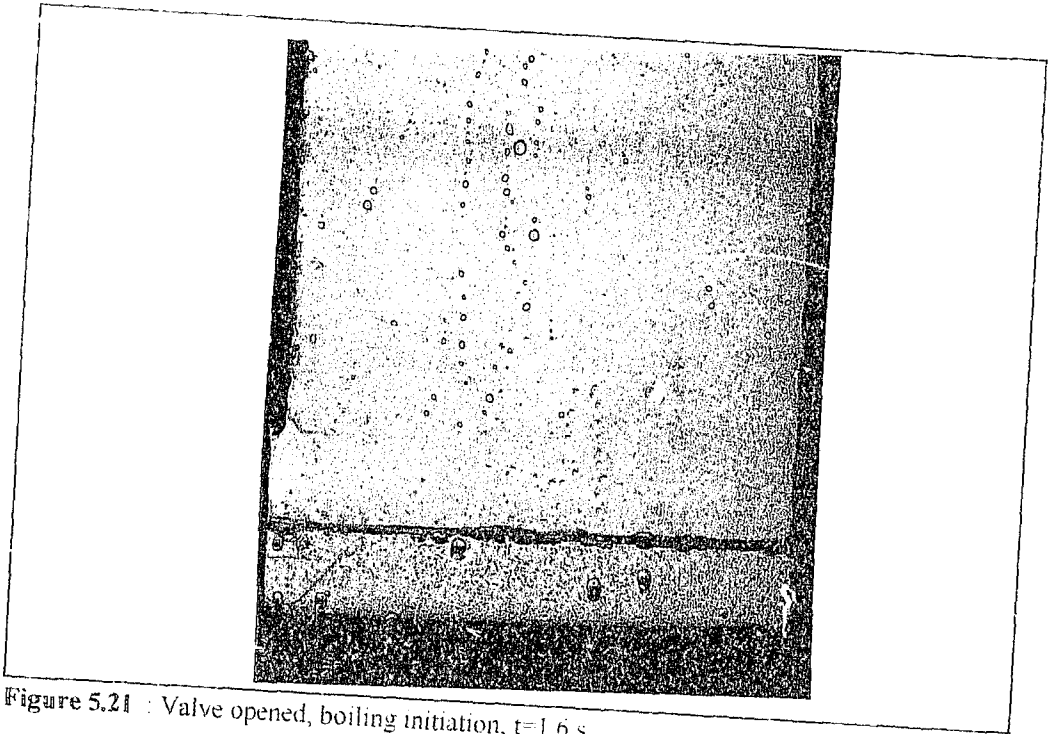


Figure 5.21 : Valve opened, boiling initiation, $t=1.6$ s

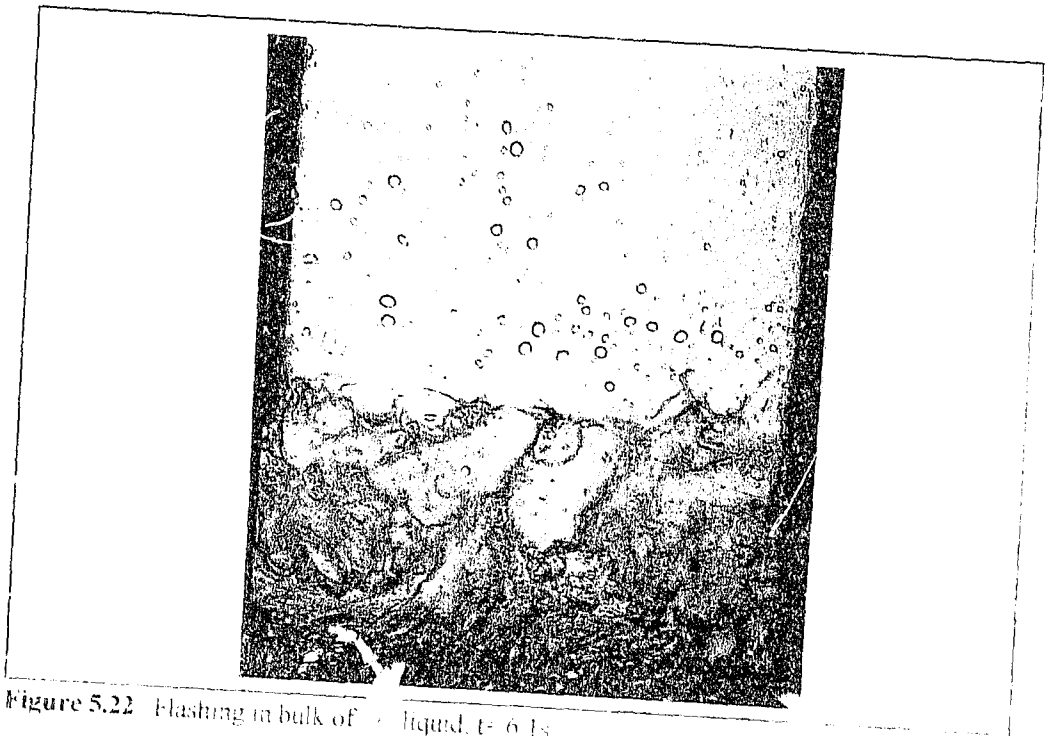


Figure 5.22 Flashing in bulk of liquid, $t=6.1$ s

After a period of about 4.2 s the boiling regime had progressed to bulk boiling throughout the water mass, shown in figure 5.22. Activity was observed to be greater closer to the surface.

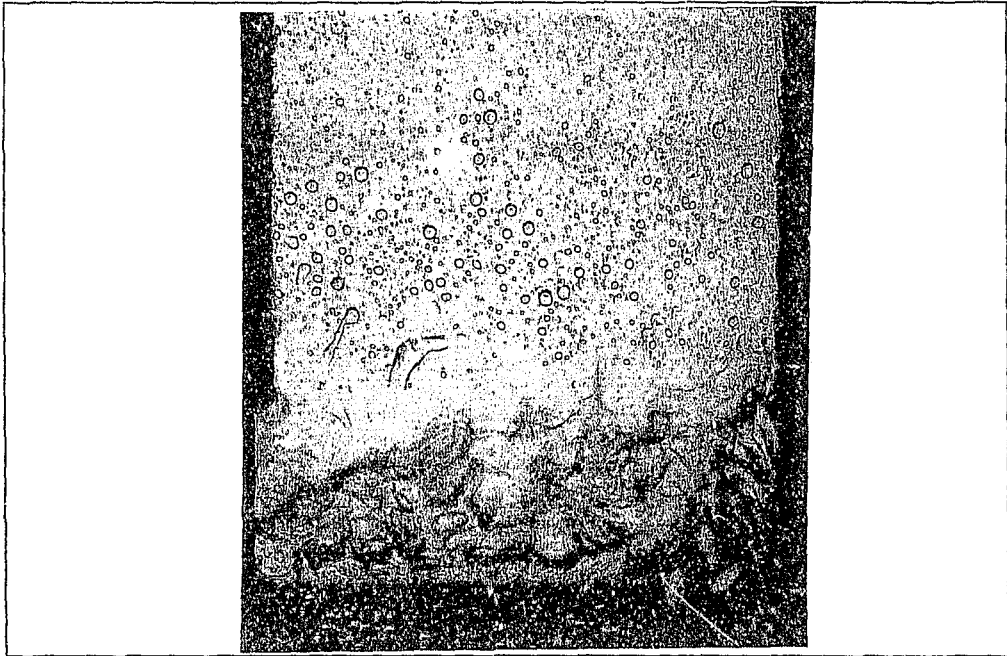


Figure 5.23 : Flashing decreasing in lower regions, $t=9.1$

The bubble activity at the lower regions decreased with time as shown in figures 5.23 through 5.25. After about 13.6 s most of the boiling was observed at the surface, with occasional bubbles rising from the lower regions. This surface boiling, seen in figure 5.24 lasted for approximately 4.7 s following which the water surface became calm, as shown in figure 5.25. Bubbles could still be observed in the liquid but did not appear to rapidly increase in size.

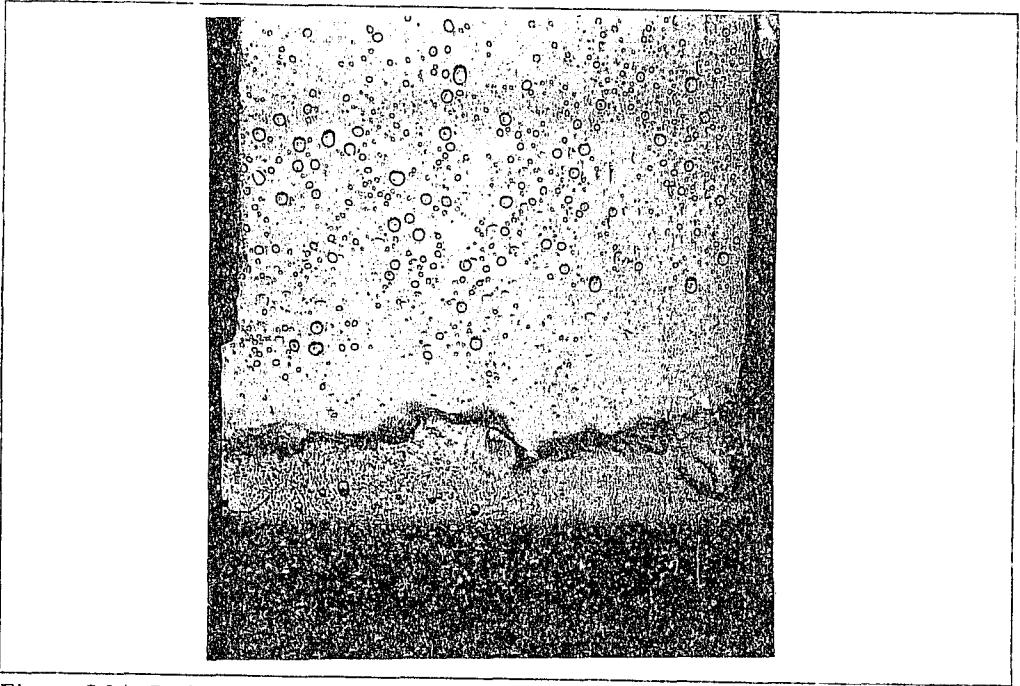


Figure 5.24 : Boiling at liquid surface, $t=16.4s$

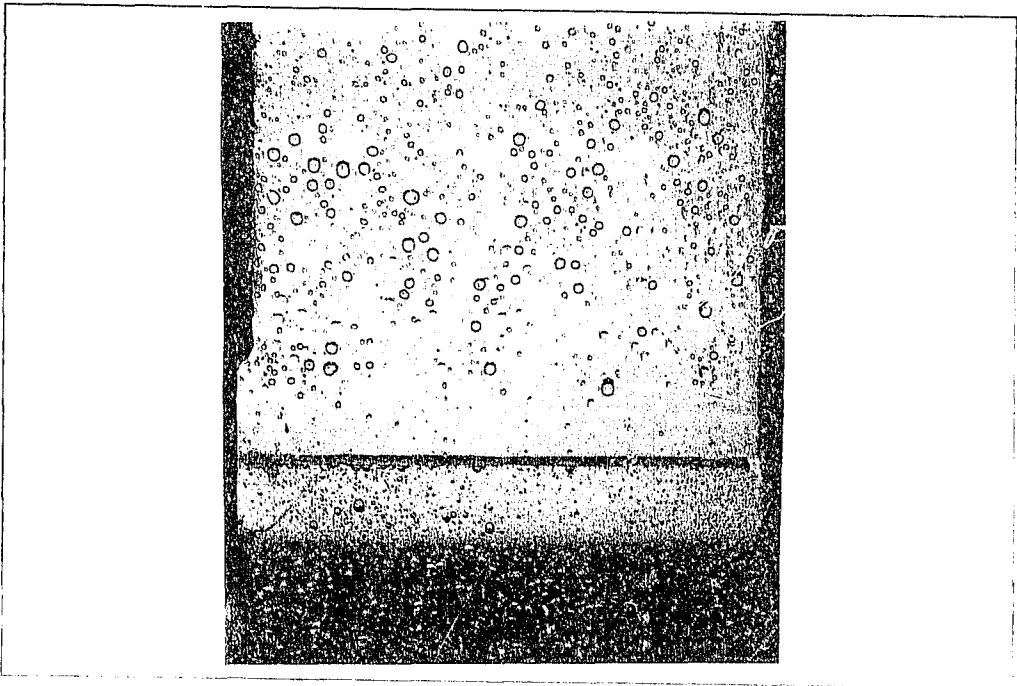


Figure 5.25 : Water surface calm, $t=19.0s$

From approximately 22.6 s, until 29.8 s, surface boiling occurred to a lesser extent. This was repeated between 41.0 s and 44.1 s. This surface boiling was sporadic, originating with isolated bubbles, formed at lower regions, rising and disturbing the water surface. Figures 5.26 through to 5.28 show the second surface boiling stage. Bubbles originated just below the surface, caused violent activity at the surface and once this ceased bubble population could be observed to have decreased. The activity at the surface shown in figures 5.27 and 5.28 is less than that shown in figures 5.22 and 5.23.

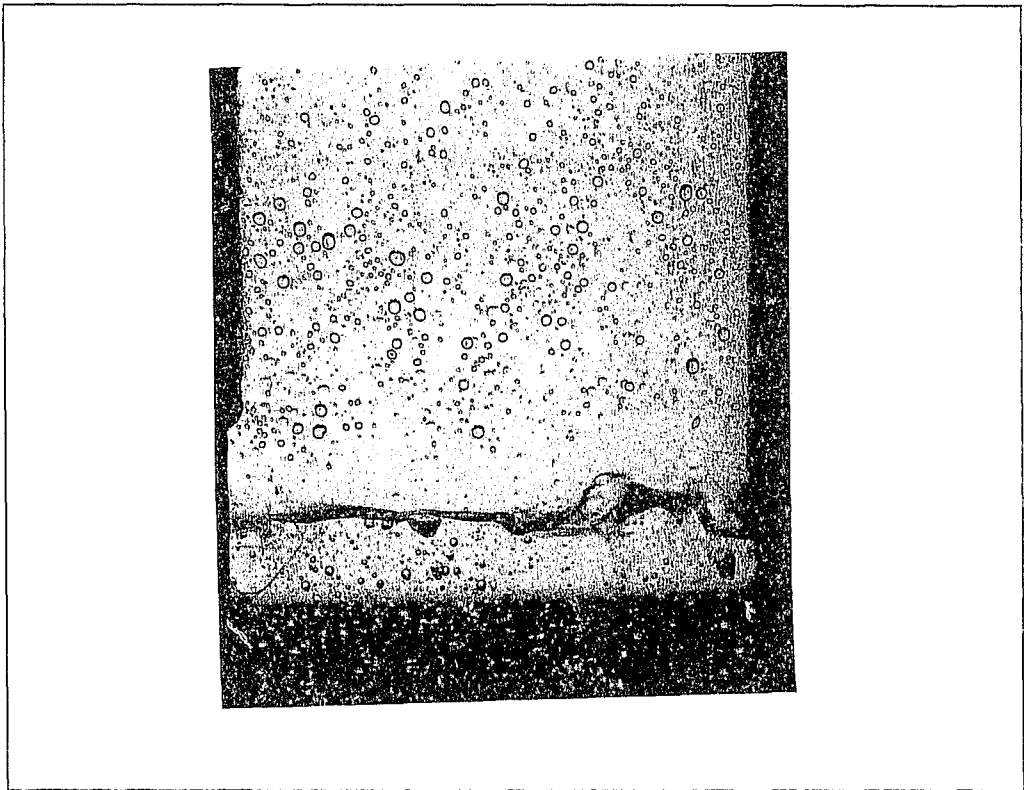


Figure 5.26 Secondary surface boiling, $t=21.4s$

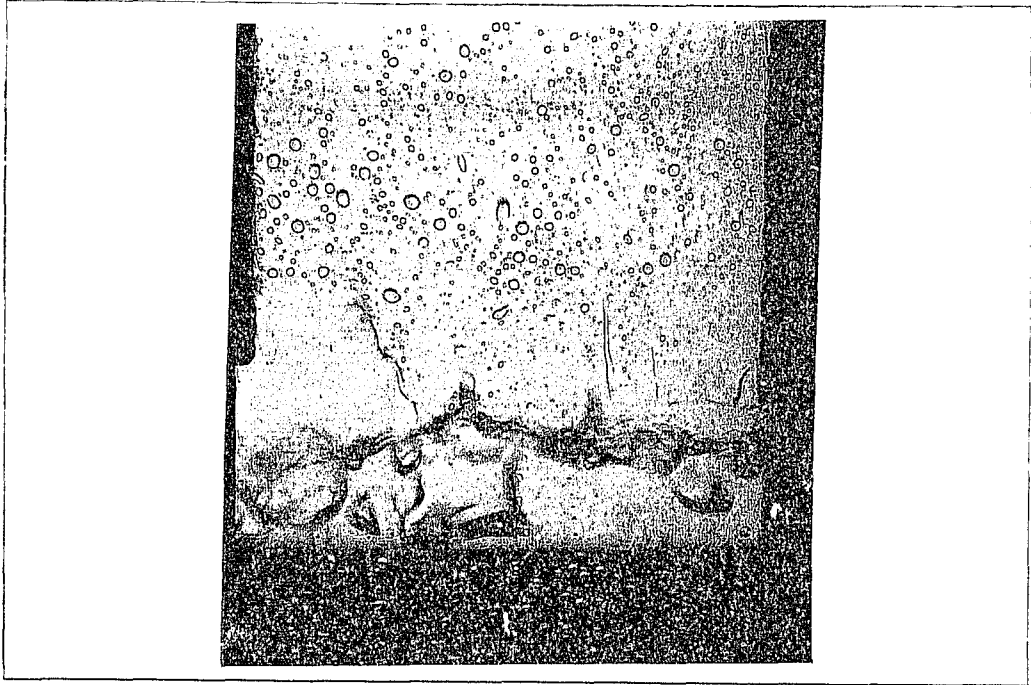


Figure 5.27 Secondary surface boiling. $t=24.3s$

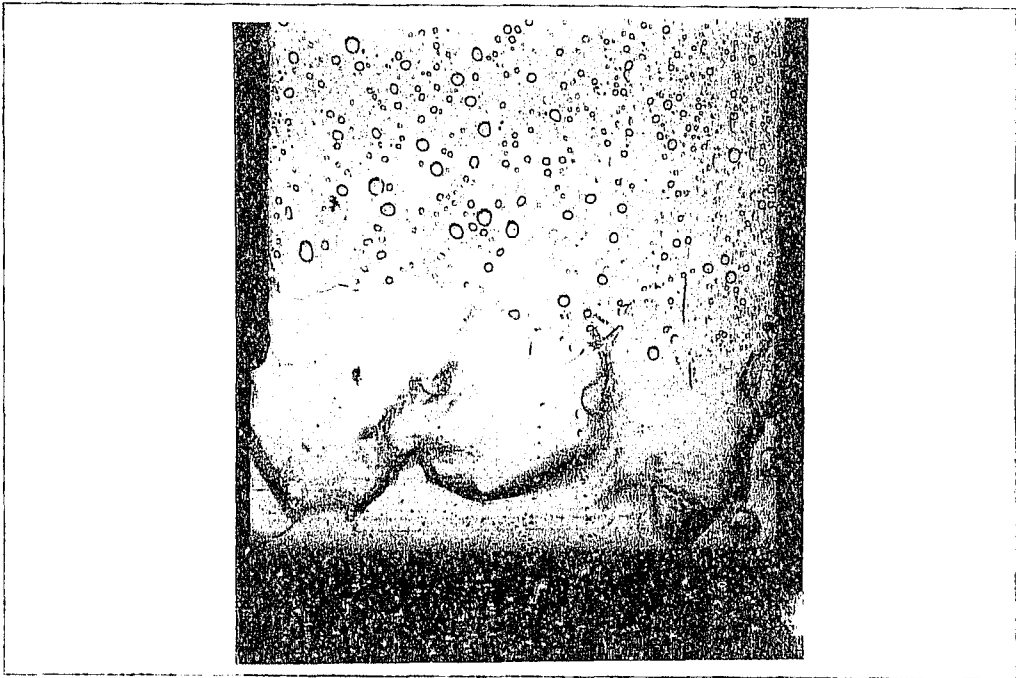


Figure 5.28 Secondary surface boiling. $t=27.5s$

Figures 5.29, and 5.30 show the third occurrence of surface boiling. Figure 5.29 shows the surface as being calm. Attention is drawn to the group of bubbles circled. These separate from the evaporator wall and rise explosively to the surface, as shown in figure 5.30. This initiated boiling across the surface which lasted about 5.7s after which the surface became calm again.

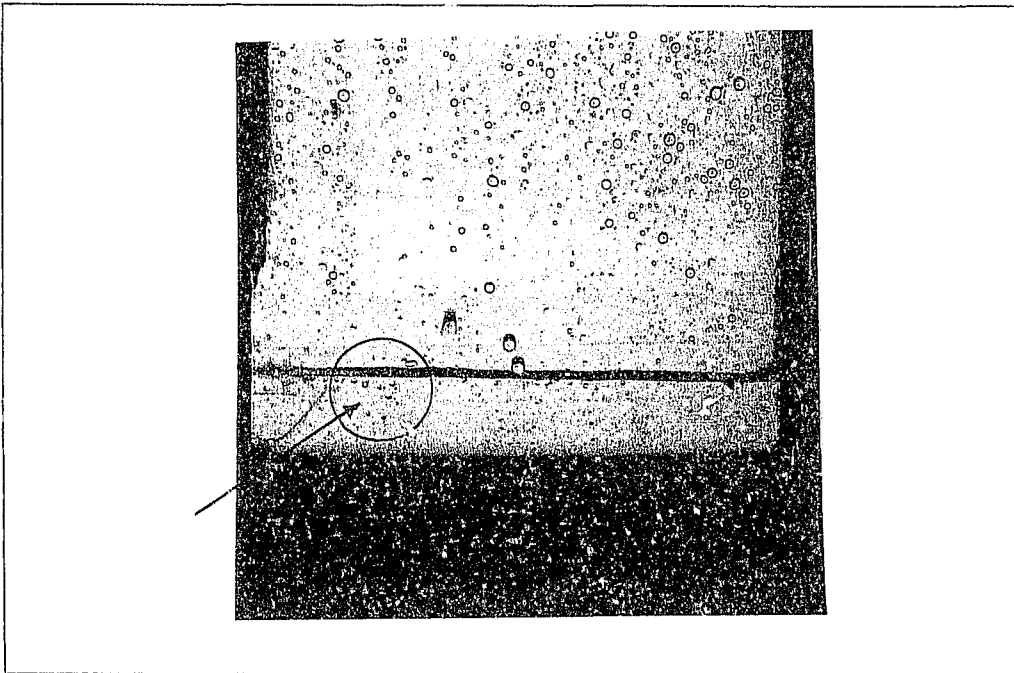


Figure 5.29 : Water surface calm, $t=37.9s$

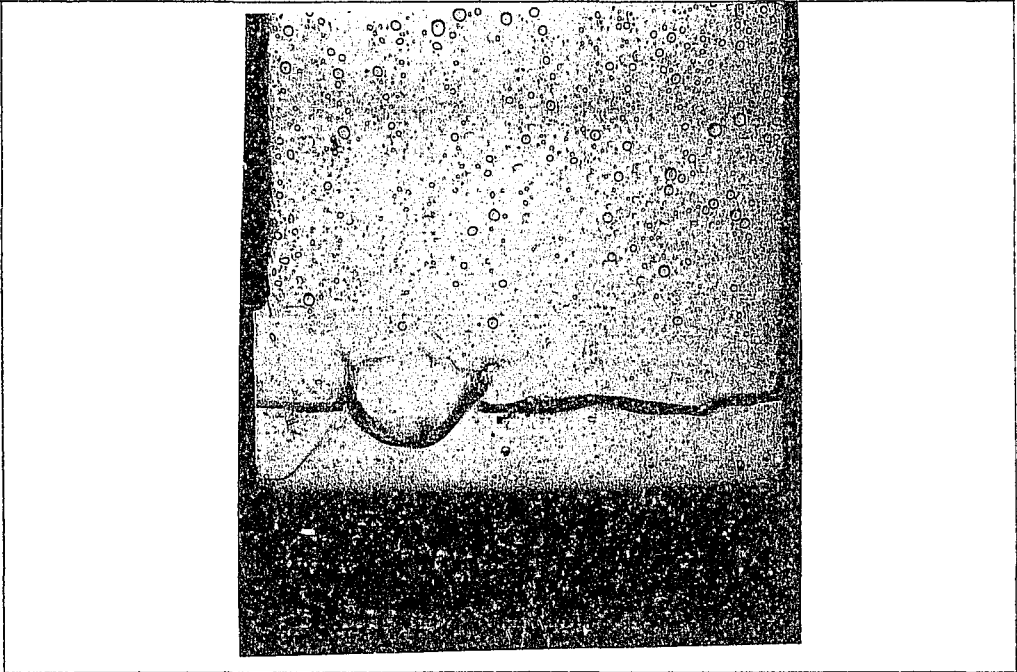


Figure 5.30 : Initiation of third surface boiling, $t=40.7s$

The time periods of the various boiling regimes observed were as follows :

TABLE 5.4 : Time span of specific regimes

Event	Start [s]	End [s]
Boiling	0.0	4.2
Bulk boiling	4.2	13.6
Surface boiling	13.6	18.3
2nd Surface Boiling	22.6	29.8
3rd Surface Boiling	41.0	44.1

5.3 Vertical Cylinder

The objective of the tests using a vertical cylinder was to examine the boiling mechanisms that take place when a control volume is subjected to rapid depressurisation.

The range of conditions under which the cylinder was decompressed is listed below.

TABLE 5.4 : Vertical cylinder test conditions

Temp °C	Initial Quantity ml
5	10 20 30 40 50
13	10 20 30 40 50
19	10 20 30 40 50
25	10 20 30 40 50
35	10 20 30 40 50

Four tests were conducted for each of the above conditions. The outputs of the instrumentation were captured using a data logger. The sampling period was 200 ms and the duration was 64 s. Typical raw data captured are shown Appendix F. These raw data were then calibrated and processed in the Quattro-Pro spreadsheet package.

The temperatures measured by the LM-35's were observed to lag those of the thermocouples due to their higher thermal mass and time constant. Figure 5.31 shows the difference in response time between a LM-35 and a thermocouple.

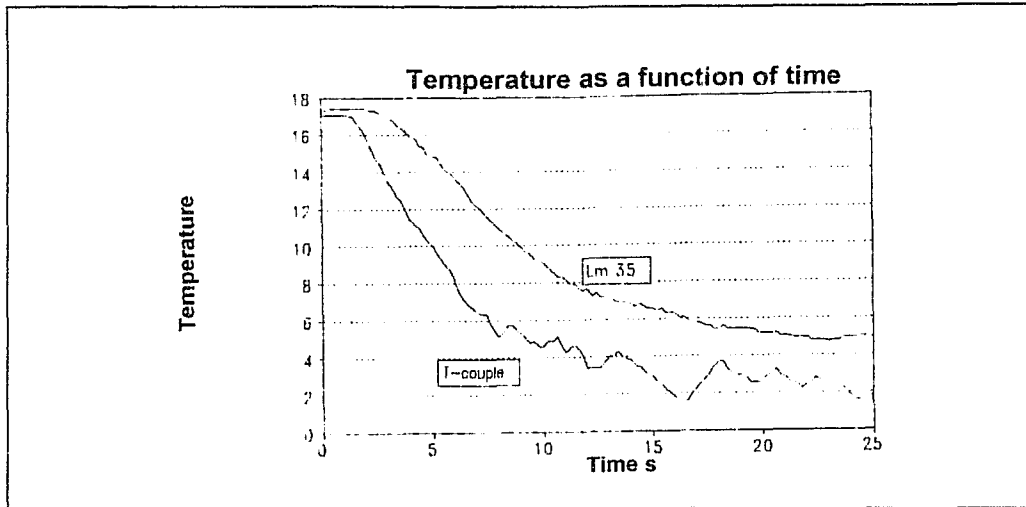


Figure 5.31 : Temperature measured by LM-35 compared to the temperature measured by a thermocouple.

An additional problem was encountered in warming the vertical cylinder to the same temperature as the water input temperature. In the initial test, the cylinder containing measured quantities of water was decompressed, emptied and then heated briefly with warm water. The measured quantity of water required for a test was poured into the cylinder. The cylinder was placed into a bucket of ice and connected to the valve. After about a minute it was decompressed. Figure 5.32 shows the typical spread in initial temperature achieved by this method.

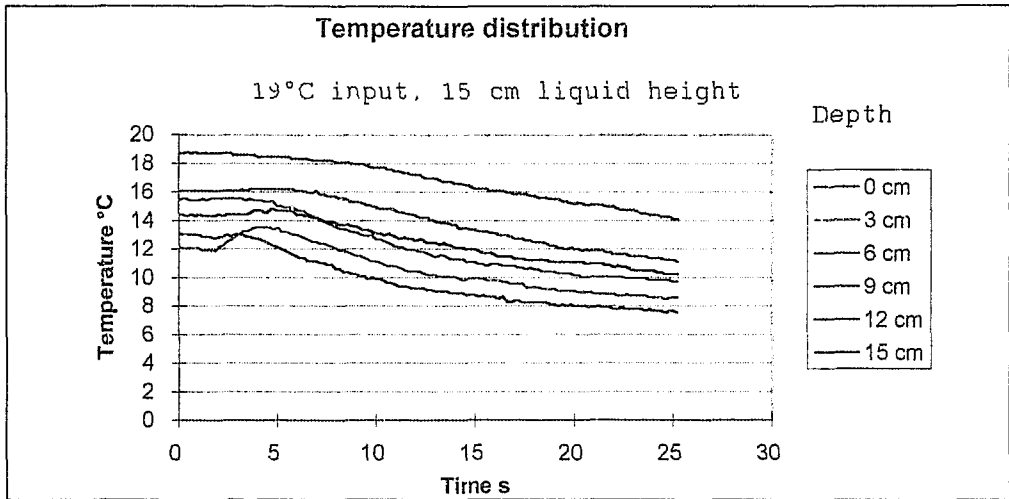


Figure 5.32 . Temperature at various depths below water surface as a function of time.

It can be seen that upon decompression ($t = 4.6s$), temperature gradients are set up through the height of the cylinder. The initial section of the graph (prior to decompression) has too great a spread in temperature to be of use, while the second gives a reasonable idea of the magnitude of the temperature gradients. Tests where the initial temperatures at the various points varied by more than 10% of the starting value, were not used.

To avoid this spread of initial temperatures, a bath of water with a heater was placed next to the cylinder. A bucket containing distilled water was placed in the bath. After a test the whole cylinder was submerged in the bath until the temperature measured on channel #1 achieved a steady state. The temperature distribution for such a test is shown in figure 5.33 where the input temperature is 19°C and the liquid height is 15 cm.

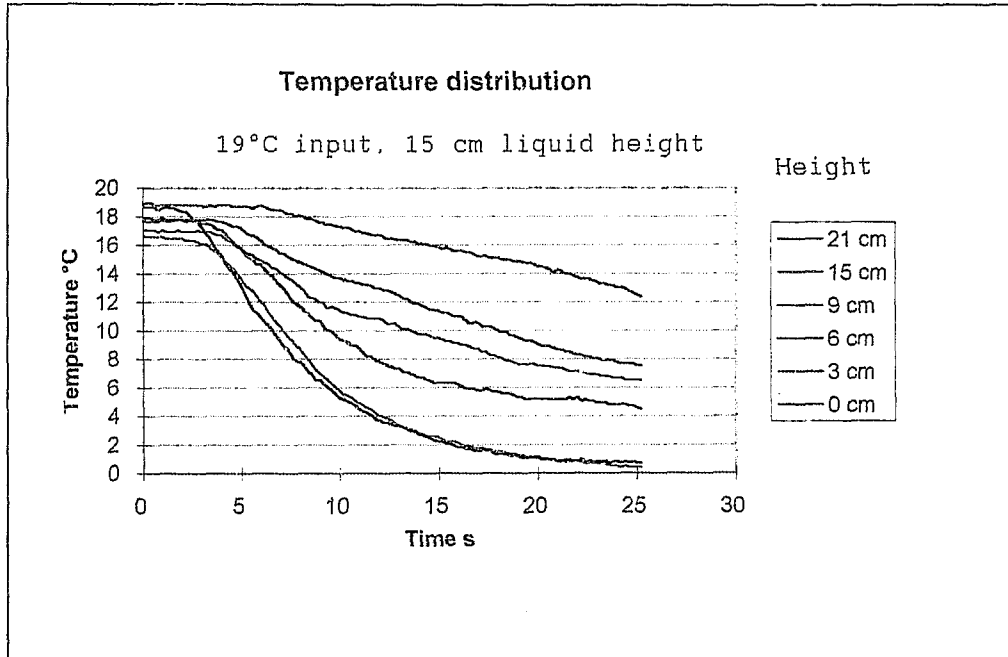


Figure 5.33 : Temperature as a function of time, preheated cylinder

As can be seen, there is less of a variation in the starting temperatures. The temperatures at liquid heights 21 cm and 15 cm converge quickly to the same temperature. This is ascribed to the fact that the temperature at the water surface and at some point a short distance away from the surface should be equal. This is shown particularly well in figure 5.34 for a test where the cylinder was not heated. The input temperature is 13°C and liquid height is 9 cm. All the LM-35 sensors above 3 cm from the bottom of the cylinder, converge to the same temperature shortly after decompression. Thus, for the bulk of the tests conducted, the LM-35 sensor data should give valid information regarding the temperature distribution shortly after flashing. The rates and coefficients predicted would be lower than those predicted using the thermocouple based results due to the higher thermal constant of the LM-35.

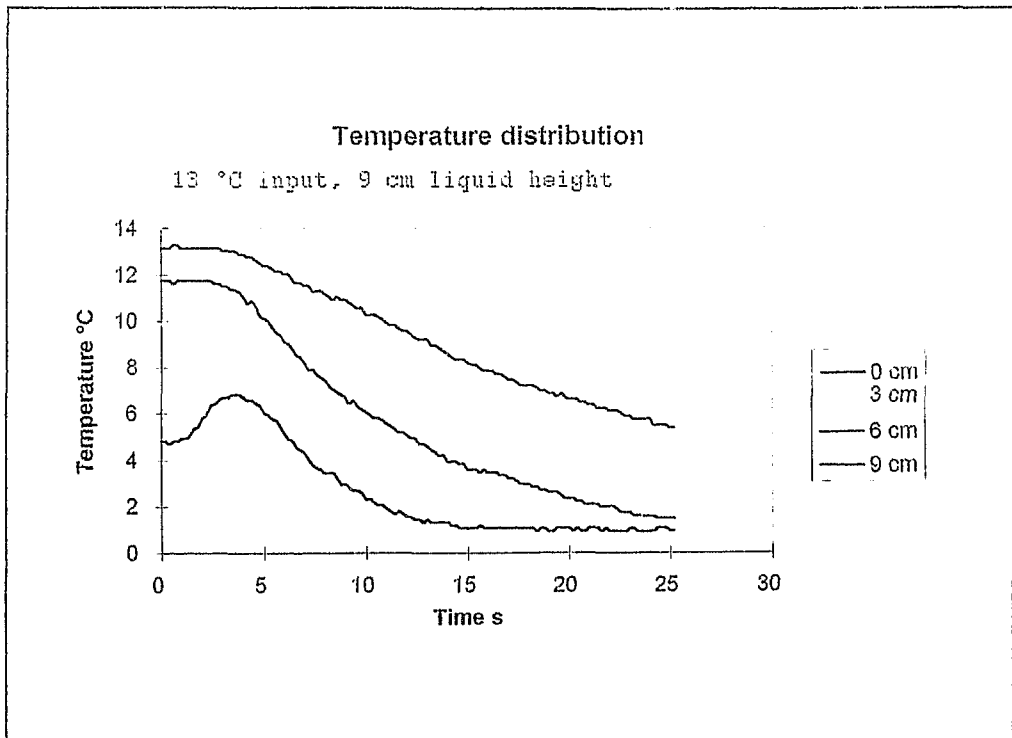


Figure 5.34 : Temperature distributions, 13 °C input, not heated.

The data obtained on the Computerscope were calibrated using a spreadsheet. Parameters such as bulk temperature, mass transfer and heat transfer were calculated. Thermophysical properties such as specific heat and enthalpy were expressed as functions of temperature and determined by the bulk water temperature. Sample calculations are presented in Appendix F.

5.3.1 Evaporator Pressure

Figure 5.35 shows typical vertical cylinder evaporator pressure as a function of time. At 1.0 s the decompression valve is opened. The evaporator pressure can be seen to rise. This is due to the flow rate of air and flashing vapour exceeding the ejector capacity. By 5.6 s the evaporator pressure had partially recovered to its starting value. It is interesting to note that it did not recover fully to its starting value until around 18.6 s. This is ascribed to the fact that upon decompression, vapour is produced raising the evaporator pressure. The evaporator pressure only decreases when the rate of vapour extraction by the ejectors exceeds the rate of generation of the water pool.

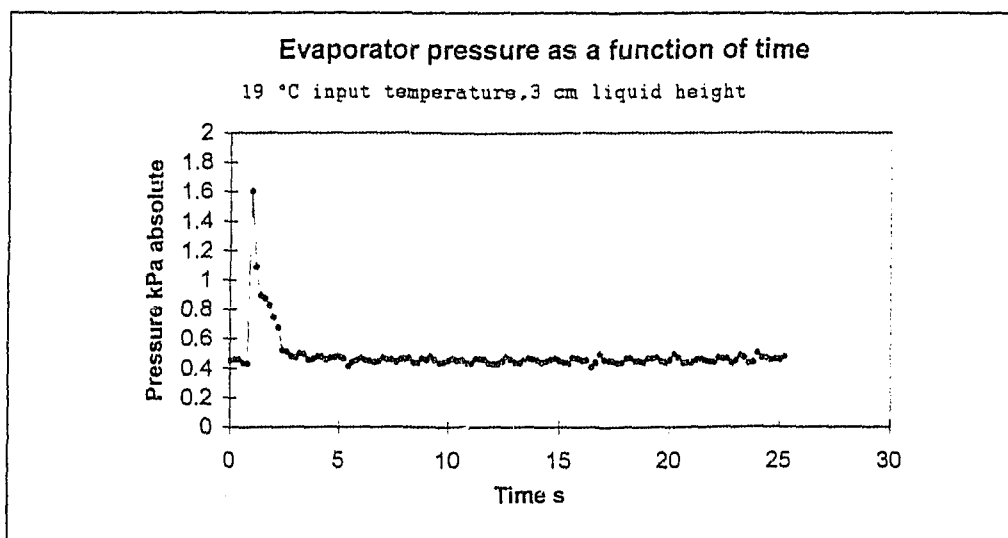


Figure 5.35 : Evaporator pressure as a function of time.

The recovery time was found to be quicker for lower liquid levels. The maximum pressure was found to be greater for lower liquid heights. This is ascribed to the fact that lower liquid heights allow more air in the cylinder. Comparing figures 5.35 and 5.36 it can be seen that the peak pressure is greater in figure 5.36 but the recovery time is slower in figure 5.35 due to greater vapour production.

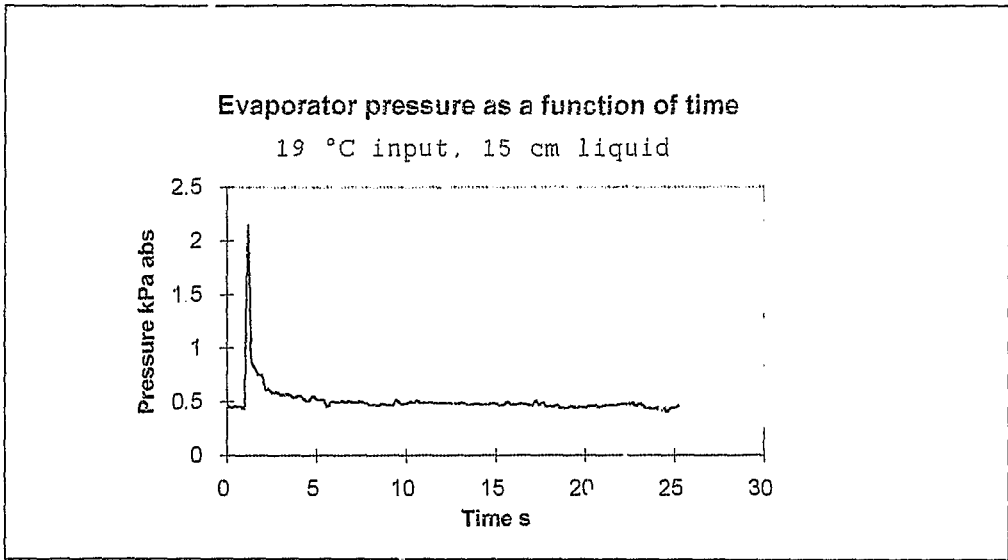


Figure 5.36 : Evaporator pressure as a function of time

5.3.2 Temperature Distribution in the Vertical Cylinder

As shown in Chapter 3, temperature gradients are set up over the height of the column due to hydrostatic pressure. Figures 5.37 and 5.38 show this clearly for a 15 cm column of water at 19°C and 40°C initial (input) water temperatures, respectively.

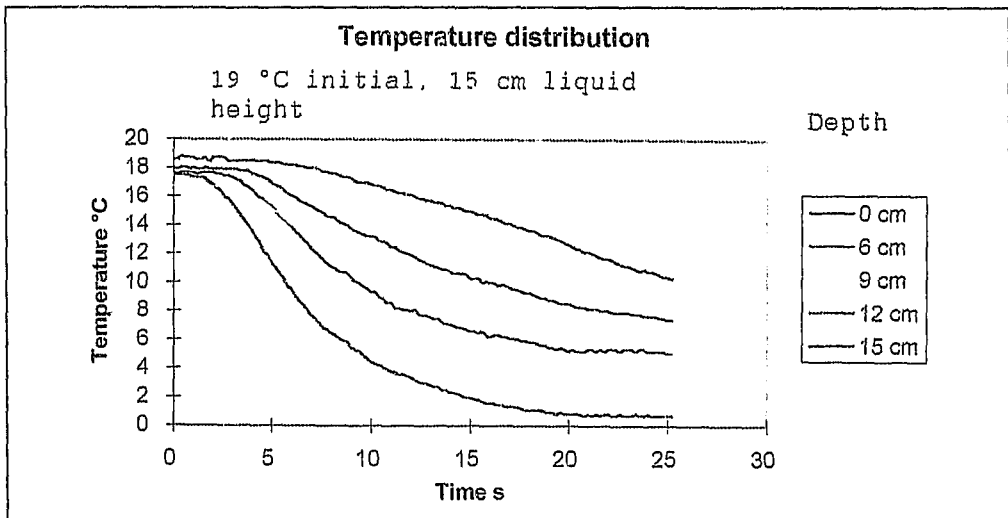


Figure 5.37 : Temperature distribution with time, 15cm height, 19°C initial temperature.

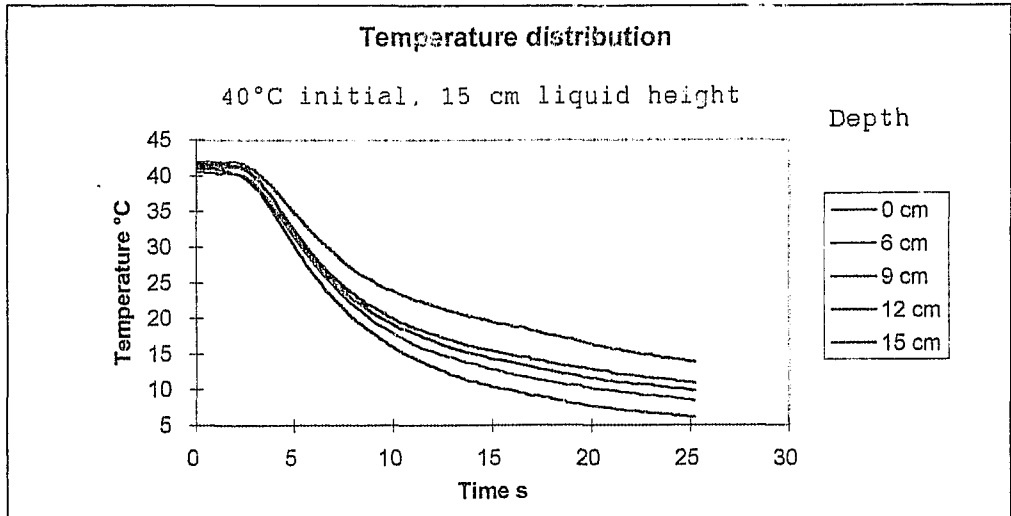


Figure 5.38 : Temperature distribution with time, 40°C initial temperature.

The pressure of the liquid surface is assumed to be at the saturation pressure corresponding to its temperature, then the pressure at any point in the column can be given by :

$$P_{hydrostatic} = p_{surface} + \rho gh \quad (5.3)$$

This pressure can then be compared to the saturation pressure at the local measured temperature.

This method of analysis is discussed further in Chapter 6.

5.3.3 Cooling Rate

The rate of change of bulk temperature was found to be high initially, decreasing in magnitude with time. The rate of change of bulk temperature for a 15 cm column height is shown in figure 5.39. The cooling rates for the lower initial temperatures are less than those at higher initial temperature.

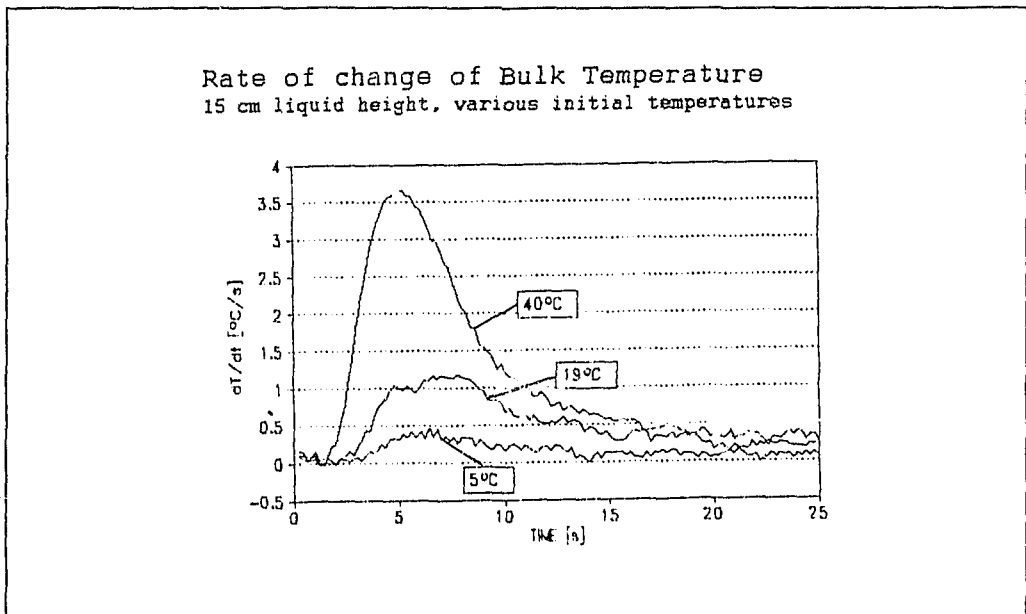


Figure 5.39 : Cooling rates for varying input temperatures

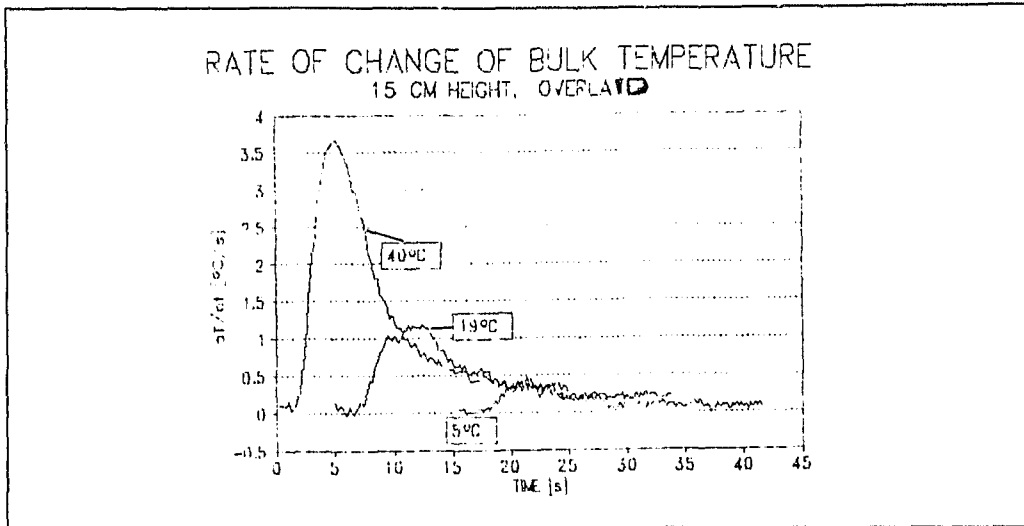


Figure 5.40 : Superimposed results of cooling rates.

If the graphs of cooling rates for the various initial temperatures are superimposed on each other, such that their values of rate of cooling correspond (ie time axes are shifted), they appear to follow similar cooling rates after the initial flashing period, as shown in figure 5.40.

This would imply that there is a parameter which would yield the same cooling rates, regardless of the initial temperature. Plotting the cooling rate as a function of bulk temperature, as shown in figure 5.41, shows that the cooling rate is not solely dependent on the bulk temperature. Superheat can therefore not be defined based on bulk temperature as identical bulk temperatures, with differing temperature gradients, yield different cooling rates.

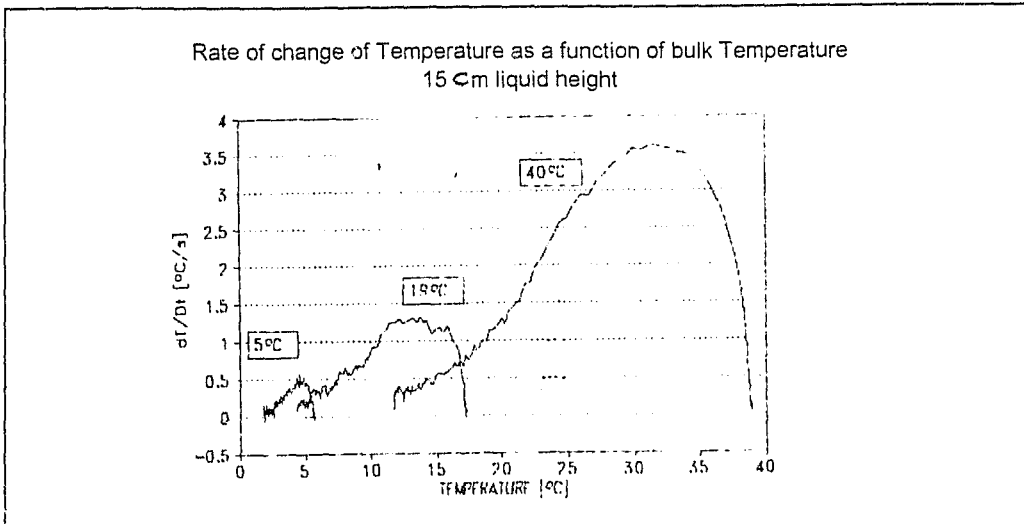


Figure 5.41: Rate of change of temperature as a function of bulk temperature for various initial water temperatures.

Plotting the rate of change of bulk temperature as a function of surface temperature yields overlaying of cooling rates at lower temperatures. The shortfall at higher temperatures can be ascribed to the fact that at higher temperatures, vigorous boiling exposes the higher liquid levels to the surface pressure. The boiling at the lower level follows the hydrostatic pressure defined by the region exposed to the surface pressure. Thus sub-cooling takes place in the lower regions in the case where boiling would be defined by the surface pressure.

The rate of cooling of the surface temperature was plotted as a function of surface temperature. Figure 5.42 shows the results for 15 cm heights and varying input temperature. The graph shows similar trends to figure 5.41, again implying that the surface temperature defines the boiling process.

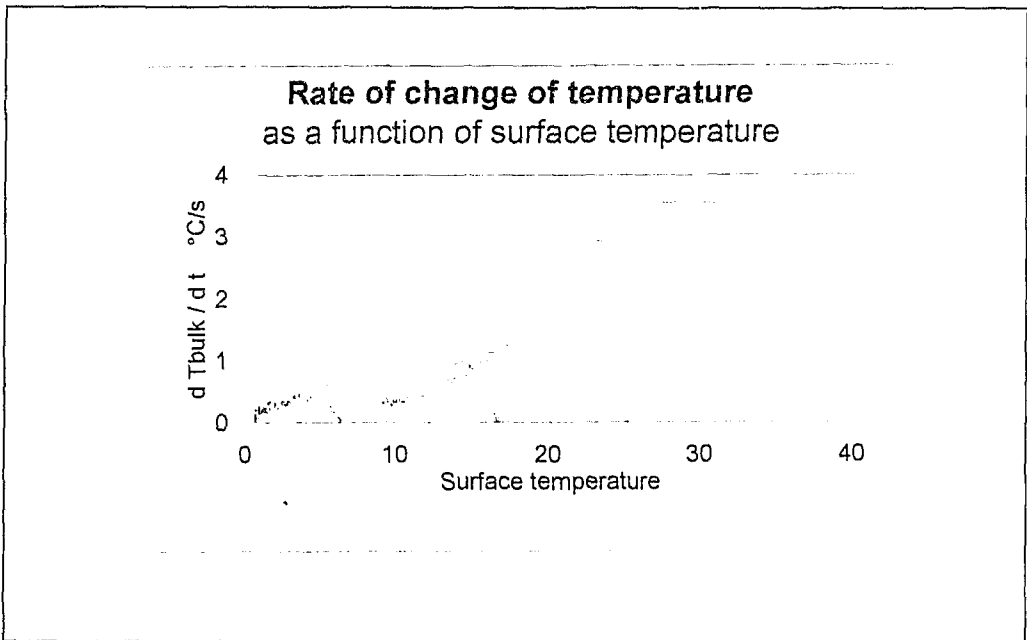


Figure 5.42 : Rate of change of temperature as a function of surface temperature

5.3.4 Mass Transfer

The bulk mass transfer rate between any two increments of time t_{i-1} and t_i was calculated by:

$$\frac{dM}{dt_i} = \frac{M * C_p(T_{bulk}) * (T_{bulk}(t_{i-1}) - T_{bulk}(t_i))}{h_{fg}(T_{bulk})} \quad (5.4)$$

The output produced by these calculations tended to be noisy as the formula is a derivative and any noise is thus amplified. To reduce this a running average was taken over 5 increments of time. Figure 5.43 shows mass transfer and bulk temperature as a function of time.

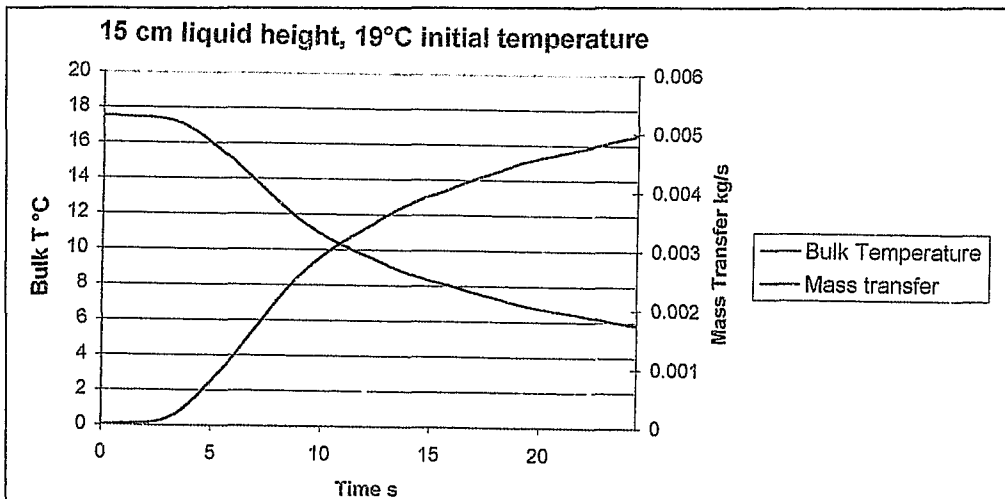


Figure 5.43 : Mass transfer and change in temperature as a function of time.

Upon decompression there is rapid vapour generation accompanied by a rapid decrease in temperature. After a while the mass transfer rate decreases. The quantity of water has a marked effect on the mass transfer rate. Comparing figures 5.44 and 5.45 it can be seen that for a small quantity of water, there is an initial burst of flashing, which is accompanied by a rapid rise in

evaporator pressure. The mass transfer rate then drops very rapidly, as does the evaporator pressure and ceases when the water freezes. For a higher quantity of water the mass transfer rate is greater as is the pressure rise.

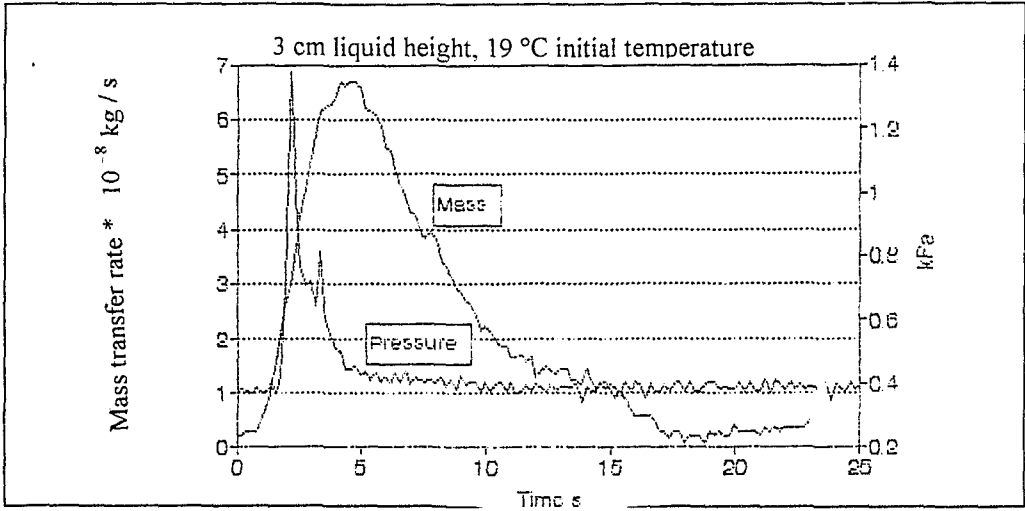


Figure 5.44 : Mass transfer rate and evaporator pressure as a function of time, 19°C input temperature, 15 cm height.

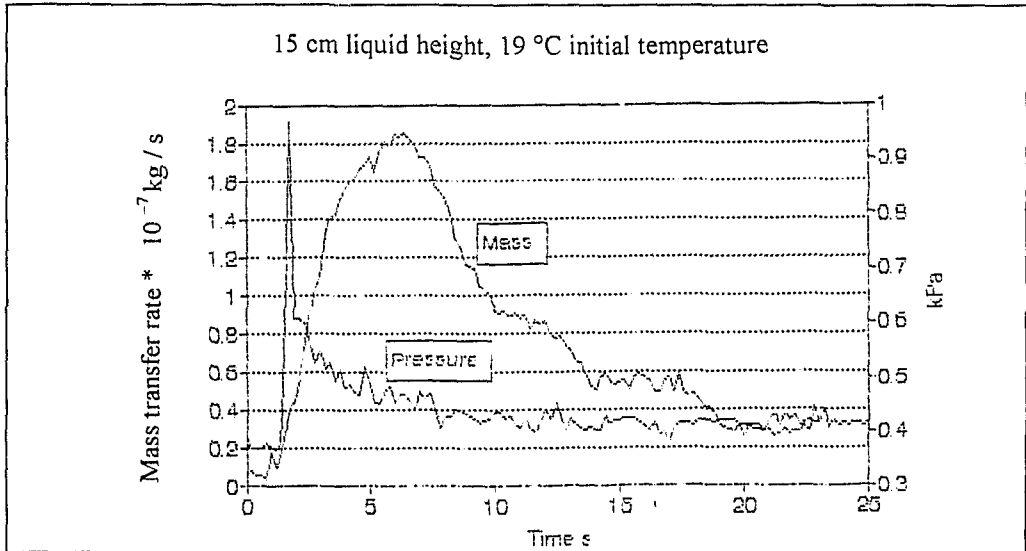


Figure 5.45 : Mass transfer rate and evaporator pressure as a function of time, 19°C input temperature, 15 cm height.

Figure 5.46 shows mass transfer plotted against surface temperature. At lower input temperatures the mass transfer rates for a given surface temperature are overlaid for a given surface temperature.

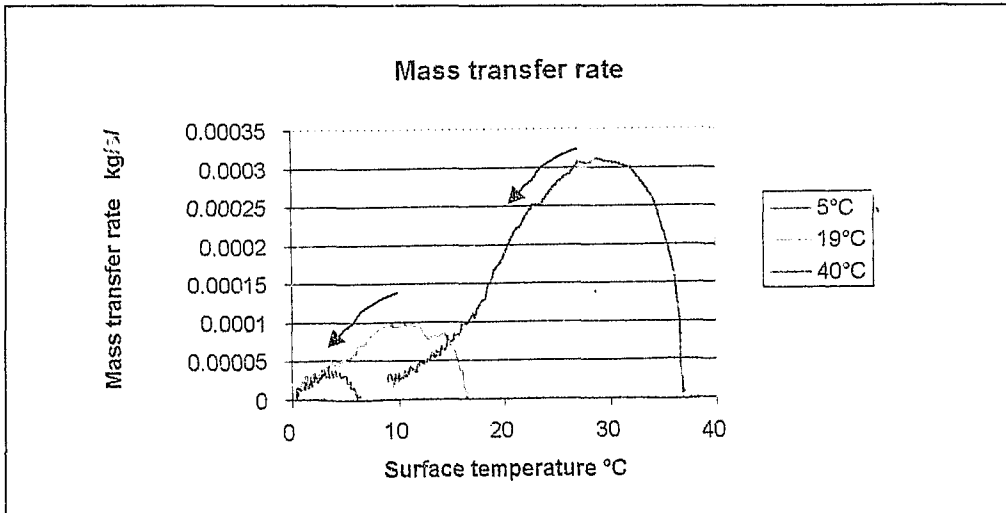


Figure 5.46 : Mass transfer rate for various initial temperatures for 15 cm column of water.

5.3.5 Mass Transfer Coefficient

From the above results it would appear that defining the driving potential for a mass transfer coefficient by solely considering the difference between the evaporator pressure and the saturation pressure corresponding to the bulk temperature of the water would yield a series of coefficients for specific conditions. Figure 5.47 shows the mass transfer coefficient defined in chapter 3.

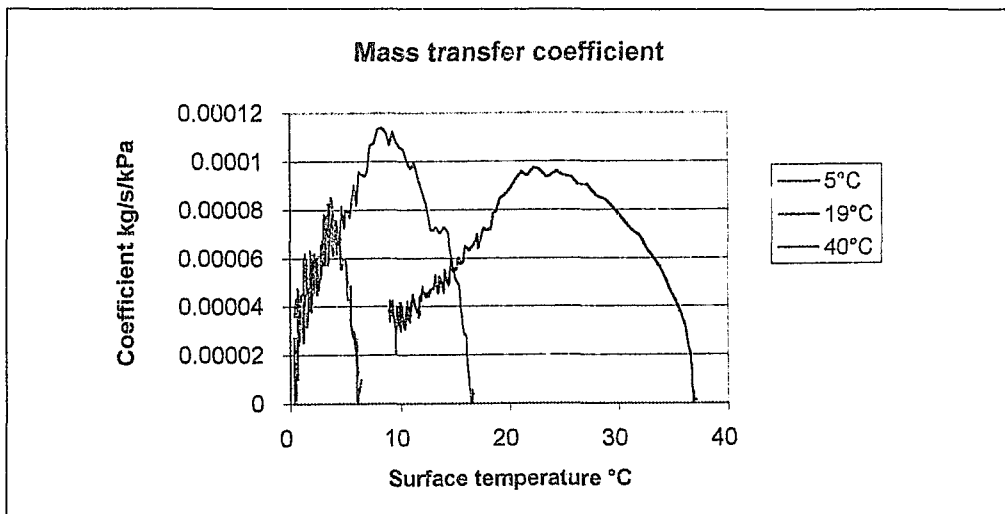


Figure 5.47 : Mass transfer coefficient based on surface temperature saturation pressure.

Similar trends are noted for the mass transfer coefficient as for the mass transfer rate. The figure seems to indicate that there is a maximum transfer coefficient of 0.0001 kg/s/kPa and hence a maximum mass transfer rate, for a given surface temperature. Fitting a line tangent to the curves of mass transfer rate yields figure 5.48.

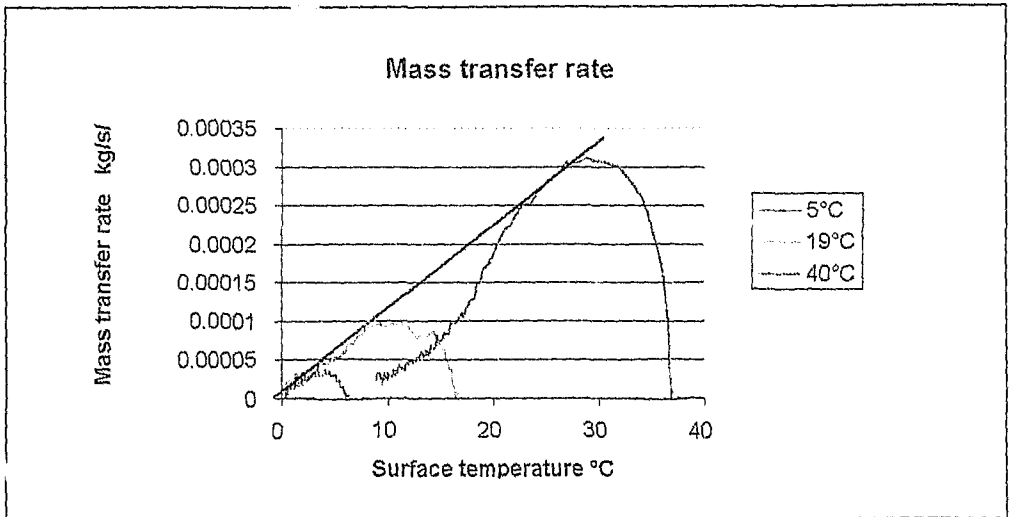


Figure 5.48 : Maximum mass transfer rate, 15 cm liquid height.

Mass transfer rates for a liquid height of 12 cm were also plotted in this way as shown in figure 5.49. The maximum coefficient was found to have decreased as shown by the decrease in slope of the tangent line.

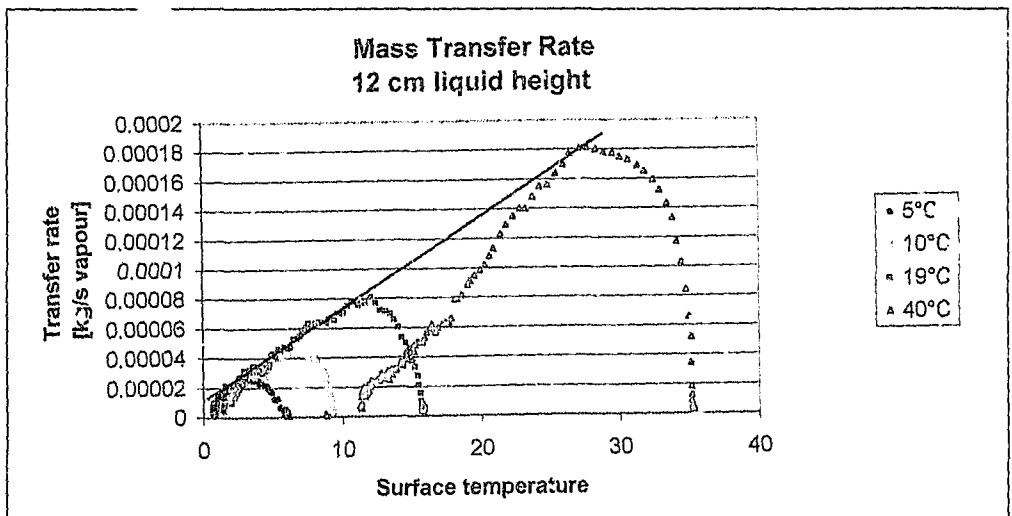


Figure 5.49 : Mass transfer rates for 12 cm liquid height.

It was decided that the coefficient was not specific enough and it was modified to include liquid height. Figure 5.50 shows that agreement is reached at low input temperatures, while higher input temperatures are not yet adequately described. The maximum rate however is described.

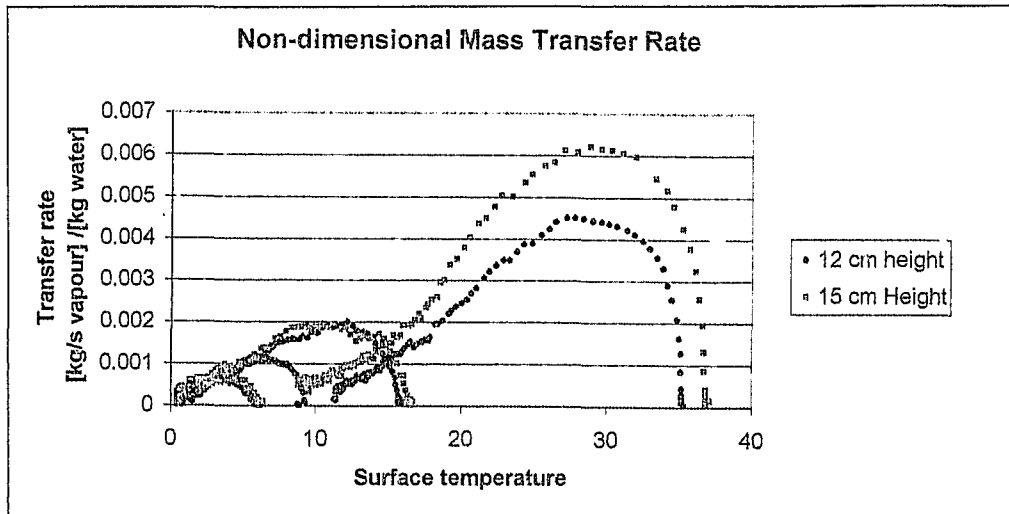


Figure 5.50 : Non-dimensional mass transfer rate as a function of surface temperature.

From the above it is evident that the rate of mass transfer depends not only on surface temperature but also on liquid height. Dividing the non-dimensional mass transfer by the liquid mass, yields figure 5.51.

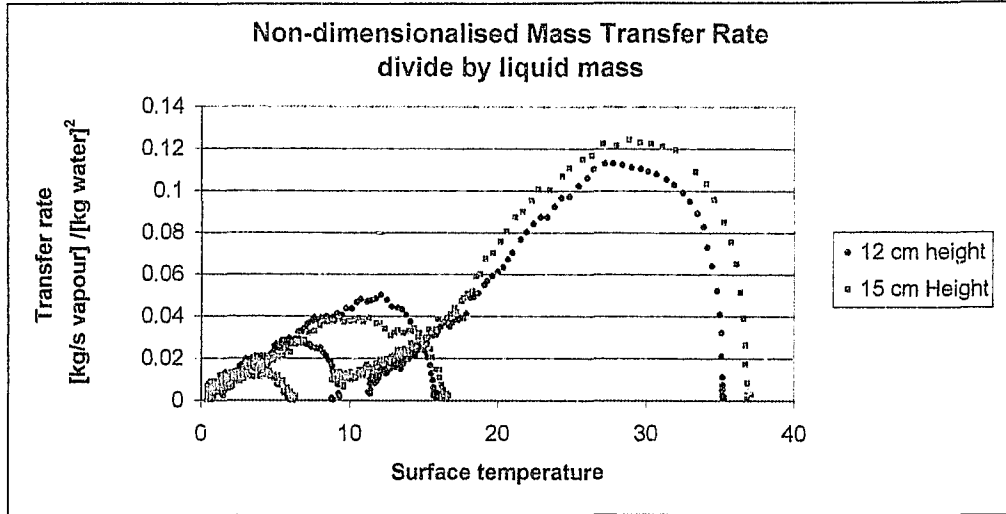


Figure 5.51 : Variation of vapour mass transfer rate over liquid flow rate, with temperature.

Maximum mass transfer rate can thus be described by the following equation:

$$\frac{dm_{\text{vapour}}}{dt} = K_m \delta P M_{\text{liquid}}^2 \quad (5.4)$$

Where the value of K_m was found to be of the order of $0.04 \text{ [kg/s]/[kg}^2\text{]/[kPa]}$, and δP is the driving potential based on surface temperature saturation pressure. For a linear increase in local temperature there is a non-linear increase in local saturation pressure and hence in the driving potential.

5.3.6 Heat Transfer Coefficient

The formulation of heat transfer (equation 3.13) was applied to the 15 cm height data, and yielded fairly consistent results over all the initial temperatures. Applying the formula over the entire time of decompression predicted exceptionally high heat transfer coefficients during the initial stages.

This is not surprising as the local change in temperature with time is very high. Figures 5.52 to 5.55 show the heat transfer coefficient at the 3 cm height as a function of time.

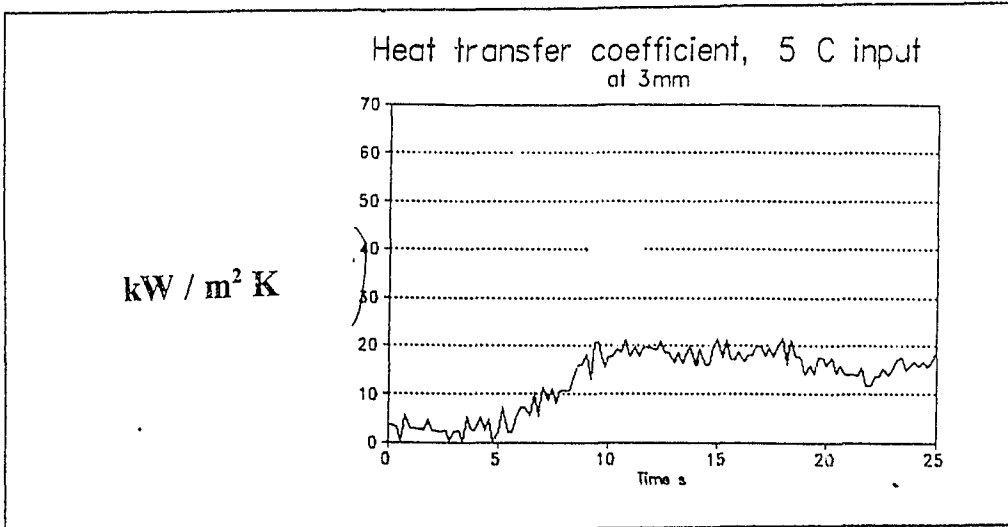


Figure 5.52 : Heat transfer coefficient 5°C input temperature and 15 cm height.

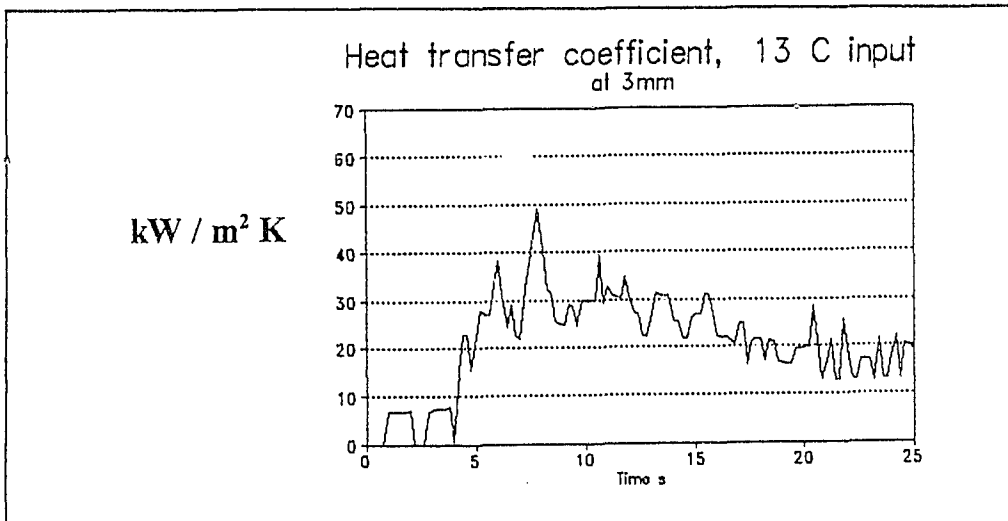


Figure 5.53 : Heat transfer coefficient 13°C input temperature

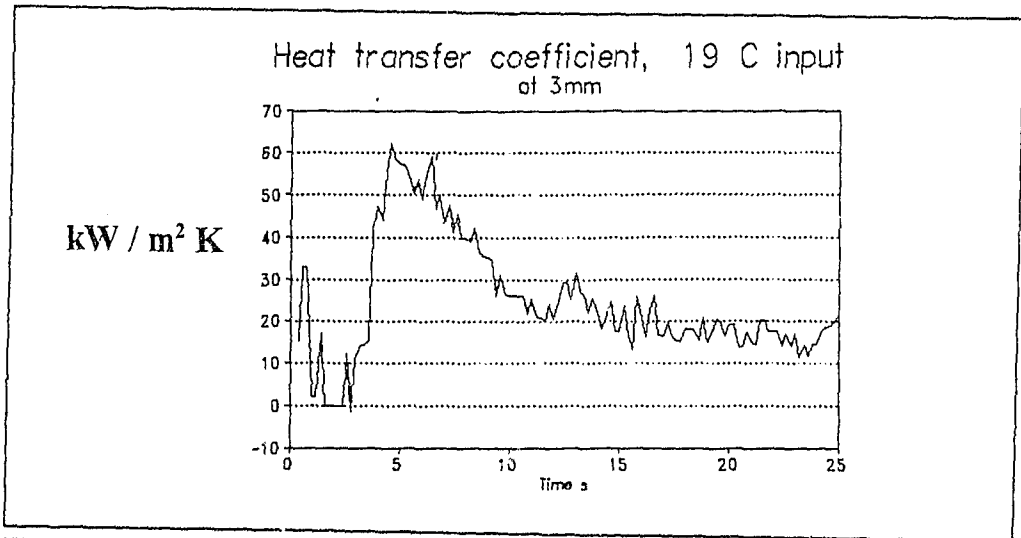


Figure 5.54 : Heat transfer coefficient 19°C input temperature.

As can be seen, once boiling ceased in the lower regions, the heat transfer coefficient decreased to a fairly steady value of between 10 to 20 $\text{kWm}^{-2}\text{K}^{-1}$. For the 40°C input temperature the heat transfer coefficient did not steady within the given time, indicating that there is a mixture of boiling and convection.

CHAPTER 6

DISCUSSION

This chapter is a discussion of the experimental results and observations, divided into the three series of tests conducted. Consideration is given to the implications of the findings on the design and modelling of water vapour compression systems.

6.1 Through-Flow Evaporator

6.1.1 Evaporator Pressure

As modelled in chapter 3, the evaporator pressure was observed to increase with increasing inlet temperature due to increasing generation of vapour. Figure 5.1 shows an increase in evaporator pressure at constant low water inlet temperature. This is ascribed to a leak in the evaporator developing during testing (the low inlet temperatures were tested last) as there was a corresponding decrease in bulk heat transfer, as observed in figure 5.5.

6.1.2 Temperature Distribution

Marked temperature differences were noted between the flashing temperature (the temperature of the water measured immediately after undergoing isenthalpic expansion across the orifice) and the temperature at the end of the horizontal plate in the evaporator, at low inlet water temperature. As the inlet water temperature increased, so this temperature difference was

observed to decrease. Flashing therefore plays a greater role in the heat transfer process at higher inlet water temperatures.

In retrospect, it was probably optimistic to expect to be able to measure heat and mass transfer coefficients accurately over such a small area as the plate and given the difficulty in accurately measuring temperatures between 0 and 10°C. It is worth noting the implications of the temperature distribution within the evaporator. For the water to exist at various temperatures in the evaporator there would have to be a pressure distribution within the evaporator. It is thus plausible that the design of evaporators needs to incorporate consideration of the flow phenomena that take place within the evaporator. When vapour is generated due to flashing there would be a local rise in pressure. This vapour then expands to the lower pressure region. In the case of the through-flow evaporator, once the water flashes due to isenthalpic expansion across the orifice, it enters the evaporator and flows over the evaporator plate. Having cooled due to the flashing process the water flowing over this plate is less superheated with respect to the saturation temperature corresponding to the evaporator pressure, than the inlet water. This phenomenon of a local increase in pressure implies that the compression device may be required to be designed for a lower pressure than that corresponding to the required water outlet temperature. The suction pressure of the compressor should thus accommodate both pressure losses due to vapour flow and localised pressure increases due to vapour generation.

6.1.3 Boiling Regimes

By far the greatest contribution to the cooling process was provided by the flashing, whereby vapour (and cooling) is generated due to isenthalpic expansion into the evaporator. A steady increase in the amount of flashing could be observed with an increase in inlet temperature, as seen in figures 5.6 to 5.7. At low water flow rate, the flashing contribution was observed to initially increase with increasing water inlet temperature, limited to 90% of the heat transfer. For a given flow rate the total evaporated mass also increases with inlet temperature. This would seem to imply that at higher flow rates, a greater difference is required between the saturation pressure of the inlet water and the evaporator pressure, for efficient flashing to occur. It could well be that too high a volumetric flow rate is produced for the system geometry and there is a “choking” effect.

Thus mass transfer increases substantially with decreasing evaporator pressure and it would appear that this is due to the flashing becoming the dominant boiling regime at higher bulk superheat.

6.1.4 Mass Transfer Coefficients

Mass transfer coefficients based on pressure increased to a maximum and then rapidly decreased. The reason for this the non-linear dependence of saturation pressure on temperature (as illustrated in figure 3.12) over the test range. The driving potential chosen for the mass transfer coefficients was thus based on temperature. Order of magnitude values for bulk and flashing mass transfer

coefficients were established for these driving potentials. It was found that removing the driving potential term from the derivation of the flashing coefficient, yielded linear results for given test conditions. The slopes of these equations were found to follow the same trend as those of the pressure - inlet temperature curves. It is thus suggested that if the performance of the compression device can be adequately modelled, then a flashing coefficient for a given evaporator geometry can be established. For the system under investigation, it is difficult to establish the ejector's performance curve as, at the time of testing, no means was readily available to establish system leakage under operating conditions.

6.1.5 Evaporator Design

Although the tests conducted could not attain sizing coefficients for evaporators in general, the objective of describing the boiling process and investigating the contribution of the various boiling regimes was met.

From a design point of view it has been shown that the inlet to a direct contact evaporator should not consist of barometric legs or any expansion device across a considerable length. From the results it can also be deduced that the evaporator needs to be a vessel of large volume to allow the flash gas to expand into the vessel without a sizeable pressure difference between the inlet and ejector (or compression device) inlet. Though energy saving can be achieved using multistage systems, pre-cooling of the inlet water would reduce the amount of flashing at the inlet and hence larger evaporators with greater water residence periods would be required.

The low value of the percentage contribution to the heat transfer rate due to evaporation along the plate shows that it is important to incorporate agitation (mechanical or utilizing cascades) in direct contact evaporators. Without agitation vertical temperature gradients would be set up in the body of the liquid which would result in low evaporation rates. While use of spray nozzles would increase the amount of flashing it is felt that agitation of any bodies of water would be essential to improve evaporator efficiency. In order to minimise pressure gradients being established within the evaporator, consideration needs to be given to the vapour flow, particularly given that water vapour has very high specific volumes, and hence flow rates, at the low pressures required to produce cooling.

Direct contact water vapour refrigeration systems should hold an advantage over indirect contact systems due to the removal of heat transfer surfaces in the evaporator and condensers. In an indirect contact heat exchanger there has to be a temperature difference between the two media in order for heat exchange to take place across the heat transfer surface. In the through flow evaporator, resistance to heat transfer is due to insufficient heat transfer area and a pressure loss between the inlet to the ejector and the evaporator due to frictional losses.

Of the regimes noted, flashing was shown to be the most efficient and thus evaporator design criteria must aim to maintain the flashing regime. Free evaporation appears to be less efficient. It is suggested that the reason for this is the fact that there is a lack of "superheat" due to the bulk of the liquid not being exposed to the lower pressure. This could be caused by a combination of hydrostatic pressure reducing superheat and a pressure differential existing between the liquid surface and inlet to the compression device.

6.2 Photographic Study

The vacuum boiling of water was described by Miyatake⁽⁴⁸⁾ as consisting of two distinct phases: flashing and surface evaporation. This view is supported by the photographic study. Upon decompression, flashing or bulk boiling was observed. The boiling agitation gradually decreased with time, ceasing first in the lower regions and eventually the water became calm.

It is suggested that the increase in hydrostatic pressure with liquid depth results in vertical temperature gradients through the liquid. Vapour generation leads to an increase in local pressure, which in turn decreases the superheat below the point where vapour is generated.

It was observed that there is some bubble growth in the bulk of the liquid after surface boiling has ceased. This implies that there is a measure of superheat within the liquid. The fact that bubbles detach from the evaporator wall just below the surface more readily than at some distance below the surface could be due to the possibility that heat transfer from the warmer lower regions to the cooler upper regions may exceed the rate at which heat is removed from the water due to evaporation at the surface. Bubbles can be expected to grow on the evaporator wall, rather than within the bulk of the liquid, as the wall surface provides both nucleation sites and a slightly greater liquid superheat due to heat ingress from the environment through the evaporator wall.

When a bubble detaches itself, it rises to the surface and expands explosively into the space above the liquid surface. The stability of the surface is disrupted and thus so are the temperature gradients. This leads to boiling being re-initiated at this disturbance and this surface boiling is maintained until the temperature gradients are established again. The fact that activity decreases

with time can be attributed to the continual decrease of bulk water temperature with time. The lower the bulk water temperature is, the more stable the system is.

Whether local flashing occurs depends not only on the local temperature and liquid height but also on the stability of the system. When boiling occurs at the surface, bubbles are more readily formed within the liquid than when the surface is still. Local pressure and temperature within the liquid, and consequently superheat, is thus dependent on both bubble activity at the water surface and the pressure above the water surface.

The fact that temperature gradients are set up would indicate that there is a value of heat transfer rate below which surface evaporation takes place and above which flashing occurs. This is likely to be a range, rather than a set value, indicated by the fact that boiling at the surface can be re-initiated. It is suggested that if the heat transfer rate from the lower regions to the higher regions is greater than the rate at which heat is removed due to evaporation, boiling will occur. If the heat transfer rate is insufficient, the pressure above the water surface will drop and bubble growth will be accelerated.

Comparing the photographs taken with those presented by Westwater[25] in Chapter 2, the bubbles observed in figure 5.22 would appear to belong to the transition or film boiling regimes. Figure 5.26 would be typical of the discrete bubble region mentioned by Gaertner [18]. From the photographic study it can be deduced that greater heat transfer takes place during the initial flash or surface boiling period.

Though there are marked differences between the nature of boiling observed in the photographic study and sub-atmospheric boiling off a heated surface presented in Chapter 2, some similarities are apparent. Figure 2.4 shows the boiling curve for water at various degrees of superheat. In experiments of this type boiling heat transfer is measured at sustained plate or wire superheat. In the boiling observed in the photographic study, the superheat diminishes with time. In effect the boiling of the pool of water can be understood by moving from right to left along the boiling curve. The pool begins at a high degree of superheat and consequently is cooled at a high rate of heat transfer. As the temperature of the bulk liquid decreases, so local superheat decreases and the violent boiling ceases in the depth of the liquid. Bubble nucleation tapers off and nucleate boiling ceases. Convective heat transfer cools the liquid further. A decrease in evaporator pressure or a detachment of a bubble has the effect of creating localised superheat which re-initiates nucleate boiling. When this boiling occurs it is observed to be violent in nature, with bubble explosively rising to the surface. This is consistent with the findings of **Raben et al** [36] who observed a discontinuity in plotted heat transfer rates in the transition between the convective and boiling heat transfer regimes.

The liquid height in figure 5.22 is almost double that of figure 5.26. This suggests that when designing evaporators for water vapour compression systems sufficient height should be allowed to prevent liquid carry over. The steam jet ejector compression system used can accommodate liquid droplets. High speed radial or centrifugal compressors however, could be far more sensitive.

6.3 Vertical Cylinder

6.3.1 The Vacuum Boiling Process

The tests conducted have verified the model presented in Chapter 3. Local vapour generation (hence pressure rise) affects the driving potential of lower region and has a limiting affect on heat transfer rates. It was observed that temperature gradients are established vertically within the liquid. It is proposed that this is due to local superheat being governed not only by the water surface pressure and local temperature, but also by the hydrostatic pressure imposed by the liquid height. Upon decompression violent boiling and hence high heat transfer occurs. The hydrostatic pressure in the liquid means that temperature gradients can be established through the liquid height. As the bulk of the water cools down the local superheat a various heights is eliminated and convection takes over from boiling.

Figures 6.1 to 6.4 show local saturation pressure based on measured temperature, compared to the addition of the surface saturation pressure and the local hydrostatic pressure. The initial temperature is 40°C with a 15 cm column height, at depths below the surface of 6, 9, 12 and 15 cm. All the figures show that boiling takes place at the given heights at, or below, the hydrostatic pressure. The slight offsets in figures 6.2 and 6.3 are due to insufficient local superheat. The cooling rate at these points would then lag that of the surface. Termination of local boiling in all four figures is the point where the slopes of the curves change significantly, i.e. the local heat transfer mechanism changes from boiling to convective heat transfer.

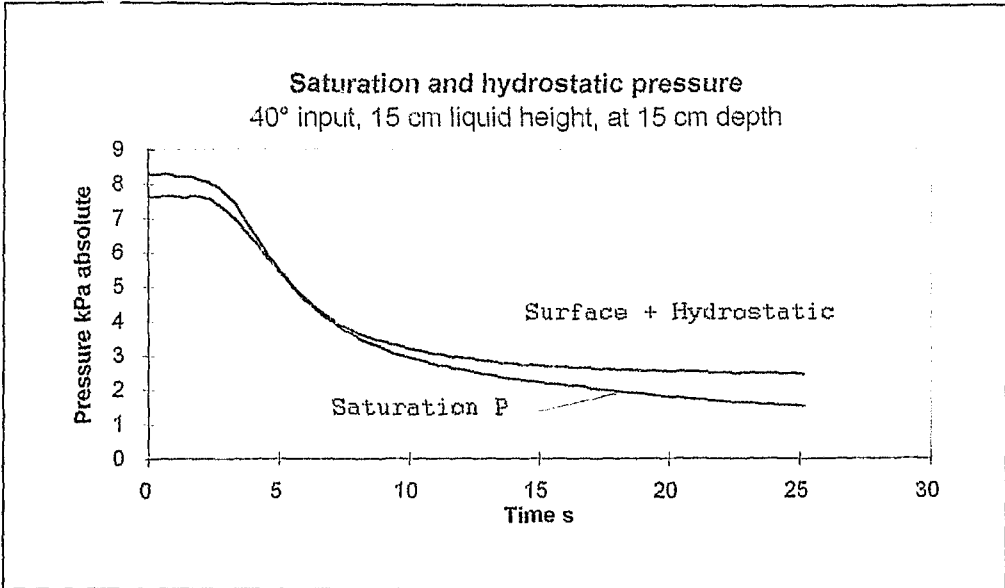


Figure 6.1 : Pressure distribution 15 cm below liquid surface

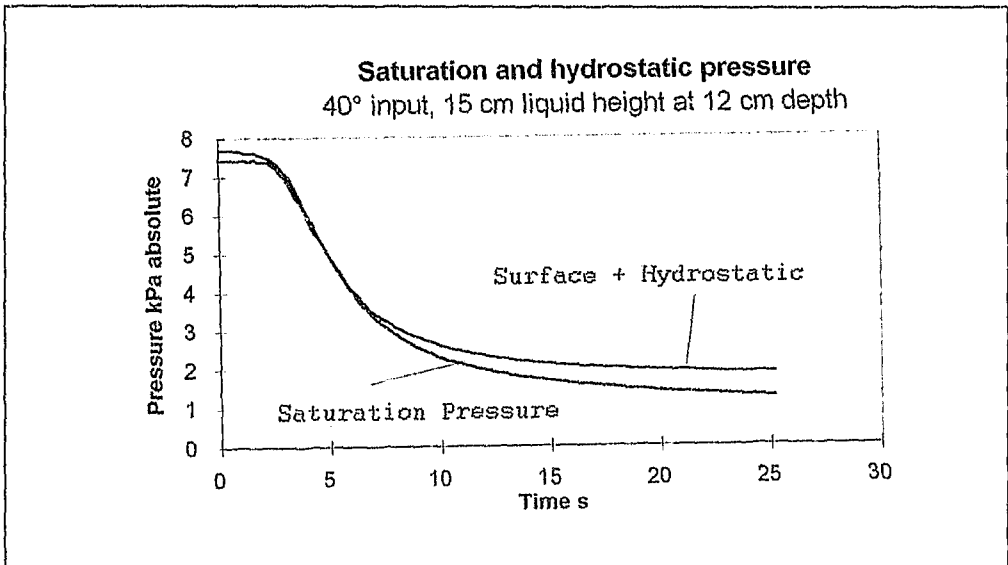


Figure 6.2: Pressure distribution 12 cm below liquid surface

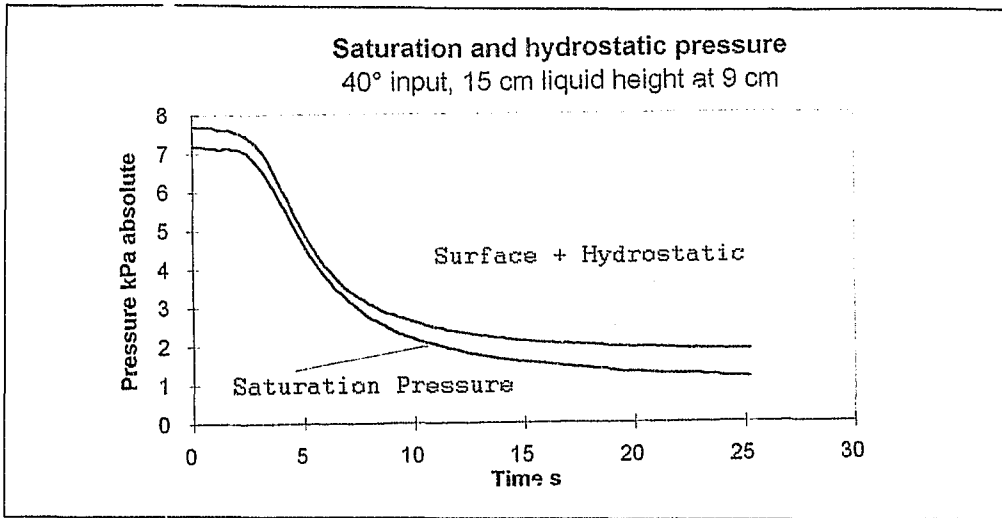


Figure 6.3 : Pressure distribution 9 cm below liquid surface

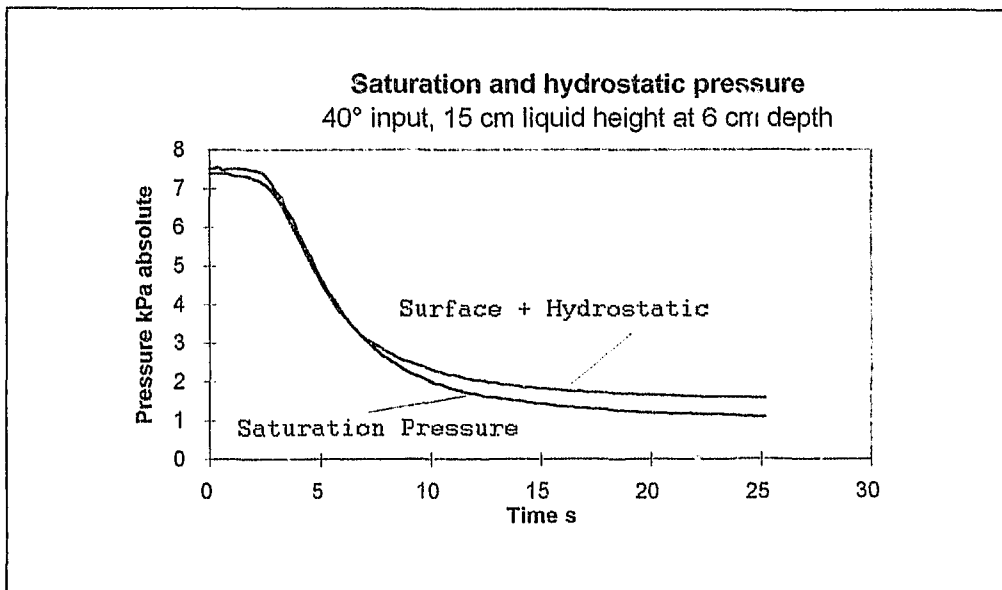


Figure 6.4 : Pressure distribution 6 cm below liquid surface

During flashing the saturation pressures at lower levels either were equal to, or had the same slope as, the sum of the surface and hydrostatic pressure. In cases where the local temperature had fallen below the saturation temperature corresponding to the hydrostatic pressure, the slope of the pressure line was seen to be lower than that of the flashing line.

In some cases the saturation pressure at the lower regions was well below that of the sum of the surface pressure and the hydrostatic pressure. In these cases boiling does not occur due to a lack of local driving potential and the cooling method is convective heat transfer. (See figure 6.5)

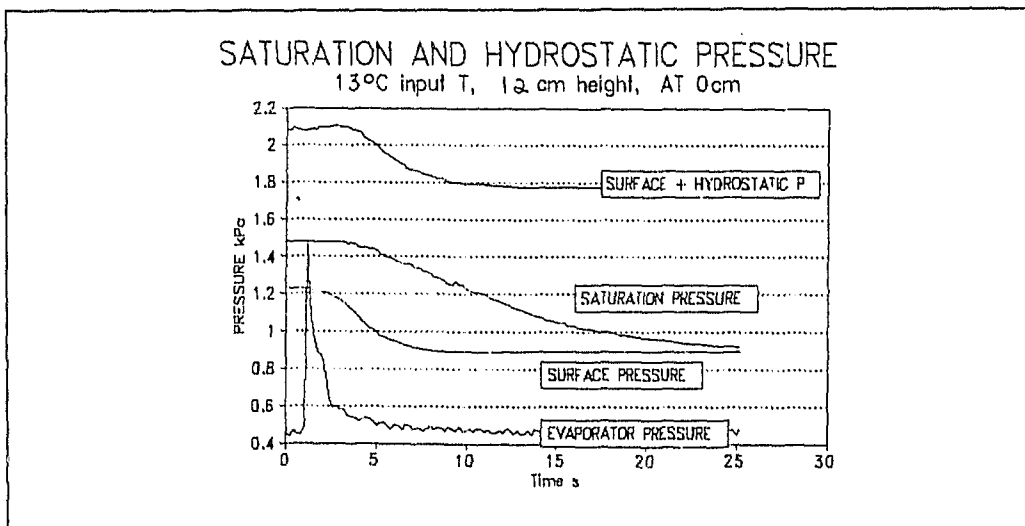


Figure 6.5 : Sub-cooled pressure distribution for convection.

This trend was observed even at low liquid heights of 3 mm. Figures 6.6 to 6.8 show the pressure lines at 3 cm heights over a range of initial temperatures. For the lower initial temperatures the base temperature is subcooled and the local cooling method is convective heat transfer. In figure 6.8 with an initial water temperature of 19°C, flashing occurs throughout the height.

The pressure corresponding to the temperature measured at 3 cm (local saturation pressure line) equals that of the hydrostatic pressure based on surface temperature (hydrostatic pressure line) and liquid height. After a short period of flashing the cooling method can be seen to change to convective heat transfer, illustrated by the saturation pressure line and the hydrostatic pressure line diverging.

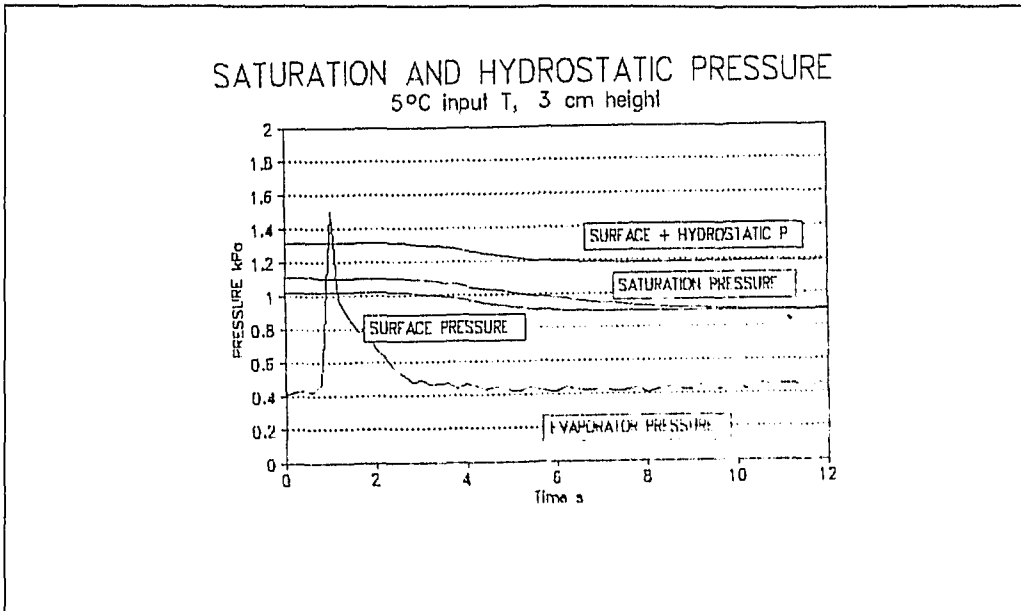


Figure 6.6 : Pressure lines for 9 cm height, at 3 cm, 5°C input.

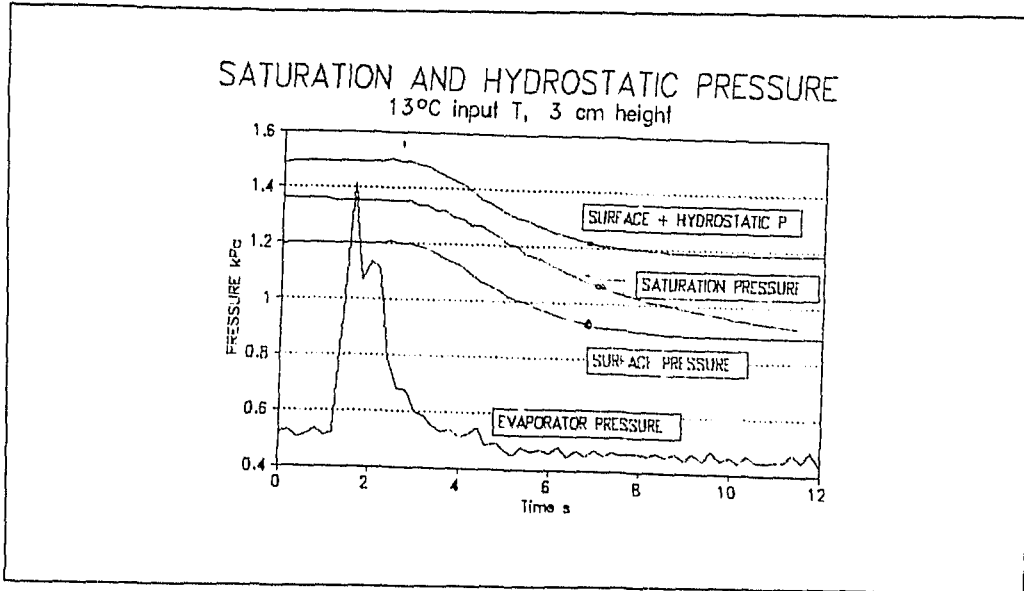


Figure 6.7 : Pressure lines, 13°C input

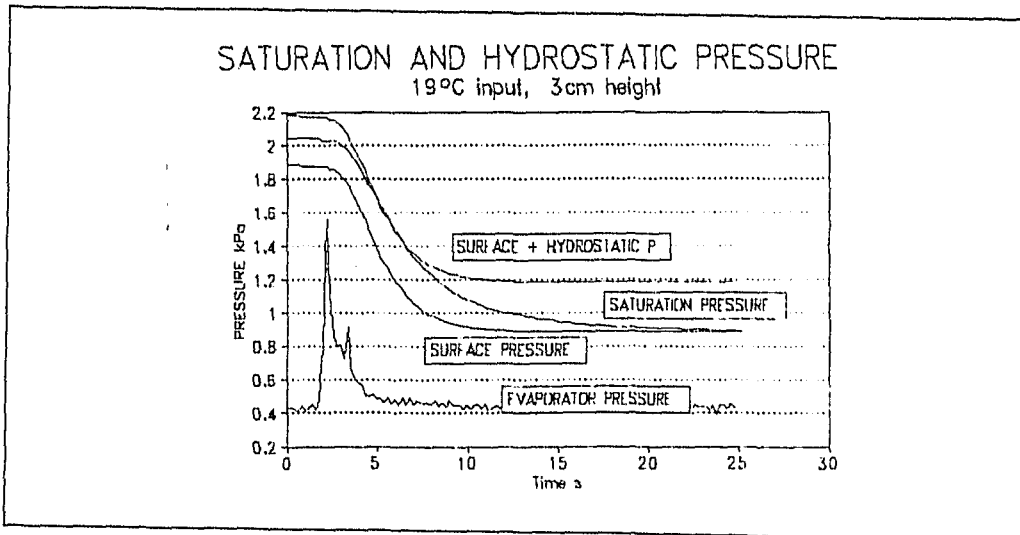


Figure 6.8 : Pressure lines, 19°C initial water temperature.

In figure 6.9 the initial temperature is 40°C . The saturation pressure at 6 cm is below that of the hydrostatic line and can be seen to be equal to the surface pressure. In such a case it is proposed that the 6 cm height is exposed to the surface pressure due to vigorous boiling and agitation of the water.

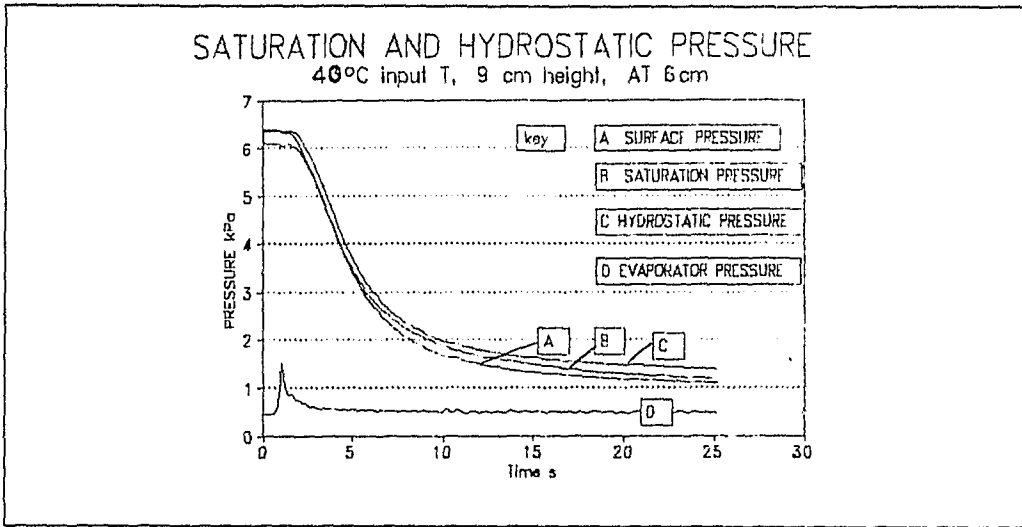


Figure 6.9 : Pressure lines, 40°C initial temperature 9 cm height, at 6 cm.

This would mean that the hydrostatic pressure of the lower regions would be controlled by the 6 cm height pressure. Referring to figure 6.10, the pressure at 3 cm height follows that of the hydrostatic pressure defined by the surface initially. Due to violent boiling the surface is broken and the water at 6 cm height boils at the same pressure as the surface. The pressure at 3 cm briefly follows the hydrostatic pressure defined by 6 cm height and at the end of boiling is sub-cooled with respect to the hydrostatic line. Convective heat transfer then takes place.

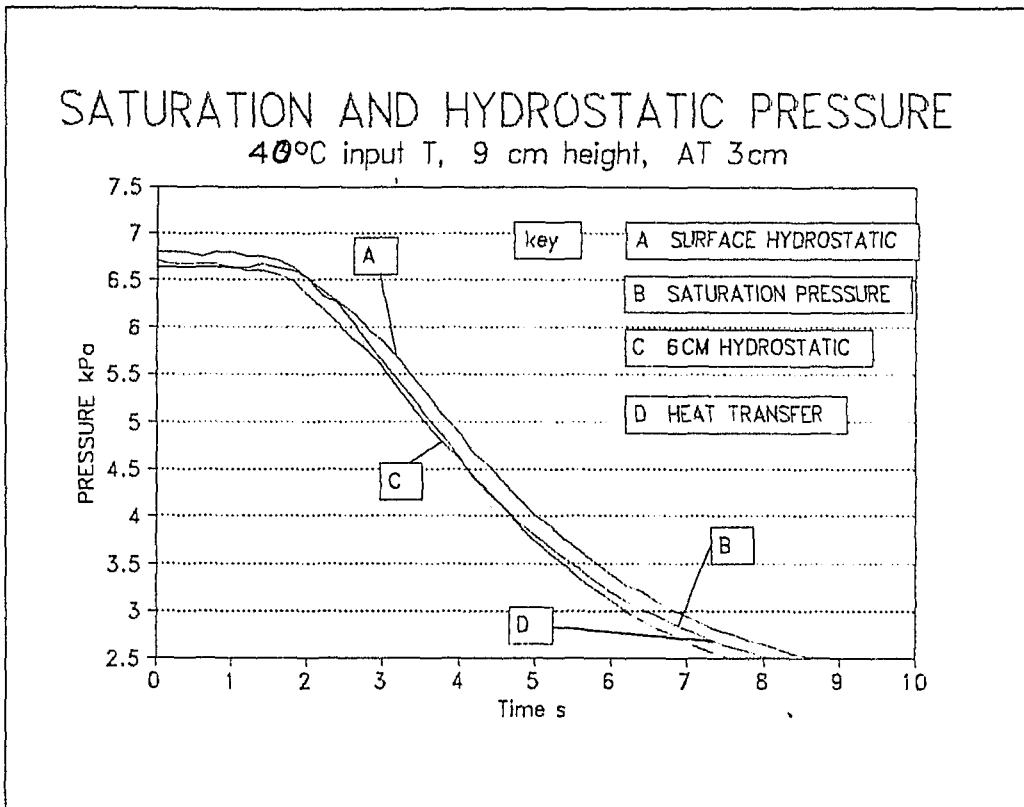


Figure 6.10 . Pressure lines for 40°C input and 9 cm height, at 3 cm.

The implications of these results are :

- 1) It may be possible to describe the boiling process exactly if the water surface temperature is known.
- 2) The local heat transfer method, ie boiling or convection, can be determined by the pressure trace

6.3.2 Non-Equilibrium Fraction

Miyatake [41] described the vacuum boiling process by defining the non-equilibrium fraction (NEF) (equation 2.5) which is a measure of the bulk superheat of a column of water relative to its initial superheat. Figures 6.11 to 6.15 show the traces of NEF as a function of time for varying liquid heights at 40°C initial temperature. The figures show similar trends to those presented by Miyatake in figure 2.20. The boiling process can be seen to be comprised of two phases: a rapid decrease in bulk temperature followed by a gradual decrease in bulk temperature.

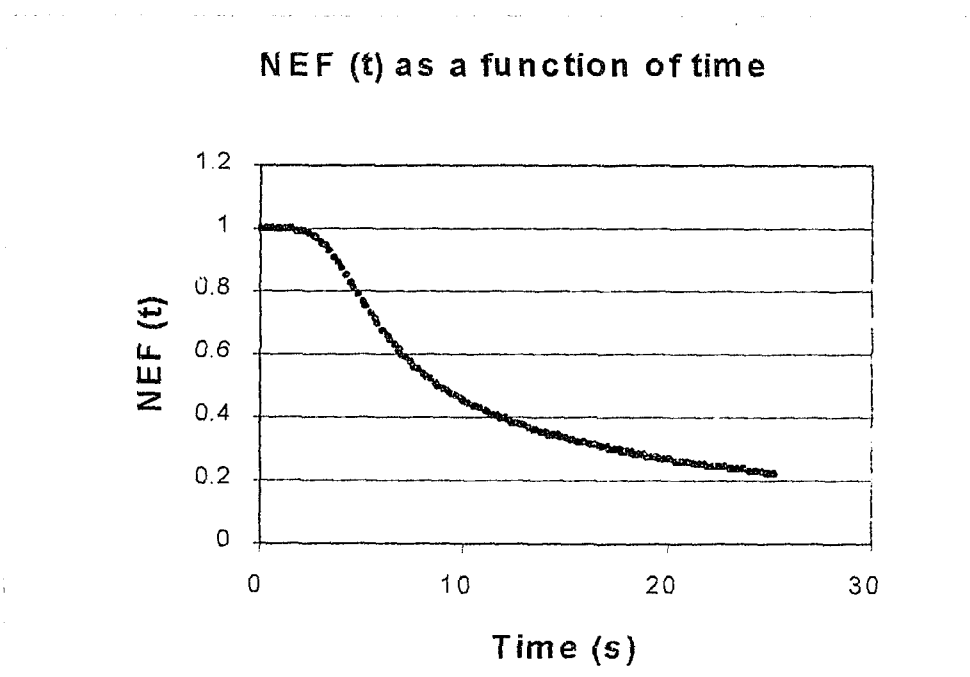


Figure 6.11 : NEF as a function of time, 40°C initial temperature 15 cm liquid height.

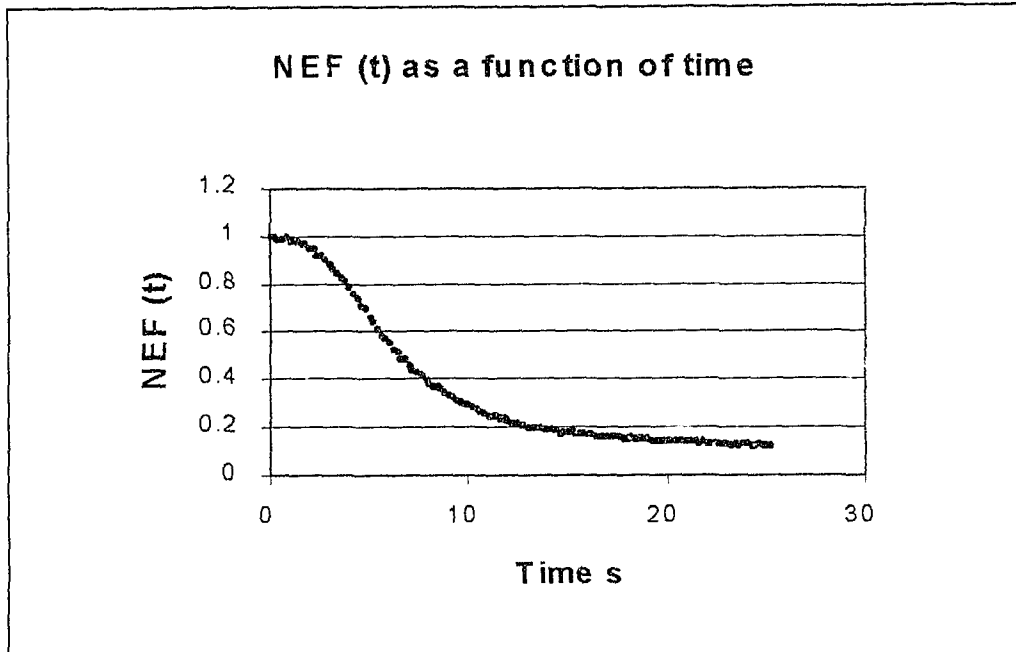


Figure 6.12 : NEF as a function of time, 40°C initial temperature 12 cm liquid height.

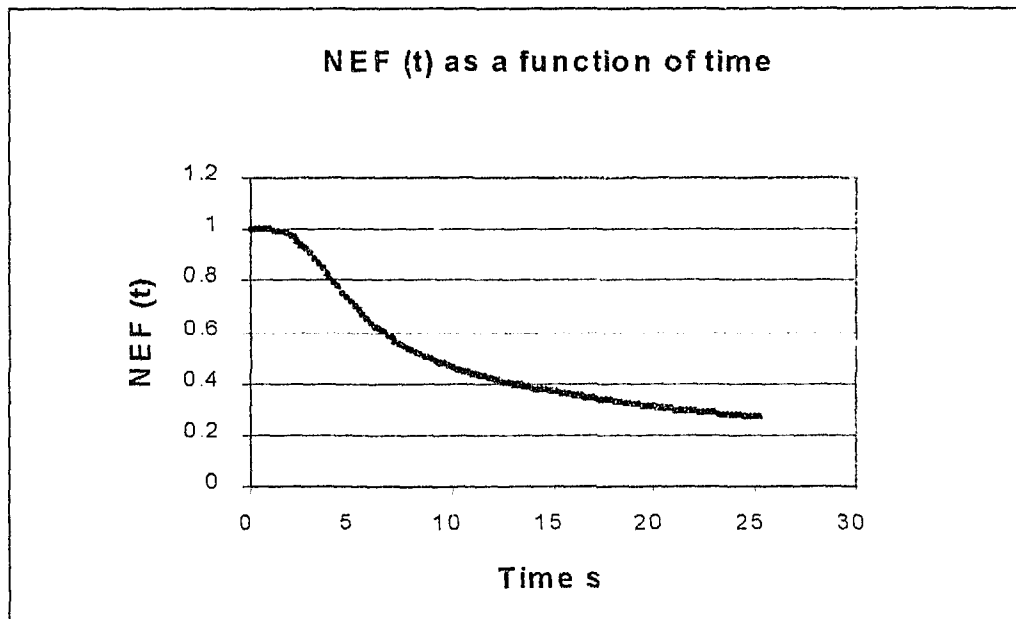


Figure 6.13 : NEF as a function of time, 40°C initial temperature 9 cm liquid height.

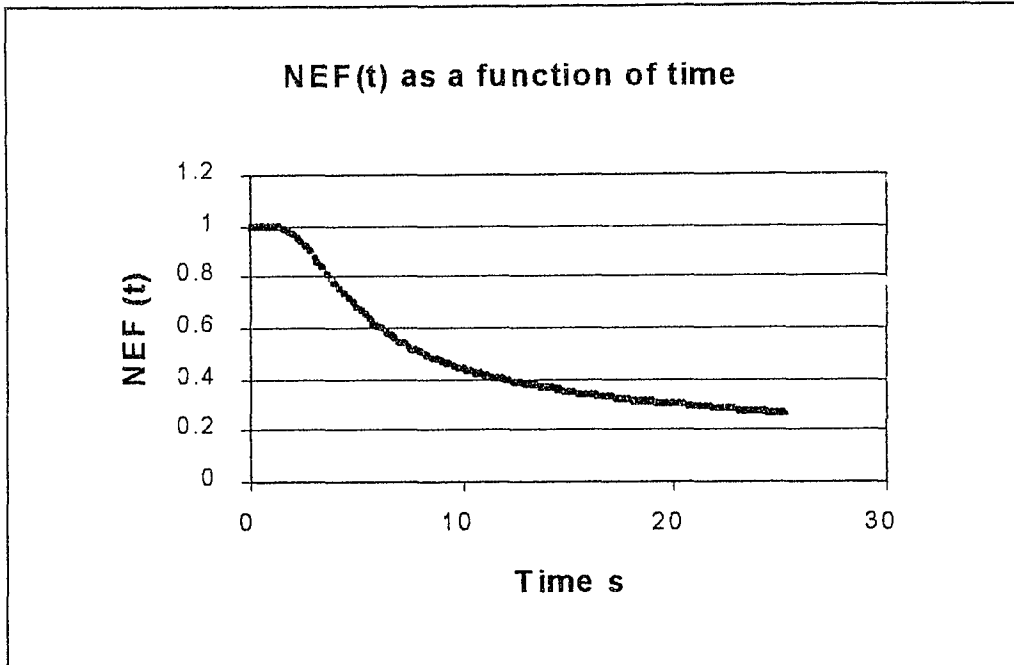


Figure 6.14 : NEF as a function of time, 40°C initial temperature 6 cm liquid height.

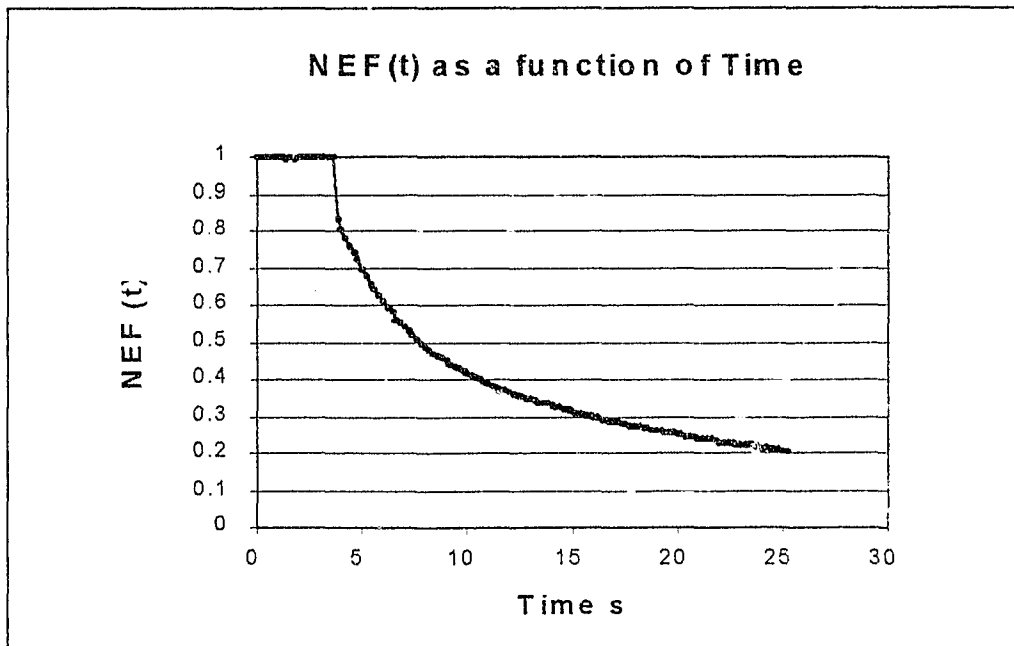


Figure 6.15 : NEF as a function of time, 40°C initial temperature 3 cm liquid height.

A key difference between the results presented and those of Miyatake is the slope graphs during the initial bulk boiling phase. Figures 6.11 - 6.15 indicate a lower rate of change of bulk temperature during this period. Though differences in initial temperature, liquid height and compressor performance would have an effect on the rate of change of bulk temperature, it is felt that the slower response of the LM 35 sensors is responsible for the NEF profile being smoothed out. The temperature profiles presented are thus qualitative in describing the boiling process but are not quantitative in establishing rates during the bulk boiling phase.

6.3.3 Evaporator Design

The results show that agitation is extremely important to efficient evaporator operation as the same bulk superheat can yield lower heat transfer rates due to temperature gradients being established by hydrostatic pressure. The substantial drop in mass transfer rate shortly after decompression best illustrates this.

Though mass transfer coefficients were developed these are too specific to the given system to be of any practical design use and due to the thermal lag of the LM-35s would be lower than the true values. Based on the results, it would seem that reducing the pressure drop between liquid surface and compression device inlet would be important in order to achieve sustained high driving potential at the liquid surface, and hence throughout the liquid height. This means that the vapour would require a large volume to expand into and hence sizing of evaporators would be likely to be governed by flow considerations rather than liquid surface area.

6.4 Project Shortcomings

Various shortcomings in the projects execution are noted below:

6.4.1 Project Focus

The project focus was primarily concentrated on the actual boiling process. In retrospect more time should have been spent on testing and establishing the performance characteristics of the ejector set. The ejector system's performance could then have been isolated from the boiling process, which would have aided both the modelling of the process and the measurement of limiting heat transfer rates.

6.4.2 Evaporator Design

The design of the evaporator should have revolved around the vapour flow dynamics. The direct contact evaporator should have been made of a non corrosive metal and not out of PVC. This would have resulted in easier sealing of the system.

6.4.3 Temperature Measurement

Platinum Resistance Thermometers should have been used to measure the temperature. Attempts to use thermocouples to measure between 0 to 10 °C proved futile, in spite of building a cold junction compensation circuit and later purchasing a cold junction compensation chip. In both cases there was too much drift on the thermocouple signal. Though the LM-35s gave adequate readings to fulfill most of the project objectives, their thermal mass meant that it was not practical to establish limiting heat transfer rates for the vertical cylinder tests.

CHAPTER 7

CONCLUSIONS AND RECOMMENDATIONS

7.1 CONCLUSIONS

7.1.1 Through-Flow Evaporator

The vacuum boiling of water in a steam jet refrigeration system was shown to consist of two distinct regimes: flashing through the expansion device, and convection-controlled surface evaporation.

Flashing was shown to dominate the heat transfer in the through-flow evaporator. Surface evaporation was shown to take place at a greater rate when the water is agitated. Agitation was effected by cascading the water once it had flowed over a flat plate. It was concluded that it is essential to agitate any body of water to prevent hydrostatic pressure gradients being established as these would allow temperature gradients to be supported. It was also concluded that the design of direct contact evaporators needs to aim at minimising pressure gradients within the evaporator set up by pressure losses due to vapour flow. In so doing the saturation pressure corresponding to the water exit temperature would be closer to the evaporator pressure. The compression device would then require a lower compression ratio and hence the coefficient of performance of the system would be increased.

The objectives of describing the boiling process and estimating the contributions of the various boiling regimes were met. The objective of deriving mass transfer coefficients was met, but only for specific test geometries. General bulk and flashing coefficients were established for three flow rates. These were found to accurately model the heat transfer rates at high degrees of superheat. Though some insight was given regarding design criteria of evaporators, the objective of establishing a general correlation for scaling of evaporators was not met.

7.1.2 Photographic Study

The vacuum boiling of water due to rapid decompression could be seen to consist of the processes of bulk boiling and convection controlled surface evaporation. Boiling re-initiation at the water surface was observed. Local boiling appears to depend not only on superheat, defined by local water height and temperature, but also on whether vertical temperature gradients are maintained within the liquid, which in turn depends on the interaction of the heat transfer rate and surface evaporation rate.

From the marked rise in liquid surface height, it was concluded that evaporators in water vapour compression systems should be designed with sufficient height to avoid liquid carry-over into the compressor.

The objective of conducting a basic photographic study of the vacuum boiling process and visualising the boiling mechanisms was met.

7.1.3 Vertical Cylinder

A model of vacuum boiling of water was proposed and shown to be accurate. The vacuum boiling of water was shown to be controlled by both the bulk liquid superheat and liquid surface temperature. An approach was developed whereby saturation pressures corresponding to local measured temperature were plotted against time and were superimposed with hydrostatic pressure between measured points. The dominant heat transfer mechanism at any point in the liquid height, during the vacuum boiling process could be identified. It was concluded that the local liquid superheat would govern whether boiling heat transfer or convective heat transfer would occur. The degree of local superheat was determined by the temperature (and pressure) of the liquid layer above it.

Limiting values of heat transfer could not be determined due to the instrumentation used for measuring temperature not being sufficiently fast to monitor rapid temperature changes. It was concluded that the results obtained were qualitative in describing the processes involved in the vacuum boiling of small columns of water, but were not quantitative in terms of determining specific rates of heat transfer during the onset of boiling.

7.2 RECOMMENDATIONS

Clearly more work is needed in the field of direct contact evaporator design and establishing mass transfer coefficients. It is recommended that tests be conducted to establish the dependence of evaporator pressure and pressure gradients within flow-through evaporators, on the volume above the water surface and the water surface area.

A suggested approach for further work regarding mass transfer coefficients is the use of different flow and evaporator geometries with a compression device with a known performance curve. The compression device suction pressure and discharge pressure and speed would be measured. From this the operating point (and compressed vapour flow rate) could be determined. The effect of varying flow and evaporator geometries on the operating point of the compressor could then be determined. Evaporator design criteria to reduce vapour flow friction losses and optimise liquid evaporating or boiling surface area could then be determined.

It is recommended that further tests be conducted using the vertical cylinder, with high resolution, fast acting temperature measurement devices to establish limiting heat transfer values through the liquid height. Once these values have been obtained the vacuum boiling of a column of water could be modelled by coupling the equations governing the performance of the compression device with heat and mass transfer relationships through the liquid height.

APPENDIX A

Assumptions made in ejector design

1. The ejectors operate under sonic conditions in the throats of the nozzles and diffusers.
2. Geometrically similar ejectors have identical specific operating characteristics.
3. Coefficients of ejection are established empirically.
4. Throat and outlet aperture diameters of the nozzles and diffusers can be calculated by developed theory. Other dimensions follow by proportionality.
5. The optimal distance from the end of the cylindrical throat of the nozzle to the start of the cylindrical throat of the diffuser is proportional to the difference in their throat diameters.
6. Condenser calculation can be based on simple theory.
7. Humidity and superheat of the steam have negligible effect on ejector dimensions.
8. The temperature of the vapour does not affect ejector calculation.
9. All dimensions can be rounded to nearest standard sizes.

APPENDIX B

EES equations

B 1 Flow-through Evaporator Model

PROCEDURE Initial(P_ev, T_in, Power : Q_flood, Q_des, P_in)

P_in:=PRESSURE(Water,t=T_in,x=0)
 T_ev:=TEMPERATURE(Water,p=P_ev,x=0)
 cp := SPECHEAT (Water,P=P_in,T=T_in-0.1)
 dTem:=T_in-T_ev
 H_fg:= ENTHALPY(Water,p=P_ev,x=1)-ENTHALPY(Water,p=P_ev,x=0)
 Q_des:=Power/H_fg
 Q_flood:= Power/(cp*dTem)

END

PROCEDURE Del_Temp(P_ev, T_in :DT)
 T_ev:=TEMPERATURE(Water,p=P_ev,x=0)
 DT1:=T_in - T_ev
 If DT1<0 Then DT:=0 Else DT:=DT1

END

PROCEDURE Equilibrium(P_in,P_ev,Q_flo,dT:Q_mev)

R := 461.52
 T_in:=TEMPERATURE(Water,p=P_in,x=0)
 cp := SPECHEAT(Water,P=P_in,T=T_in-0.1)*1000
 h_fg:=(ENTHALPY(Water,P=P_ev,x=1)-ENTHALPY(Water,P=P_ev,x=0))*1000
 T_ev := TEMPERATURE(Water,P=P_ev,x=0)
 T_ba := (T_in+T_ev)/2
 P_ba:= (P_in+P_ev)/2
 cp_ba:=SPECHEAT(Water,p=P_ba,t=T_ba-0.1)*1000
 h_fg_ba:=(ENTHALPY(Water,P=P_ba,x=1)-ENTHALPY(Water,P=P_ba,x=0))*1000
 Q_mev := Q_flo*(-p*dT {+ (cp_ba*R * T_ba^(2)) / (h_fg_ba *1000* P_ba)})/h_fg

END

PROCEDURE Mass_con (Mass_in,P_ev_init, Vol,Q_mev,Q_des, P_ev :P_ev_out,
 Mass_out)
 R2:=461.52
 H_fg_ev:=(ENTHALPY(Water,p=P_ev,x=1)-ENTHALPY(Water,p=P_ev,x=0))*1000

B 2

T_ev:=TEMPERATURE(Water,p=P_ev,x=0)

Mass_out := Mass_in + Q_mev - Q_des

If (Mass_out < 0) Then P_ev_out := P_ev Else P_ev_out := P_ev +
(Mass_out)*R2/Vol/(1/T_ev-R2/H_fg_ev)/1000

END

P_ev[1]=0.8719

P_ev_init = 0.8719

T_in = 273.15 + 27

Power = 2 {kw}

Vol = 0.1

CALL Initial(P_ev[1], T_in, Power :Q_flo, Q_des,P_in)

Mass_in[1]=0

DUPLICATE i=1,10

CALL Del_Temp(P_ev[i], T_in: DT[i])

CALL Equilibrium(P_in,P_ev[i],Q_flo,DT[i]:Q_mev[i])

CALL Mass_con (Mass_in[i],P_ev_init,Vol,Q_mev[i],Q_des,P_ev[i]:P_ev[i+1],Mass_in[1+i])

END

DUPLICATE i=1,20

P[i]= 0.7 + i/10

T[i]= TEMPERATURE(Water,x=0,p=p[i])

END

B 2 Flow-through Evaporator Mass Transfer Model

Q=1.164*10⁽⁻²⁾

P_ev= (3.127/4/103-4e-3)/16e-3*4{(1.191)}

t_in=13

t_noz=11

t_4=6.3

p_noz=pressure(Water,x=0,t=t_noz)

h_in=enthalpy(Water,p=83.3,t=t_in)

hf_noz=ENTHALPY(Water,x=0,t=t_noz)

hg_noz=ENTHALPY(Water,x=1,t=t_noz)

m_noz=(h_in-hf_noz)/(hg_noz-hf_noz)*Q

```
cp_noz=specheat(Water,p=p_noz,t=t_noz-0.001)
```

```
{point 1}
```

```
km_1=m_1/(p_1-p_ev)
```

```
t_1=8.8
```

```
t_1b= t_noz - m_1*(hg_1-hf_1)/(cp_noz*Q)
```

```
hf_1=ENTHALPY(Water,x=0,t=t_1)
```

```
hg_1=ENTHALPY(Water,x=1,t=t_1)
```

```
m_1=(hf_noz-hf_1)/(hg_1-hf_1)*Q
```

```
p_1=pressure(Water,x=0,t=t_1)
```

```
cp_1=SPECHEAT(Water,p=p_1,t=t_1-0.0001)
```

```
{point 2}
```

```
km_2=m_2/(p_1-P_ev)
```

```
t_2=7.2
```

```
t_2b= t_1 - m_2*(hg_2-hf_2)/(cp_1*Q)
```

```
hf_2=ENTHALPY(Water,x=0,t=t_2)
```

```
hg_2=ENTHALPY(Water,x=1,t=t_2)
```

```
m_2=(hf_1-hf_2)/(hg_2-hf_2)*Q
```

```
p_2=PRESSURE(Water,x=0,t=t_2)
```

```
cp_2=SPECHEAT(Water,p=p_2,t=t_2-0.0001)
```

```
{point 3}
```

```
km_3= m_3 / (p_3-p_ev)
```

```
t_3=6.3
```

```
hf_3=ENTHALPY(Water,x=0,t=t_3)
```

```
hg_3=ENTHALPY(Water,x=1,t=t_3)
```

```
m_3=(hf_2-hf_3)/(hg_3-hf_3)*Q
```

```
p_3=PRESSURE(Water,x=0,t=t_3)
```

```
cp_3=SPECHEAT(Water,p=p_3,t=t_3-0.0001)
```

```
t_3b= t_2 - m_3*(hg_3-hf_3)/(cp_2*Q)
```

```
{Point 4}
```

```
hf_4=ENTHALPY(Water,x=0,t=t_4)
```

```
hg_4=ENTHALPY(Water,x=1,t=t_4)
```

```
m_4=(hf_3-hf_4)/(hg_4-hf_4)*Q
```

```
p_4=PRESSURE(Water,x=0,t=t_4)
```

```
cp_4=SPECHEAT(Water,p=p_4,t=t_4-0.0001)
```

$$M_{tot1} = Q * ((cp_4 + cp_noz) / 2) * (t_{in} - t_{4}) / ((hg_4 + hg_noz) / 2 - (hf_4 + hf_noz) / 2)$$

$$M_{tot2} = m_1 + m_2 + m_3 + m_4 + m_{noz}$$

B 3 Temperature Sensor Calibration

N=20

DUPLICATE i=1,N {copy data from Lookup table into X and Y arrays}

x[i]=P[i]

y[i]=T[i]

yP[i]=a0+a1*x[i]+a2*x[i]^2

END

{Regression formulae to find a0, a1, and a2}

$$0 = -2 * \text{SUM}(y[i] - yP[i], i=1, N)$$

$$0 = -2 * \text{SUM}(x[i] * (y[i] - yP[i]), i=1, N)$$

$$0 = -2 * \text{SUM}(x[i]^2 * (y[i] - yP[i]), i=1, N)$$

$$\text{/bias} = \text{SUM}(yP[i] - y[i], i=1, N)$$

$$\text{sigma} = \text{SUM}((yP[i] - y[i])^2, i=1, N)$$

APPENDIX C

DESIGN OPTIONS FOR STEAM JET EJECTOR SYSTEMS

From a layout point of view, substantial savings can be incurred by a slight modification of the standard primary ejector and booster ejector configuration, by introducing a pre-evaporator between the evaporator and the primary condenser. The primary ejector is then replaced by two ejectors, with a lower compression ratio, as illustrated by figure C.1.

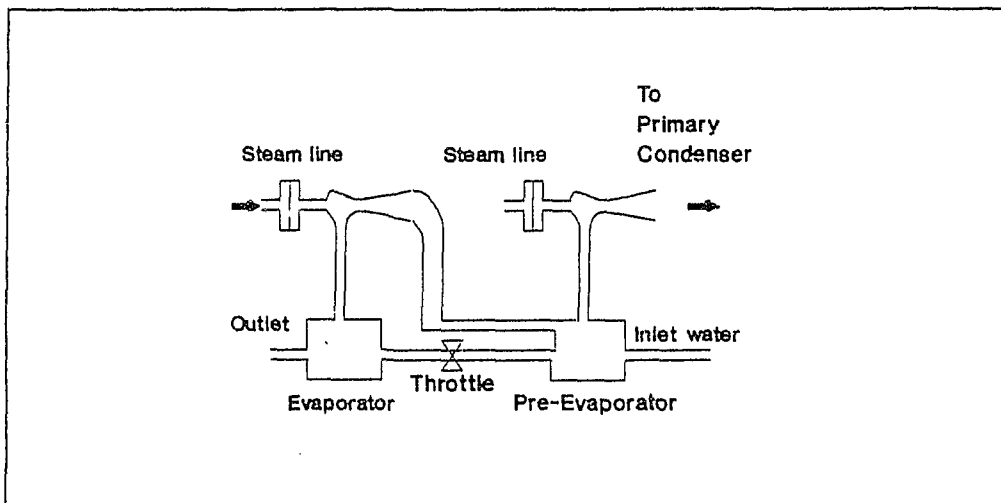


Figure C.1 : Standard configuration and pre-evaporator modification.

C 2

A comparison between these two systems is given below. The design parameters are as follows:

Power	1 MW	Condenser η	100 %
Evaporator T	1°C	Evaporator P	0.657 kPa
Condenser T	20°C-30°C	Steam P	0.6 MPa

Design data was taken from Vil'der's diagram for the determination of coefficients of injection.

The existence of non-condensibles was neglected.

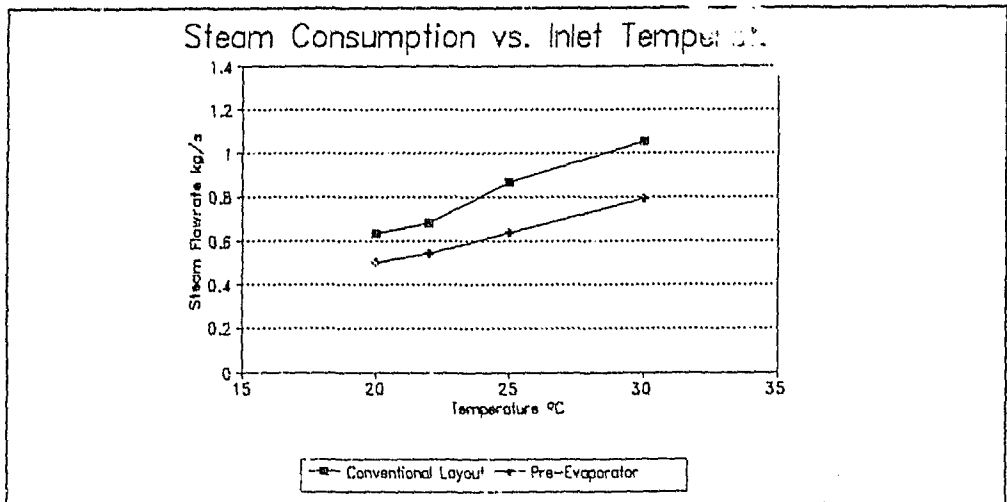


Figure C.2 : Steam consumption

As can be seen from figure C.2, savings of around 25 % in steam consumption can be achieved.

D 1

APPENDIX D

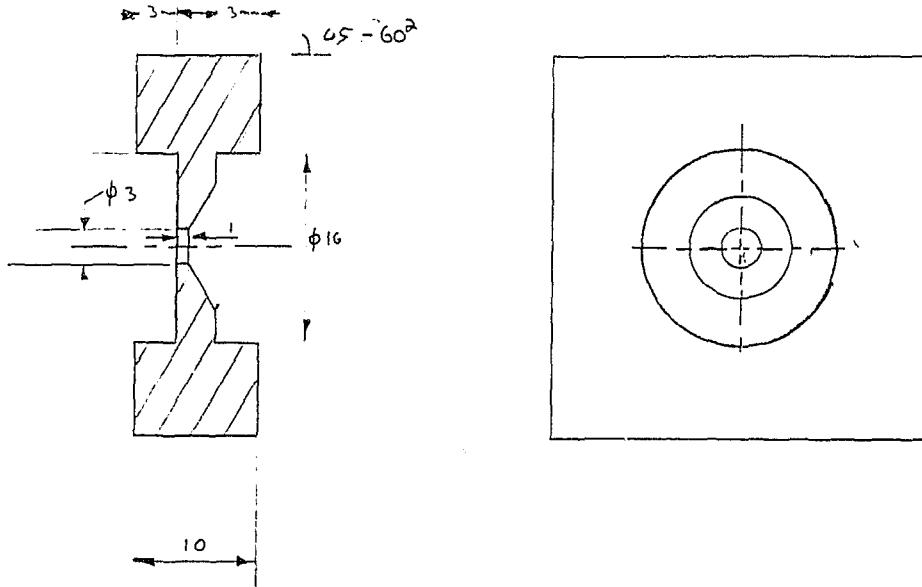
Design Drawings

D.1 Flow Through Evaporator Design Drawings

List of Drawings	Page
Inlet orifice	D 2
Flow-through evaporator component drawings	D 3-6
Flow-through evaporator assembly	D 7

D2

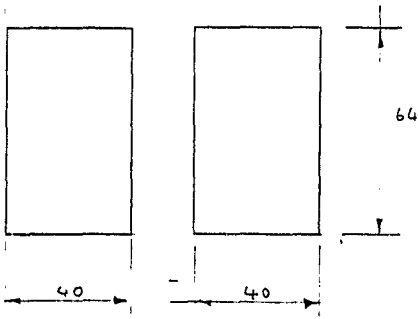
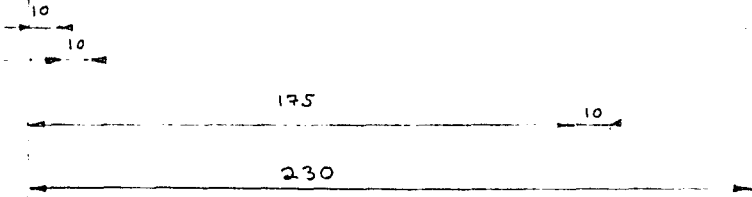
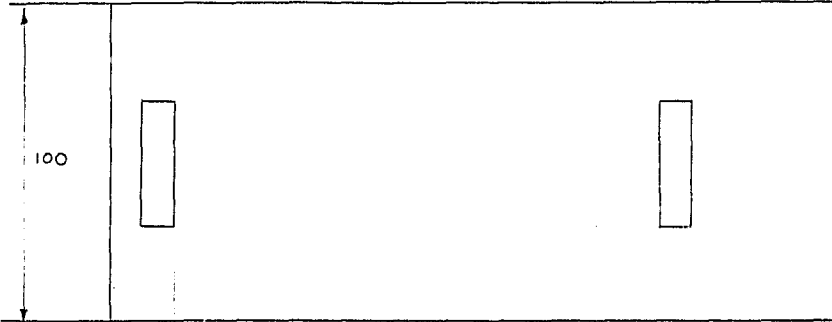
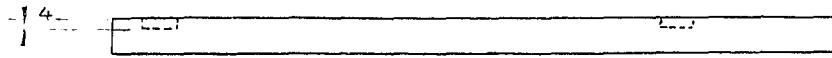
Inlet Orifice :



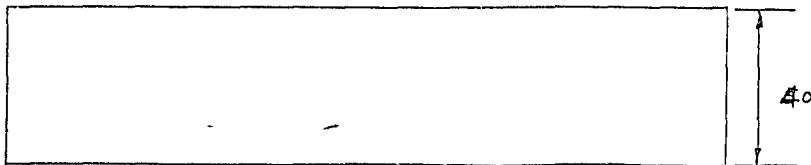
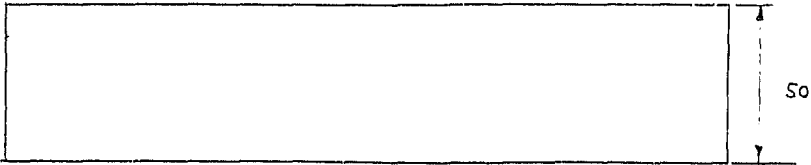
S. R MITCHLEY
WITS 1993

MATERIAL PVC
THICKNESS 10 mm

D3



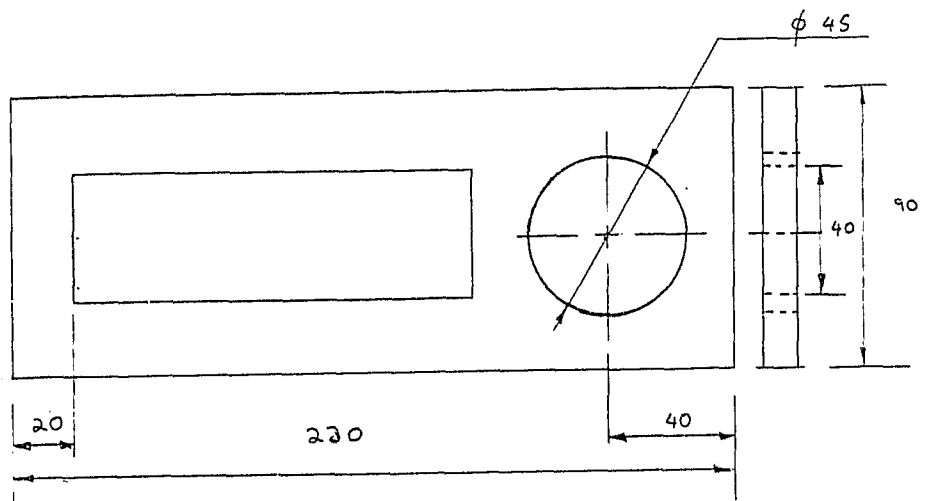
2x



S.R. MITCHELLEY
W/TS 1923

MATERIAL : PERSPEX
THICKNESS : 10 mm.

D4



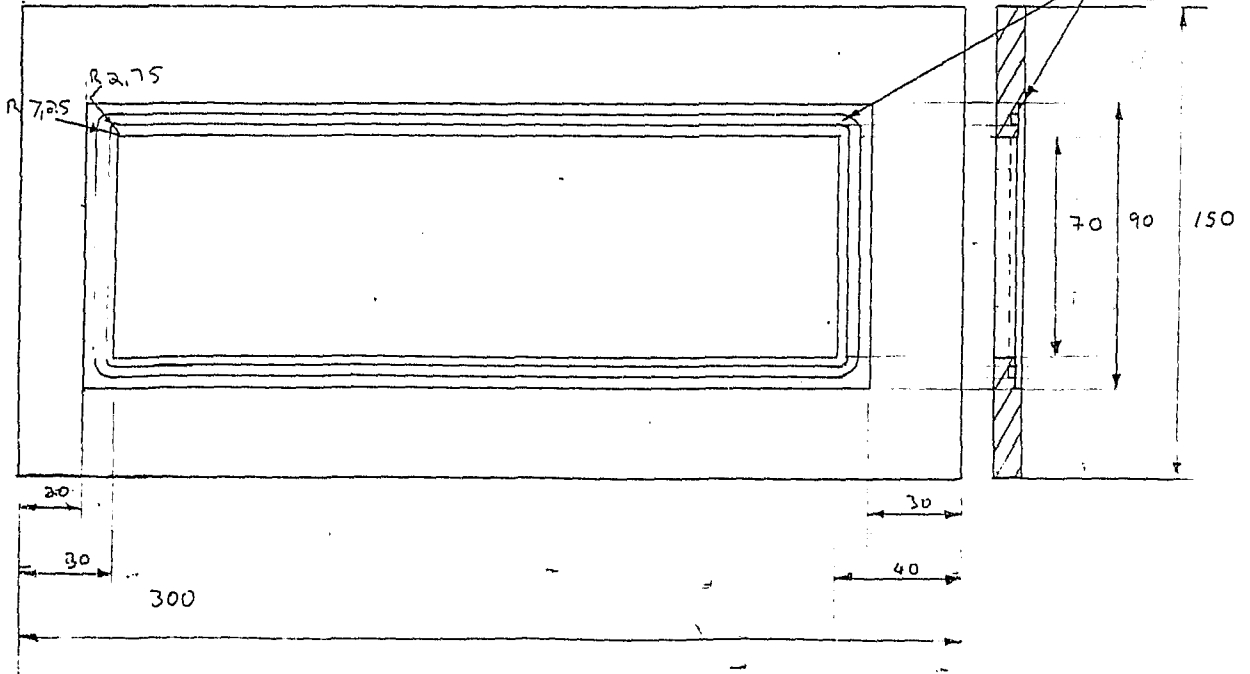
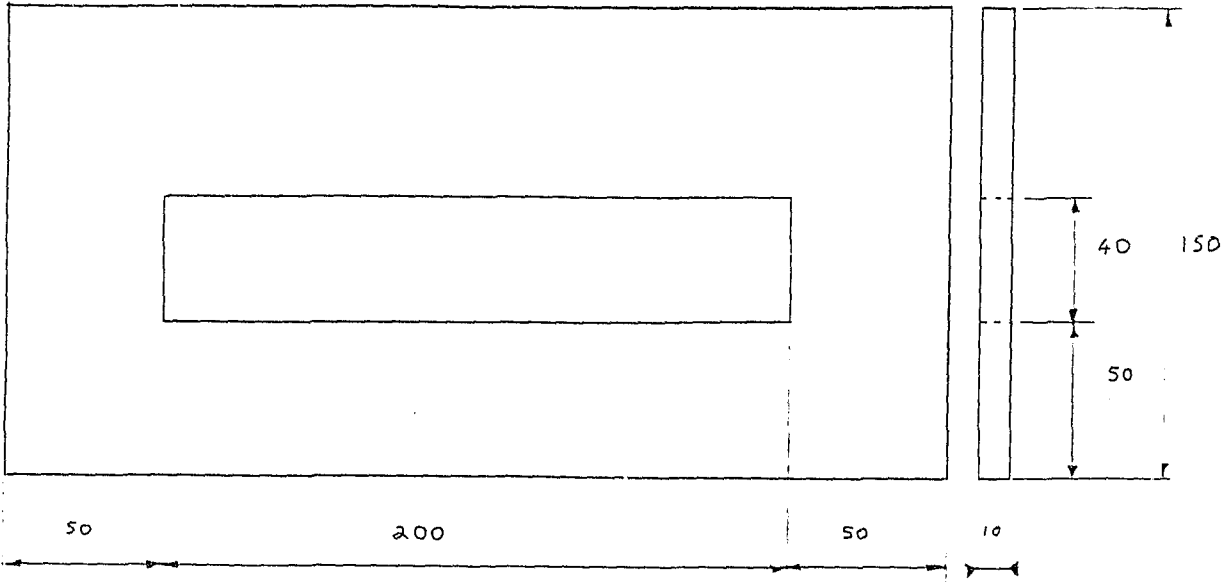
S.R MITCHLEY

WITS 1993

MATERIAL : PVC

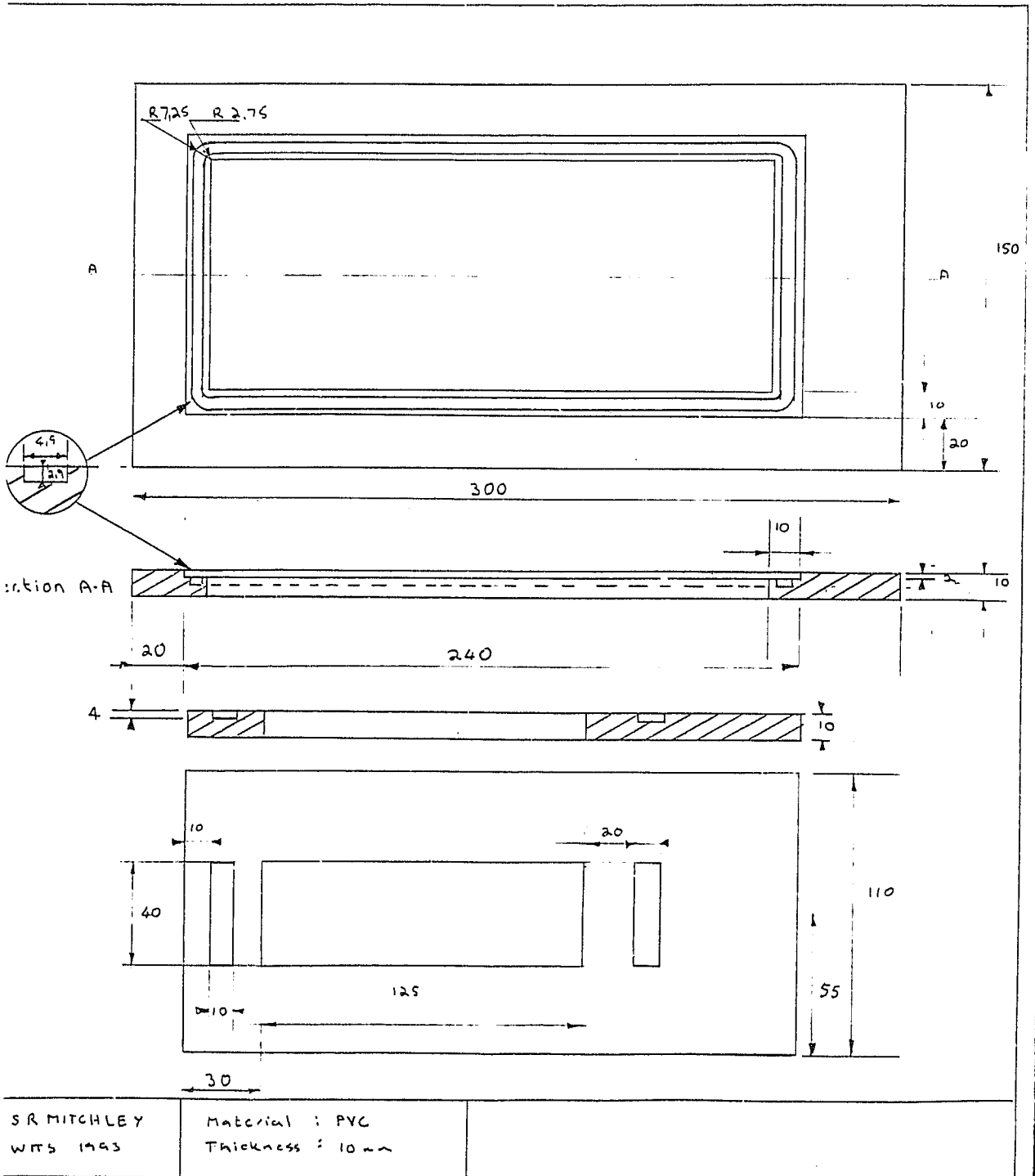
THICKNES : 10 mm

D5



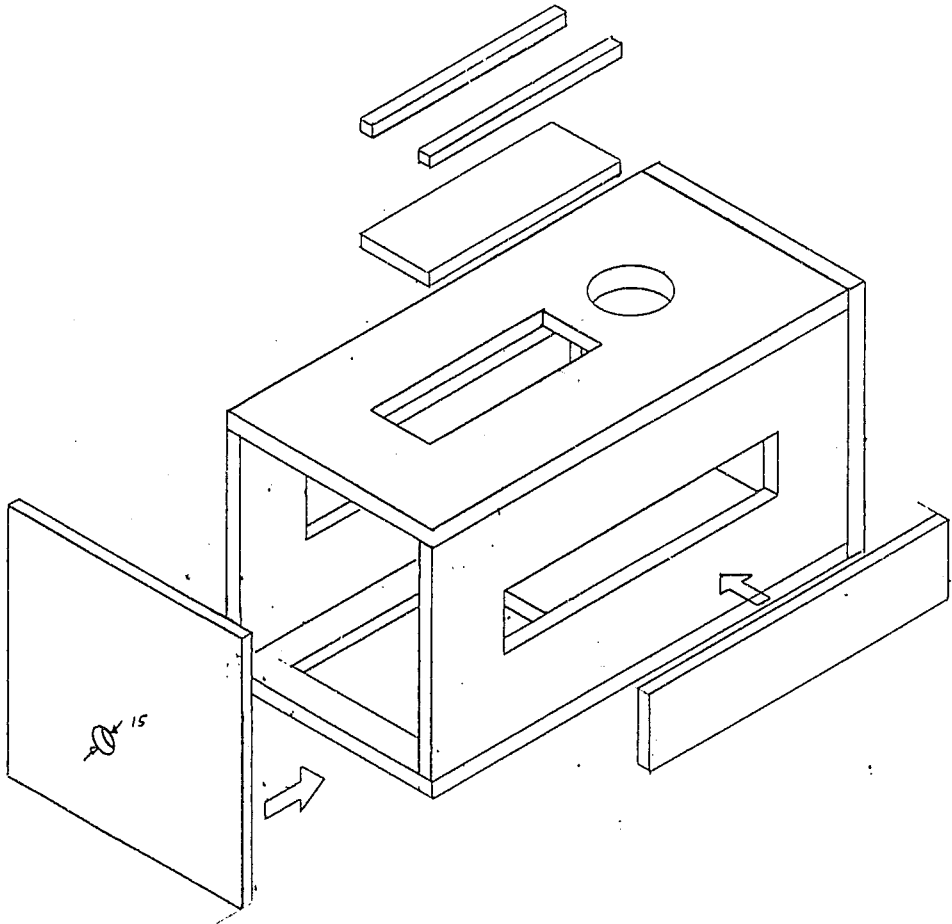
SR Mitchley Wils 1993	Material : PVC Thickness : 10mm	QUANTITY : TOP 1 BOTTOM 1	
--------------------------	------------------------------------	------------------------------	--

D 6



D7

ASSEMBLY



APPENDIX E

INSTRUMENTATION CALIBRATION DATA

E.1 Temperature Measurement

The LM35 temperature sensors (specification sheet included) have a long term stability of $\pm 0.01^\circ\text{C}$. It was thus decided to calibrate the temperature sensors to a mercury thermometer with a calibration certificate and resolution of 0.1°C . The sensors were kept in close proximity of the thermometer and were immersed in a pool of heated water. The water was agitated to ensure that local temperature fluctuations were kept to a minimum.

E.1.1 Vertical cylinder calibration data

Thermometer Reading $^\circ\text{C}$	T1 mV	T2 mV	T3 mV	T4 mV	T5 mV	T6 mV
15.3	14.3	14.50	14.36	14.45	14.60	15.57
3.0	0.2	0.17	0.18	0.17	0.17	0.51
12.2	11.26	11.39	11.28	11.39	11.52	12.53
18.5	17.63	17.74	17.61	17.72	17.91	18.87
26.0	24.98	25.1	24.95	25.07	25.32	26.23
4.3	3.38	3.66	3.47	3.58	3.69	4.59
16.7	15.72	15.74	15.80	15.82	15.99	16.99
20.5	19.55	19.68	19.55	19.64	19.85	20.85
23.0	22.12	22.21	22.08	22.19	22.43	23.40
29.0	27.95	28.02	27.88	28.00	28.31	29.24
10.0	9.10	10.32	9.32	9.20	9.09	9.20

A quadratic curve was fitted to each data set, establishing calibration constants for each of the LM-35s used in the vertical cylinder testing. The quadratic fit routine was applied in the EES program. The program listing for the quadratic fit is presented in Appendix B.

E.2

Vertical Cylinder calibration constants :

The following constants were used to convert the raw data readings in millivolts to temperatures.

LM35 #	a0	a1	a2
1	2.2	20.962	2.833
2	2.1	19.939	3.954
3	2.2	20.734	3.147
4	2.1	21.152	2.538
5	2.2	20.617	2.872
6	2.0	18.942	3.808

E.1.2 Through flow evaporator calibration data

Thermometer °C	Spare1 mV	Spare 2 mV	Spare3 mV
4.0	0.035	0.036	0.035
9.7	0.083	0.087	0.083
14.0	0.128	0.130	0.127
17.7	0.164	0.168	0.164
22.6	0.213	0.216	0.212
26.8	0.256	0.260	0.255
29.1	0.278	0.282	0.278
11.6	0.103	0.108	0.104

Through flow evaporator calibration constants :

LM35 #	a0	a1	a2
Spare 1	0.3	28.326	-2.448
Spare 2	0.3	26.524	-0.796
Spare 3	-0.1	29.007	-2.553

E.3

Thermometer Reading °C	T1 V	T2 V	T3 V	T4 V	T5 V	T6 V	T7 mV
15.5	0.659	0.683	0.751	0.737	0.688	0.717	N.A
19.8	0.795	0.834	0.908	0.864	0.839	0.874	N.A
24.1	0.966	1.035	1.074	1.059	0.991	1.079	N.A
32.1	1.289	1.362	1.386	1.367	1.303	1.391	34.6
34.0	1.372	1.455	1.474	1.464	1.391	1.445	35.4
8.0	0.399	0.371	0.444	0.429	0.371	0.415	11.4
13.0	0.556	0.605	0.678	0.654	0.600	0.654	16.4
17.8	0.737	0.776	0.834	0.820	0.751	0.825	20.2
20.8	0.869	0.898	0.971	0.947	0.854	0.942	24.2
24.4	1.010	1.040	1.123	1.083	1.025	1.079	27.8
16.9	0.717	0.742	0.815	0.805	0.732	0.781	20.3

Temperature °C	T8 V
3.9	0.057
2.8	0.042
9.3	0.104
16.4	0.175
23.0	0.240
22.8	0.239
38.0	0.390
37.0	0.380
36.0	0.370
35.0	0.360

Calibration constants :

LM35 #	a0	a1	a2
1	-0.4	23.602	1.168
2	-0.6	23.532	0.3257
3	-1.9	21.502	2.066
4	-2.2	23.340	1.113
5	-0.6	22.665	1.787
6	-1.8	26.267	-0.5128
7	-2.0	23.460	0.9012
8	-2.1	21.346	2.635

Handwritten note:
 1/25
 2014 10/27

E.2 Pressure Measurement

Kent-Taylor Deltapi K Series Transmitter type K (specification sheet follows)

Due to shock loading on the transmitter, the calibration was checked before each set of tests. To calibrate the pressure transmitter a vacuum pump was connected to the transmitter, a Vacuum gauge and a McLeod Gauge. The Voltage across a 102.7 ohm resistor connected to the transmitter and the McLeod Gauge reading were measured in increments of 5 Torr on the Vacuum gauge. 0.0 kPa abs was set at 0.4108 V and 4 kPa at 2.054 V.

The "Computerscope" data logger imports data multiplied by four. The pressure reading for a given data point can be established as follows:

$$P \text{ abs} = 2 * ((\text{Reading} / 4) - 0.4108) / (1.873 - 0.4108) \text{ kPa}$$

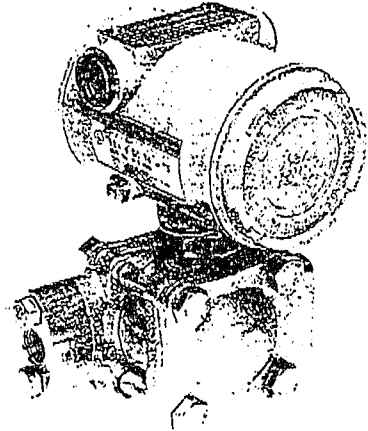
E.3 Specification Sheets

**Model K-AC
 Transmitter for absolute pressure**

spans: from 2.2 to 3000 kPa
 overrange limit: up to 16 MPa

Specification sheet

- High accuracy with wide choice of measuring ranges
- Compact, rugged, lightweight, easy to install and service
- Modular construction - high commonality of parts - optimum field interchangeability
- Non-interacting external zero & span and external damping adjustments
- Unique inductive sensing * with advanced electronics guarantees high stability and reliability
- Compatible with all 2-wire systems
- Complies with relevant IEC, NEMA and SAMA requirements for test procedures and environmental protection
- Meets NACE specification MR-01-75, 1984 revision
- Flameproof and Intrinsic Safety CENELEC approvals



Sensor code

RANGE AND SPAN LIMITS

J	0	2.2	10	13
K	0	4.7	28	28
L	0	11.7	70	76
M	0	25	150	150
N	0	135	800	800
P	0	300	3000	3000

Range limits (kPa abs) $\frac{URL}{LRL}$ Lower and Upper

Minimum span (kPa abs) $\frac{Min.}{Max.}$
 Maximum span (kPa abs)

FEATURES

Model K-AC, the absolute pressure variant of the Kent-Taylor Deltapi K Series³ of electronic transmitters, provides accurate measurements in spans of up to 3000 kPa at an allowable line overpressure of up to 16 MPa.

It incorporates a unique inductive sensing and measuring system that provides consistently reliable and stable performance under all types of process conditions, coupled with simple test and calibration procedures and minimum maintenance requirements.

The Deltapi K transmitter comprises two main elements: a sensor and an electronics module.

The sensor which has the absolute zero reference on one side converts the pressure of the process fluid (liquid, gas or vapour) into proportionate changes of two inductance values from which the electronics module produces a standard output signal. Six versions of sensors are available to suit the measuring ranges or spans to be used.

The electronics module, including all coarse and fine adjustments, process terminations, etc.; comprising the top works, is contained within a waterproof housing mounted on the bottom works containing the sensor, process flanges, drain/vent valve, etc.

* Protected by one or more of the following Patents:
 Italy n. 23219-A/81 and n. 21983-A/83
 Europe n. 71581

U.S.A. n. 4538465 and 4559829
 Spain n. 513994 and 534062
 Japan n. 1583573

FUNCTIONAL SPECIFICATIONS

Sensor	SPAN LIMITS absolute pressure min and max	RANGE LIMITS absolute pressure	OVERRANGE LIMIT (absolute)	PROOF PRESSURE (SAMA PMC 27.1)
J	2.2 and 13 kPa 22 and 130 mbar 16.5 and 97.5 mmHg	0 and 13 kPa 0 and 130 mbar 0 and 97.5 mmHg		
K	4.7 and 28 kPa 47 and 280 mbar 35.2 and 210 mmHg	0 and 28 kPa 0 and 280 mbar 0 and 210 mmHg		
L	11.7 and 70 kPa 117 and 700 mbar 87.7 and 525 mmHg	0 and 70 kPa 0 and 700 mbar 0 and 525 mmHg	16 MPa (*) 160 bar (*) 2320 psi (*)	48 MPa 480 bar 6960 psi
M	25 and 150 kPa 250 and 1500 mbar 188 and 1125 mmHg	0 and 150 kPa 0 and 1500 mbar 0 and 1125 mmHg		
N	135 and 800 kPa 1.35 and 8 bar 19.5 and 116 psi	0 and 800 kPa 0 and 8 bar 0 and 116 psi		
P	500 and 3000 kPa 5 and 30 bar 72.5 and 435 psi	0 and 3000 kPa 0 and 30 bar 0 and 435 psi		

(*) Equal to Maximum Working Pressure.

(*) 14 MPa, 140 bar or 2030 psi with AISI 304 ss flange bolting.

Service :

Liquid, gas and vapour applications.

Span adjustment

- Internal coarse step (switch selector)

- External fine continuous

Zero adjustment:

External fine continuous

Suppression adjustment

- Internal coarse step (switch selector)

- External fine continuous

Zero suppression (maximum)

Zero and span can be adjusted to any value as long as:

- calibrated span \geq minimum span

- upper range - value \leq URL

- lower range - value \geq LRL

Damping

Time constant (63%):

- Standard : 0.5 s

- Optional : adjustable from 0.2 to 2.5 s

This is in addition to the sensor response time of 200 msec.

Normal operating pressure limits

operates within specifications between line pressures of 0 kPa abs, 0 mbar abs or 0 psia and the Upper Range Limits.

Volume of process chamber

10 cm³ approx.

Volumetric displacement

< 0.1 cm³ for max span.

Power supply

The transmitter operates on 12 to 42 Vdc with no load and is protected against reverse polarity connection.

Power-up time

Operation within specification in less than 2 sec. with minimum damping.

Insulation resistance

> 100 M Ω @ 500 Vdc (1000 Vdc option)

Output signal

Two-wire 4 to 20 mA dc.

Ripple content on the output

less than 2% at 33.4 kHz

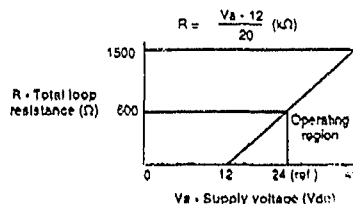
Load limitations - total loop resistance including optional remote indicator line: see figure below

Line resistance to remote indicator : 15 Ω max

Internal resistance of the optional output meter:

- 3.6 Ω for 36 mm scale

- 5.7 Ω for 90 mm scale



Operating conditions

	Temperature °C (°F)		Ambient pressure (absolute)	Relative Humidity (%)	Vibration (IEC 654-3)	EM/RFI (SAMA PMC 33.1)	Supply voltage Vdc (2)	Output load Ω (3)
	Process (1)	Ambient						
Reference	Any value between +15 and +35 \pm 2 K (+59 and +95 \pm 3)		96 kPa \pm 10% 960 mbar \pm 10% 720 mmHg \pm 10%	60 \pm 25%	None	None	24 \pm 0.5	600
Normal (4)	-43 to +120 (+45 to +248)	-25 to +85 (-13 to +185)			Severity class: steady state $f = 1$ to 10 Hz displ. 1.5 mm-acc. 0.5g	Class 2-abc Field strengths up to 10 V/m (6)	12 and 42	0 and 1500
Operative limits with Silicone oil or inert fill fluid (5)	-43 and +120 (-45 and +248)	-43 and +85 (-45 and +185)	Atmospheric pressure	0 and 100 condens. permissible	$f = 10$ to 60 Hz displ. 0.15 mm $f = 60$ to 500 Hz-acc. 2g	Class 3-abc Field strengths up to 30 V/m (6)		
Transport & storage limits (5)	Not applicable				Severity class: unusual • Velocity = 300 mm/s $f = 1$ to 150 Hz		Not applicable	

(1) Process temperature above 85 °C (185 °F) require derating the ambient limits by 1.5 : 1 ratio. (2) Refer to "power supply" requirements.
 (3) Refer to external loop "load limitations". (4) Performance stated under "Operating influences". (5) No damage.
 (6) Frequency range: 20 to 1000MHz.

Materials

Process isolating diaphragm and gasket seats (*)

- Standard: AISI 316 L ss.
- Optional: Hastelloy C 2760; Monel 400 ϕ ; Tantalum; Special, as specified.

Process flange and adapter (*)

- Standard: zinc plated carbon steel with chrome passivation.
- Optional: AISI 316 L ss; Hastelloy C ϕ ; Monel 400 ϕ ; Special, as specified.

Blank Flange

- Standard: zinc plated carbon steel with chrome passivation.
- Optional: AISI 316 L ss.

Plug and drain/vent valve (*) (**)

- Standard: AISI 303 ss.
- Optional: AISI 316 L ss; Hastelloy C ϕ ; Monel 400 ϕ ; Special, as specified.

Gaskets (*)

- Standard: Viton ϕ .
- Optional: Buna N; PTFE; Special, as specified.

Other parts of sensor

17-4-PH ss ϕ and series 300 ss.

Bolts and nuts

- Standard: zinc plated carbon steel bolts per ASTM-A-193-B7 and nuts per ASTM-A-194-2H.
- Optional: 17-4-PH ss ϕ ; AISI 304 ss; cadmium plated alloy steel bolts per ASTM-A-193-B7M and nuts per ASTM-A-194-2HM in compliance with NACE MR-01-75, class II.

Housing and covers

Die cast low copper and magnesium aluminium alloy (GD Al Si 12; Cu \leq 2.5%) with beige (RAL 1001) baked epoxy -sin finish.

Covers O-ring: Buna N.

Electrical connection plug:

Carbon steel

Electrical connection adaptor:

Aluminium alloy

Sensor fill fluid

- Standard: Silicone oil
- Optional: Perfluorinated polyethers (Galden ϕ)

Adjustments: AISI 316 ss.

Tagging

AISI 316 ss data plate attached to the electronics housing with stainless steel screws. AISI 316 ss tag fastened to the transmitter with stainless steel wire for customer's tag data up to a maximum of 56 characters and spaces on two lines for tag number and tag name, and up to a maximum of 28 characters and spaces for calibration details.

Mounting bracket (***)

- Standard: zinc plated carbon steel with chrome passivation.
- Optional: AISI 304 ss.

Calibration

- Standard: at maximum span, zero based range, ambient temperature and pressure.
- Optional: at specified range and ambient conditions; at operating temperature.

Mounting bracket

- Standard: flat type, either for vertical 60 mm (2in) stand pipe or surface mounting
- Optional: universal type, for vertical and horizontal 60 mm (2in) stand pipes, or surface mounting.

Optional extras

1/2 NPT flange adapter.

Output meter: plug-in type.

Available scales are 0 to 100% linear with indication on 36 mm or 90 mm scale.

Special scaling available.

External damping adjustment

Cleaning procedure for oxygen service

Preparation for hydrogen service

Environmental protection

Wet and dust-laden atmospheres

The transmitter is dust and sand tight and protected against immersion effects as defined by IEC 144 (1963) to IP 67 or by NEMA 6.

Suitable for tropical climate operation as defined in DIN 40.040. application class GQC.

Hazardous atmospheres

With or without output meter

INTRINSIC SAFETY:

- BASEEFA BS 5501 ; Part 7 (CENELEC EN 50020) certificate no. Ex 85B2245 EEx ia IIC T4 (Tamb 90°C)/T6 (Tamb 40°C)
- SAA AS 2980.1 - 1985 and 2980.7 - 1987 Certificate no. Ex 896 Ex Ia IIC T6 for use in Class 1, Zone 0

TYPE N PROTECTION:

- BASEEFA BS 4683:3:1972 for use in Zone 2 Areas certificate no. Ex 85243 Ex N II T4 (Tamb 90°C) / T6 (Tamb 40°C)

FLAMEPROOF:

- LCIE NFC 23518 (CENELEC EN 50018) certificate no. 87.B6084 EEx d IIC T5 (Tamb 90°C)/T6(Tamb 70°C).

Process connection

On process flange: 1/4 NPT.

On adapter: 1/2 14 NPT.

Electrical connections

- Standard: two 1/2 NPT threaded conduit entries.
- Optional: one M20x1.5 or PG 13.5 metric adaptor and one 1/2 NPT plug suitable for explosion proof installations.

Terminal block

- Standard : two terminals for signal wiring up to 2.5 mm² (14 AWG) and two terminals for remote or built-in indicator or in-process checks. Cable shield connection terminal is provided.
- Optional: two additional terminals for remote indicator wiring up to 2.5 mm² (14 AWG) and two test jacks (40 - 200 mV) compatible with 2 mm dia miniature plugs.

Grounding

Internal and external 6 mm² (10 AWG) ground termination points are provided.

Mounting position

Any, with sensing diaphragm vertical. Electronics housing may be rotated to any position. A positive stop prevents over travel.

Mass

5.8 kg approx (12.8 lbs) without options.

Packing

Expanded polythene box.

Instrument code list

See publication C, 15.1E3

ϕ Hastelloy is a Cabot Corporation trademark
 ϕ Monel is an International Nickel Co. trademark
 ϕ Galden is a Montellus trademark
 ϕ Viton is a Dupont de Nemour trademark
 ϕ 17-4-PH is an Armco Steel Corp. trademark

(*) Wetted parts of the transmitter
 (***) As standard the drain/vent valve is fitted on side top of process flange and plug on process connection axis. Plug is of same material as requested drain/vent valve.
 (****) U-bolt material: AISI 400 ss. screws material: high-strength alloy steel or AISI 304 ss.

3-YEAR WARRANTY

The Company warrants the Deltapi K Series of transmitters of its own manufacture to be free from defects in materials and workmanship under normal conditions of use. Authorized Taylor Representatives worldwide will either replace or repair free of charge any instrument found to be defective within the warranty period. Responsibility for application, material selection

PERFORMANCE SPECIFICATIONS

Unless otherwise stated performance specifications are given at reference operating conditions and zero based range for transmitter with isolating diaphragm in AISI 316 L ss and Silicone oil fill.

Test procedures and operating influences are in accordance with relevant IEC and SAMA standards.

Unless otherwise modified, all errors are quoted as percentages of output span.

Total effect is the maximum effect (zero and span shifts) at any point in the calibrated range.

Accuracy

Accuracy rating (*):

- for sensors J, K, L, M : $\pm 0.25\%$ ($\pm 0.20\%$ on application) of calibrated span

- for sensors N, P : $\pm 0.30\%$ ($\pm 0.25\%$ on application) of calibrated span

Independent linearity:

- for sensors J, K, L, M : $\pm 0.10\%$

- for sensors N, P : $\pm 0.20\%$

Repeatability: $<0.05\%$

Hysteresis:

- for sensors J, K, L, M : $\leq 0.10\%$

- for sensors N, P : $\leq 0.15\%$

Dead band: negligible

(*) Includes combined effects of terminal based linearity, hysteresis and repeatability

Operating influences

Ambient temperature per 10 K (18°F) change between the limits of -25°C and +85°C (-13 to +185 °F)

- on zero : $\pm 0.10\%$ of URL

- on span : $\pm 0.10\%$ of reading

Overrange

Total effect: $\pm 0.50\%$ of URL for 16 MPa, 160 bar or 2320 psi.

Supply voltage

Within voltage/load specified limits the total effect is less than 0.01%/V.

Load

Within load/voltage specified limits the total effect from 0 to max. load is less than 0.1%.

Warm-up

No effect per 10% and 90% input after 5min., 1h and 4h.

EMI/RFI

Total effect : $\pm 0.10\%$ from 20 to 1000 MHz and for field strengths up to 10 V/m when instrument is properly installed with or without output meter.

Humidity: $\pm 0.05\%$ @ +40 °C (104°F) and 92% RH per 12 hours

Vibration

Total effect from 1 to 500 Hz and acceleration up to 20 m/s² (2g) in any axis:

- for sensors L, M, N, P : $\pm 0.05\%$

- for sensor K : $\pm 0.10\%$

- for sensor J : $\pm 0.15\%$

DC magnetic field effect at 0 and 100% input up to 50 Gauss (5 mTesla)

- zero shift: less than 0.1%

- span shift: less than 0.1%

Effect on calibration after a long term exposure at more than 1300 Gauss (130 mTesla) : negligible.

Common mode interference

No effect from 100 V rms @ 50 Hz, or 50 Vdc

Series mode interference

No effect from 1 V rms @ 50 Hz

Mounting position

Rotations in plane of diaphragm have no effect.

A tilt to 90° from vertical causes maximum zero shifts of :

- 0.2 kPa, 2 mbar or 1.5 mmHg for sensors L, M, N, P

- 0.4 kPa, 4 mbar or 3 mmHg for sensor K

- 0.5 kPa, 5 mbar or 3.75 mmHg for sensor J

which can be corrected with the zero adjustment.

Output meter

Indication accuracy:

$\pm 1.5\%$ fsd, 90 mm scale

$\pm 2\%$ fsd, 36 mm scale

Stability

$\pm 0.15\%$ of URL over a six-month period.



National
Semiconductor
Corporation

LM35/LM35A/LM35C/LM35CA/LM35D Precision Centigrade Temperature Sensors

General Description

The LM35 series are precision integrated-circuit temperature sensors, whose output voltage is linearly proportional to the Celsius (Centigrade) temperature. The LM35 thus has an advantage over linear temperature sensors calibrated in $^{\circ}$ Kelvin, as the user is not required to subtract a large constant voltage from its output to obtain convenient Centigrade scaling. The LM35 does not require any external calibration or trimming to provide typical accuracies of $\pm 1/2^{\circ}\text{C}$ at room temperature and $\pm 3/4^{\circ}\text{C}$ over a full -55 to $+150^{\circ}\text{C}$ temperature range. Low cost is assured by trimming and calibration at the wafer level. The LM35's low output impedance, linear output, and precise inherent calibration make interfacing to readout or control circuitry especially easy. It can be used with single power supplies, or with plus and minus supplies. As it draws only $60\ \mu\text{A}$ from its supply, it has very low self-heating, less than 0.1°C in still air. The LM35 is rated to operate over a -55° to $+150^{\circ}\text{C}$ temperature range, while the LM35C is rated for a -40° to $+110^{\circ}\text{C}$ range (-10° with improved accuracy). The LM35 series is

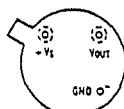
available packaged in hermetic TO-46 transistor packages, while the LM35C is also available in the plastic TO-92 transistor package.

Features

- Calibrated directly in $^{\circ}$ Celsius (Centigrade)
- Linear $+10.0\ \text{mV}/^{\circ}\text{C}$ scale factor
- 0.5°C accuracy guaranteeable (at $+25^{\circ}\text{C}$)
- Rated for full -55° to $+150^{\circ}\text{C}$ range
- Suitable for remote applications
- Low cost due to wafer-level trimming
- Operates from 4 to 30 volts
- Less than $60\ \mu\text{A}$ current drain
- Low self-heating, 0.08°C in still air
- Nonlinearity only $\pm 1/2^{\circ}\text{C}$ typical
- Low impedance output, $0.1\ \Omega$ for 1 mA load

Connection Diagrams

TO-46
Metal Can Package*



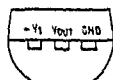
BOTTOM VIEW

TL/H/5516-1

*Case is connected to negative pin

Order Number LM35H, LM35AH,
LM35CH, LM35CAH or LM35DCH
See NS Package Number H03H

TO-92
Plastic Package

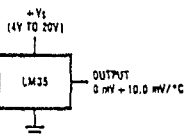


BOTTOM VIEW

TL/H/5516-2

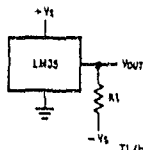
Order Number LM35CZ or LM35DZ
See NS Package Number Z03A

Typical Applications



TL/H/5516-3

FIGURE 1. Basic Centigrade Temperature Sensor ($+2^{\circ}\text{C}$ to $+150^{\circ}\text{C}$)



TL/H/5516-4

Choose $R_1 = -V_S/50\ \mu\text{A}$

$V_{\text{OUT}} = +1,500\ \text{mV}$ at $+150^{\circ}\text{C}$
 $= +250\ \text{mV}$ at $+25^{\circ}\text{C}$
 $= -550\ \text{mV}$ at -55°C

FIGURE 2. Full-Range Centigrade Temperature Sensor

Absolute Maximum Ratings (Note 1)

Military/Aerospace specified devices are required, contact the National Semiconductor Sales Office/Distributors for availability and specifications.

Supply Voltage	+35V to -0.2V
Input Voltage	+6V to -1.0V
Output Current	10 mA
Storage Temp., TO-46 Package,	-60°C to +180°C
TO-92 Package,	-50°C to +150°C
Solder Temp. (Soldering, 10 seconds):	
TO-46 Package,	300°C
TO-92 Package,	260°C

Specified Operating Temperature Range: T_{MIN} to T_{MAX} (Note 2)

LM35, LM35A	-55°C to +150°C
LM35C, LM35CA	-40°C to +110°C
LM35D	0°C to +100°C

Electrical Characteristics (Note 1) (Note 3)

Parameter	Conditions	LM35A			LM35CA			Units (Max.)
		Typical	Tested Limit (Note 4)	Design Limit (Note 5)	Typical	Tested Limit (Note 4)	Design Limit (Note 5)	
Accuracy (9.7)	$T_A = -25^\circ\text{C}$	± 0.2	± 0.5		± 0.2	± 0.5	± 1.0	$^\circ\text{C}$
	$T_A = -10^\circ\text{C}$	± 0.3			± 0.3		± 1.0	$^\circ\text{C}$
	$T_A = T_{MAX}$	± 0.4	± 1.0		± 0.4	± 1.0	± 1.5	$^\circ\text{C}$
	$T_A = T_{MIN}$	± 0.4	± 1.0		± 0.4		± 1.5	$^\circ\text{C}$
Linearity (9.8)	$T_{MIN} \leq T_A \leq T_{MAX}$	± 0.18		± 0.35	± 0.15		± 0.3	$^\circ\text{C}$
Load Regulation (Slope)	$T_{MIN} \leq T_A \leq T_{MAX}$	-10.0	$-9.9,$ -10.1		-10.0		$-9.9,$ $+10.1$	mV/ $^\circ\text{C}$
Line Regulation (9.10) $I_L \leq 1 \text{ mA}$	$T_A = -25^\circ\text{C}$	± 0.4	± 1.0		± 0.4	± 1.0	± 3.0	mV/mA
	$T_{MIN} \leq T_A \leq T_{MAX}$	± 0.5		± 3.0	± 0.5		± 3.0	mV/mA
Voltage Regulation (9.11)	$T_A = -25^\circ\text{C}$	± 0.01	± 0.05		± 0.01	± 0.05		mV/V
	$4V \leq V_S \leq 30V$	± 0.02		± 0.1	± 0.02		± 0.1	mV/V
Quiescent Current (9.9)	$V_S = -5V, +25^\circ\text{C}$	56	67	131	56	67	114	μA
	$V_S = -5V$	105			91			μA
	$V_S = -30V, +25^\circ\text{C}$	56.2	68	133	56.2	68	116	μA
	$V_S = -30V$	105.5			91.5			μA
Line Regulation of Quiescent Current (9.13)	$4V \leq V_S \leq 30V, -25^\circ\text{C}$	0.2	1.0	2.0	0.2	1.0	2.0	μA
	$4V \leq V_S \leq 30V$	0.5			0.5			μA
Temperature Coefficient of Quiescent Current		$+0.39$		$+0.5$	-0.39		-0.5	$\mu\text{A}/^\circ\text{C}$
Maximum Temperature Rated Accuracy	In circuit of Figure 1, $I_L = 0$	$+1.5$		$+2.0$	$+1.5$		-2.0	$^\circ\text{C}$
Long Term Stability	$T_J = T_{MAX}$, for 1000 hours	± 0.08			± 0.08			$^\circ\text{C}$

Note 1: Unless otherwise noted, these specifications apply: $-55^\circ\text{C} \leq T_J \leq +150^\circ\text{C}$ for the LM35 and LM35A, $-40^\circ\text{C} \leq T_J \leq +110^\circ\text{C}$ for the LM35C and LM35CA, and $0^\circ\text{C} \leq T_J \leq +100^\circ\text{C}$ for the LM35D. $V_S = +5\text{Vdc}$ and $I_{LOAD} = 50 \mu\text{A}$, in the circuit of Figure 2. These specifications also apply from -2°C to T_{MAX} in the circuit of Figure 1. Specifications in boldface apply over the full rated temperature range.

Note 2: Thermal resistance of the TO-46 package is $44^\circ\text{C}/\text{W}$, junction to ambient, and $24^\circ\text{C}/\text{W}$, junction to case. Thermal resistance of the TO-92 package is $10^\circ\text{C}/\text{W}$, junction to ambient.

Applications

The LM35 can be applied easily in the same way as other integrated-circuit temperature sensors. It can be glued or cemented to a surface and its temperature will be within about 0.01°C of the surface temperature.

This presumes that the ambient air temperature is almost the same as the surface temperature; if the air temperature were much higher or lower than the surface temperature, the actual temperature of the LM35 die would be at an intermediate temperature between the surface temperature and the air temperature. This is especially true for the TO-92 plastic package, where the copper leads are the principal thermal path to carry heat into the device, so its temperature might be closer to the air temperature than to the surface temperature.

To minimize this problem, be sure that the wiring to the LM35, as it leaves the device, is held at the same temperature as the surface of interest. The easiest way to do this is to cover up these wires with a bead of epoxy which will insure that the leads and wires are all at the same temperature as the surface, and that the LM35 die's temperature will not be affected by the air temperature.

The TO-46 metal package can also be soldered to a metal surface or pipe without damage. Of course, in that case the V- terminal of the circuit will be grounded to that metal. Alternatively, the LM35 can be mounted inside a sealed and metal lube, and can then be dipped into a bath or screwed into a threaded hole in a tank. As with any IC, the LM35 and accompanying wiring and circuits must be kept insulated and dry, to avoid leakage and corrosion. This is especially true if the circuit may operate at cold temperatures where condensation can occur. Printed-circuit coatings and varnishes such as Humiseal and epoxy paints or dips are often used to insure that moisture cannot corrode the LM35 or its connections.

These devices are sometimes soldered to a small lightweight heat fin, to decrease the thermal time constant and speed up the response in slowly-moving air. On the other hand, a small thermal mass may be added to the sensor, to give the steadiest reading despite small deviations in the air temperature.

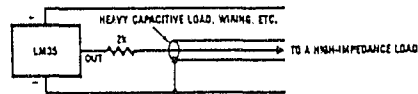
Temperature Rise of LM35 Due To Self-heating (Thermal Resistance)

	TO-46, no heat sink	TO-46, small heat fin*	TO-92, no heat sink	TO-92, small heat fin**
Still air	400°C/W	100°C/W	180°C/W	140°C/W
Moving air	100°C/W	40°C/W	90°C/W	70°C/W
Still oil	100°C/W	40°C/W	90°C/W	70°C/W
Stirred oil	50°C/W	30°C/W	45°C/W	40°C/W
(Clamped to metal, Infinite heat sink)	(24°C/W)			

* Wakefield type 201, or 1" disc of 0.020" sheet brass, soldered to case, or similar.

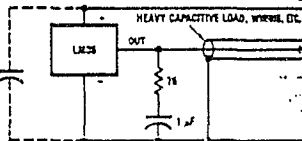
** TO-92 package glued and leads soldered to 1" square of $\frac{1}{16}$ " printed circuit board with 2 oz. foil or similar.

Typical Applications (Continued)



TL/H/5516-10

FIGURE 3. LM35 with Decoupling from Capacitive Load



TL/H/5516-11

FIGURE 4. LM35 with R-C Damper

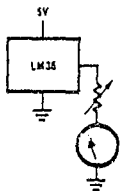
CAPACITIVE LOADS

Like most micropower circuits, the LM35 has a limited ability to drive heavy capacitive loads. The LM35 by itself is able to drive 50 pF without special precautions. If heavier loads are anticipated, it is easy to isolate or decouple the load with a resistor; see Figure 3. Or you can improve the tolerance of capacitance with a series R-C damper from output to ground; see Figure 4.

When the LM35 is applied with a 200Ω load resistor as shown in Figure 5, 6, or 8, it is relatively immune to wiring

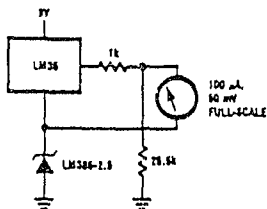
capacitance because the capacitance forms a bypass from ground to input, not on the output. However, as with any linear circuit connected to wires in a hostile environment, its performance can be affected adversely by intense electromagnetic sources such as relays, radio transmitters, motors with arcing brushes, SCR transients, etc., as its wiring can act as a receiving antenna and its internal junctions can act as rectifiers. For best results in such cases, a bypass capacitor from V_{IN} to ground and a series R-C damper such as 75Ω in series with 0.2 or 1 μF from output to ground are often useful. These are shown in Figures 13, 14, and 16.

Typical Applications (Continued)

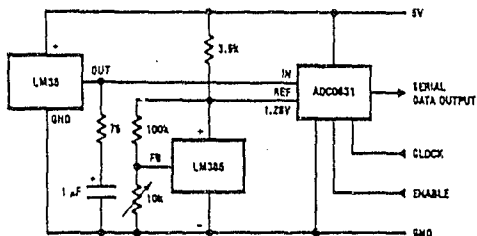


TL/H/5516-11

FIGURE 11. Centigrade Thermometer (Analog Meter)

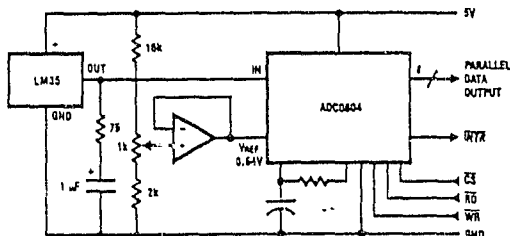


TL/H/5516-12

FIGURE 12. Expanded Scale Thermometer
(50° to 80° Fahrenheit, for Example Shown)

TL/H/5516-13

FIGURE 13. Temperature To Digital Converter (Serial Output) (+128°C Full Scale)



TL/H/5516-14

FIGURE 14. Temperature To Digital Converter (Parallel TRI-STATE® Outputs for
Standard Data Bus to μP Interface) (128°C Full Scale)

F

APPENDIX F
EXPERIMENTAL RESULTS

F1.1

F 1

Through-Flow evaporator Results

0.0245 kg/s Results F_{12} averaged

TIN	QFLOW	T1	T4	Tbout	PEV1	t3
12.591	0.000023	6.568	4.01	2.97	0.8691	5.38
12.558	0.000023	6.67	4.213	3.01	0.8137	5.5
12.545	0.000023	5.684	3.262	2.19	0.8119	4.287
12.51	0.000023	6.3184	3.617	2.47	0.8057	5.058
12.47	0.000023	5.728	3.264	2	0.7094	4.36
12.485	0.000023	4.365	2.084	1.45	0.8095	3.198
12.4566	0.000023	5.731	3.063	1.98	0.7887	4.51
12.451	0.000023	5.649	3.394	1.94	0.6956	4.422
12.433	0.000023	2.09	0.749	-0.5	0.5799	0.435
12.44	0.000023	1.52	0.453	-0.7	0.5748	0.045
13.9	2.45E-05	1.12	0.42	-0.4	0.5732	0.05
13.9	2.45E-05	1.11	0.48	-0.5	0.5645	0.04
13.86	2.45E-05	1.21	0.4	-0.6	0.5713	0.02
13.86	2.45E-05	1.2	0.39	-0.6	0.5654	0.02
13.85	2.45E-05	1.1	0.33	-0.7	0.5629	0.02
13.85	2.45E-05	1.1	0.44	-0.5	0.573	0.08
13.84	2.45E-05	1.12	0.34	-0.7	0.5578	0.04
13.85	2.45E-05	2.04	0.51	0.21	0.7122	0.75
13.83	2.45E-05	4.59	1.92	1.62	0.8095	3.7
13.87	2.45E-05	5.83	3.49	2.59	0.859	4.93
13.87	2.45E-05	6.79	4.22	3.56	0.8675	6.02
13.89	2.45E-05	6.67	4	3.11	0.8229	5.65
21.98	2.27E-05	1.43	0.54	-0.3	0.5724	0.03
15.86	2.27E-05	1.43	0.6	-0.2	0.5178	0.05
15.86	2.27E-05	1.45	0.68	-0.2	0.5134	0.14
15.85	2.27E-05	1.53	0.66	-0.2	0.5773	0.03
15.86	2.27E-05	1.46	0.7	-0.2	0.573	0.12
15.84	2.27E-05	1.51	0.63	-0.3	0.5092	0.03
15.85	2.27E-05	1.36	0.57	-0.3	0.5777	0.06
15.84	2.27E-05	1.33	0.63	-0.2	0.5756	0.07
15.8	2.27E-05	1.5	0.72	-0.2	0.5753	0.1
15.81	2.27E-05	1.54	0.65	-0.2	0.5769	0.03
15.81	2.27E-05	1.59	0.68	-0.1	0.5772	0.07
17.5	2.34E-05	1.74	0.74	0.05	0.5828	0.23
17.49	2.34E-05	1.82	0.78	0.08	0.5845	0.27
17.5	2.34E-05	1.66	0.73	-0.1	0.5802	0.15
17.5	2.34E-05	1.55	0.74	-0.1	0.5725	0.09
17.5	2.34E-05	1.62	0.74	0.05	0.586	0.16
17.49	2.34E-05	1.85	0.76	0.05	0.5827	0.24
17.54	2.34E-05	1.69	0.75	0.04	0.5855	0.19
17.52	2.34E-05	1.82	0.78	0.27	0.5894	0.37
17.54	2.34E-05	1.8	0.8	0.21	0.5878	0.372
18.36	2.85E-05	2.27	1.11	0.54	0.5978	0.58

F 1.3

19.25	2.85E-05	2.32	F 1.31	0.53	0.5996	0.5
19.25	2.85E-05	2.15	1.12	0.56	0.5954	0.66
19.22	2.85E-05	2.1	1.09	0.52	0.5958	0.53
19.22	2.85E-05	2.06	1.08	0.53	0.5951	0.5
19.14	2.85E-05	2.3	1.05	0.54	0.5993	0.55
19.11	2.85E-05	2.24	1.03	0.55	0.5985	0.48
19.11	2.85E-05	2.16	1.07	0.57	0.6043	0.55
19.07	2.85E-05	2.35	1.19	0.58	0.5982	0.7
19.06	2.85E-05	2.15	1.09	0.52	0.5957	0.55
19.05	2.85E-05	2.11	1.07	0.53	0.5923	0.58
21.89	2.44E-05	2.96	1.644	1.06	0.6165	1.25
21.72	2.44E-05	2.87	1.58	1	0.6136	1.161
21.65	2.44E-05	2.83	1.59	1.05	0.6254	1.2
21.64	2.44E-05	2.98	1.7	1.14	0.6197	1.39
21.622	2.44E-05	2.81	1.63	1.04	0.6261	1.25
20.66	2.44E-05	2.83	1.6	1.06	0.6186	1.22
20.63	2.44E-05	2.8	1.6	1.03	0.6152	1.19
20.62	2.44E-05	2.84	1.57	1.03	0.6144	1.14
20.61	2.44E-05	2.73	1.57	1.03	0.6202	1.17
20.58	2.44E-05	2.74	1.57	1.01	0.6138	1.14
24.98	2.38E-05	3.45	2.18	1.57	0.6438	1.95
24.81	2.38E-05	3.48	2.15	1.49	0.6341	1.82
24.68	2.38E-05	3.68	2.23	1.86	0.6581	2.26
24.69	2.38E-05	3.52	2.27	1.65	0.6491	2.04
24.54	2.38E-05	3.36	2.08	1.42	0.6387	1.744
24.51	2.38E-05	3.26	2.07	1.44	0.6358	1.75
24.42	2.38E-05	3.48	2.23	1.66	0.651	2.01
24.24	2.38E-05	3.35	2.16	1.42	0.6356	1.79
24.16	2.38E-05	3.24	2.06	1.43	0.6366	1.73
24.05	2.38E-05	3.33	2.05	1.36	0.6394	1.71
32	2.49E-05	6.69	5.06	4.34	0.7652	5.37
34.3	2.49E-05	5.99	4.25	3.83	0.7351	4.51
34.6	2.49E-05	5.76	4.16	3.92	0.7366	4.44
34.8	2.49E-05	5.76	4.17	3.93	0.7556	4.51
34.9	2.49E-05	5.78	4.15	3.82	0.7373	4.34
35.1	2.49E-05	5.81	4.15	3.82	0.7377	4.39
34.9	2.49E-05	5.5	4.05	3.75	0.7398	4.2
24.3	2.49E-05	3.55	2.16	1.61	0.6453	1.94
34.6	2.49E-05	5.49	4.02	3.7	0.7257	4.16
34.5	2.49E-05	5.31	3.86	3.6	0.721	3.95
34	2.49E-05	5.24	3.71	3.4	0.7147	3.8
33.9	2.49E-05	5.2	3.66	3.39	0.7247	3.75
33.8	2.49E-05	5.04	3.61	3.4	0.7178	3.71
33.6	2.49E-05	5.12	3.61	3.32	0.7086	3.7
33.5	2.49E-05	4.99	3.54	3.27	0.7065	3.65
33.3	2.49E-05	4.95	3.49	3.25	0.7082	3.61

F1.4
0.0584 kg/s Results Averaged

TIN	QFLOW	T1	T4	Tbout	PEV1	t3
7.6	5.95E-05	1.66	1.14	0.09		0.55
7.6	5.95E-05	1.4	0.9	-0.11		0.31
7.6	5.95E-05	1.27	0.87	-0.14		0.3
7.6	5.95E-05	1.18	0.83	-0.19		0.233
7.6	5.95E-05	1.37	0.86	-0.34	0.995	0.23
7.6	5.95E-05	1.27	0.79	-0.3	0.992	0.17
7.6	5.95E-05	1.11	0.84	-0.25	0.985	0.16
7.6	5.95E-05	1.1	0.79	-0.3	0.983	0.138
7.6	5.95E-05	1.21	0.78	-0.33	0.985	0.14
7.6	5.95E-05	1.19	0.79	-0.27	0.976	0.1
10.5	5.85E-05	2.18	1.51	0.66	0.991	1.1
10.5	5.85E-05	2.27	1.51	0.64	0.961	1.05
10.5	5.85E-05	2.24	1.5	0.63	0.962	1.03
10.5	5.85E-05	2.23	1.48	0.59	0.948	1.02
10.5	5.85E-05	2.1	1.48	0.64	0.951	1.03
10.5	5.85E-05	2.26	1.45	0.61	0.94	1.07
10.5	5.85E-05	2.12	1.5	0.65	0.926	1.06
10.5	5.85E-05	2.21	1.47	0.64	0.928	1.06
10.5	5.85E-05	2.21	1.49	0.66	0.93	1
10.5	5.85E-05	2	1.48	0.68	0.927	1.022
9.93	5.85E-05	1.68	1.29	0.41	0.84	0.74
9.83	5.85E-05	1.74	1.25	0.36	0.833	0.632
9.76	5.85E-05	1.66	1.24	0.37	0.821	0.733
9.72	5.85E-05	1.76	1.25	0.38	0.819	0.67
9.71	5.85E-05	1.677	1.26	0.39	0.812	0.7011
9.77	5.85E-05		1.28	0.39	0.815	0.664
9.76	5.85E-05		1.25	0.32	0.813	0.648
9.71	5.85E-05	1.76	1.22	0.24	0.808	0.641
9.8	5.85E-05	1.7	1.23	0.29	0.799	0.766
9.75	5.85E-05	1.78	1.22	0.211	0.785	0.634
8.23	5.85E-05	0.61	0.68	-0.62	0.724	0.02
8.18	5.85E-05	0.76	0.65	-0.66	0.719	0.01
8.16	5.85E-05	0.57	0.62	-0.76	0.718	0.02
8.24	5.85E-05	0.64	0.72	-0.61	0.707	0.03
8.23	5.85E-05	0.81	0.65	-0.5	0.695	0.02
8.24	5.85E-05	0.72	0.71	-0.67	0.694	0.03
8.23	5.85E-05	0.81	0.67	-0.66	0.684	0
8.21	5.85E-05	0.74	0.6	-0.76	0.684	0.02
8.24	5.85E-05	0.54	0.61	-0.74	0.674	0.02
8.24	5.85E-05	0.55	0.6	-0.75	0.681	0.024
8.22	5.85E-05	0.722	0.57	-0.79	0.675	0.0013
15.28	5.85E-05	4.19	3.23	2.53	0.765	3.11
15.29	5.85E-05	4.09	3.24	2.52	0.766	3.13

F 1.5

15.31	5.85E-05	4.08	3.15	2.47	0.761	3.04
15.29	5.85E-05	4.13	3.15	2.43	0.756	
15.3	5.85E-05	4.05	3.15	2.44	0.733	
15.28	5.85E-05	3.99	3.15	2.43	0.741	
15.24	5.85E-05	4.12	3.12	2.39	0.741	
15.23	5.85E-05	4.1	3.1	2.36	0.738	
15.25	5.85E-05	3.93	3.09	2.37	0.745	
15.23	5.85E-05	4.09	3.11	2.35	0.671	
14.22	5.85E-05	3.56	2.69	1.83	0.682	
14.26	5.85E-05	3.62	2.67	1.8	0.679	
14.27	5.85E-05	3.6	2.68	1.86	0.664	
14.27	5.85E-05	3.53	2.7	1.83	0.683	
14.26	5.85E-05	3.54	2.69	1.82	0.675	
14.22	5.85E-05	3.65	2.65	1.81	0.675	
14.22	5.85E-05	3.62	2.66	1.8	0.664	
14.22	5.85E-05	3.52	2.68	1.82	0.665	
14.23	5.85E-05	3.52	2.69	1.83	0.669	
14.16	5.85E-05	3.6	2.66	1.79	0.658	
19.84	5.85E-05	5.99	4.36	3.89	0.739	
19.84	5.85E-05	5.76	4.39	3.93	0.748	
19.84	5.85E-05	5.71	4.37	3.93	0.742	
19.3	5.85E-05	5.78	4.3	3.88	0.736	
19.81	5.85E-05	5.72	4.39	3.96	0.735	
19.77	5.85E-05	5.71	4.4	3.95	0.736	
19.74	5.85E-05	5.8	4.38	3.95	0.74	
19.7	5.85E-05	5.8	4.36	3.93	0.733	
19.65	5.85E-05	5.84	4.31	3.91	0.742	
19.6	5.85E-05	5.8	4.31	3.9	0.734	
19.57	5.85E-05	5.78	4.3	3.9	0.733	
17.37	5.71E-05	5.23	3.96	3.28	0.703	
17.35	5.71E-05	4.91	3.72	3.15	0.699	
17.33	5.71E-05	4.85	3.66	3.1	0.699	
17.32	5.71E-05	4.78	3.64	3.08	0.698	
17.26	5.71E-05	4.97	3.58	3.06	0.704	
17.26	5.71E-05	4.82	3.63	3.06	0.697	
17.24	5.71E-05	4.87	3.58	3.05	0.7	
17.22	5.71E-05	4.84	3.57	3.06	0.694	
17.22	5.71E-05	4.75	3.61	3.09	0.696	
17.11	5.71E-05	4.83	3.57	3.07	0.697	
17.14	5.71E-05	4.83	3.6	3.06	0.693	

5.84E-05

F1.6
0.0671 kg/s Results Averaged

TIN	QFLOW	T1	T4	Tbout	PEV1
12.28	6.3E-05	6.594	2.972	1.845	0.62646
12.31	6.3E-05	6.703	2.973	1.853	0.629
12.31	6.3E-05	6.673	2.987	1.8389	0.6258
12.26	6.3E-05	6.718	2.977	1.833	0.6265
12.28	6.3E-05	6.53	2.965	1.824	0.62702
12.3	6.3E-05	6.66	2.987	1.82	0.6267
12.3	6.3E-05	6.75	2.98	1.8046	0.6258
12.3	6.3E-05	6.843	3.124	2.1897	0.6279
12.27	6.3E-05	6.478	2.444	2.444	0.6313
12.3	6.3E-05	6.7598	2.9789	1.8638	0.6283
12.28	6.3E-05	6.718	2.992	1.6327	0.6253
14.27	6.5E-05	7.271	4.066	3.476	0.6691
14.27	6.5E-05	7.364	4.0578	3.473	0.671
14.24	6.5E-05	7.287	4.0708	3.48	0.6695
14.91	6.5E-05	7.171	4.063	3.5049	0.6694
14.9	6.5E-05	7.3	4.05	3.471	0.6695
14.89	6.5E-05	7.284	4.051	3.478	0.6685
14.92	6.5E-05	7.171	4.064	3.47	0.668
14.26	6.5E-05	7.2545	4.064	3.4904	0.6693
14.27	6.5E-05	7.2319	4.056	3.511	0.66868
14.79	6.5E-05	7.2988	4.06	3.503	0.6705
14.93	6.5E-05	7.236	4.054	3.497	0.6682
20.79	7.3E-05	8.157	6.4822	5.987	0.7771
20.88	7.3E-05	7.861	6.517	6.012	0.7818
20.92	7.3E-05	7.58	6.544	6.072	0.7827
20.86	7.3E-05	8.151	6.515	6	0.7795
20.85	7.3E-05	8.01	6.509	6	0.7804
21.19	7.3E-05	8.09	6.645	6.1907	0.7888
21.11	7.3E-05	8.25	6.604	6.124	0.7862
21.03	7.3E-05	8.292	6.585	6.0828	0.7887
20.98	7.3E-05	7.976	6.569	6.124	0.7843
24.27	6.6E-05	8.443	7.737	7.648	0.8415
24.19	6.6E-05	8.592	7.712	7.589	0.84468
24.16	6.6E-05	8.555	7.704	7.59	0.84115
24.53	6.6E-05	8.8756	7.784	7.69	0.8447
24.49	6.6E-05	8.9485	7.788	7.662	0.8462
24.39	6.6E-05	8.762	7.767	7.6758	0.843
24.29	6.6E-05	8.63	7.712	7.635	0.8441
24.8	6.6E-05	9.21	7.867	7.765	0.8525
24.69	6.6E-05	8.96	7.873	7.72	0.8478
24.65	6.6E-05	9.31	7.832	7.72	0.8468
24.57	6.6E-05	8.96	7.811	7.68	0.8469
15.88	6.9E-05	7.075	4.541	4	0.69739

F 1.7

15.99	6.9E-05	6.886	F4.75	3.998	0.6954
15.99	6.9E-05	6.821	4.585	4.033	0.697
15.97	6.9E-05	7.041	4.595	4.013	0.6979
15.93	6.9E-05	7.034	4.577	4.042	0.6976
15.91	6.9E-05	5.973	3.87	3.803	0.689
15.98	6.9E-05	6.568	4.222	3.884	0.6951
16.01	6.9E-05	6.539	4.468	3.998	0.6948
16.02	6.9E-05	6.75	4.535	4.027	0.6977

F2.1

F 2 Vertical Cylinder Results

The following figure shows a sample of data recorded during vertical cylinder testing:

```
Title: vert-26/08/94
ENABLED CHANNELS: 1,2,3,4,5,7,8,A,B,C,D,E,F
SAMPLING TIME: 200 mSec
TOTAL SAMPLES: 128
SAMPLES COLLECTED: 128

+0.000 +0.000 +0.000 +0.000 +0.000 +0.000 +0.000 +0.000 +0.000 +0.000 +0.000 +0.000
+0.000
+0.234 +0.258 +0.156 +0.200 +0.175 +0.195 -2.978 +2.255 +0.507 +2.221 +2.275 +2.192
+9.995
+0.239 +0.258 +0.151 +0.200 +0.175 +0.195 -3.037 +2.255 +0.517 +2.216 +2.275 +2.192
+9.995
+0.239 +0.258 +0.151 +0.200 +0.175 +0.195 -2.890 +2.250 +0.517 +2.226 +2.275 +2.187
+9.995
+0.234 +0.258 +0.156 +0.200 +0.170 +0.195 -2.988 +2.255 +0.527 +2.221 +2.275 +2.182
```

Figure F.1 : Typical raw data from the computerscope.

These raw data were imported into a spreadsheet package and the calibration formulae presented in Appendix E applied. Sample calculations of temperature profiles, saturation and hydrostatic pressure, NEF(t) are presented below.

Raw data : 40°C initial water temperature, 15 cm column height Test 1

T bulk (t₀) = 40.905 °C

T evap (t₀) = 0.2639 °C as P evap (t₀) = 0.62023 kPa abs

T 21 cm	T 15 cm	T 9 cm	T 6 cm	T 3 cm	T 0 cm	P evap
1.503	1.508	1.567	1.506	1.572	1.582	-6.25
1.479	1.489	1.545	1.489	1.557	1.567	-5.81
1.464	1.469	1.528	1.469	1.533	1.547	-5.484
1.43	1.44	1.499	1.445	1.503	1.528	-5.117
1.396	1.406	1.469	1.42	1.479	1.506	-4.897
1.367	1.372	1.445	1.391	1.455	1.489	-4.716

F2.2

Temperature profiles

Column1:

$$T_{21 \text{ cm (1)}} = 0.7 \cdot 25,062 (1.503 \cdot 1.009 - 0.0037) + 0.1311 (1.503 \cdot 1.009 - 0.037)^2 \\ = 40.803 \text{ }^\circ\text{C}$$

$$T_{21 \text{ cm (2)}} = 0.7 \cdot 25,062 (1.478 \cdot 1.009 - 0.0037) + 0.1311 (1.478 \cdot 1.009 - 0.037)^2 \\ = 40.803 \text{ }^\circ\text{C}$$

etc....

$$P_{\text{evap (1)}} = (-(-6.25 \cdot 4) + 0.4108) / (1,873 - 0.4108)^2 \\ = 1.5753 \text{ kPa}$$

$$P_{\text{evap (2)}} = (-(-5.81 \cdot 4) + 0.4108) / (1,873 - 0.4108)^2 \\ = 1.4248 \text{ kPa}$$

Tabulated results:

T 21 cm	T 15 cm	T 9 cm	T 6 cm	T 3 cm	T 0 cm
38.91	37.84	40.34	39.27	40.19	41.05
38.30	37.35	39.70	38.78	39.82	40.67
37.91	36.83	39.33	38.26	39.21	40.15
37.04	36.09	38.62	37.64	38.46	39.66
36.17	35.22	37.86	36.99	37.85	39.15
35.42	34.34	37.25	36.24	37.25	38.66

NEF

$$NEF = \frac{(T_{15} + T_9) + (T_9 + T_6)/2 + (T_6 + T_3)/2 + (T_3 + T_0)/2}{5} - T_{\text{evap, air}}$$

$$NEF (1) = \frac{(37.84 + 40.34) + (37.84 + 40.34)/2 + (39.27 + 40.19)/2 + (40.19 + 41.05)/2}{5} - 0.2639$$

$$= 0.96951$$

The results presented are grouped in terms of liquid height and ordered in terms of initial temperature.

List of Results:

5°C initial temperature test 1
 5°C initial temperature test 2
 5°C initial temperature test 3
 5°C initial temperature test 4
 13°C initial temperature test 1
 13°C initial temperature test 2
 13°C initial temperature test 3
 19°C initial temperature test 1
 19°C initial temperature test 2
 19°C initial temperature test 3
 19°C initial temperature test 4
 40°C initial temperature test 1
 40°C initial temperature test 2
 40°C initial temperature test 3

5°C initial temperature test 1
 5°C initial temperature test 2
 5°C initial temperature test 3
 13°C initial temperature test 1
 13°C initial temperature test 2
 13°C initial temperature test 3
 19°C initial temperature test 1
 19°C initial temperature test 2
 19°C initial temperature test 3
 25°C initial temperature test 1
 25°C initial temperature test 2
 35°C initial temperature test 1
 35°C initial temperature test 2
 40°C initial temperature test 1
 40°C initial temperature test 2
 40°C initial temperature test 3
 40°C initial temperature test 4

5°C initial temperature test 1
 5°C initial temperature test 2
 5°C initial temperature test 3
 5°C initial temperature test 4
 13°C initial temperature test 1
 13°C initial temperature test 2
 13°C initial temperature test 3
 13°C initial temperature test 4

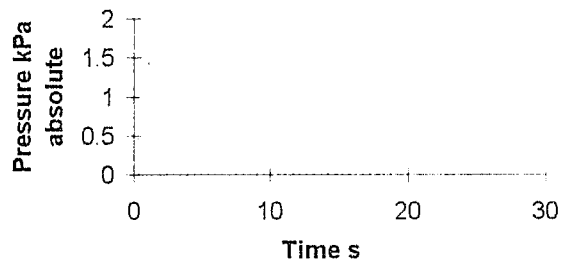
19°C initial temperature test 1
19°C initial temperature test 2
19°C initial temperature test 3
19°C initial temperature test 4
40°C initial temperature test 1
40°C initial temperature test 2
40°C initial temperature test 3

5°C initial temperature test 1
5°C initial temperature test 2
5°C initial temperature test 3
5°C initial temperature test 4
13°C initial temperature test 1
13°C initial temperature test 2
13°C initial temperature test 3
13°C initial temperature test 4
25°C initial temperature test 1
25°C initial temperature test 2
25°C initial temperature test 3
25°C initial temperature test 4
40°C initial temperature test 1
40°C initial temperature test 2
40°C initial temperature test 3
40°C initial temperature test 4

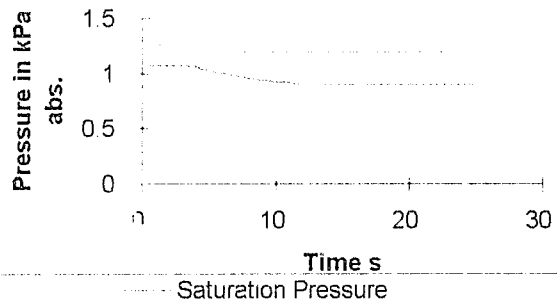
5°C initial temperature test 1
5°C initial temperature test 2
5°C initial temperature test 3
5°C initial temperature test 4
13°C initial temperature test 1
13°C initial temperature test 2
13°C initial temperature test 4
19°C initial temperature test 1
19°C initial temperature test 2
19°C initial temperature test 3
19°C initial temperature test 4
40°C initial temperature test 1
40°C initial temperature test 2
40°C initial temperature test 3
40°C initial temperature test 4

5 °C initial temperature, 3 cm liquid height, test 1

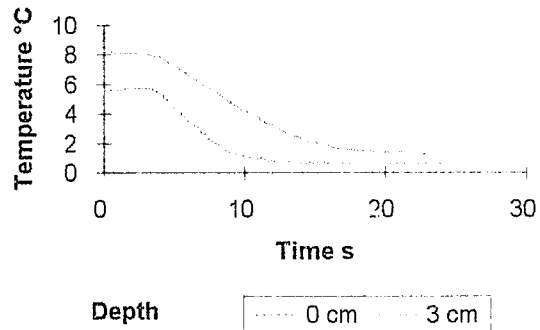
Evaporator pressure as a function of time



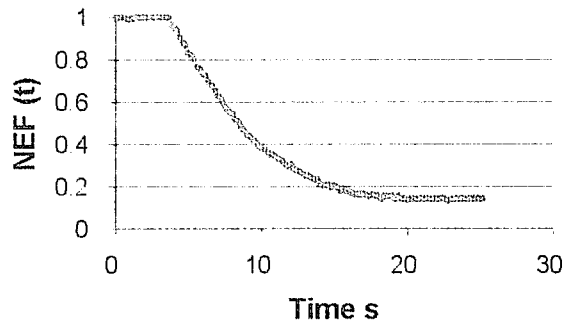
Hydrostatic and Saturation pressure



Temperature distribution

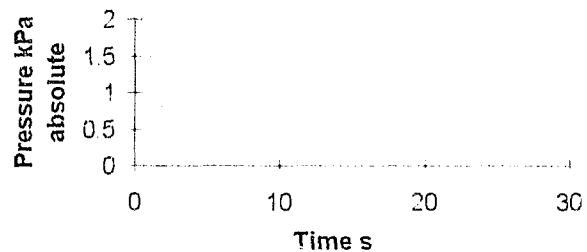


NEF(t) as a function of Time

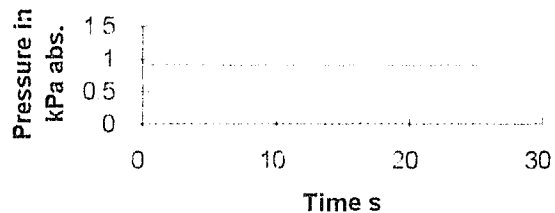


5 °C initial temperature, 3 cm liquid height, test 2

Evaporator pressure as a function of time

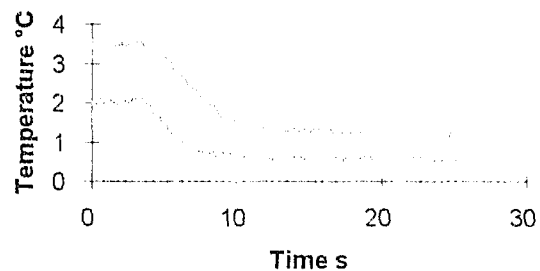


Hydrostatic and Saturation pressure



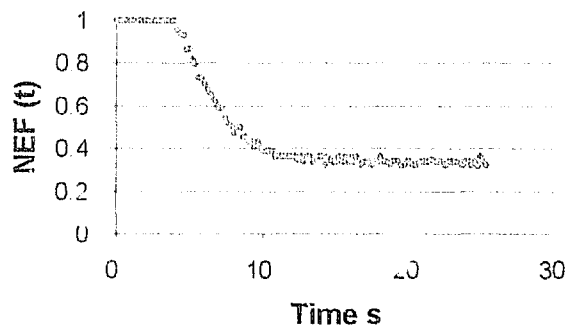
— Saturation Pressure
— Surface + Hydrostatic Pressure

Temperature distribution



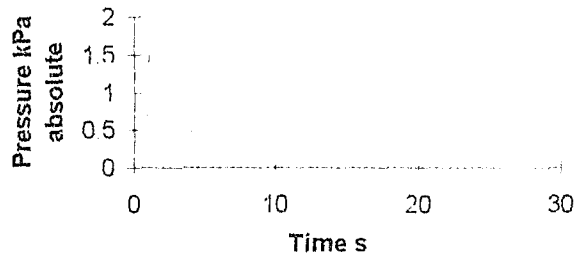
Depth — 0 cm — 3 cm

NEF(t) as a function of Time

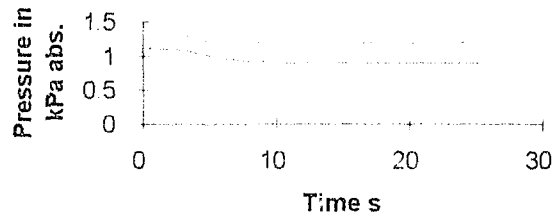


5°C initial temperature, 3 cm liquid height, test 3

Evaporator pressure as a function of time

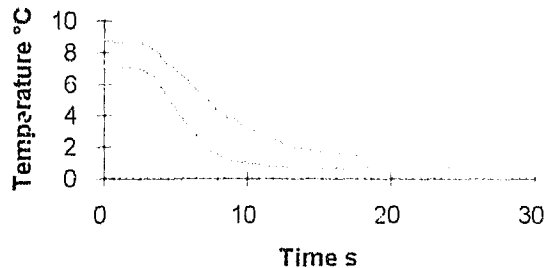


Hydrostatic and Saturation pressure



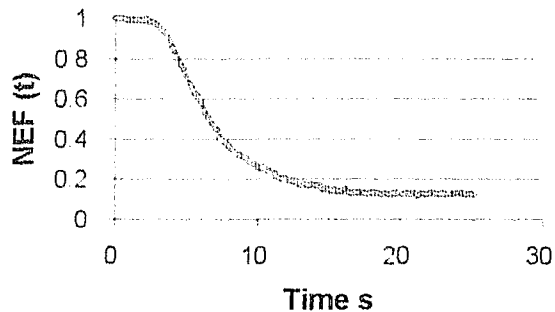
— Surface + Hydrostatic - - - Saturation Pressure

Temperature distribution



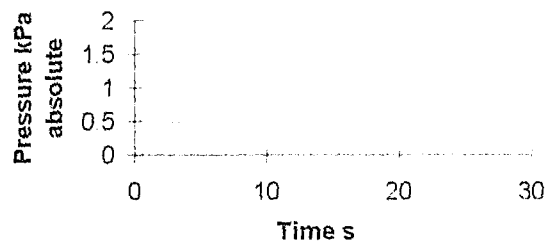
--- 0 cm — 3 cm

NEF(t) as a function of Time

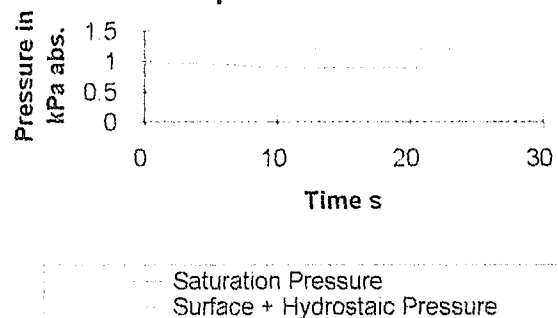


5 °C initial temperature, 3 cm liquid height, test 4

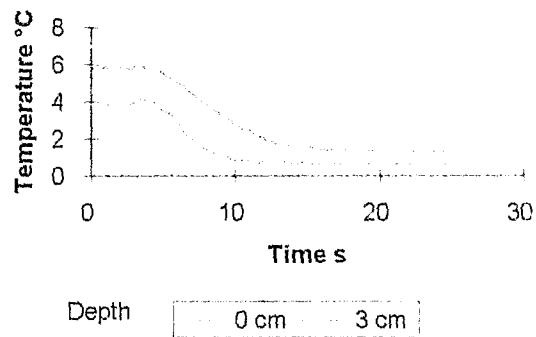
Evaporator pressure as a function of time



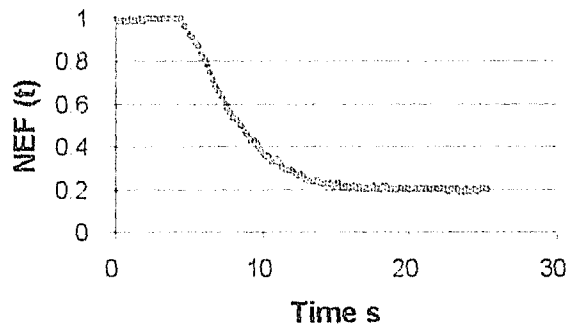
Hydrostatic and Saturation pressure



Temperature distribution

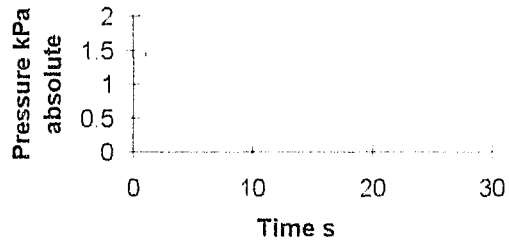


NEF(t) as a function of Time

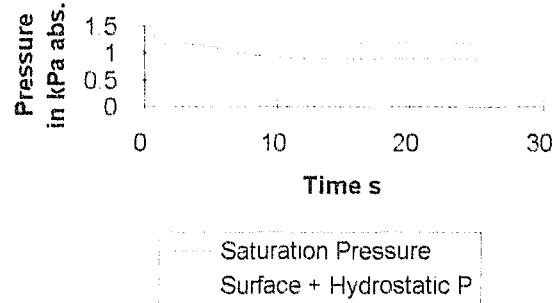


13 °C initial temperature, 3 cm liquid height, test 1

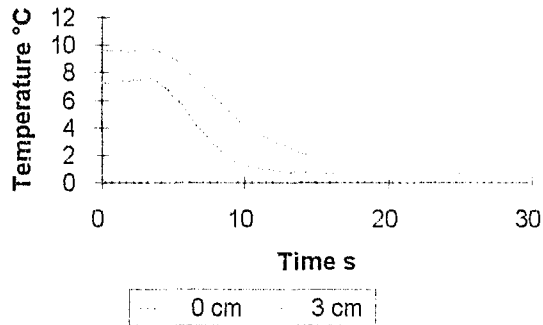
Evaporator pressure as a function of time



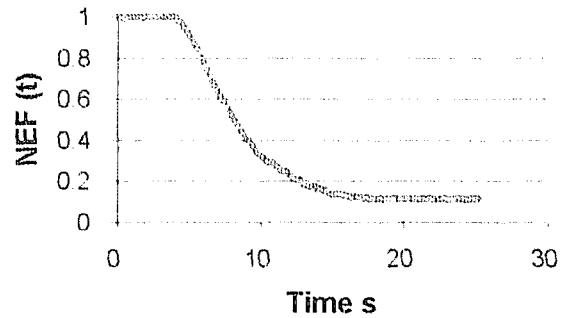
Hydrostatic and Saturation pressure



Temperature distribution

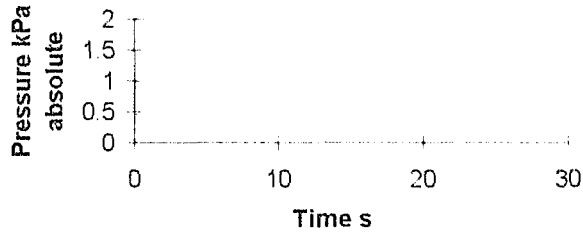


NEF(t) as a function of Time

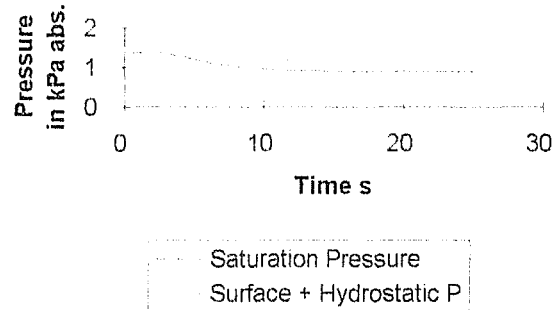


13 °C initial temperature, 3 cm liquid height, test 2

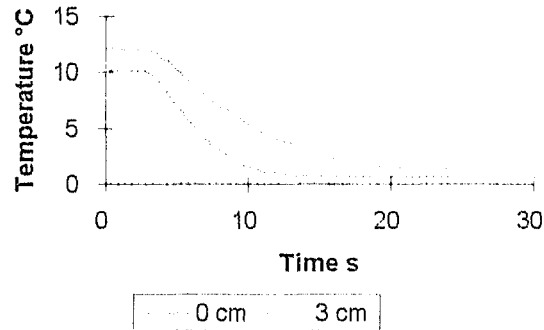
Evaporator pressure as a function of time



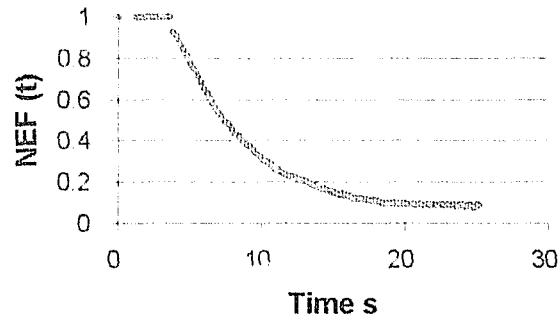
Hydrostatic and Saturation pressure



Temperature distribution

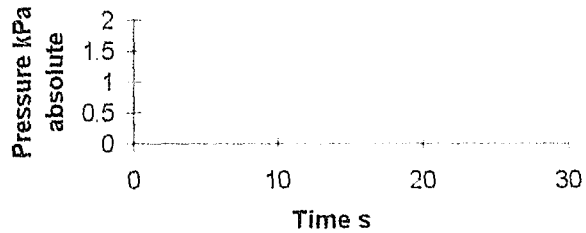


NEF(t) as a function of Time

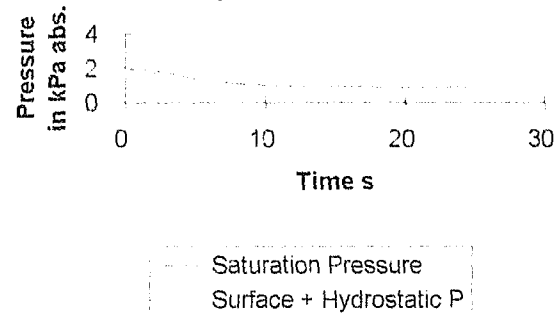


13 °C initial temperature, 3 cm liquid height, test 3

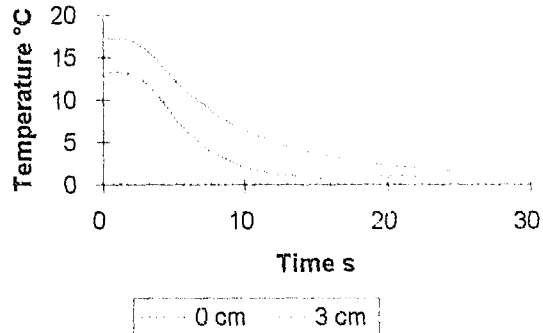
Evaporator pressure as a function of time



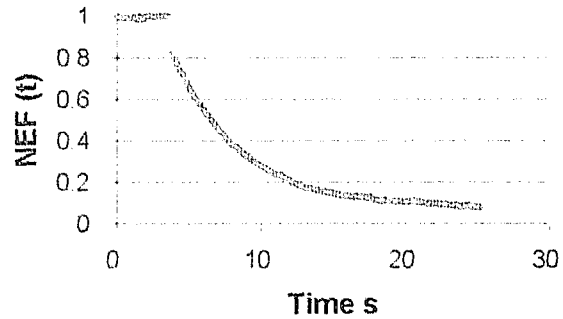
Hydrostatic and Saturation pressure



Temperature distribution

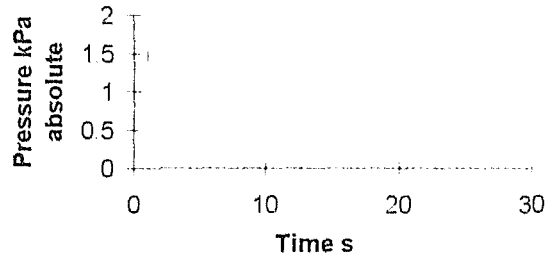


NEF(t) as a function of Time

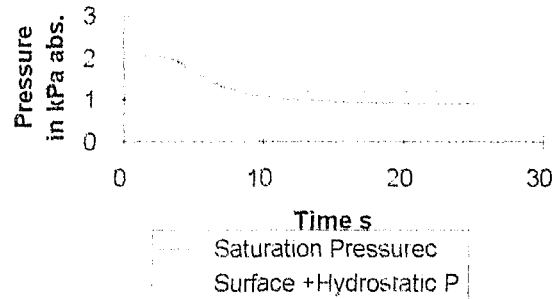


19 °C initial temperature, 3 cm liquid height, test 1

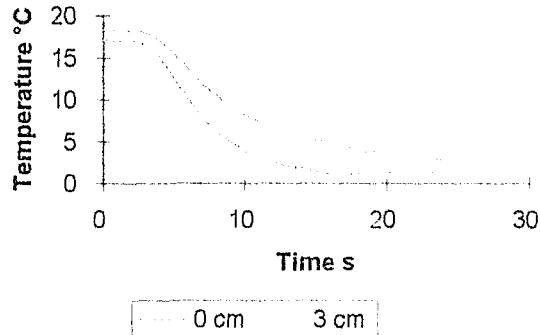
Evaporator pressure as a function of time



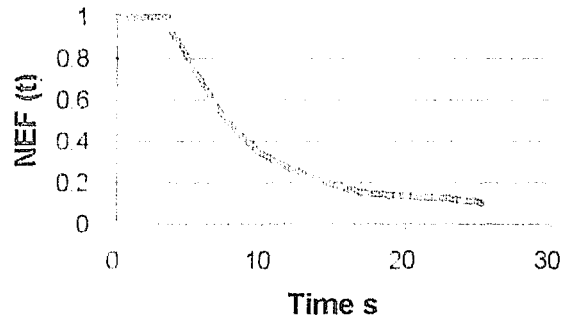
Hydrostatic and Saturation pressure



Temperature distribution

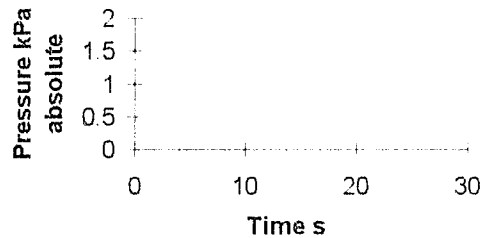


NEF(t) as a function of Time

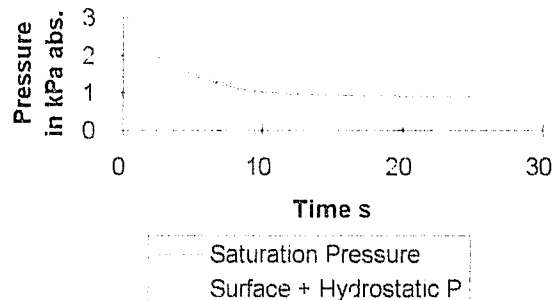


19 °C initial temperature, 3 cm liquid height, test 2

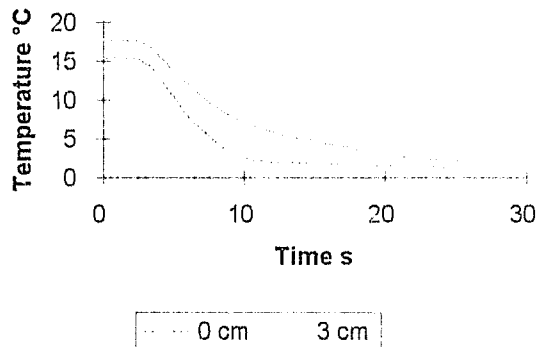
Evaporator pressure as a function of time



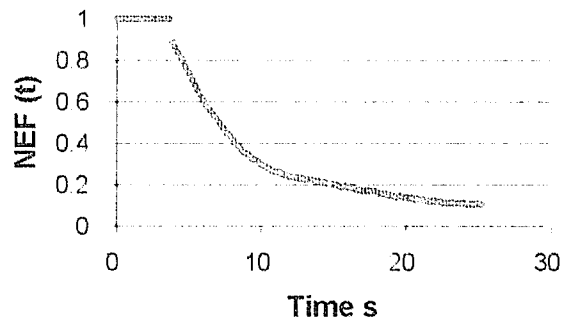
Hydrostatic and Saturation pressure



Temperature distribution

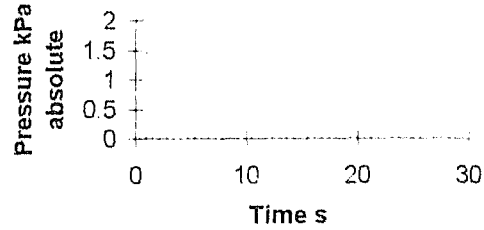


NEF(t) as a function of Time

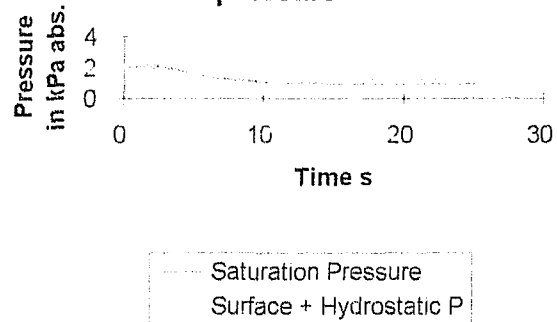


19 °C initial temperature, 3 cm liquid height, test 3

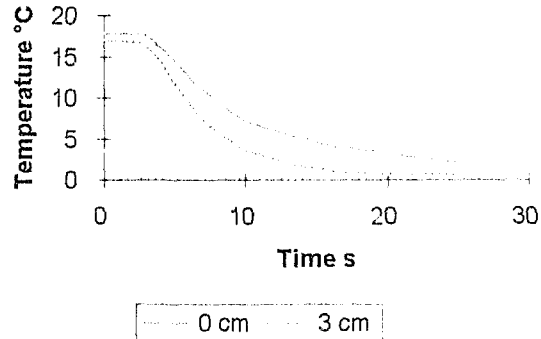
Evaporator pressure as a function of time



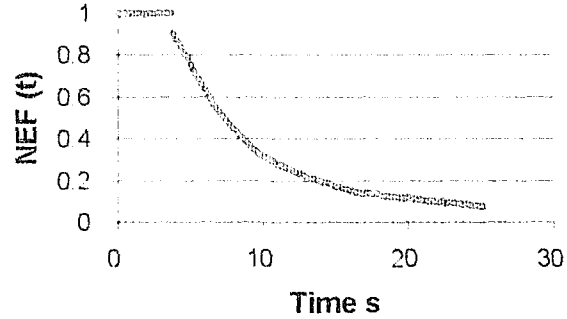
Hydrostatic and Saturation pressure



Temperature distribution

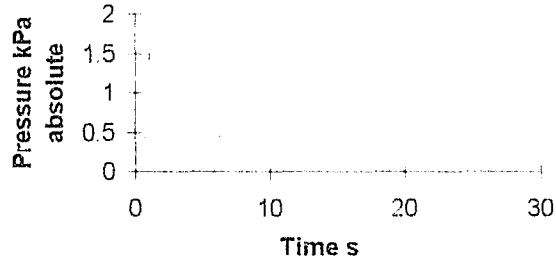


NEF(t) as a function of Time

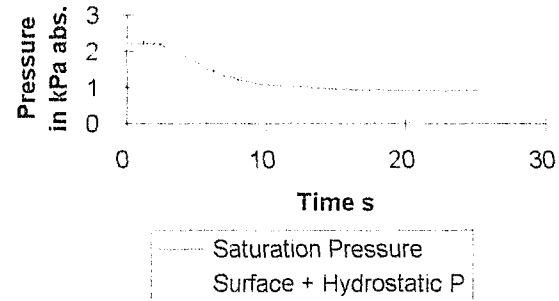


19 °C initial temperature, 3 cm liquid height, test 4

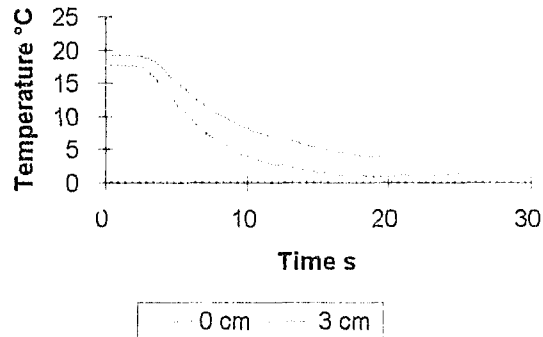
Evaporator pressure as a function of time



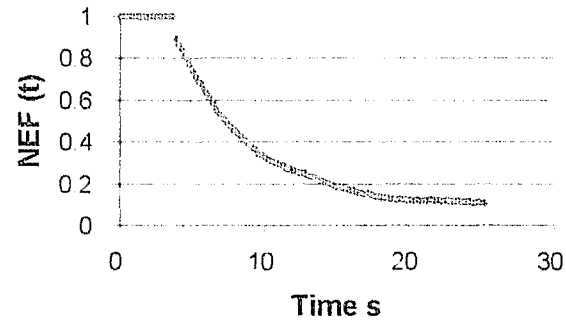
Hydrostatic and Saturation pressure



Temperature distribution

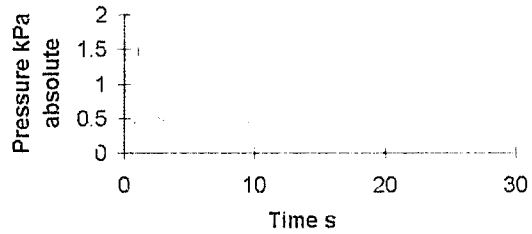


NEF(t) as a function of Time

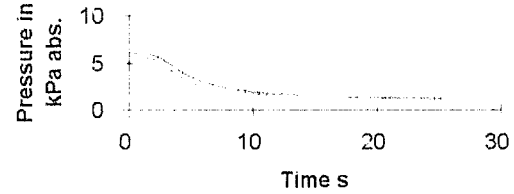


40°C initial temperature, 3 cm liquid height, test 1

Evaporator pressure as a function of time

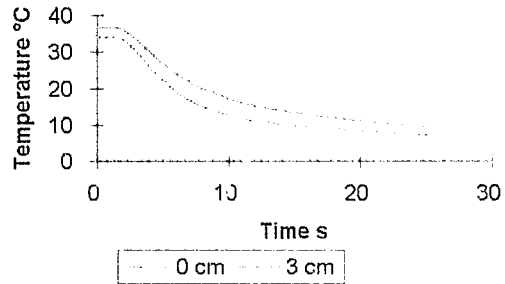


Hydrostatic and Saturation pressure

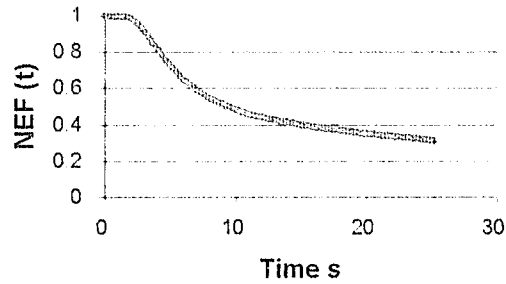


..... Surface + Hydrostatic - - - Saturation Pressure

Temperature distribution

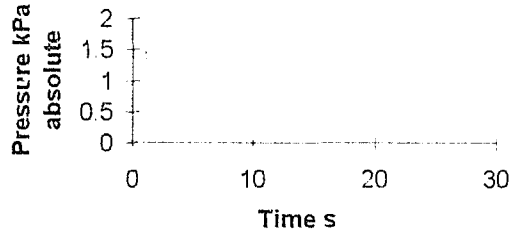


NEF(t) as a function of Time

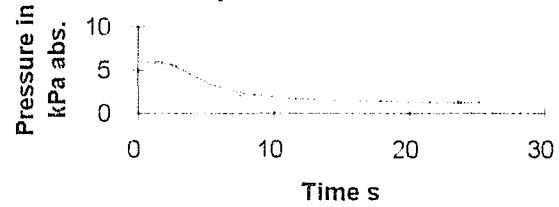


40 °C initial temperature, 3 cm liquid height, test 2

Evaporator pressure as a function of time

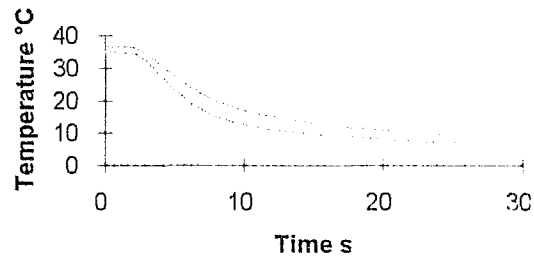


Hydrostatic and Saturation pressure



--- Saturation Pressure
--- Surface + Hydrostatic Pressure

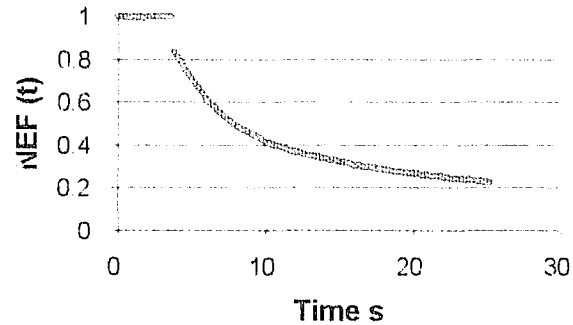
Temperature distribution



Depth

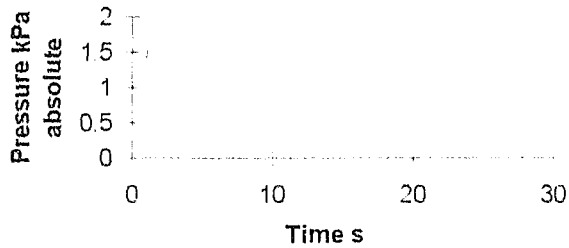
--- 0 cm --- 3 cm

NEF(t) as a function of Time

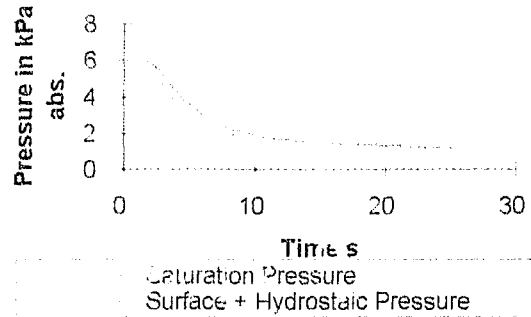


40 °C initial temperature, 3 cm liquid height, test 3

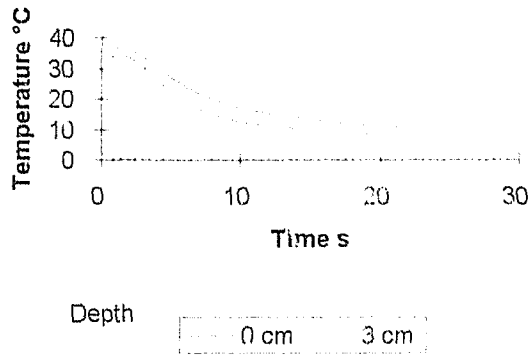
Evaporator pressure as a function of time



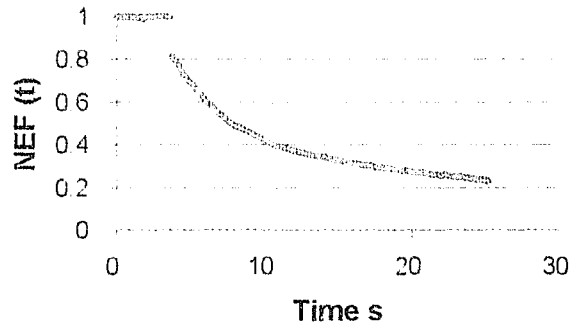
Hydrostatic and Saturation pressure



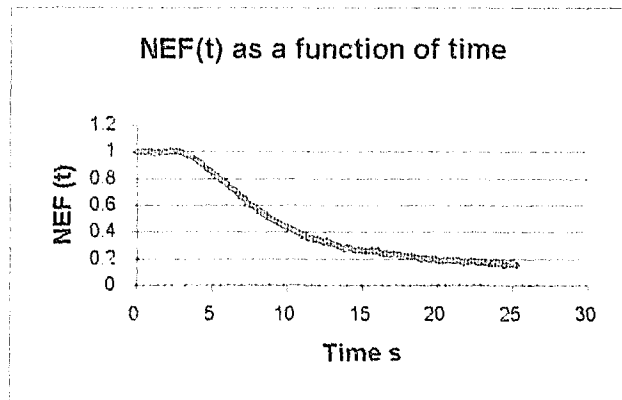
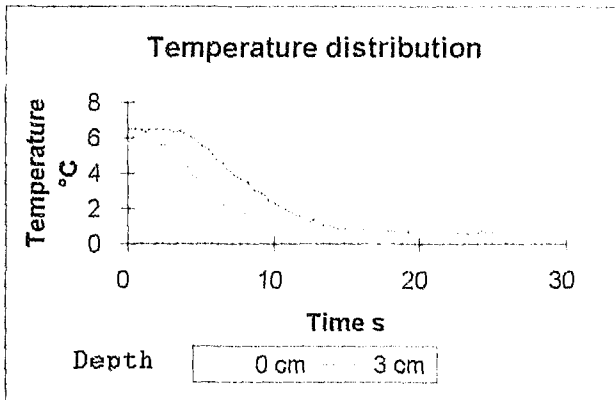
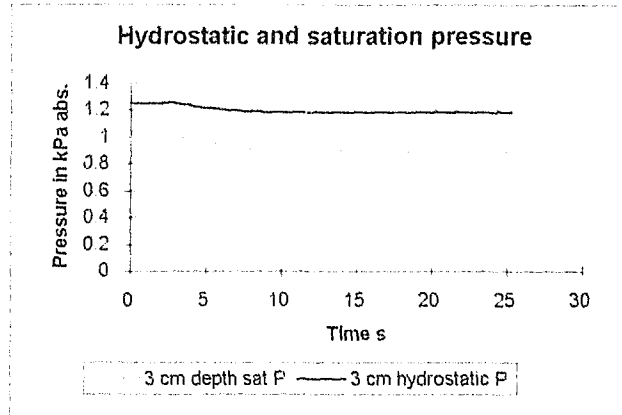
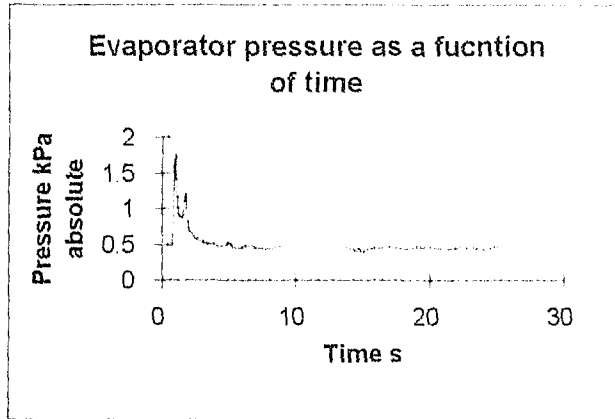
Temperature distribution



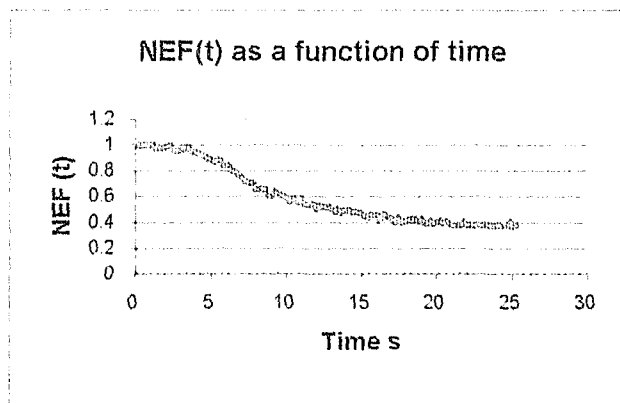
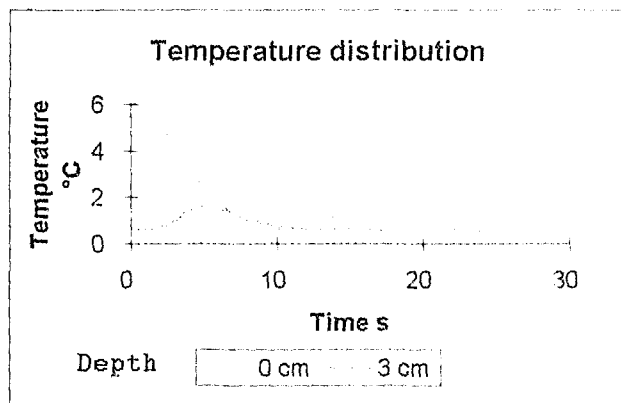
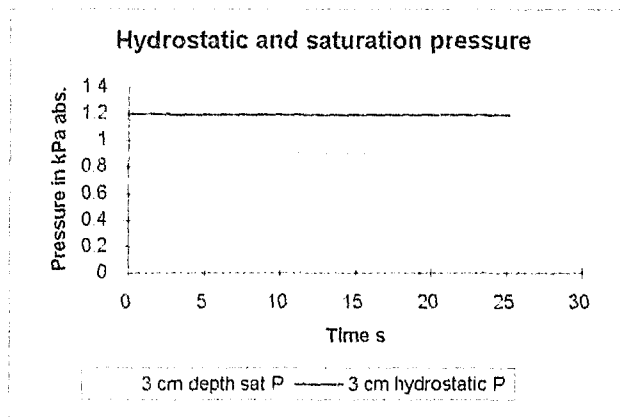
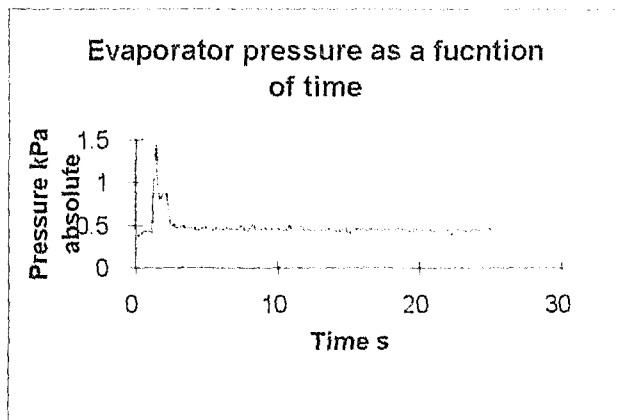
NEF(t) as a function of Time



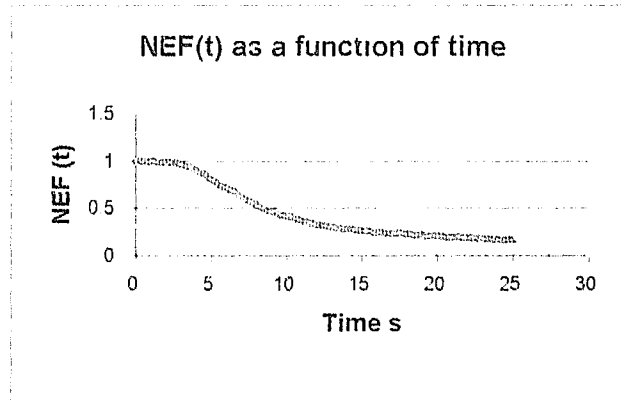
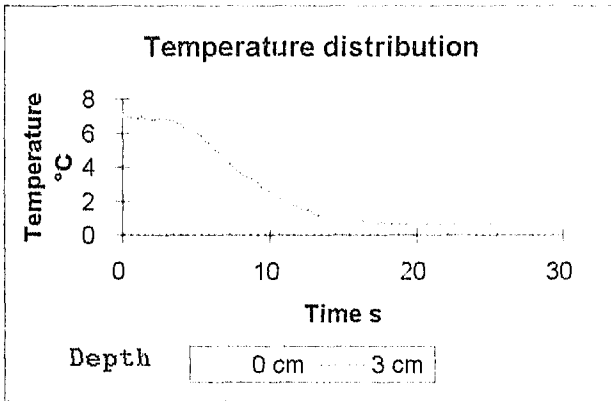
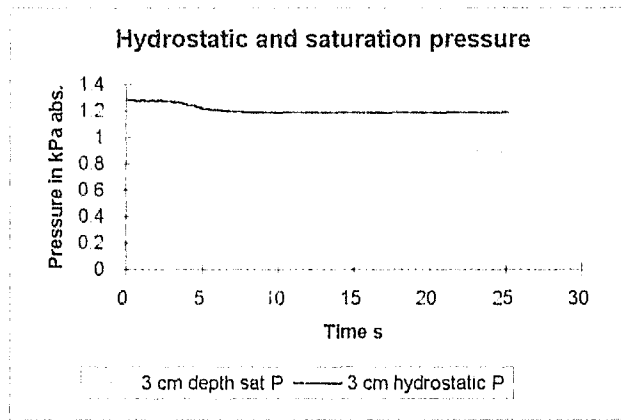
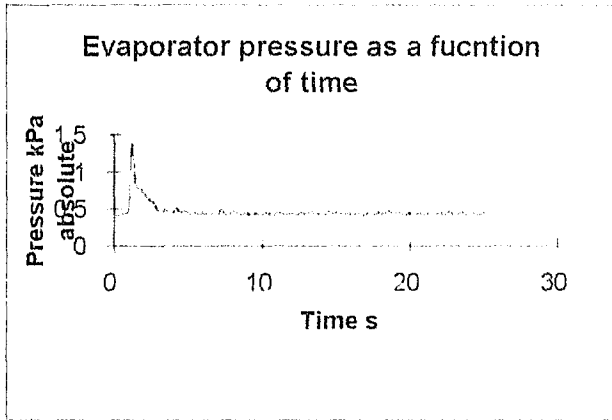
5°C initial, 6 cm liquid height, test 1



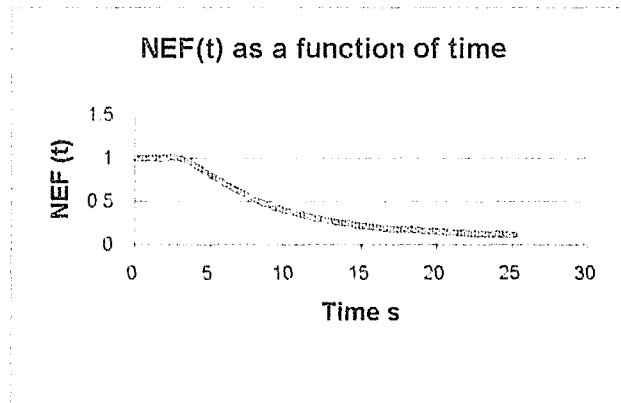
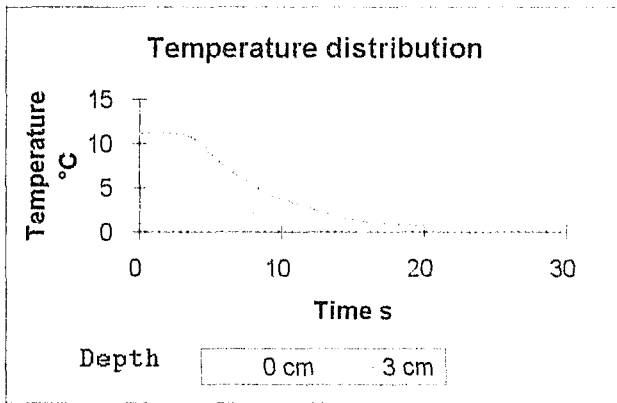
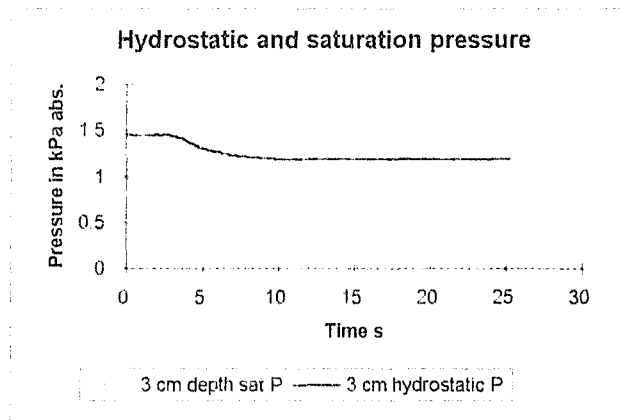
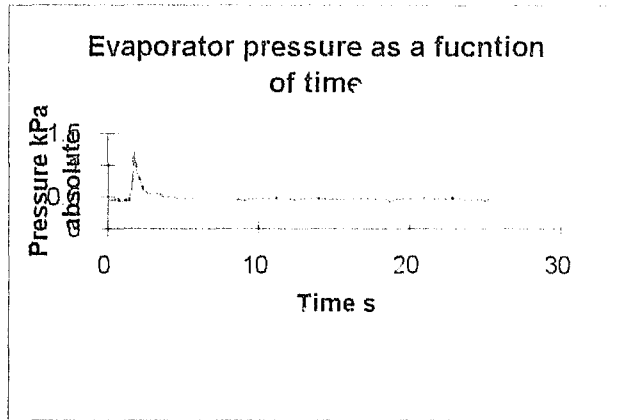
5°C initial, 6 cm liquid height, test 2



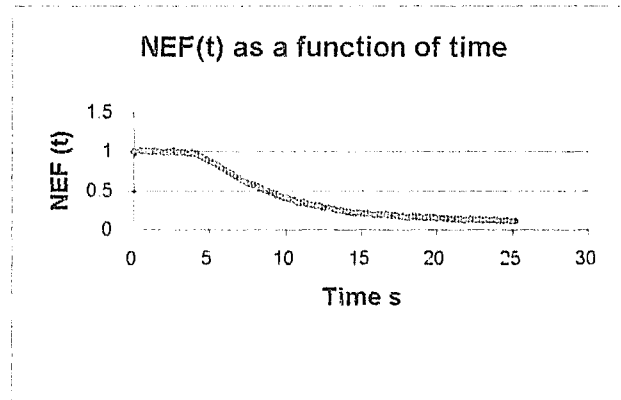
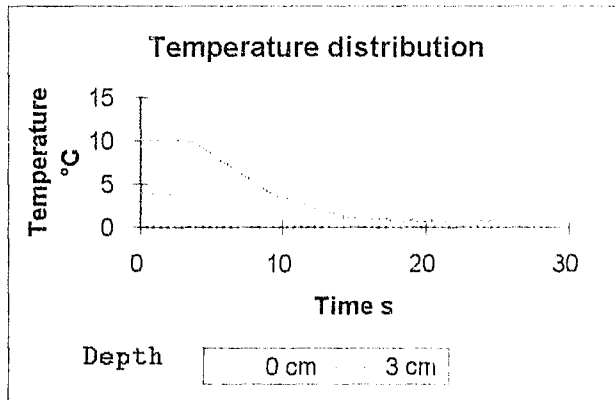
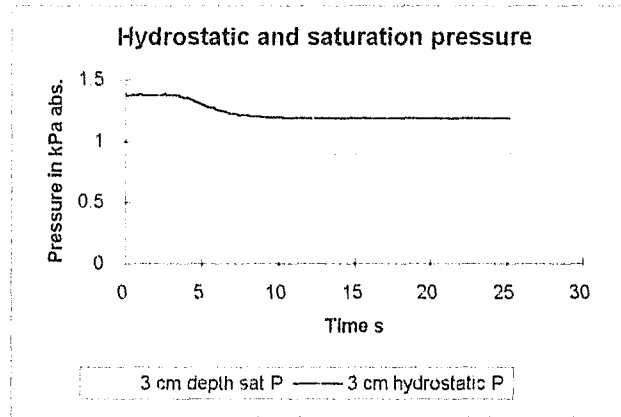
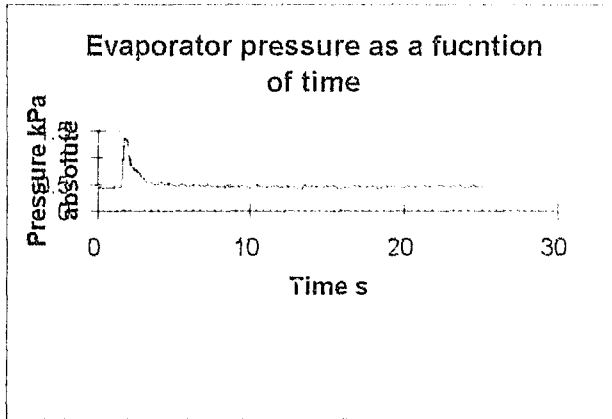
5°C initial, 6 cm liquid height, test 3



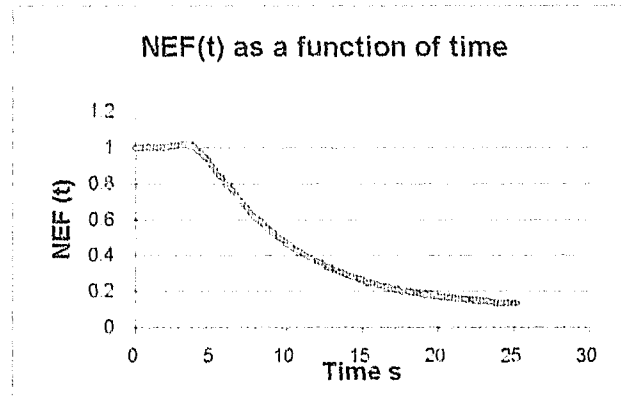
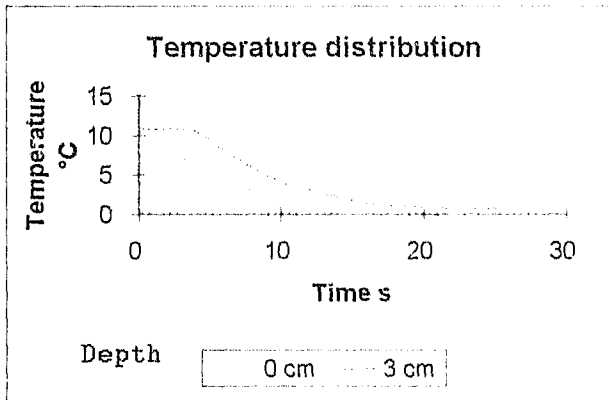
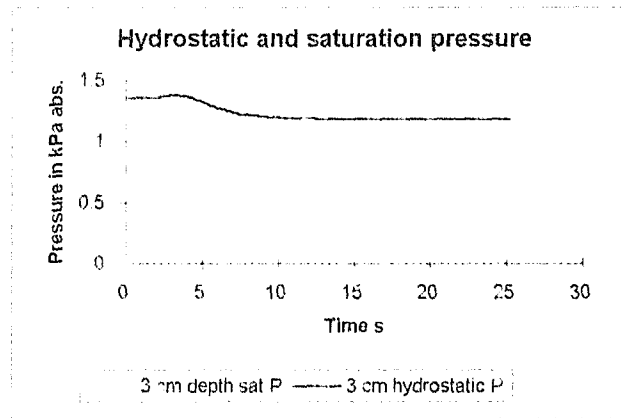
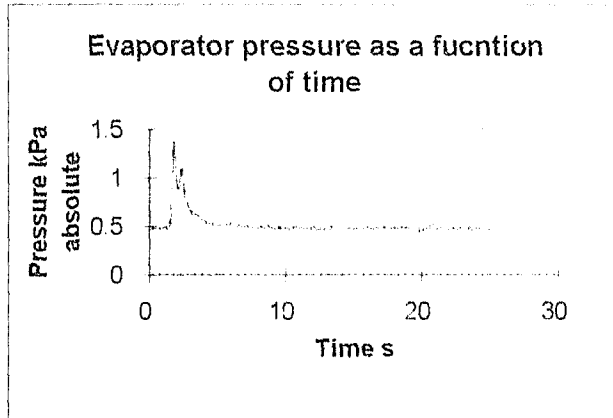
13°C initial, 6 cm liquid height, test 1



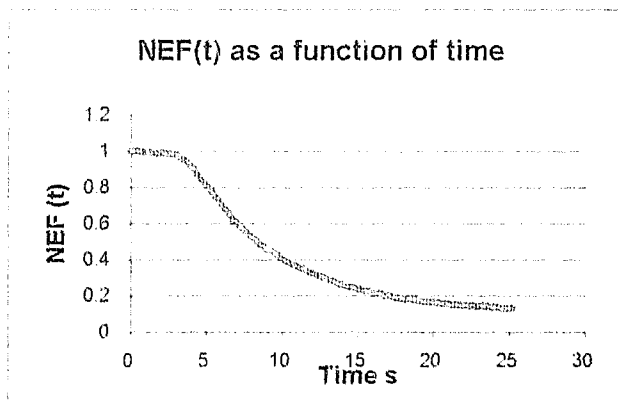
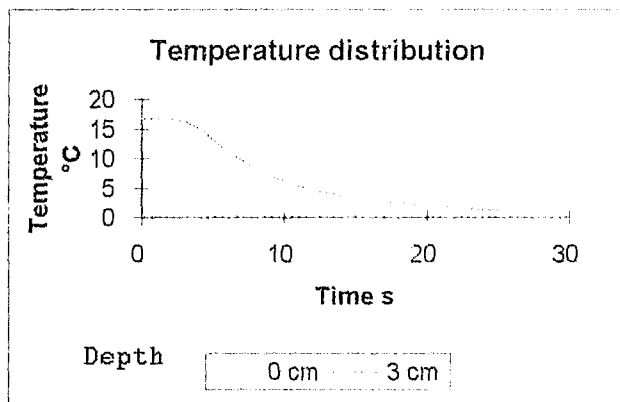
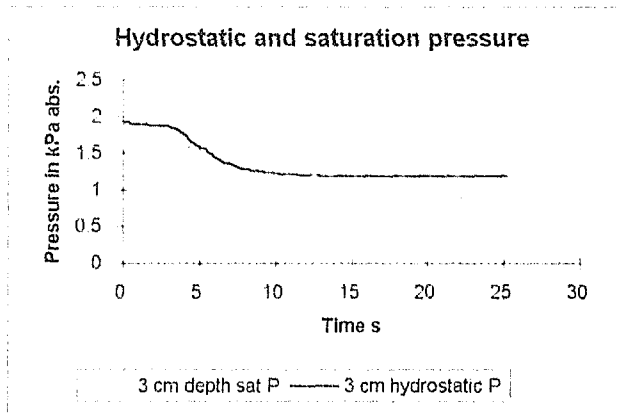
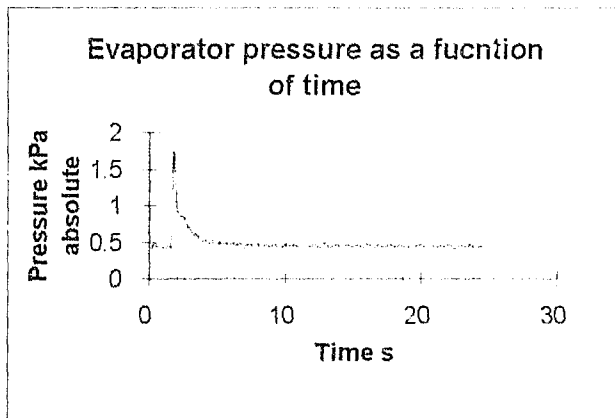
13°C initial, 6 cm liquid height, test 2



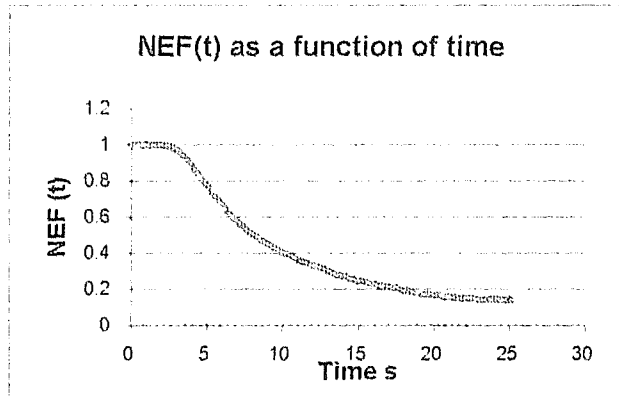
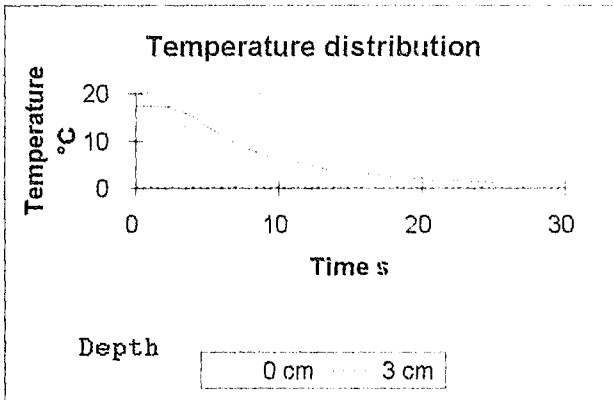
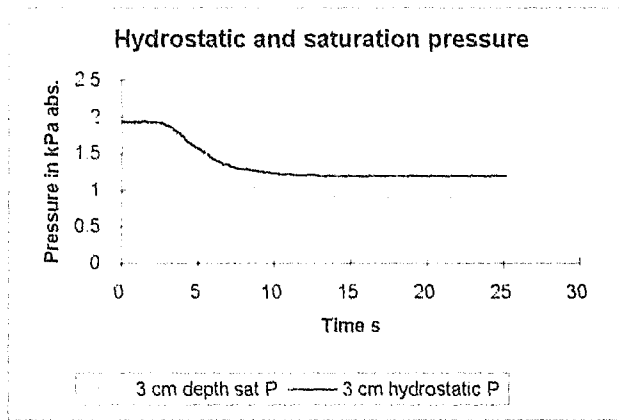
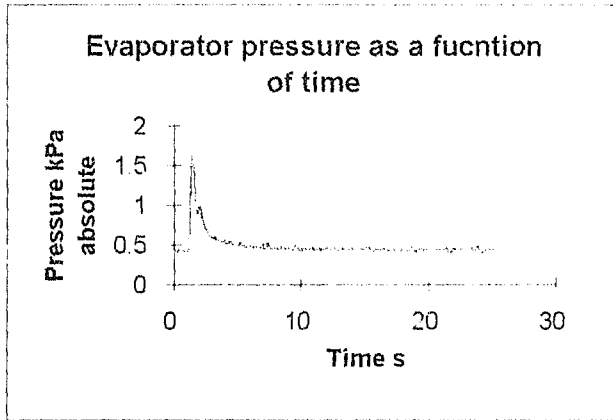
13°C initial, 6 cm liquid height. test 3



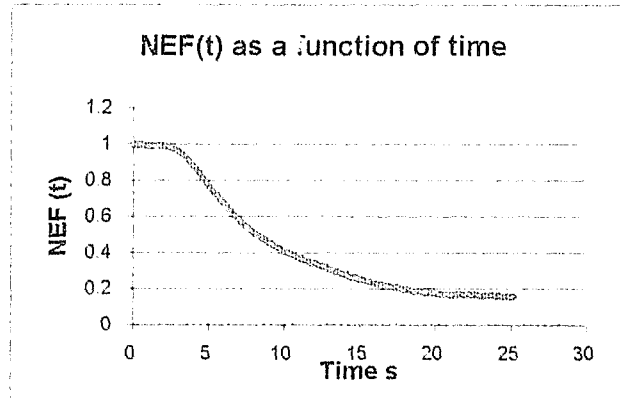
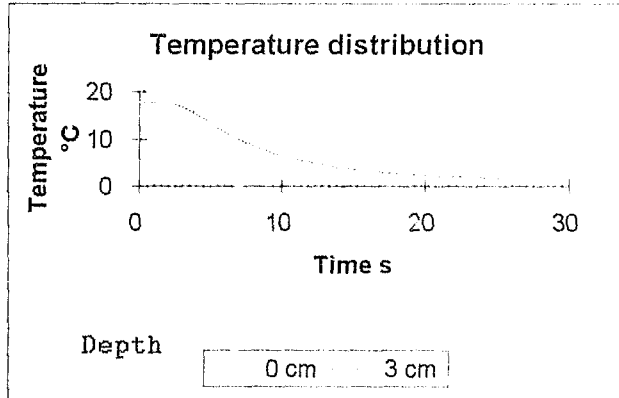
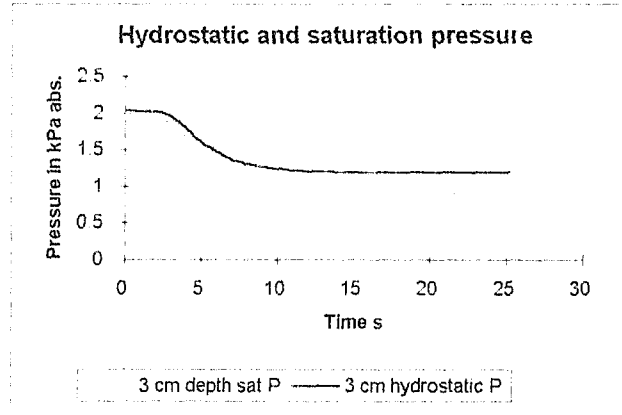
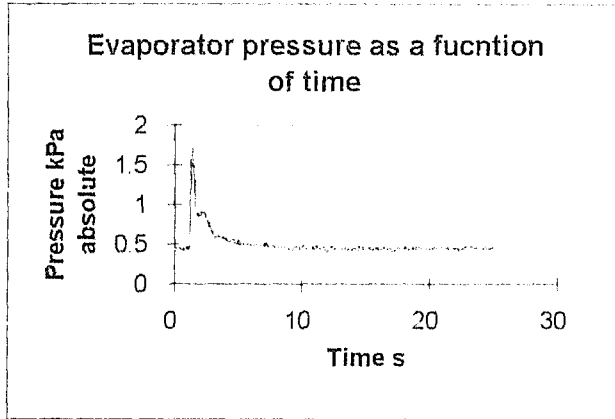
19°C initial, 6 cm liquid height, test 1



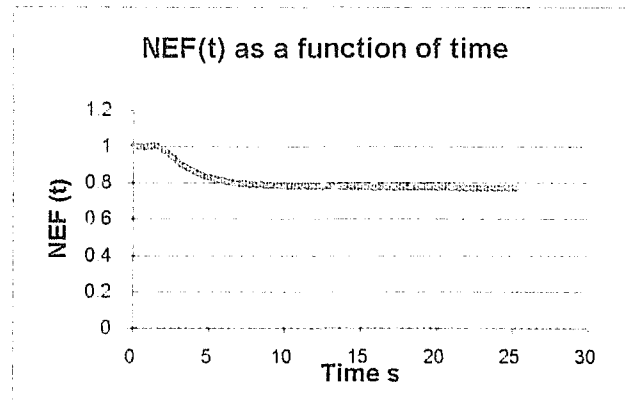
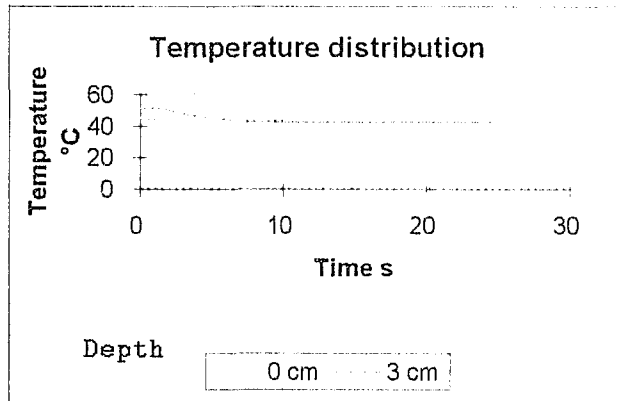
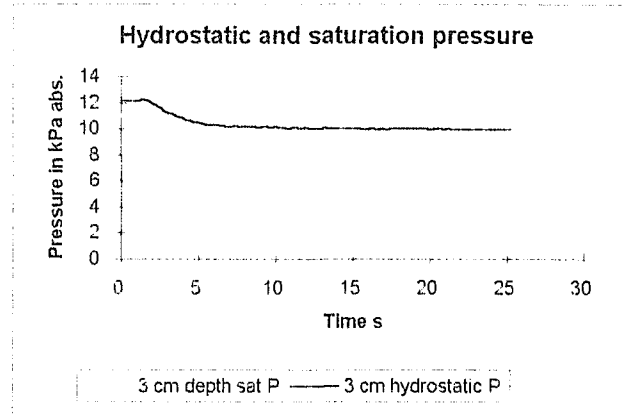
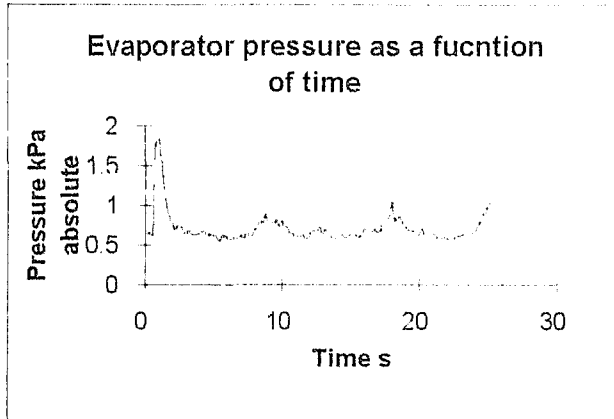
19°C initial, 6 cm liquid height, test 2



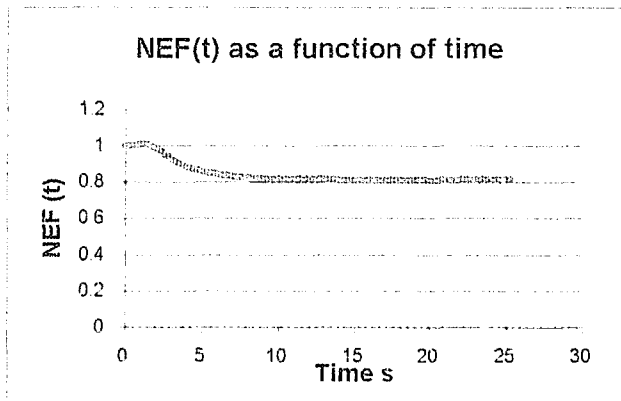
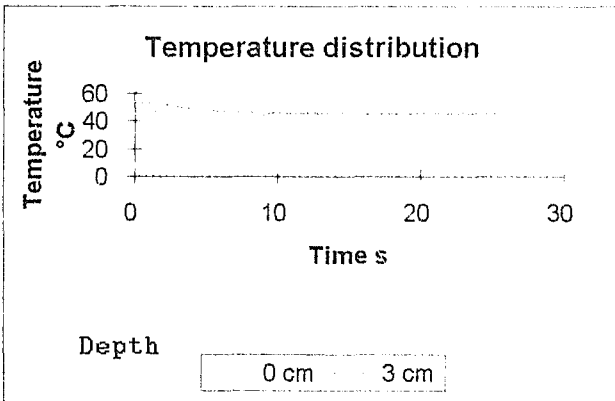
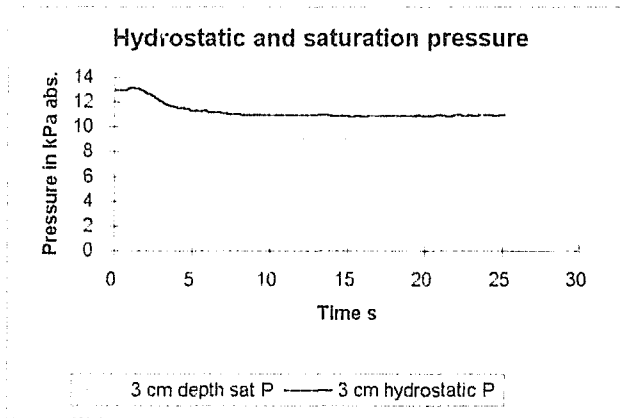
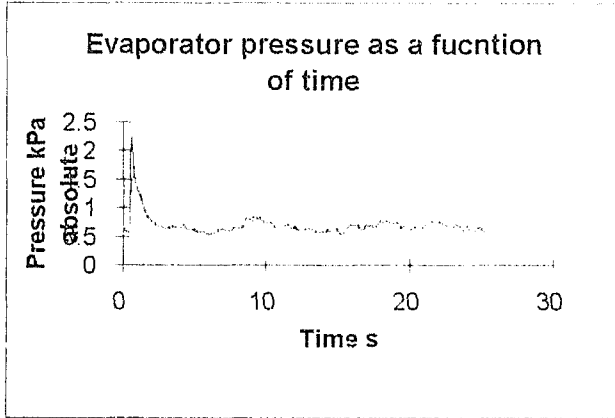
19°C initial, 6 cm liquid height, test 3



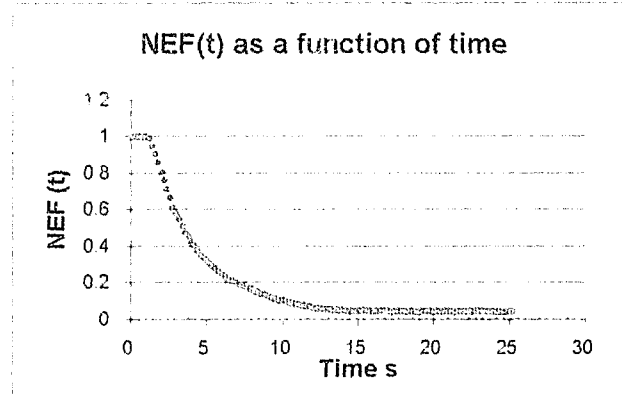
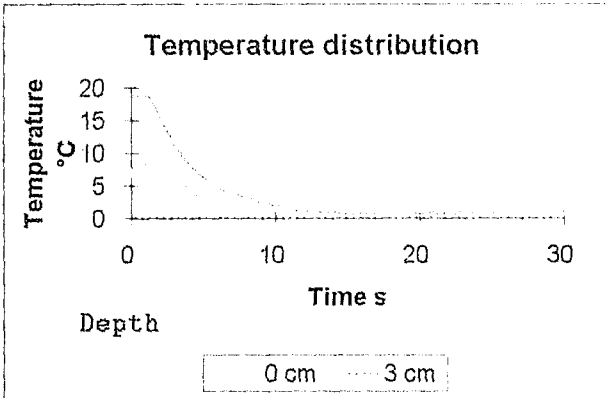
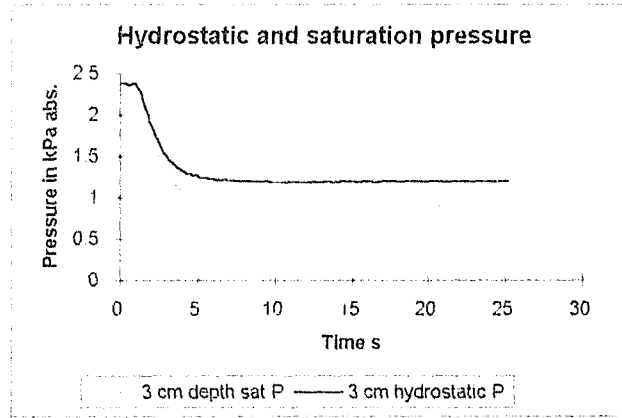
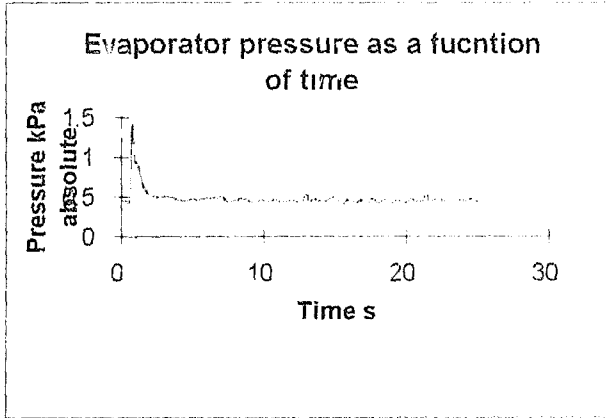
25°C initial, 6 cm liquid height, test 1



25°C initial, 6 cm liquid height, test 2

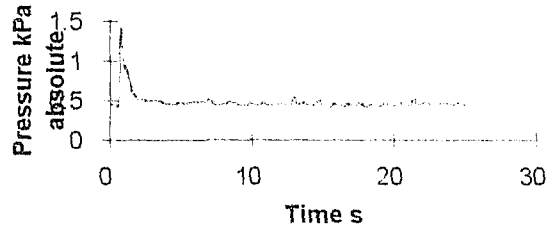


35°C initial, 6 cm liquid height, test 1

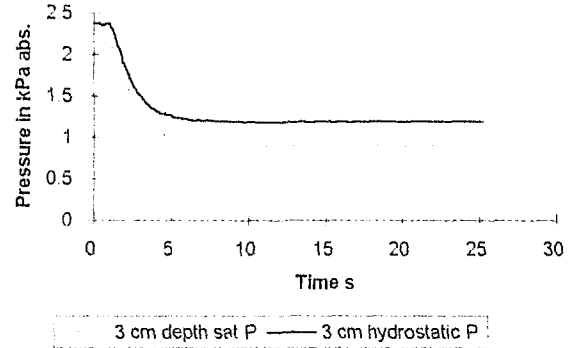


35°C initial, 6 cm liquid height, test 1

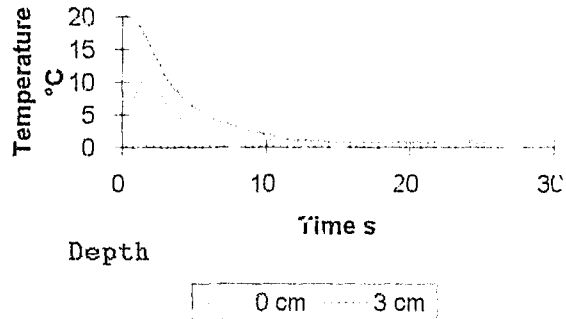
Evaporator pressure as a function of time



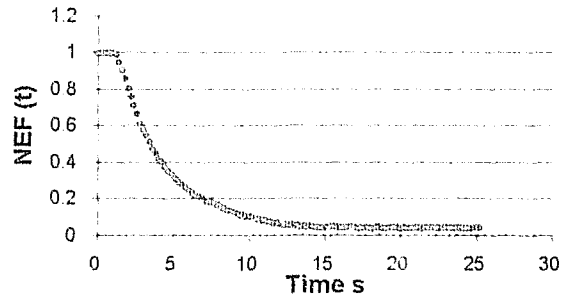
Hydrostatic and saturation pressure



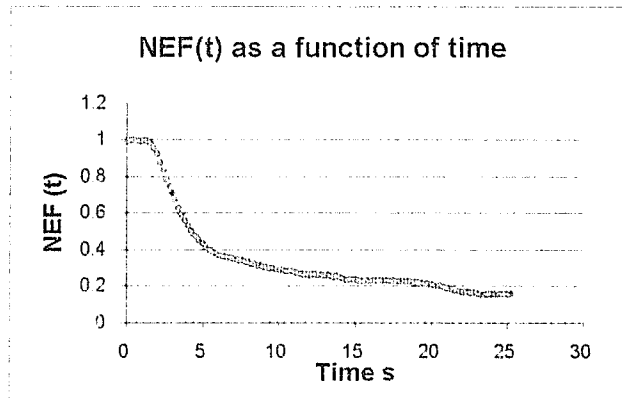
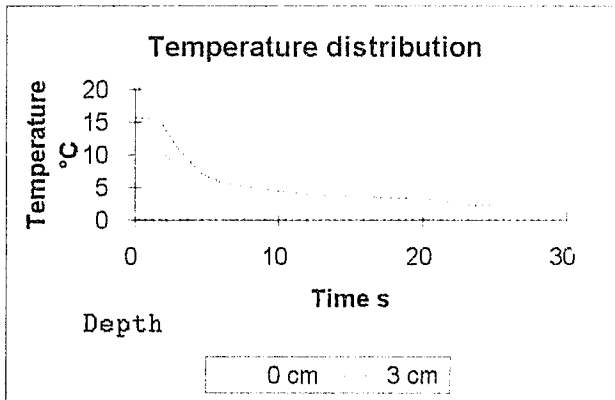
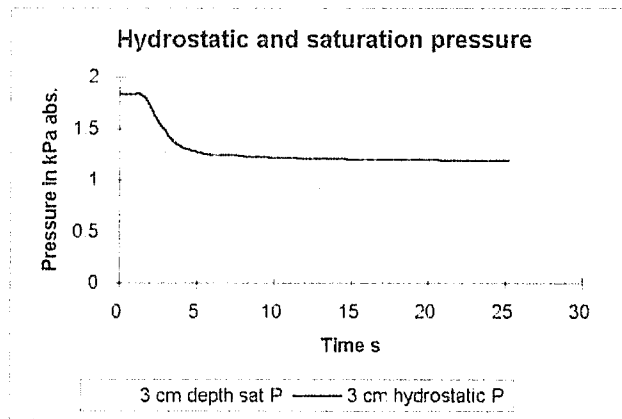
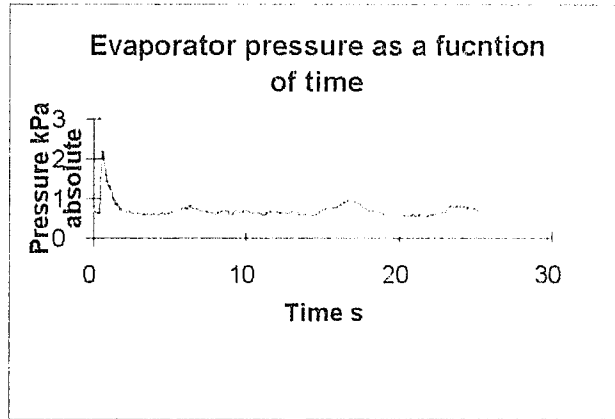
Temperature distribution



NEF(t) as a function of time

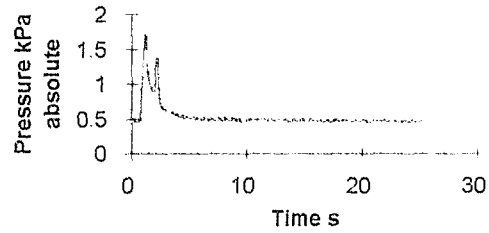


35°C initial, 6 cm liquid height, test 2

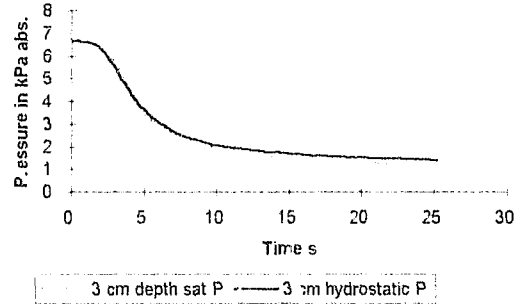


40°C initial, 6 cm liquid height, test 1

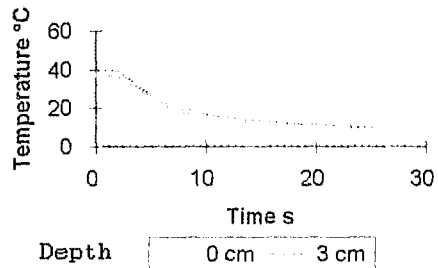
Evaporator pressure as a function of time



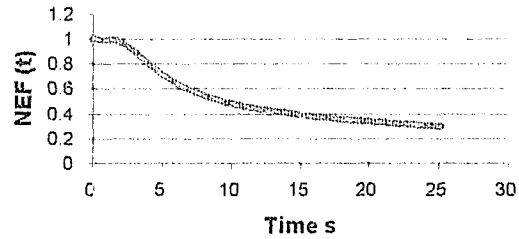
Hydrostatic and saturation pressure



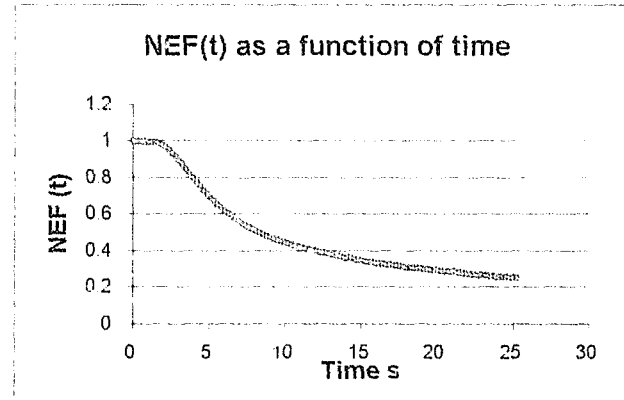
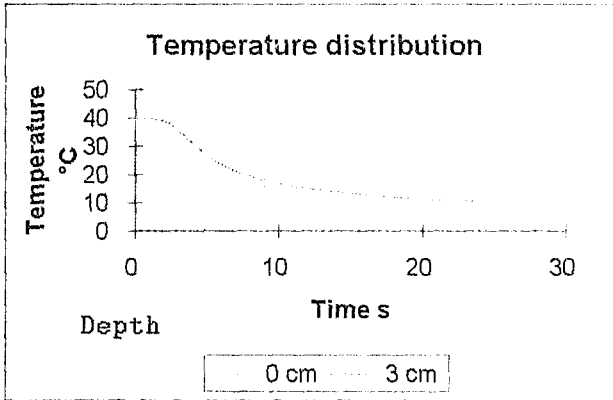
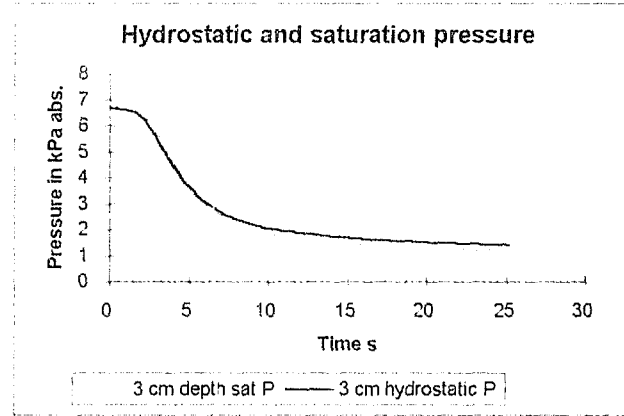
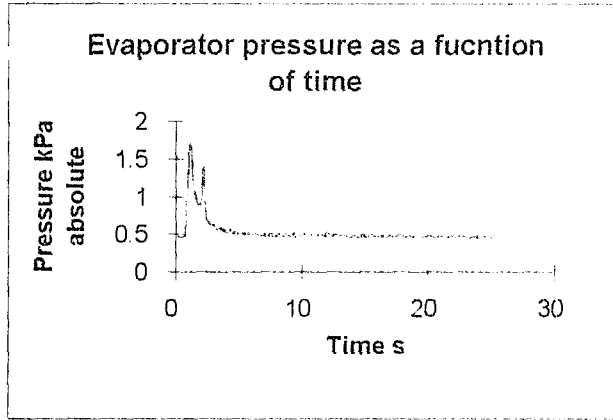
Temperature distribution



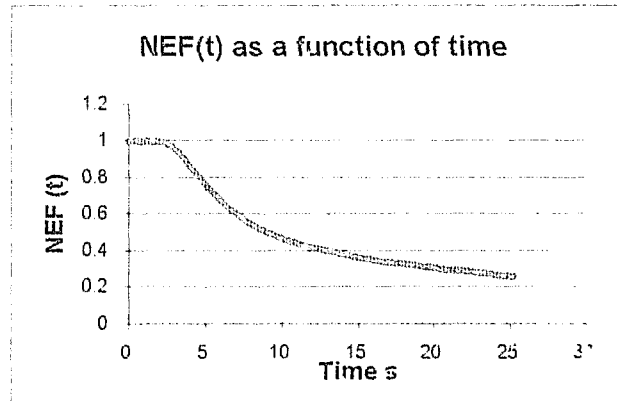
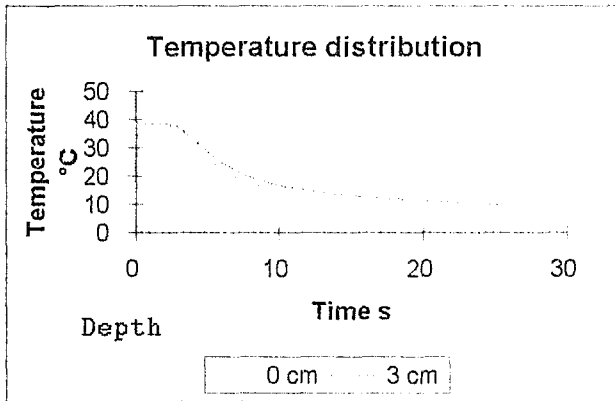
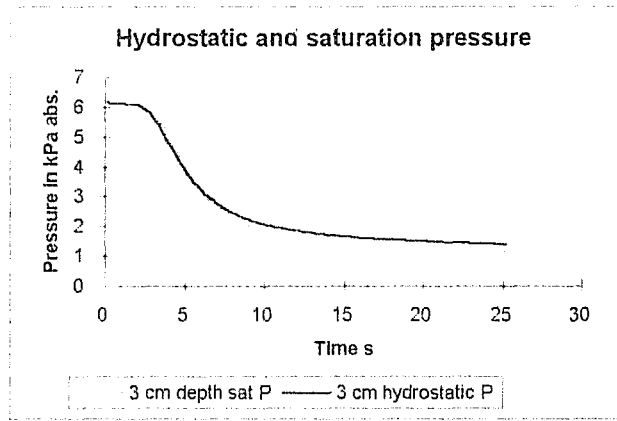
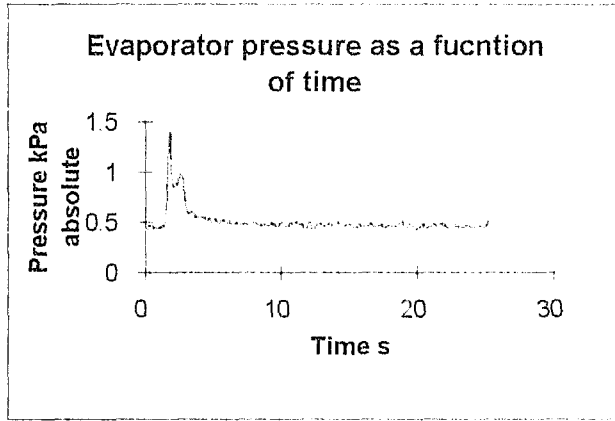
NEF(t) as a function of time



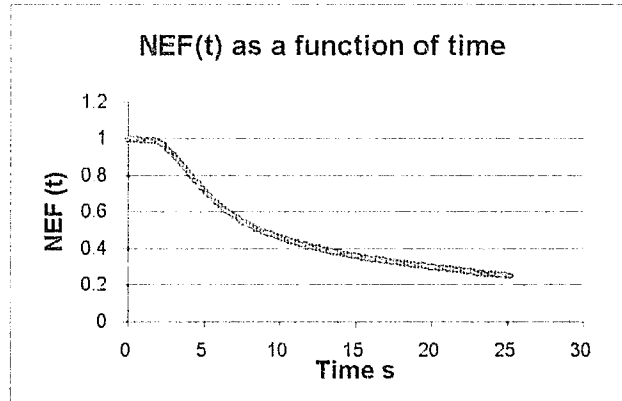
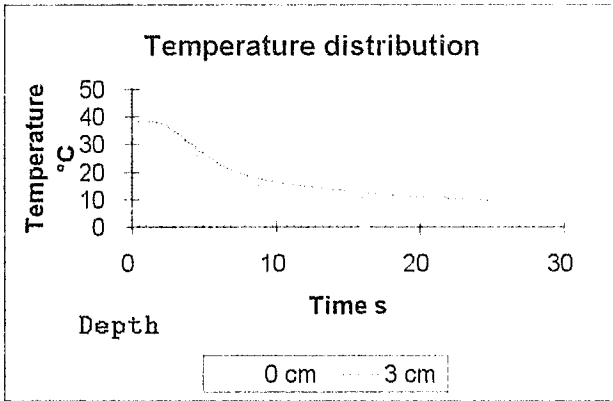
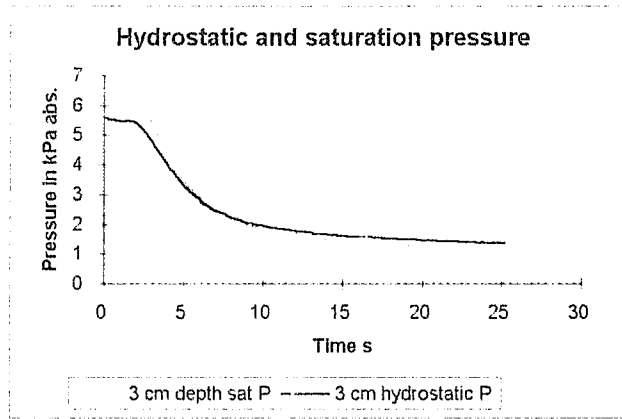
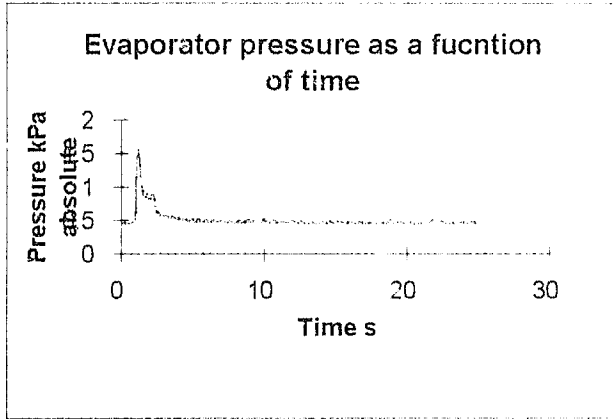
40°C initial, 6 cm liquid height, test 2



40°C initial, 6 cm liquid height, test 3

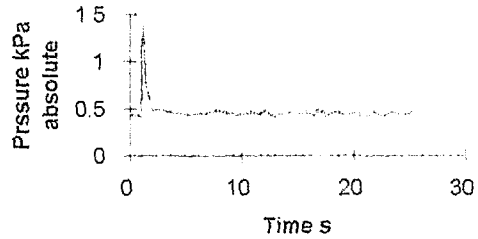


40°C initial, 6 cm liquid height, test 4

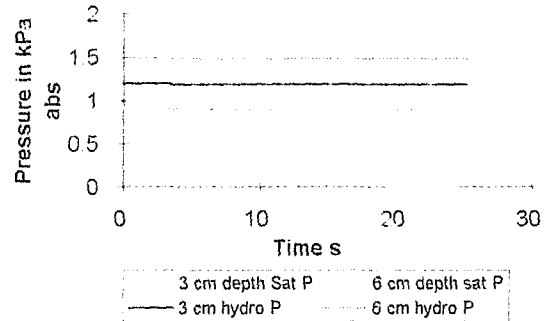


5°C initial, 9 cm liquid height, test 1

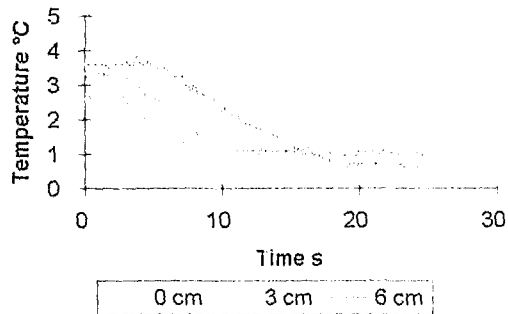
Evaporator pressure as a function of time



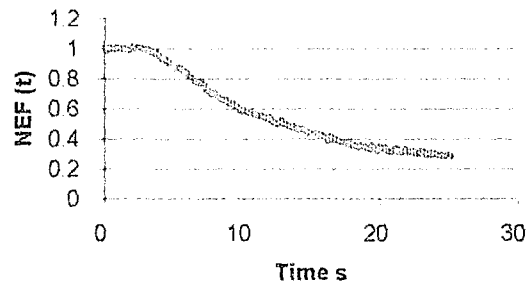
Hydrostatic and Saturation pressure



Temperature distribution

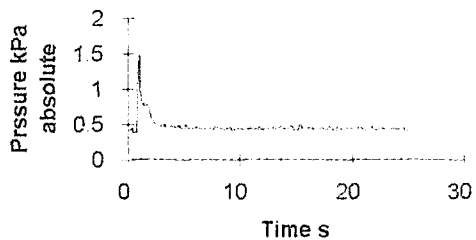


NEF (t) as a function of time

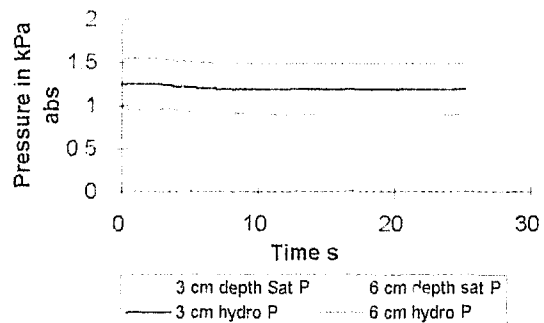


5°C initial, 9 cm liquid height, test 2

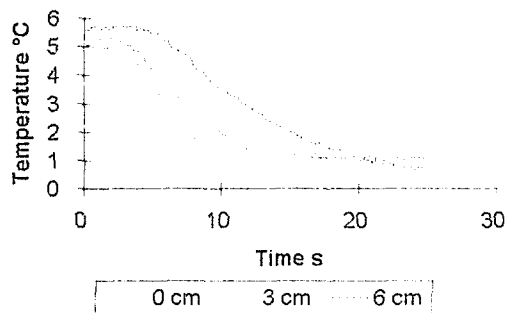
Evaporator pressure as a function of time



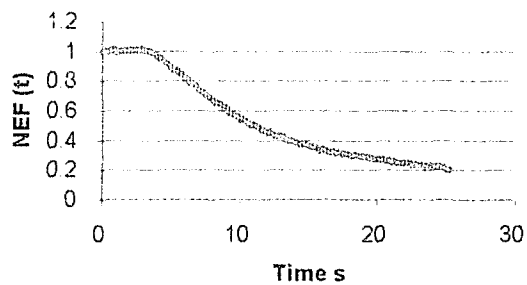
Hydrostatic and Saturation pressure



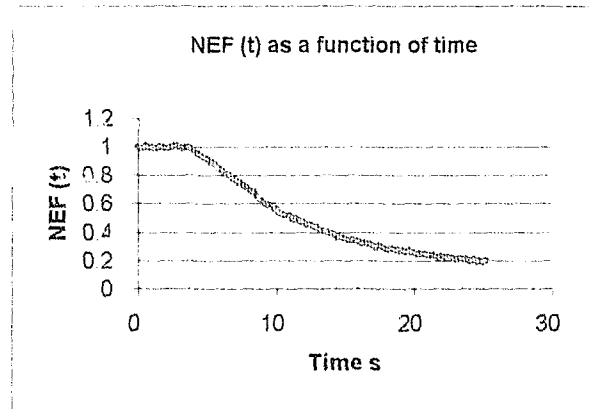
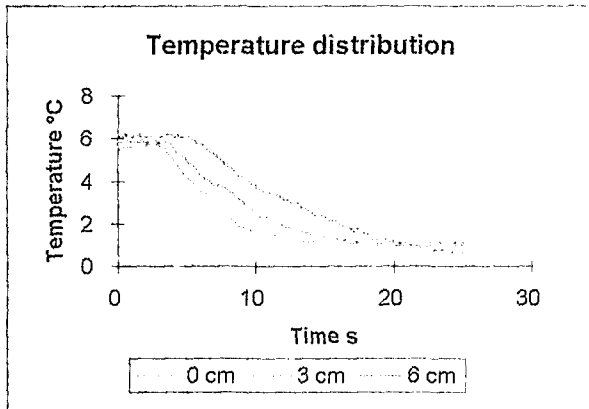
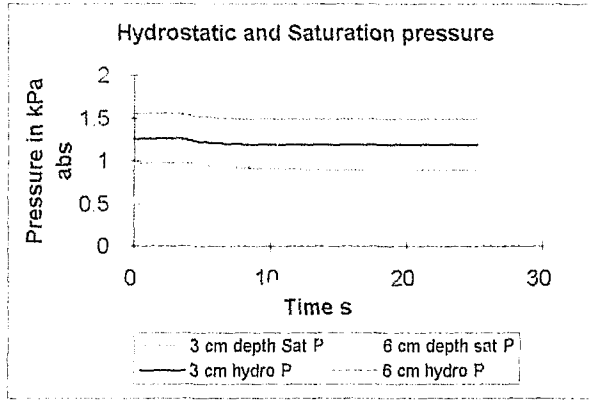
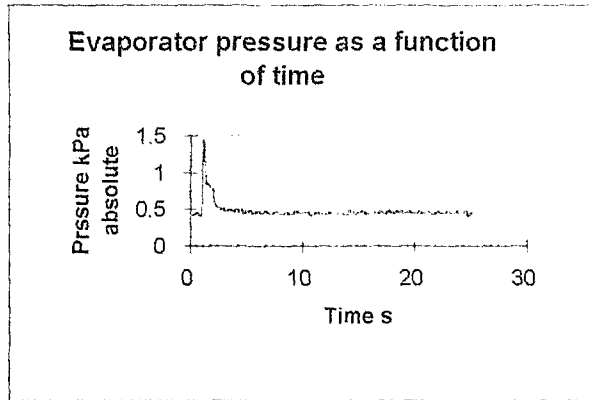
Temperature distribution



NEF (t) as a function of time

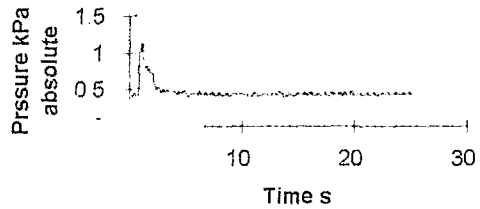


5°C initial, 9 cm liquid height, test 3

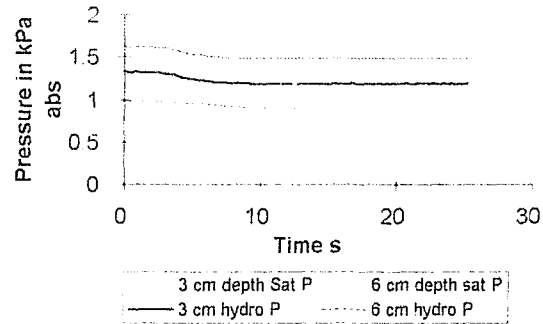


5°C initial, 9 cm liquid height, test 4

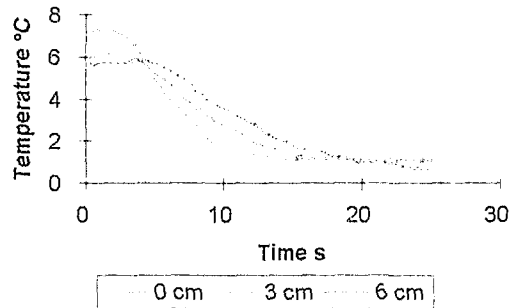
Evaporator pressure as a function of time



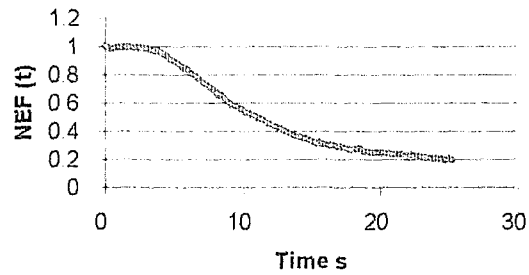
Hydrostatic and Saturation pressure



Temperature distribution

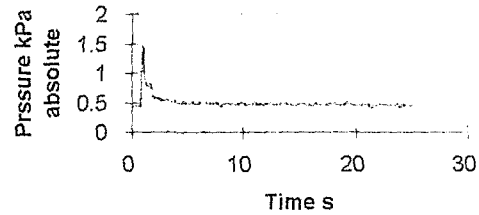


NEF (t) as a function of time

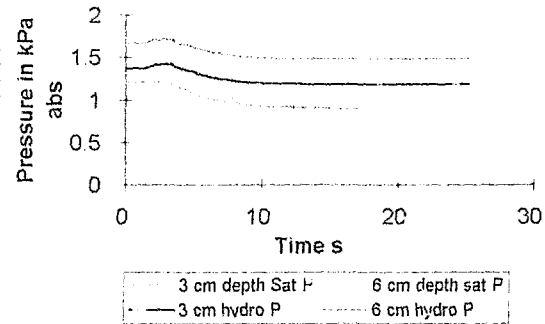


13°C initial, 9 cm liquid height, test 1

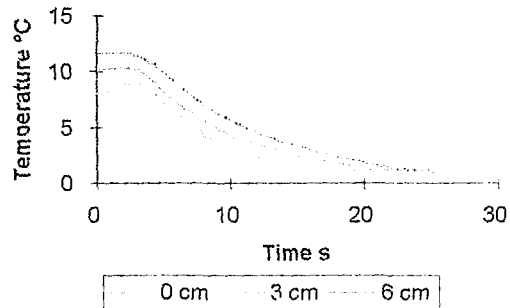
Evaporator pressure as a function of time



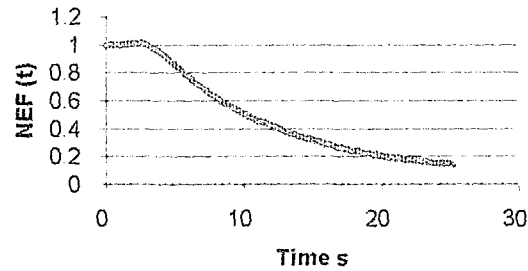
Hydrostatic and Saturation pressure



Temperature distribution

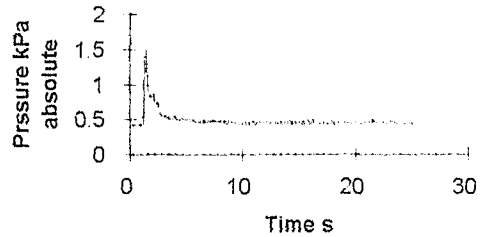


NEF (t) as a function of time

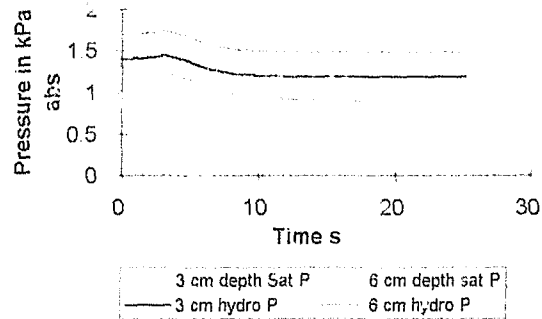


13°C initial, 9 cm liquid height, test 2

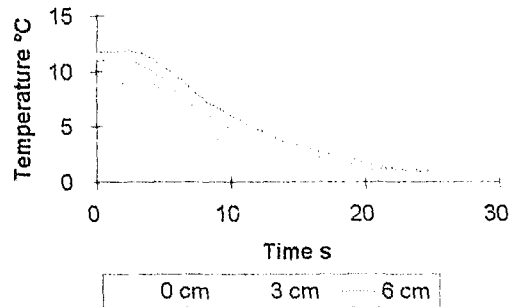
Evaporator pressure as a function of time



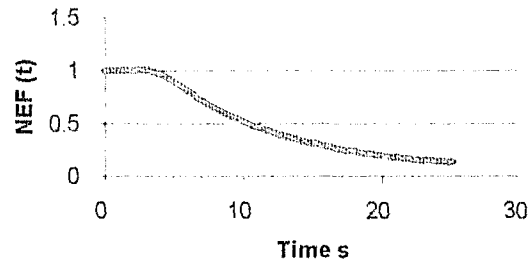
Hydrostatic and Saturation pressure



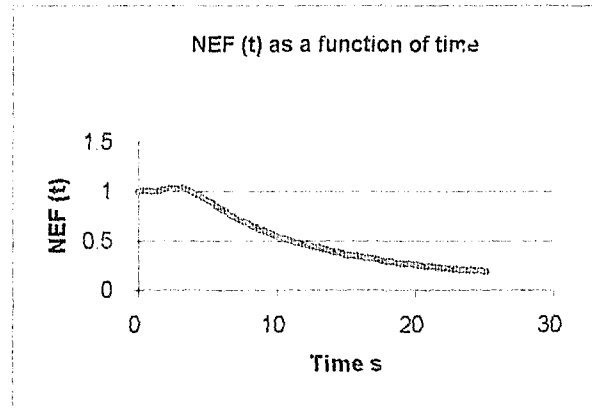
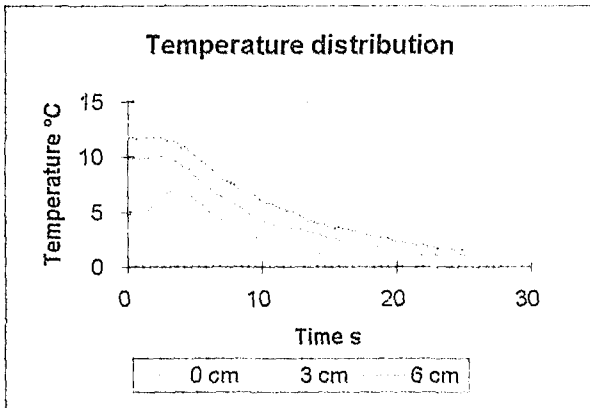
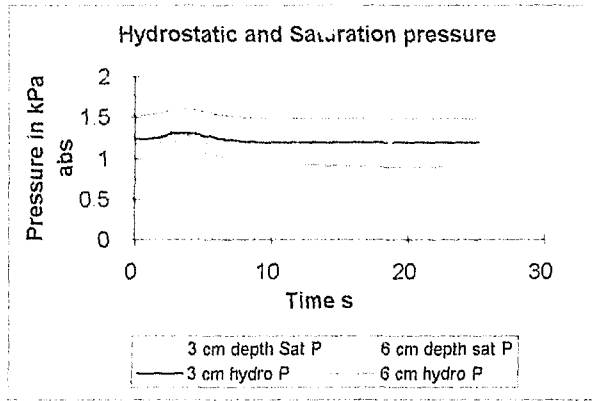
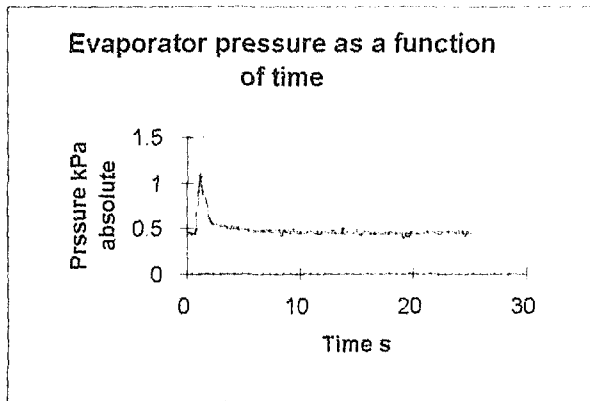
Temperature distribution



NEF (t) as a function of time

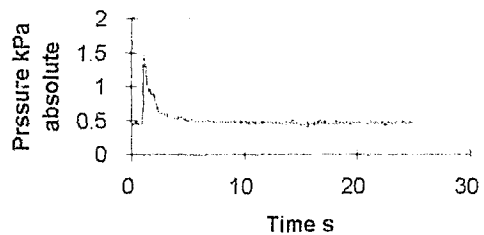


13°C initial, 9 cm liquid height, test 3

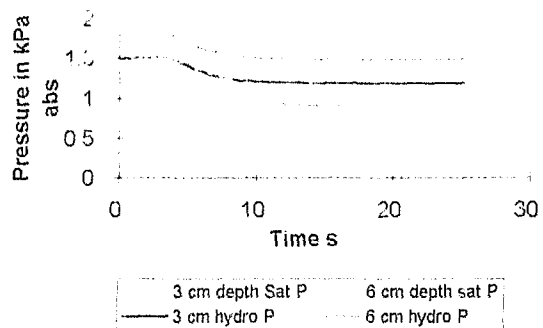


13°C initial, 9 cm liquid height, test 4

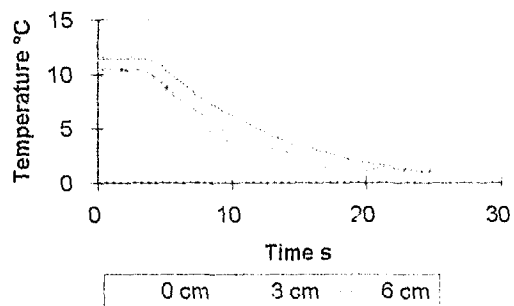
Evaporator pressure as a function of time



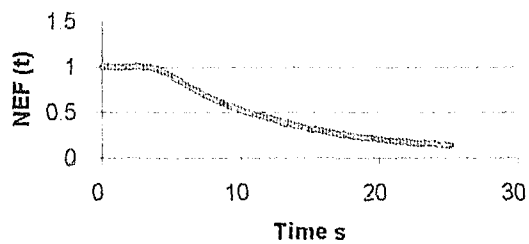
Hydrostatic and Saturation pressure



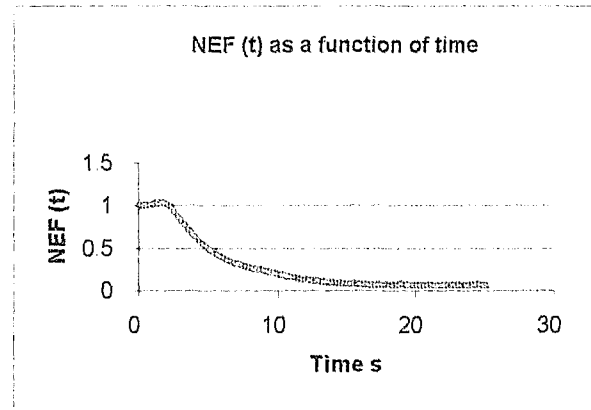
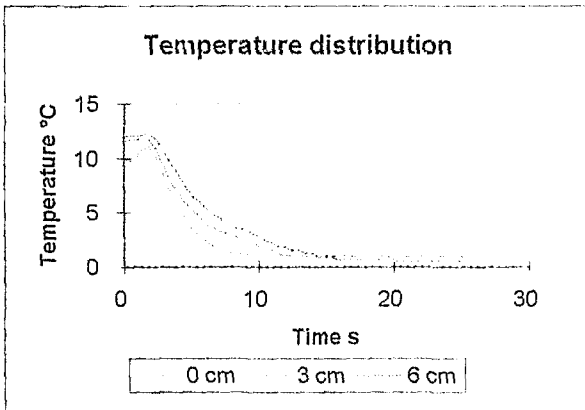
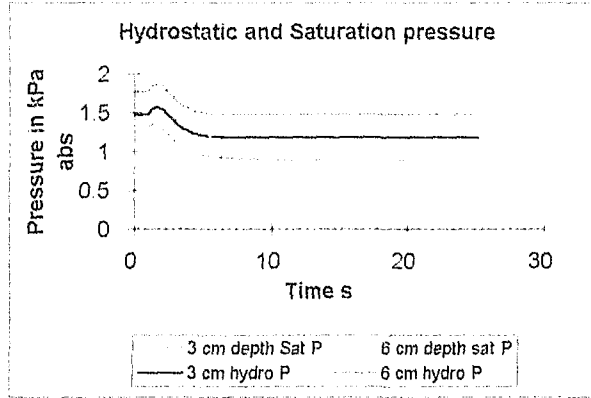
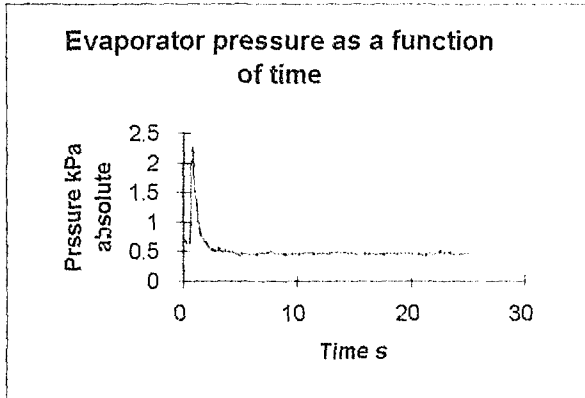
Temperature distribution



NEF (t) as a function of time

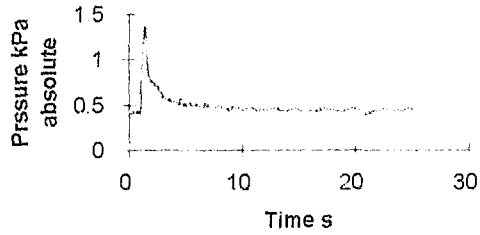


19°C initial, 9 cm liquid height, test 1

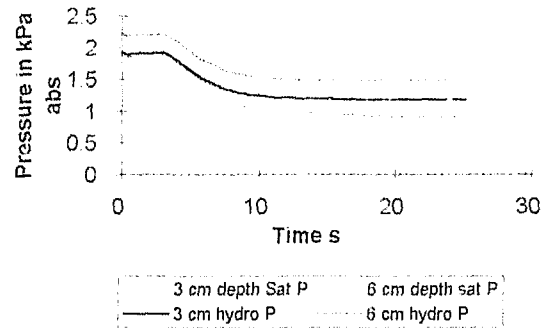


19°C initial, 9 cm liquid height, test 2

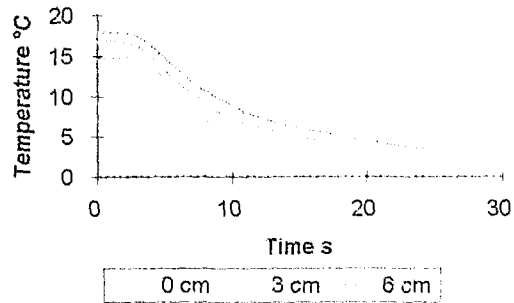
Evaporator pressure as a function of time



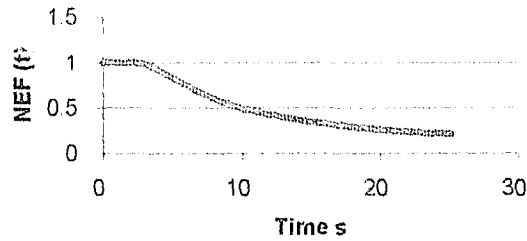
Hydrostatic and Saturation pressure



Temperature distribution

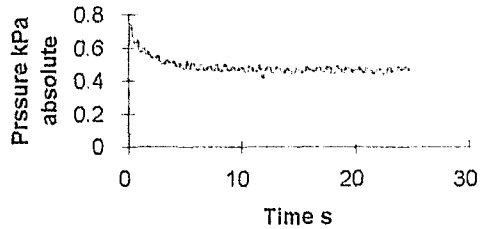


NEF (t) as a function of time

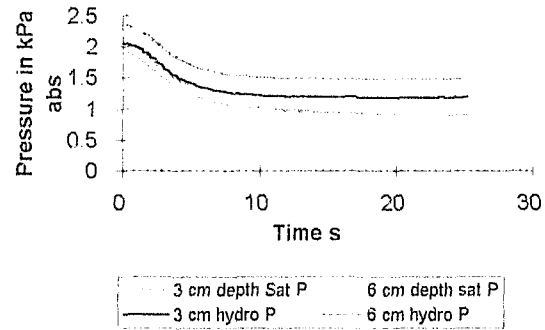


19°C initial, 9 cm liquid height, test 3

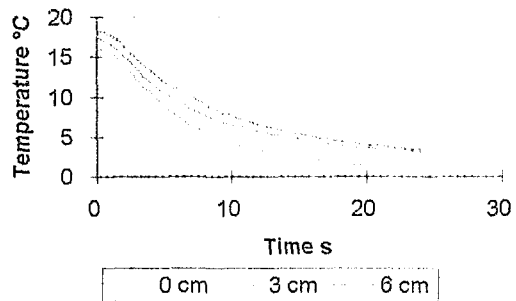
Evaporator pressure as a function of time



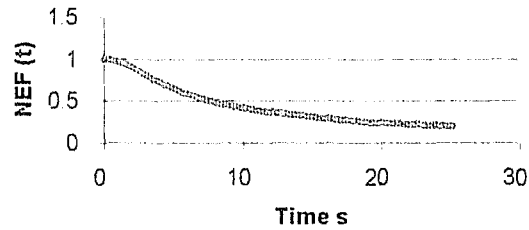
Hydrostatic and Saturation pressure



Temperature distribution

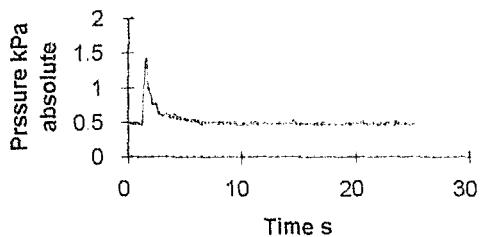


NEF (t) as a function of time

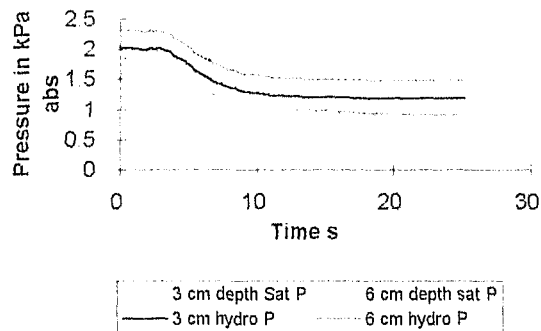


19°C initial, 9 cm liquid height, test 4

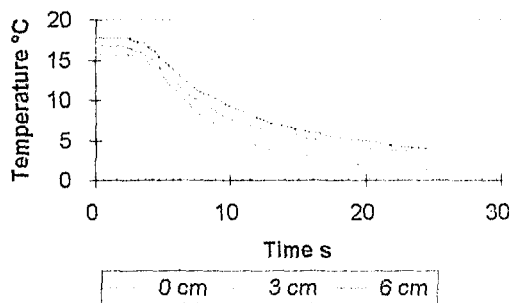
Evaporator pressure as a function of time



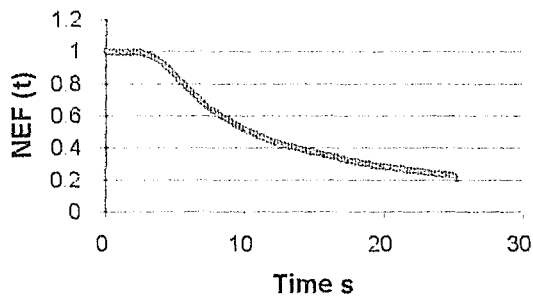
Hydrostatic and Saturation pressure



Temperature distribution

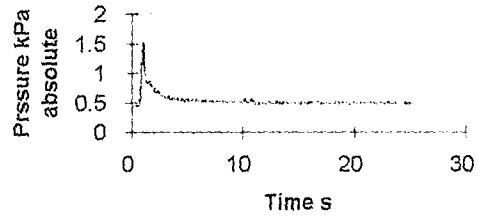


NEF (t) as a function of time

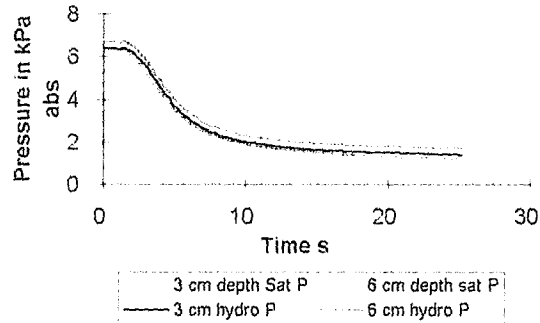


40°C initial, 9 cm liquid height, test 1

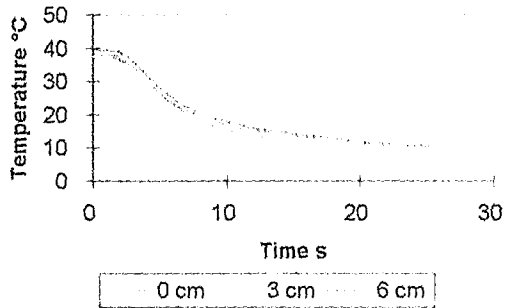
Evaporator pressure as a function of time



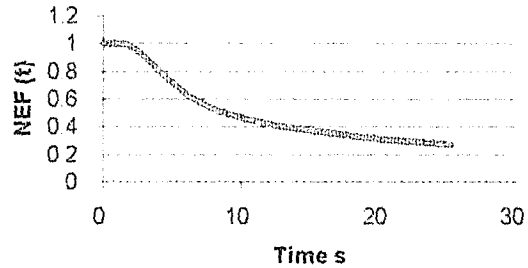
Hydrostatic and Saturation pressure



Temperature distribution

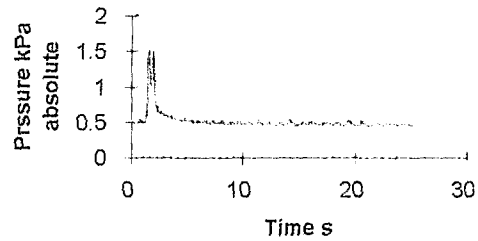


NEF (t) as a function of time

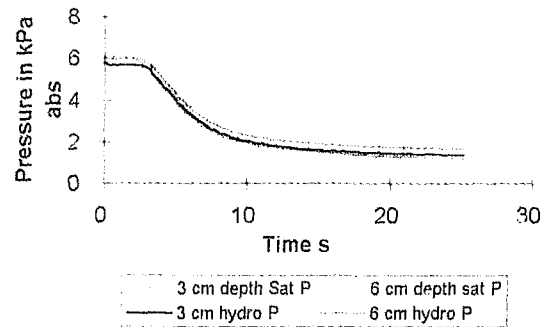


40°C initial, 9 cm liquid height, test 2

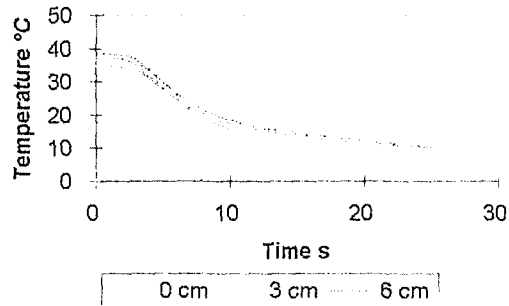
Evaporator pressure as a function of time



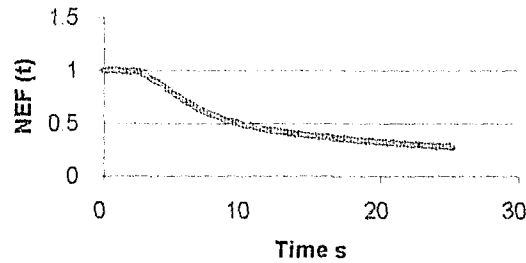
Hydrostatic and Saturation pressure



Temperature distribution

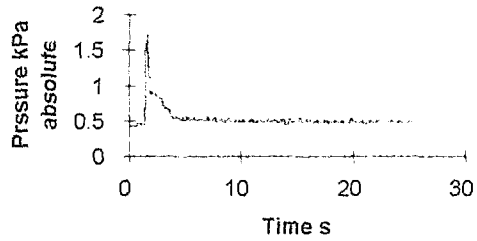


NEF (t) as a function of time

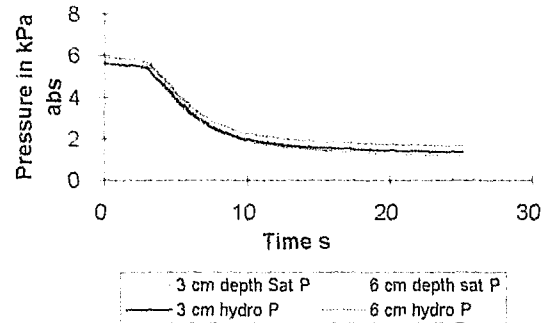


40°C initial, 9 cm liquid height, test 3

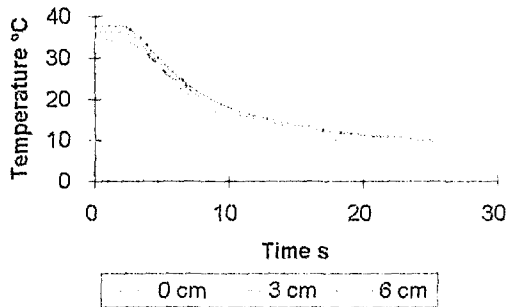
Evaporator pressure as a function of time



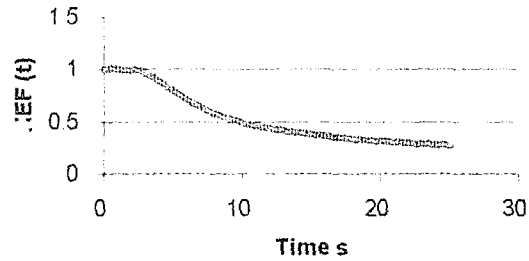
Hydrostatic and Saturation pressure



Temperature distribution

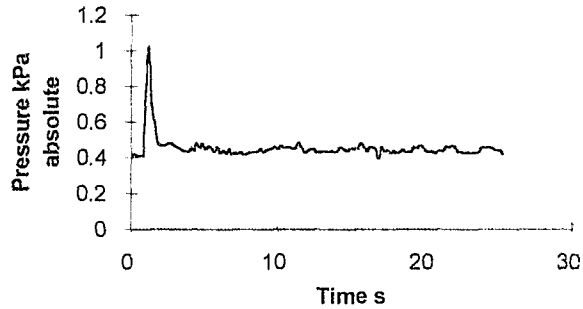


NEF (t) as a function of time

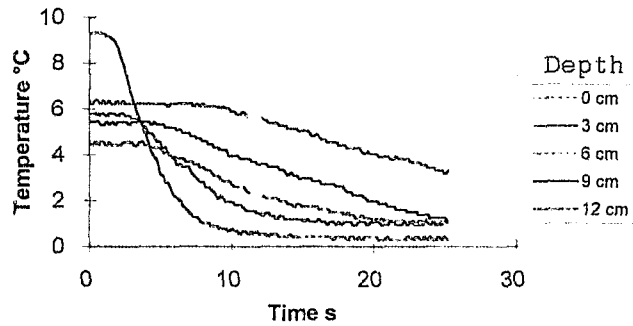


5 °C initial, 12 cm liquid height, test 1

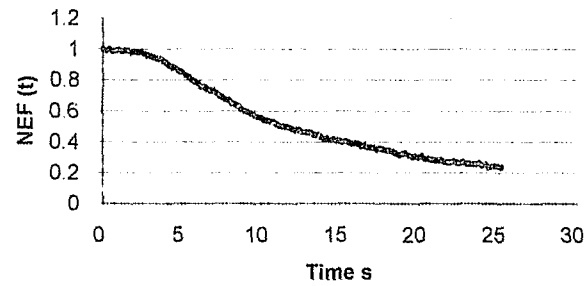
Evaporator pressure as a function of time



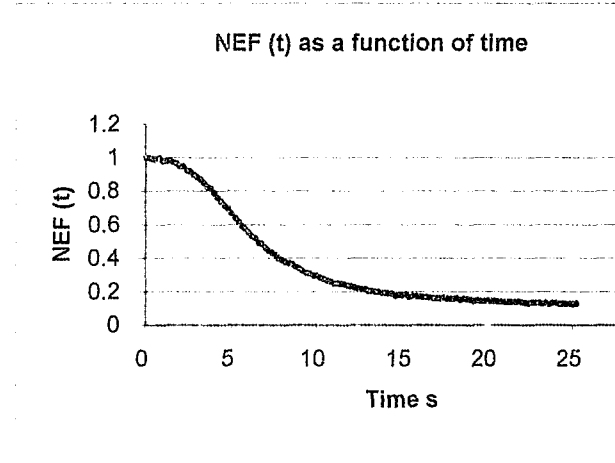
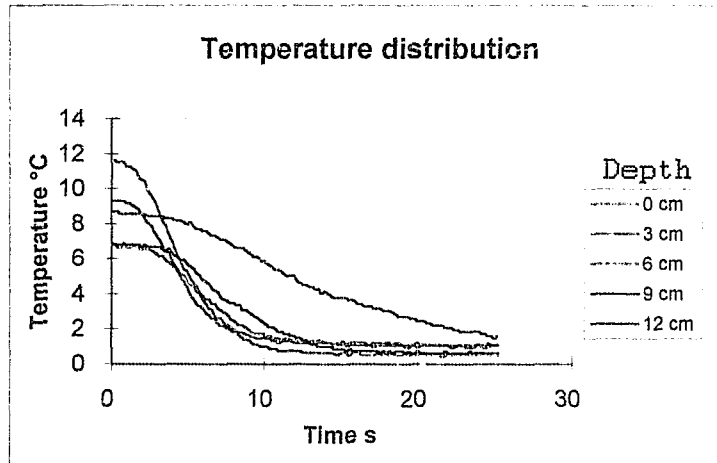
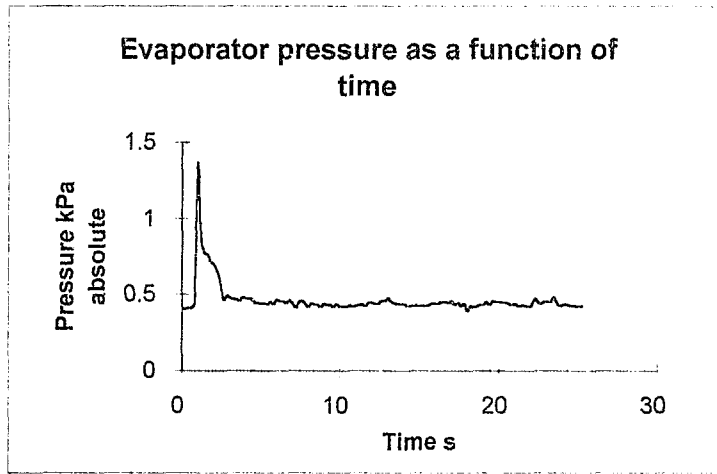
Temperature distribution



NEF (t) as a function of time

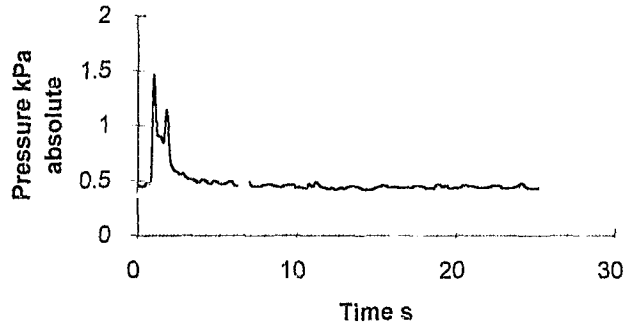


5 °C initial, 12 cm liquid height, test 2

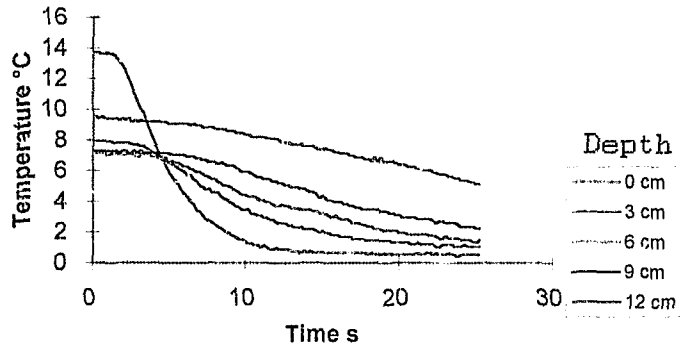


5 °C initial, 12 cm liquid height, test 3

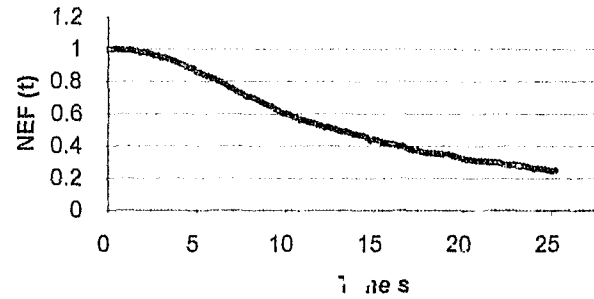
Evaporator pressure as a function of time



Temperature distribution

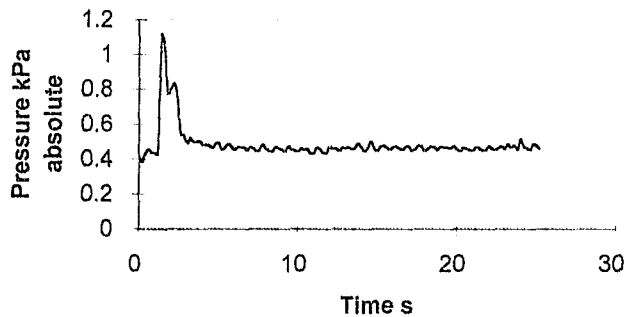


NEF (t) as a function of time

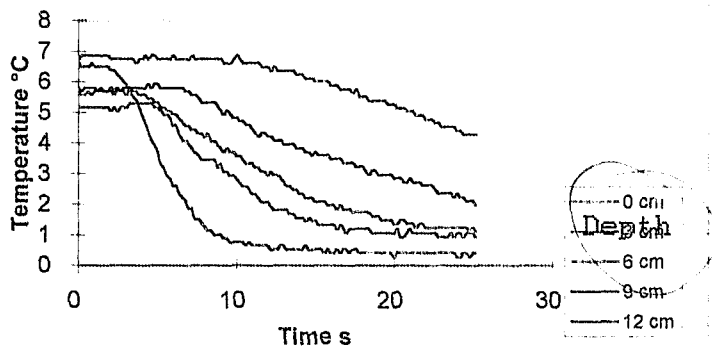


5 °C initial, 12 cm liquid height, test 4

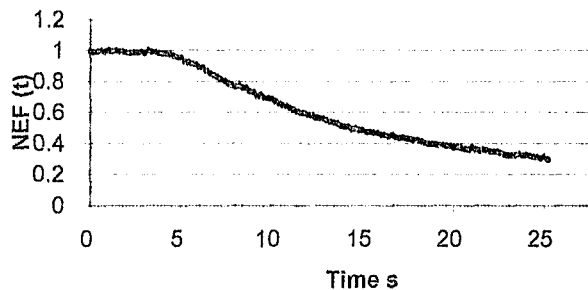
Evaporator pressure as a function of time



Temperature distribution

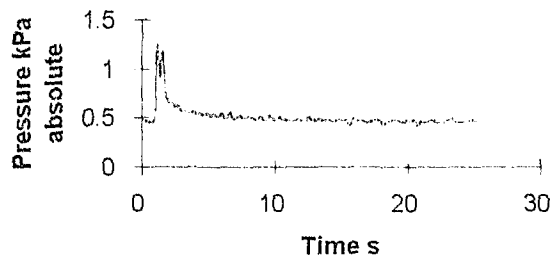


NEF (t) as a function of time

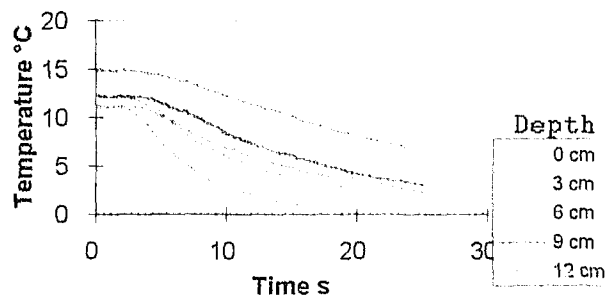


13 °C initial, 12 cm liquid height, test 1

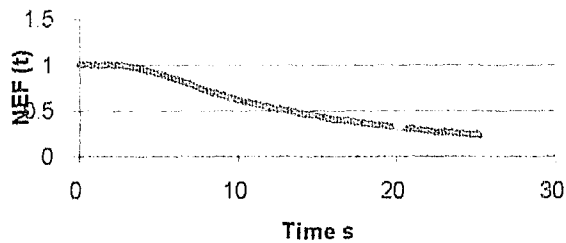
Evaporator pressure as a function of time



Temperature distribution

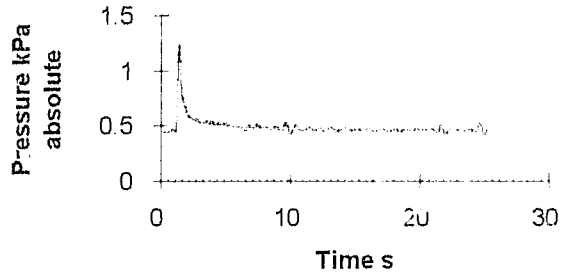


NEF (t) as a function of time

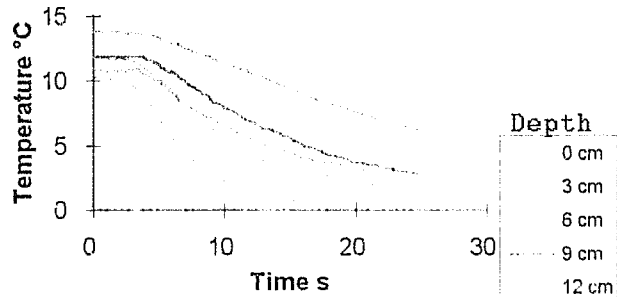


13 °C initial, 12 cm liquid height, test 2

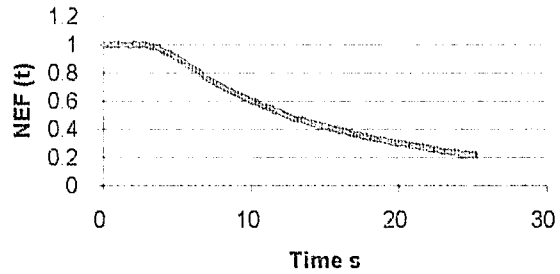
Evaporator pressure as a function of time



Temperature distribution

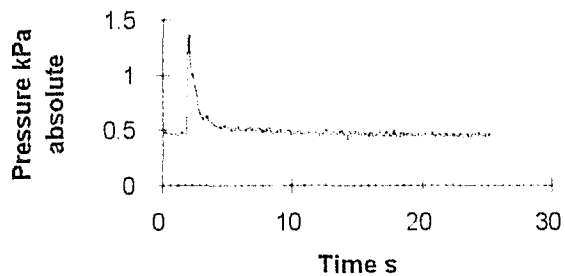


NEF (t) as a function of time

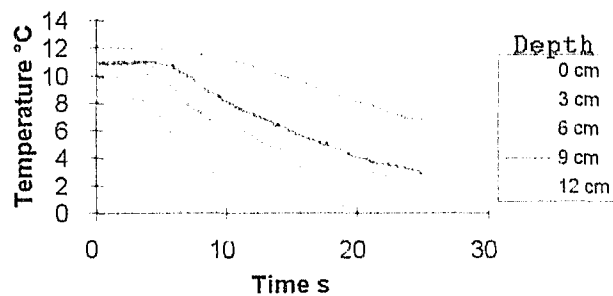


13 °C initial, 12 cm liquid height, test 3

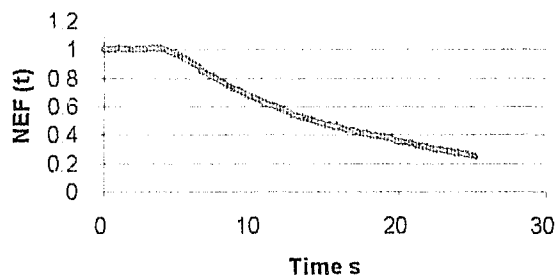
Evaporator pressure as a function of time



Temperature distribution

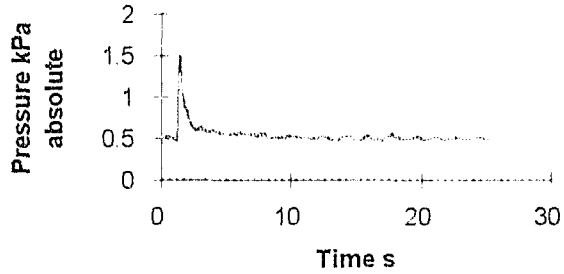


NEF (t) as a function of time

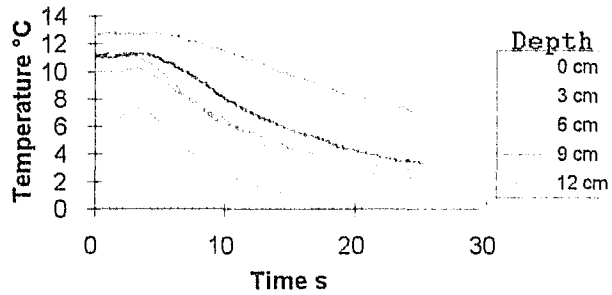


13 °C initial, 12 cm liquid height, test 4

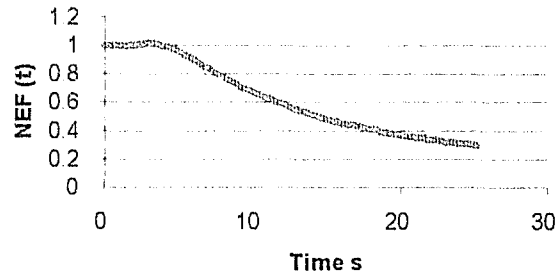
Evaporator pressure as a function of time



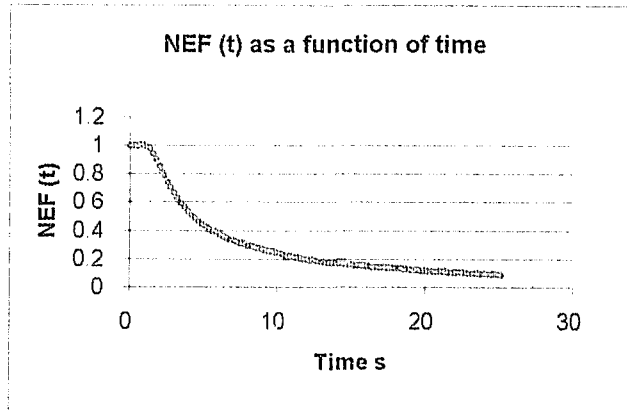
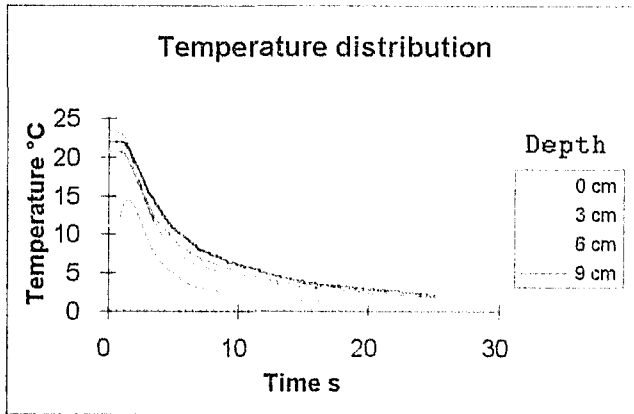
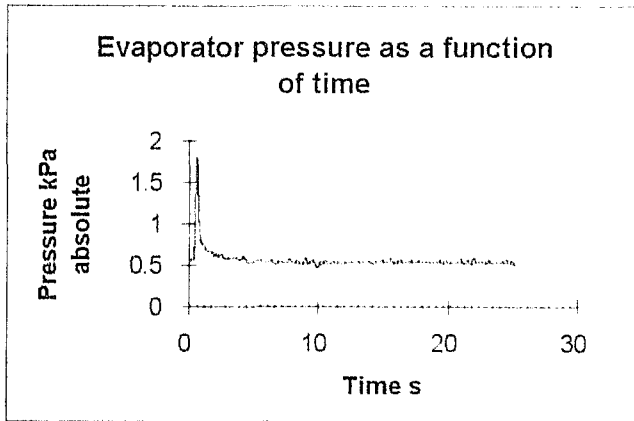
Temperature distribution



NEF (t) as a function of time

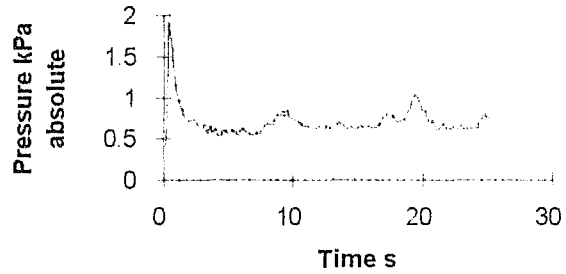


25 °C initial, 12 cm liquid height, test 1

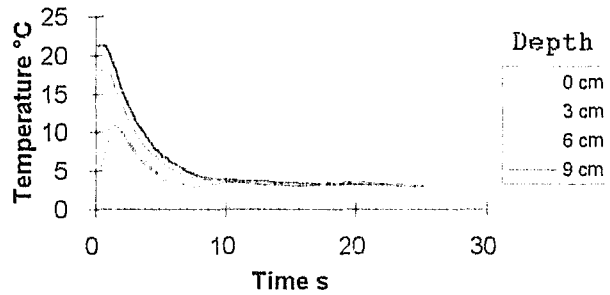


25 °C initial, 12 cm liquid height, test 2

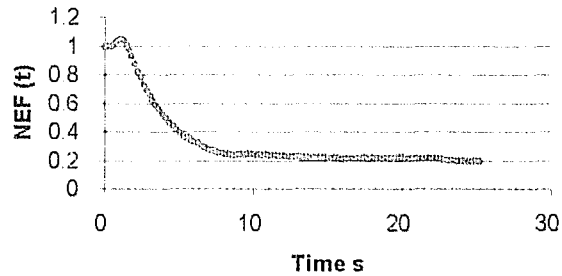
Evaporator pressure as a function of time



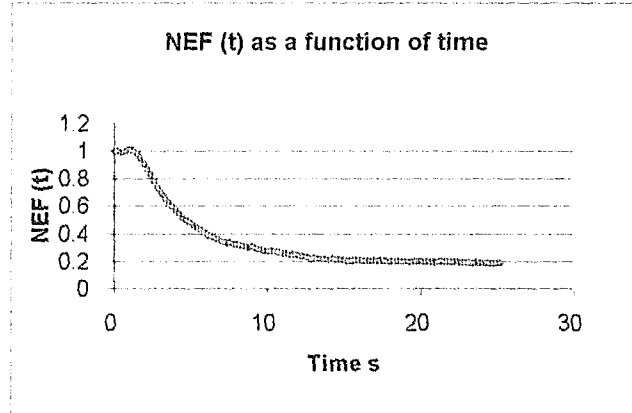
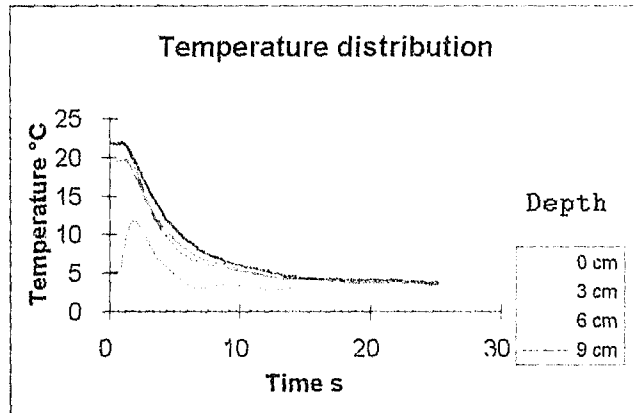
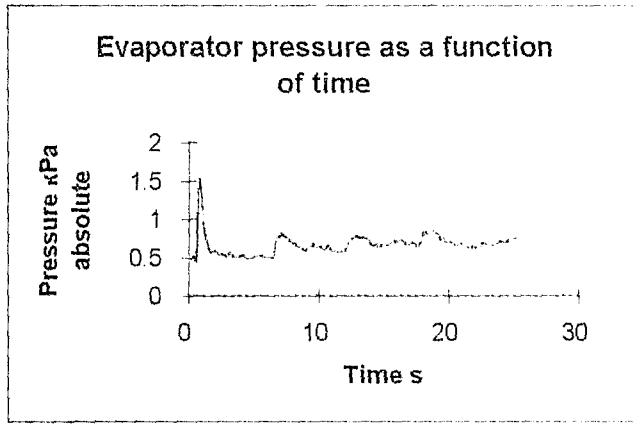
Temperature distribution



NEF (t) as a function of time

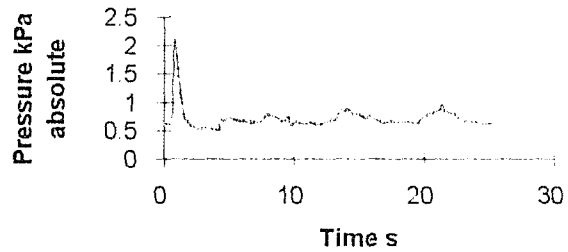


25 °C initial, 12 cm liquid height, test 3

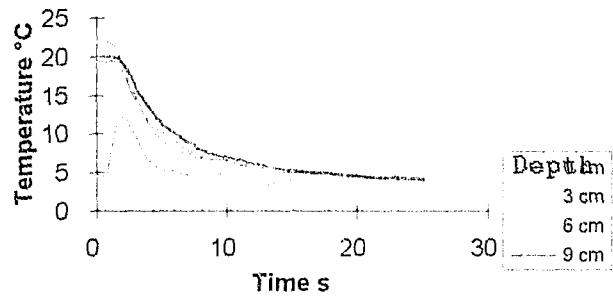


25 °C initial, 12 cm liquid height, test 4

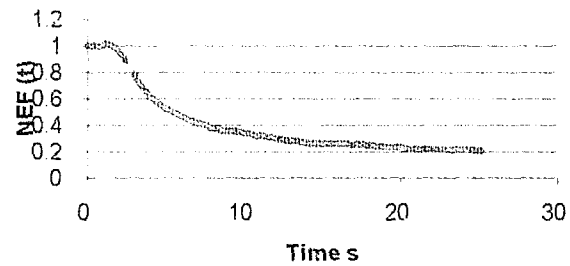
Evaporator pressure as a function of time



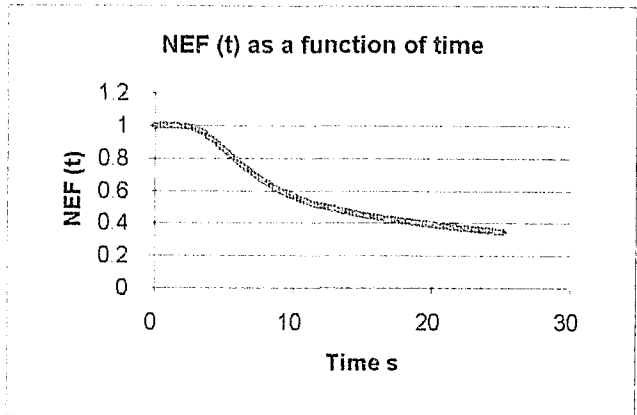
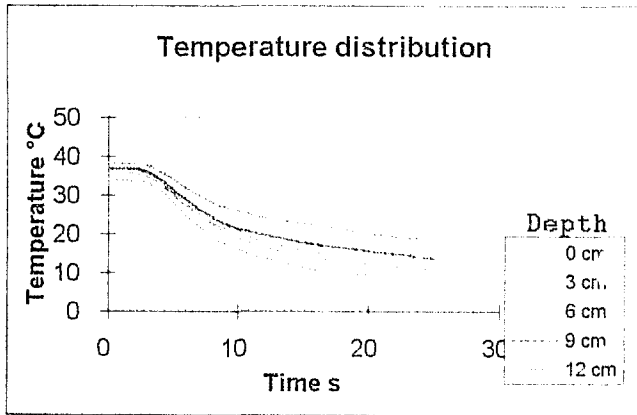
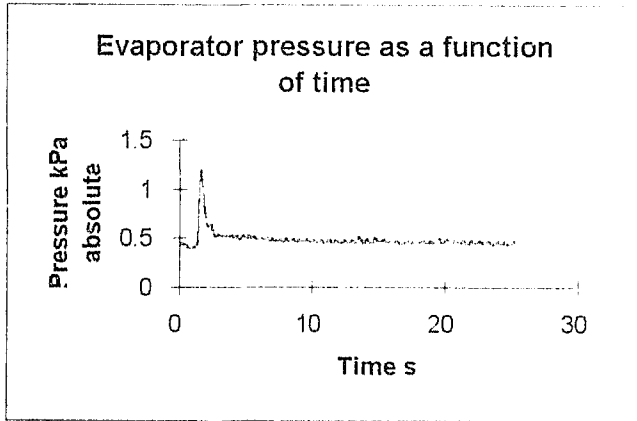
Temperature distribution



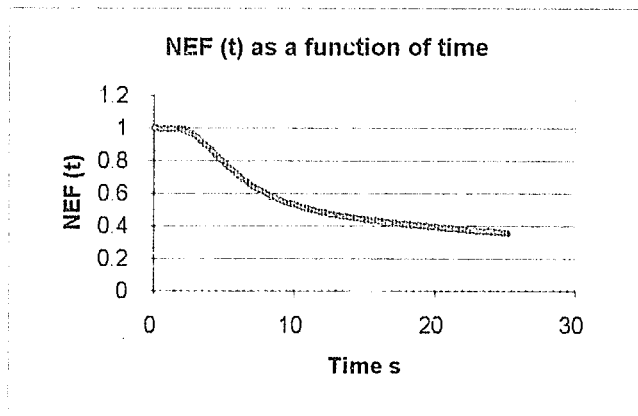
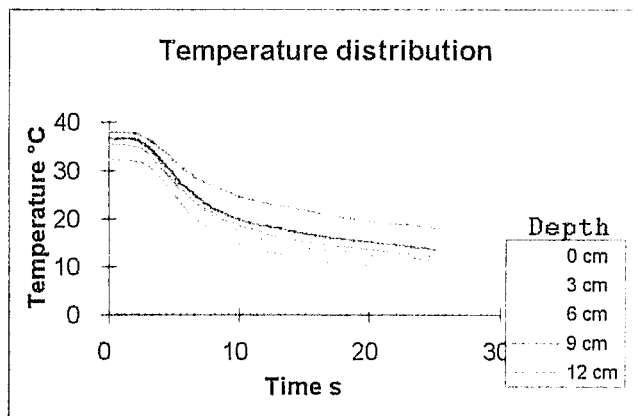
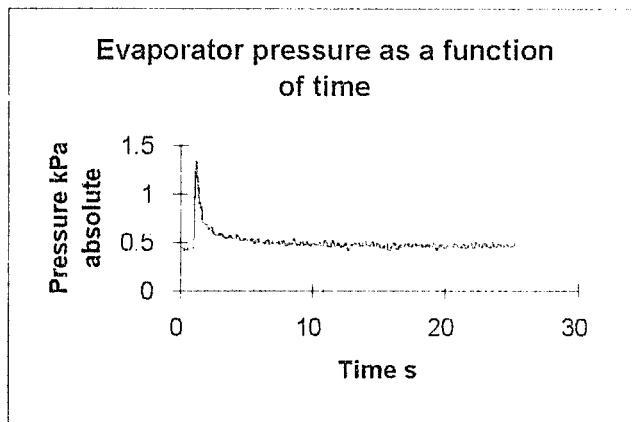
NEF (t) as a function of time



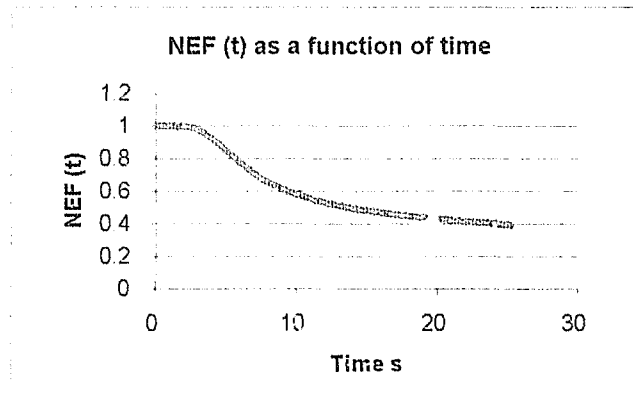
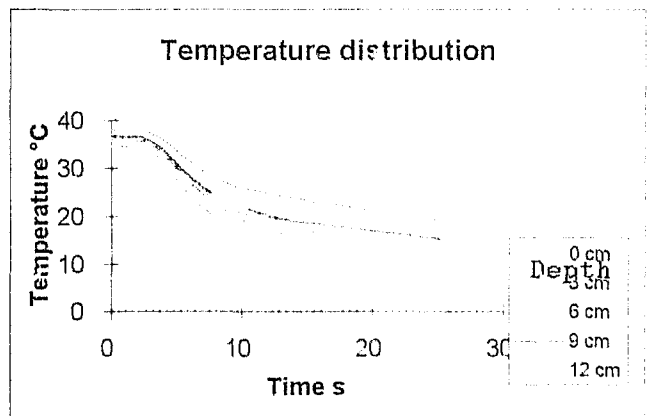
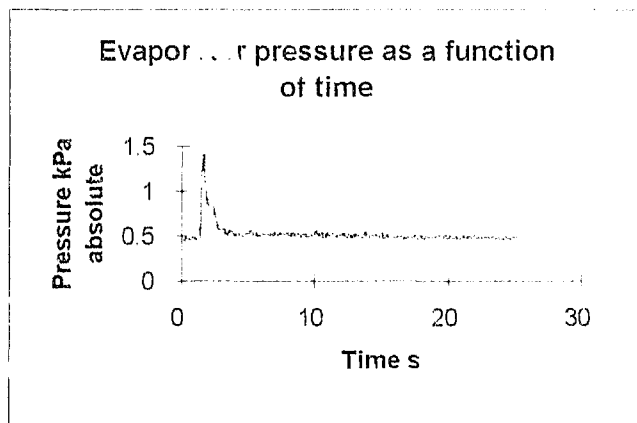
40°C initial, 12 cm liquid height, test 1



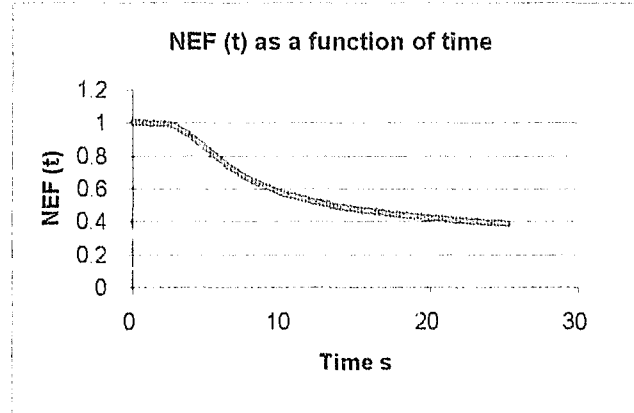
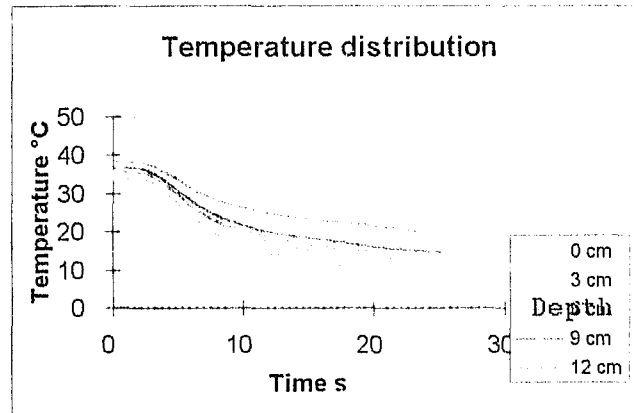
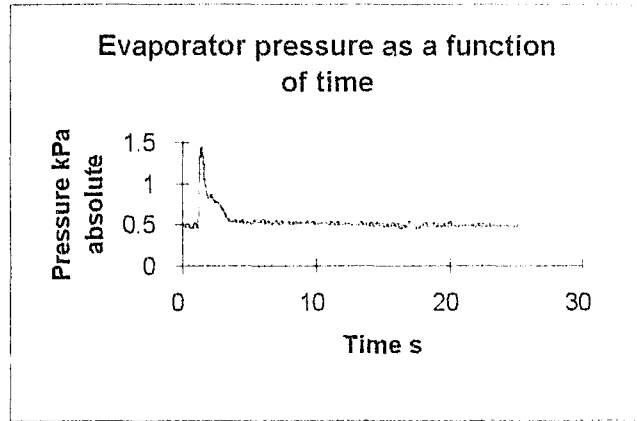
40°C initial, 12 cm liquid height, test 2



40°C initial, 12 cm liquid height, test 3

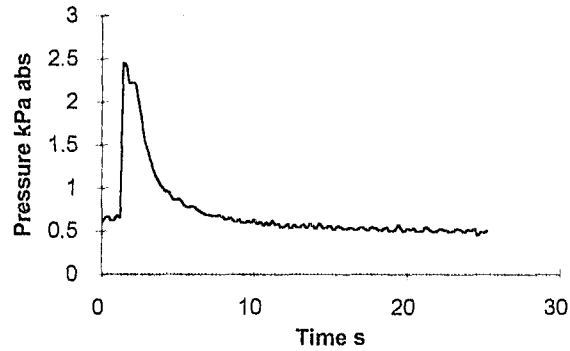


40°C initial, 12 cm liquid height, test 4

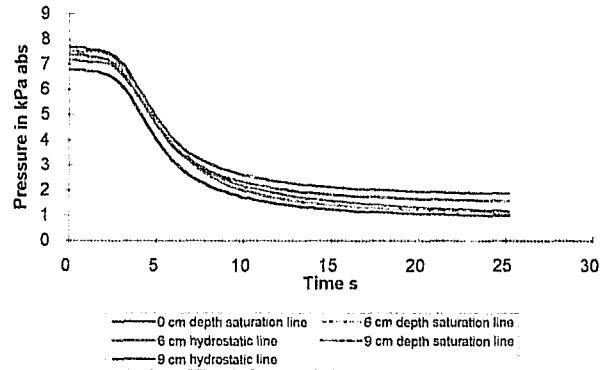


5°C initial, 15 cm liquid height, test 1

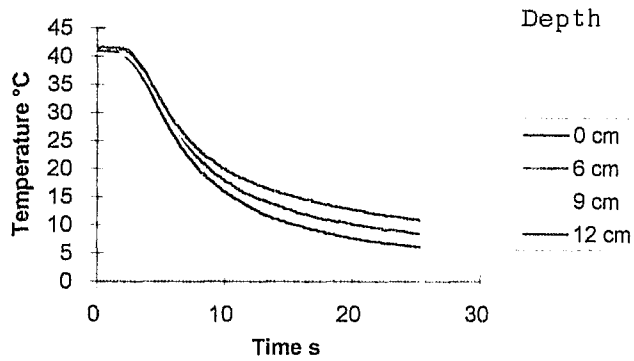
Evaporator pressure as a function of time



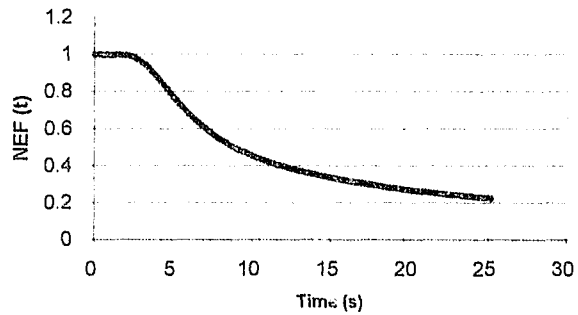
Hydrostatic and Saturation pressure



Temperature distribution

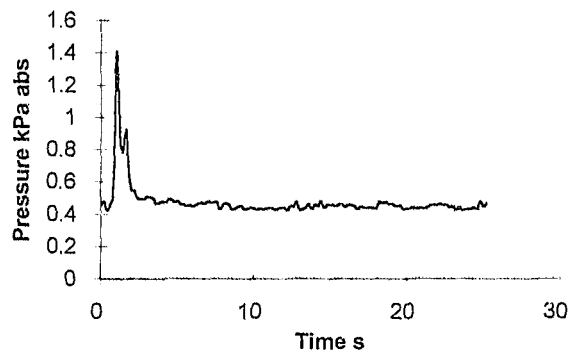


NEF (t) as a function of time

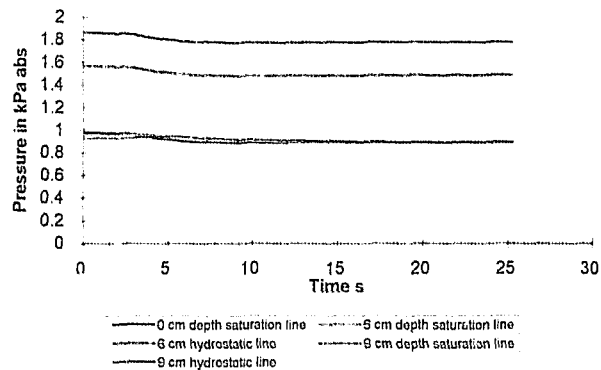


5°C initial, 15 cm liquid height, test 2

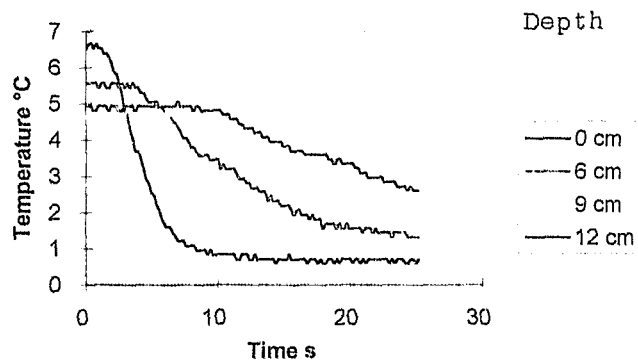
Evaporator pressure as a function of time



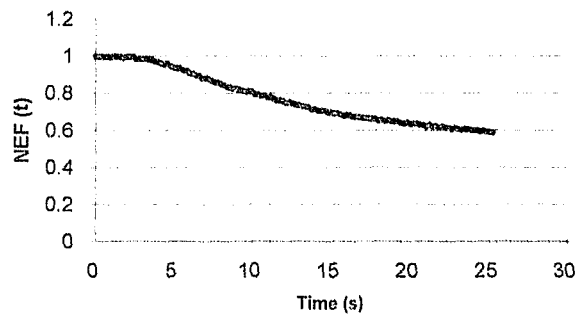
Hydrostatic and Saturation pressure



Temperature distribution

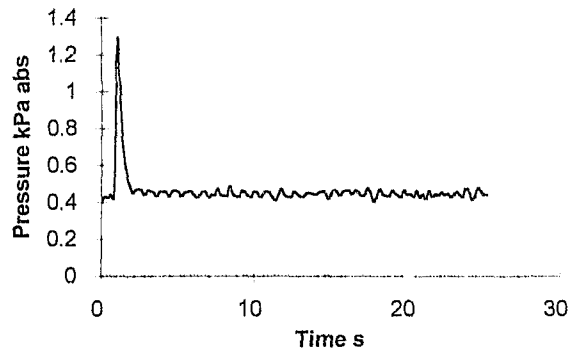


NEF (t) as a function of time

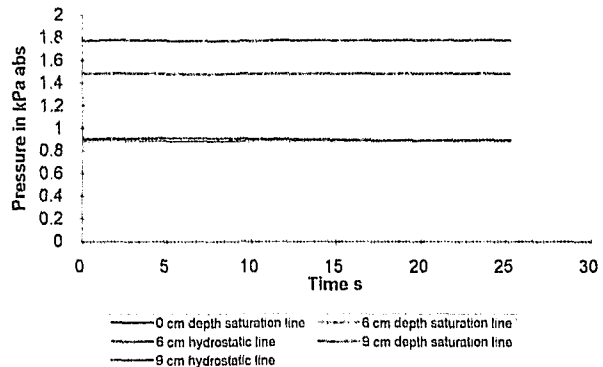


5°C initial, 15 cm liquid height, test 3

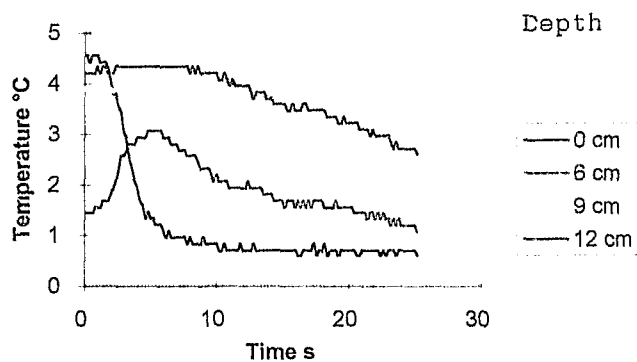
Evaporator pressure as a function of time



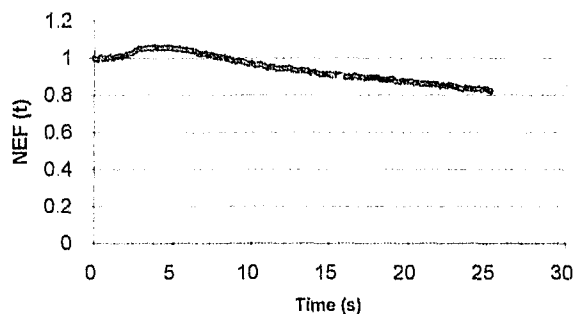
Hydrostatic and Saturation pressure



Temperature distribution

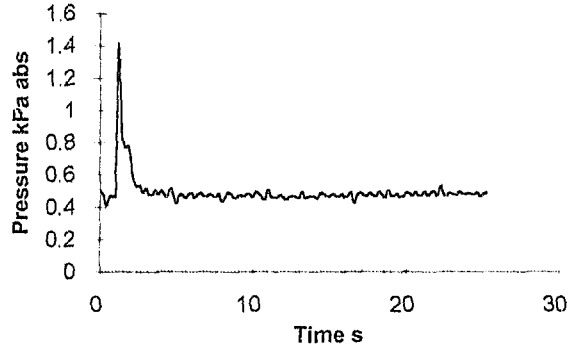


NEF (t) as a function of time

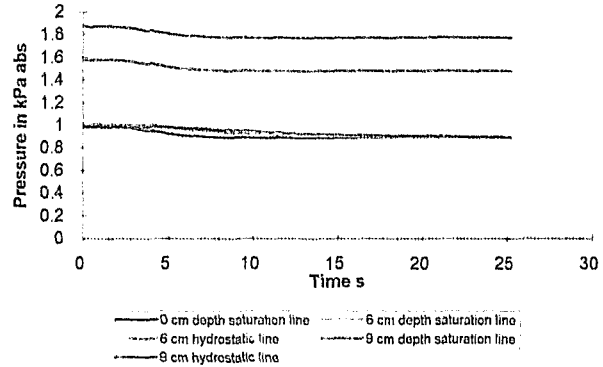


5°C initial, 15 cm liquid height, test 4

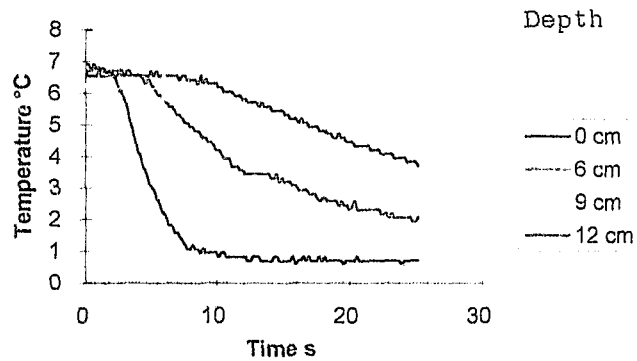
Evaporator pressure as a function of time



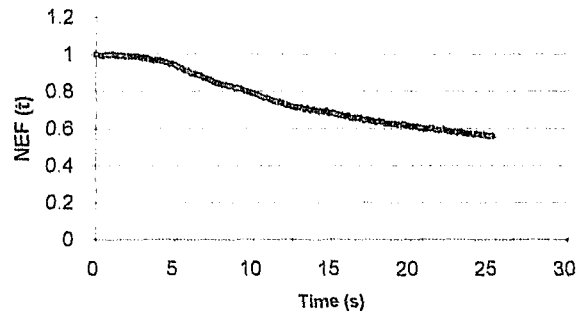
Hydrostatic and Saturation pressure



Temperature distribution

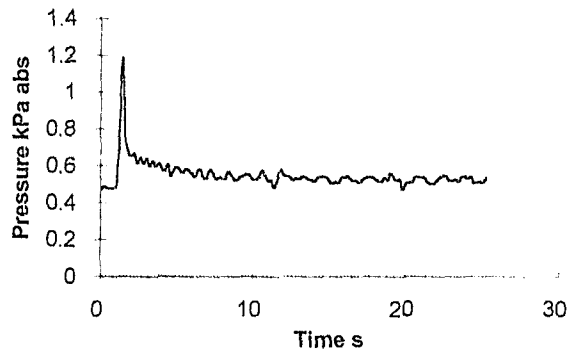


NEF (t) as a function of time

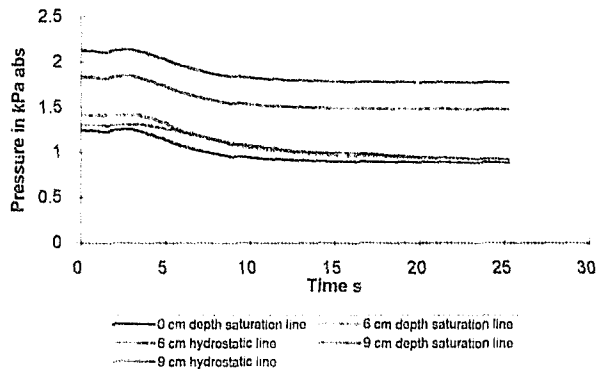


13°C initial, 15 cm liquid height, test 1

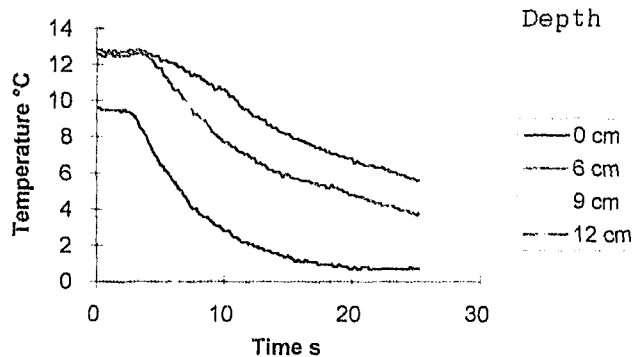
Evaporator pressure as a function of time



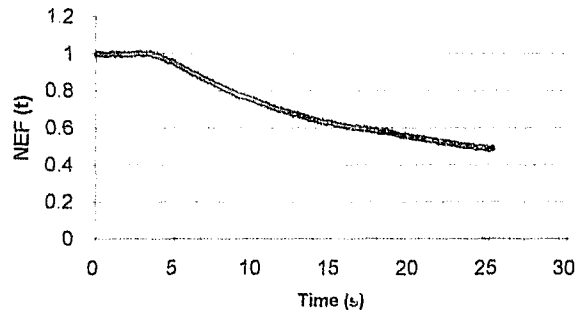
Hydrostatic and Saturation pressure



Temperature distribution

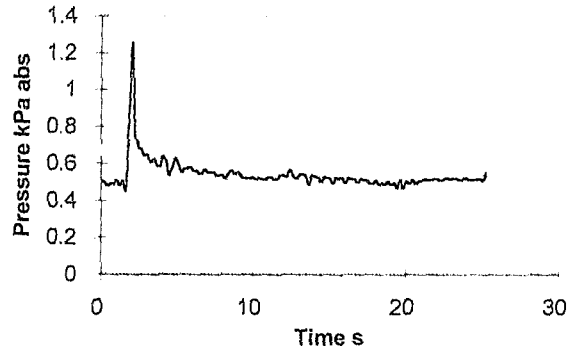


NEF (t) as a function of time

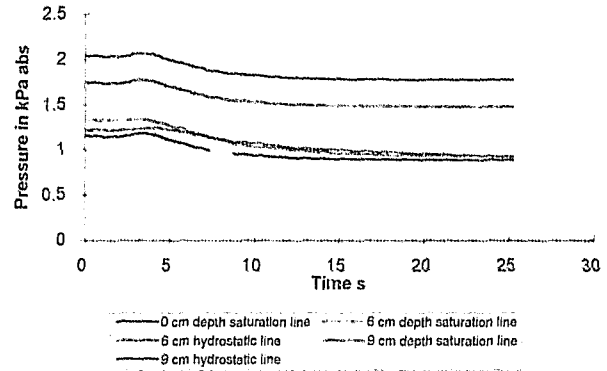


13°C initial, 15 cm liquid height, test 2

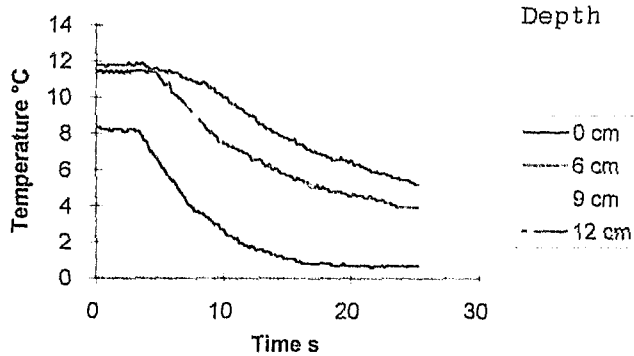
Evaporator pressure as a function of time



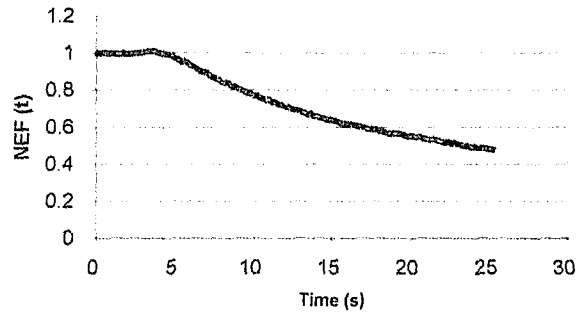
Hydrostatic and Saturation pressure



Temperature distribution

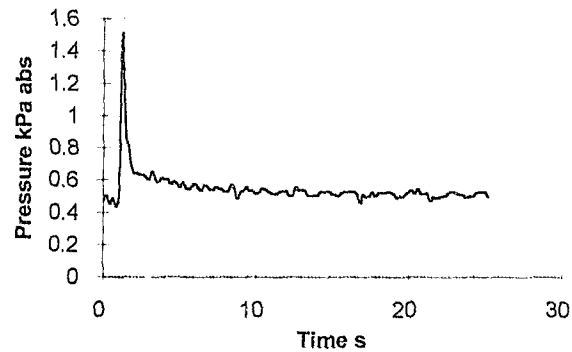


NEF (t) as a function of time

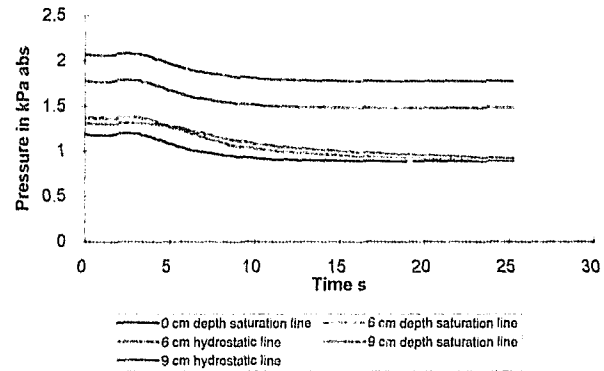


13°C initial, 15 cm liquid height, test 4

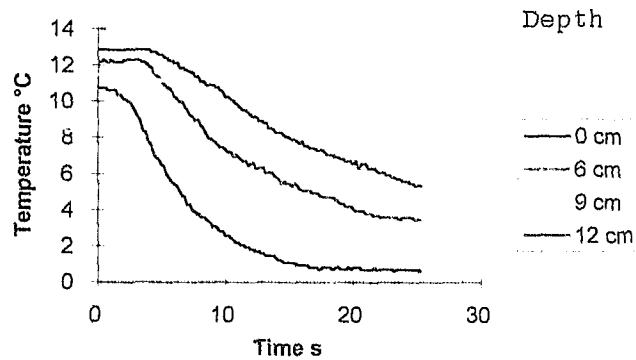
Evaporator pressure as a function of time



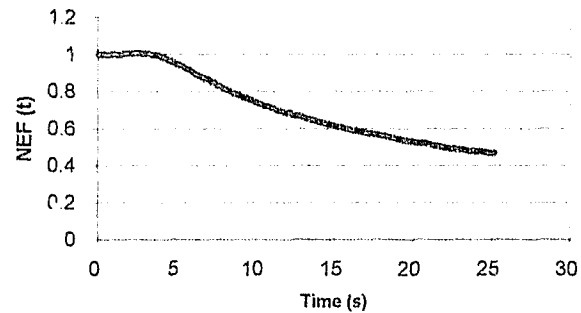
Hydrostatic and Saturation pressure



Temperature distribution

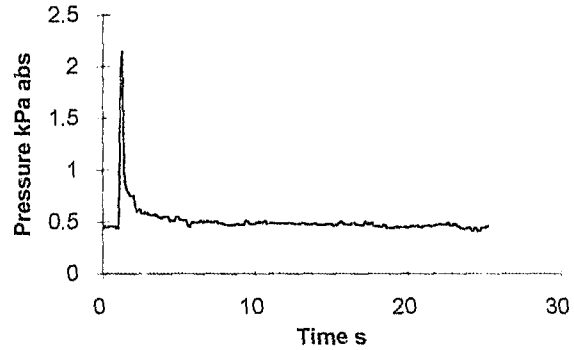


NEF (t) as a function of time

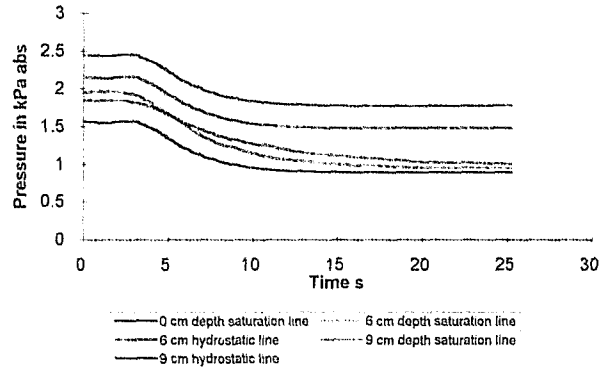


19°C initial, 15 cm liquid height, test 1

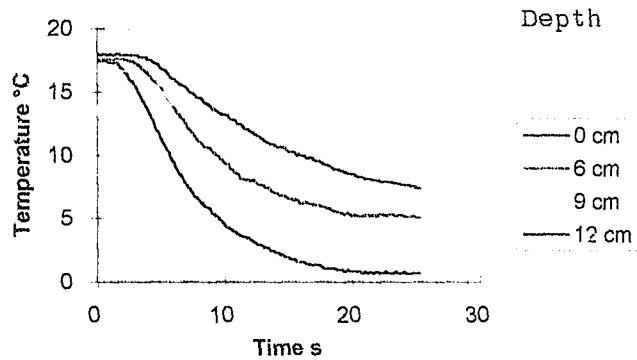
Evaporator pressure as a function of time



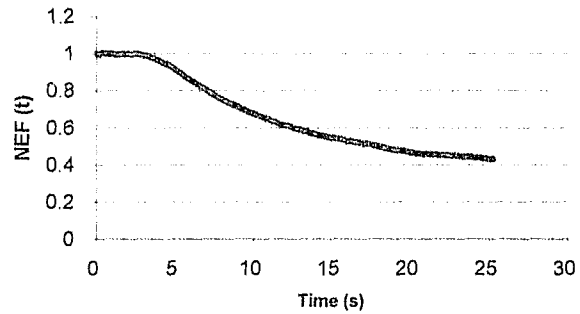
Hydrostatic and Saturation pressure



Temperature distribution

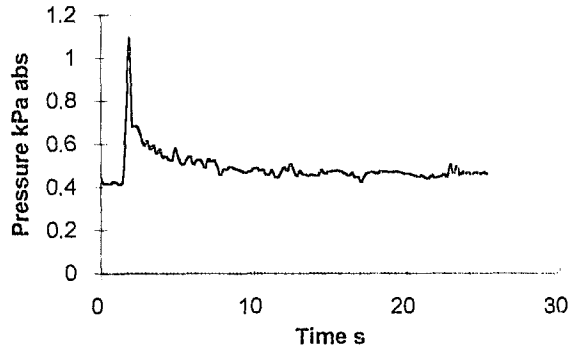


NEF (t) as a function of time

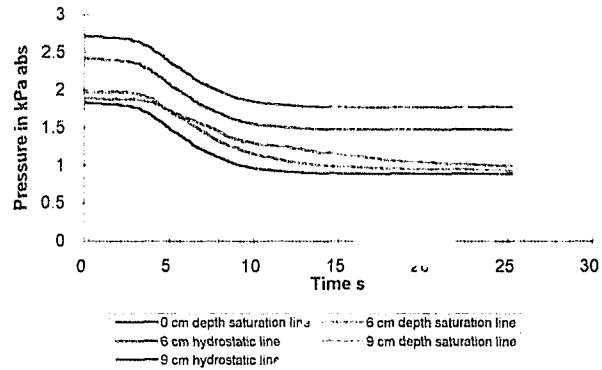


19°C initial, 15 cm liquid height, test 2

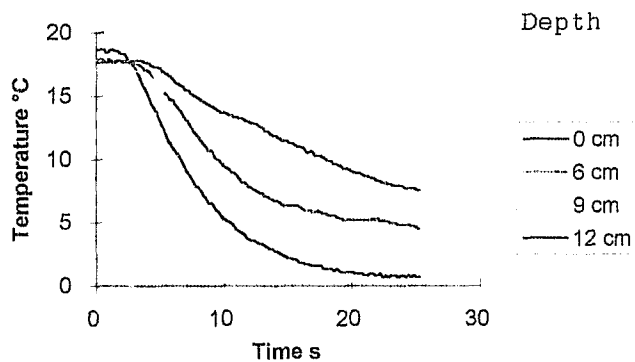
Evaporator pressure as a function of time



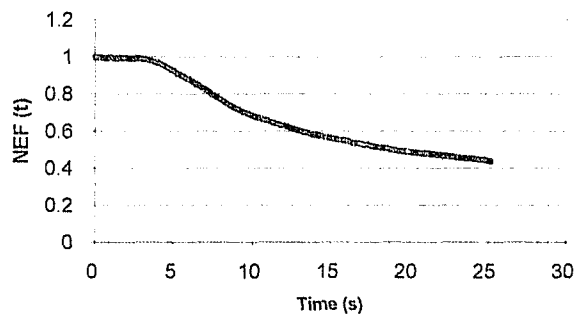
Hydrostatic and Saturation pressure



Temperature distribution

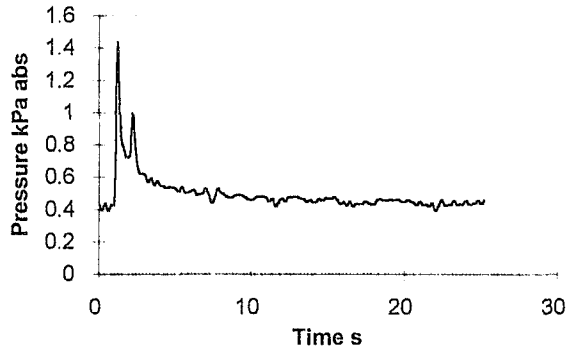


NEF (t) as a function of time

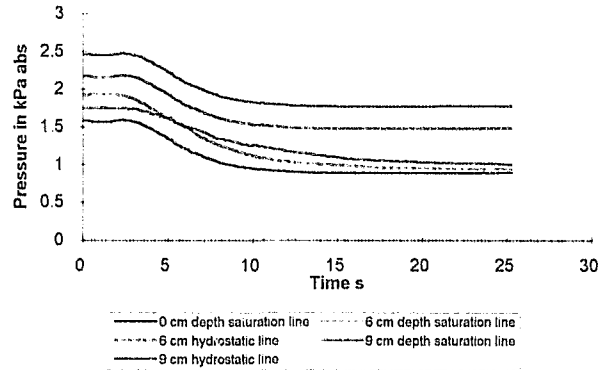


19°C initial, 15 cm liquid height, test 3

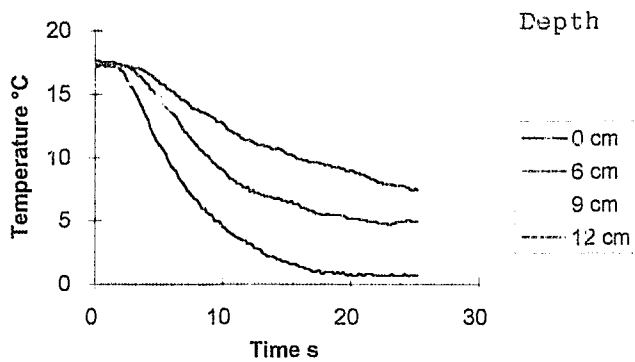
Evaporator pressure as a function of time



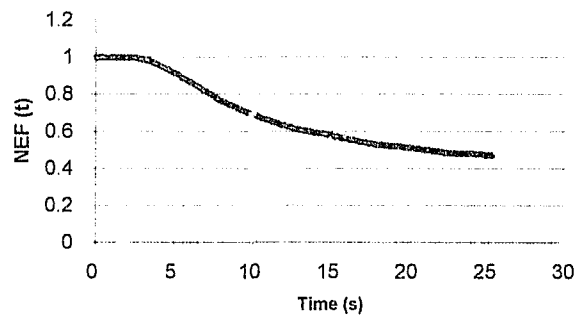
Hydrostatic and Saturation pressure



Temperature distribution

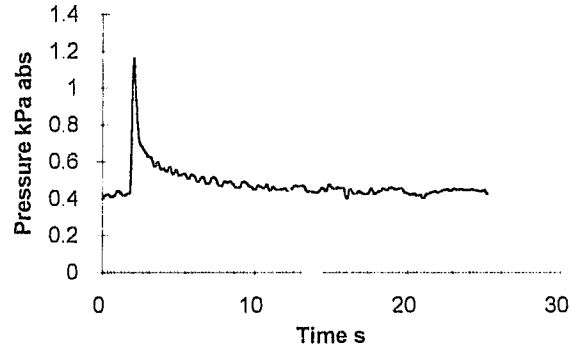


NEF (t) as a function of time

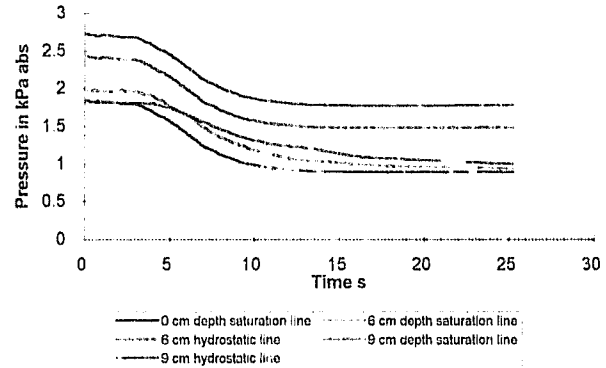


19°C initial, 15 cm liquid height, test 4

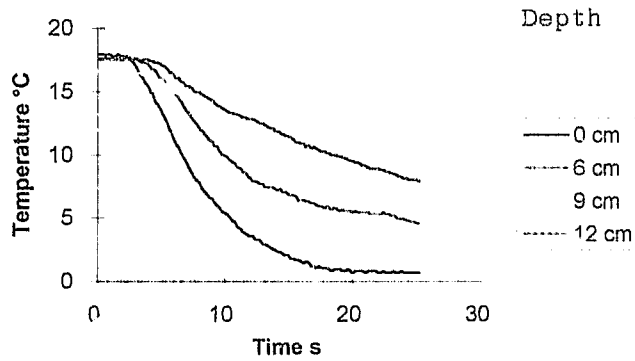
Evaporator pressure as a function of time



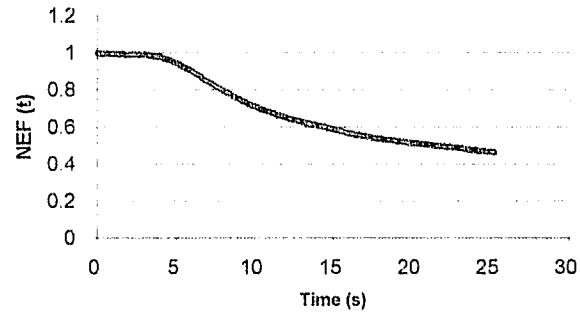
Hydrostatic and Saturation pressure



Temperature distribution

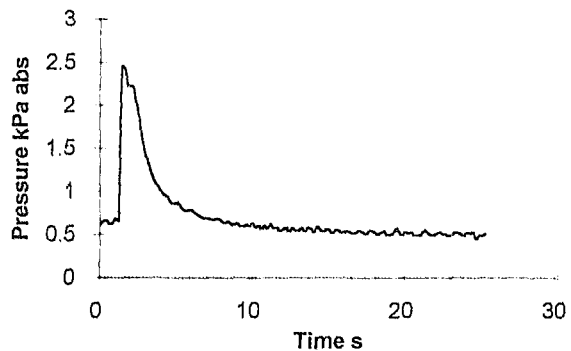


NEF (t) as a function of time

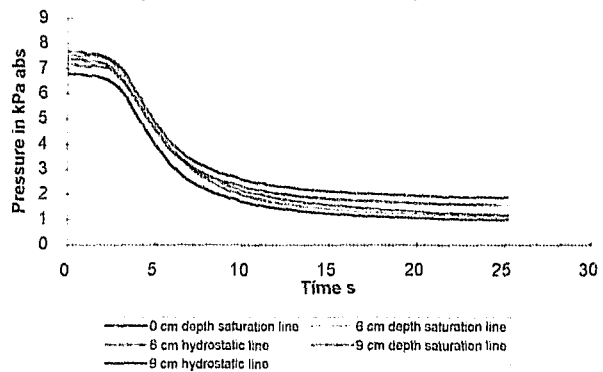


40°C initial, 15 cm liquid height, test 1

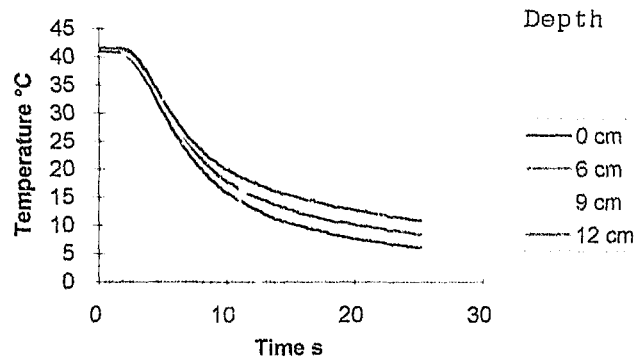
Evaporator pressure as a function of time



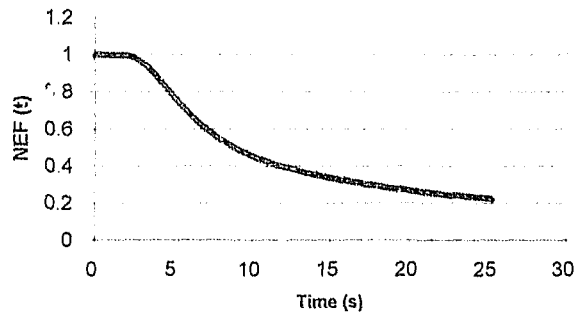
Hydrostatic and Saturation pressure



Temperature distribution

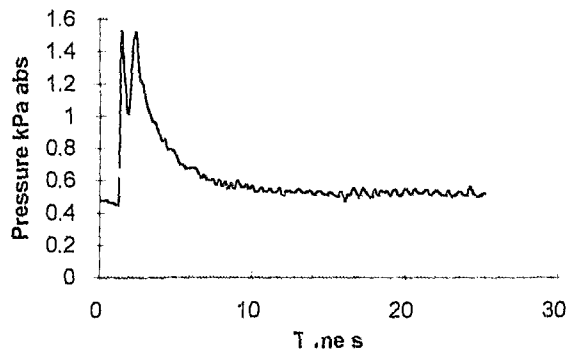


NEF (t) as a function of time

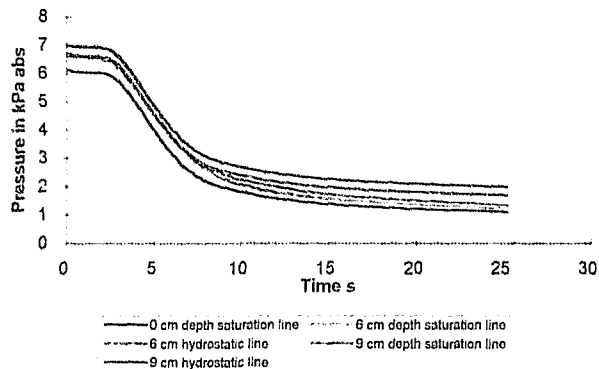


40°C initial, 15 cm liquid height, test 2

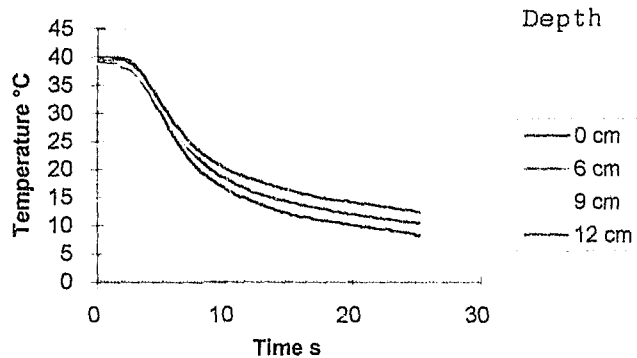
Evaporator pressure as a function of time



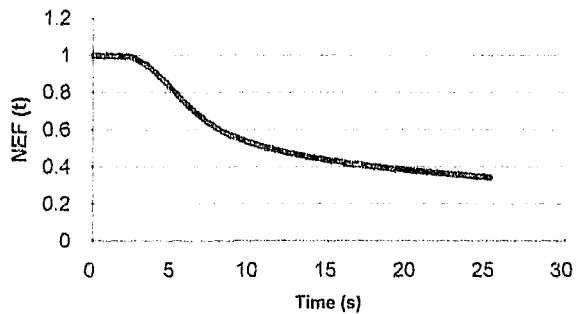
Hydrostatic and Saturation pressure



Temperature distribution

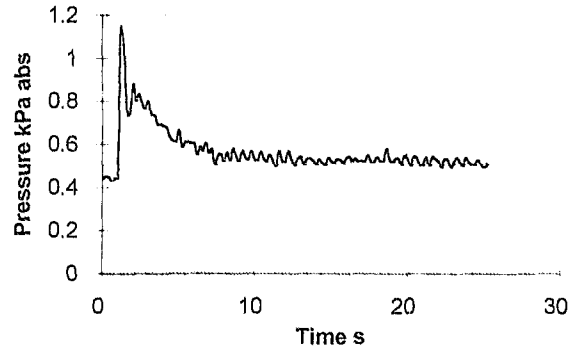


NEF (t) as a function of time

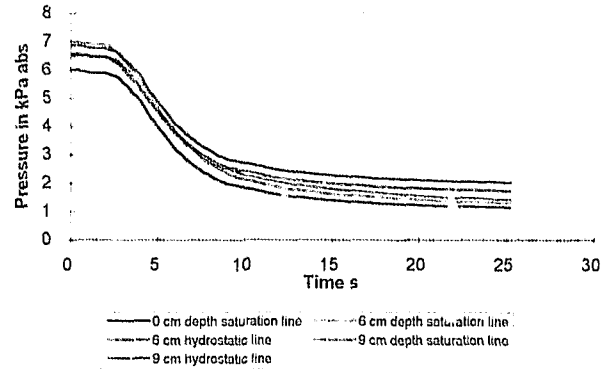


40°C initial, 15 cm liquid height, test 3

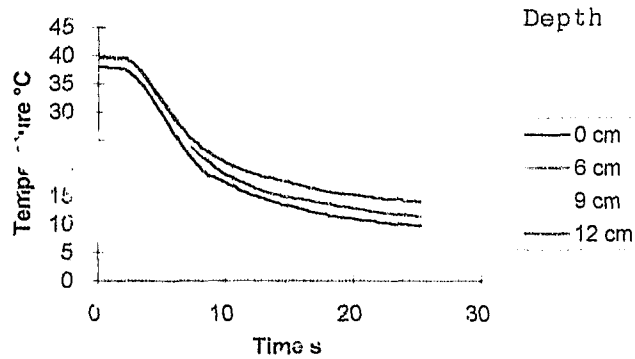
Evaporator pressure as a function of time



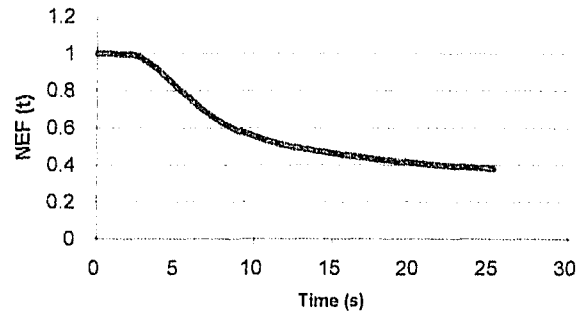
Hydrostatic and Saturation pressure



Temperature distribution

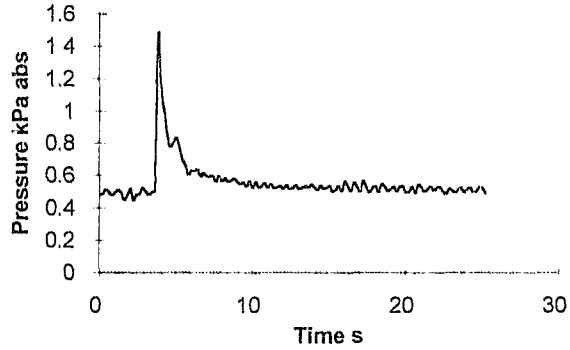


NEF (t) as a function of time

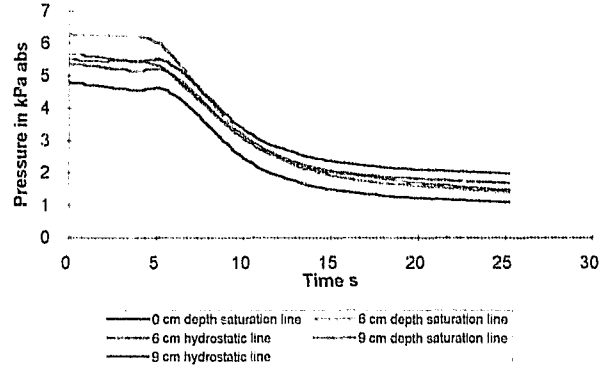


40°C initial, 15 cm liquid height, test 4

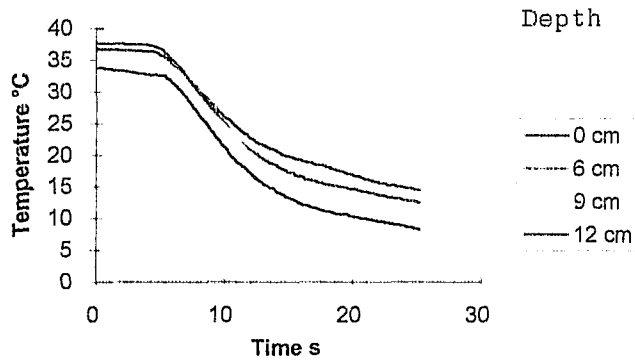
Evaporator pressure as a function of time



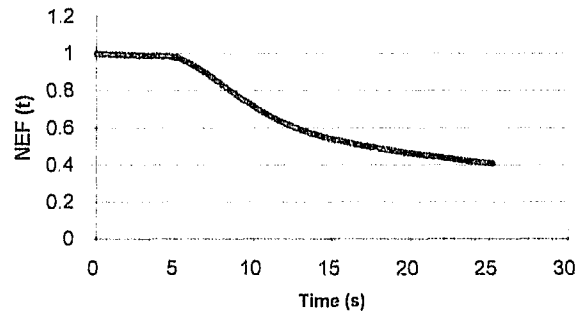
Hydrostatic and Saturation pressure



Temperature distribution



NEF (t) as a function of time




APPENDIX G


**Paper :
Vacuum Boiling in a
Water Vapour Refrigeration System**



 NKF
Norwegian Society
of Refrigeration

 NTNU
Norwegian University of
Science and Technology

 SINTEF
Energy

 VVS
Norwegian Society
of HVAC Engineers
NORVAC

NATURAL WORKING FLUIDS '98

IIR - Gustav Lorentzen Conference

June 2-5, 1998
Oslo, Norway

Joint meeting of the
International Institute of Refrigeration
Sections B and E

PREPRINTS

ASheet

VACUUM BOILING IN A WATER VAPOUR REFRIGERATION SYSTEM

T.J. SHEER and S.R. MITCHLEY

School of Mechanical Engineering
University of the Witwatersrand
Private Bag 3, WITS, 2050
Johannesburg, South Africa

ABSTRACT

The aim of this experimental project was to describe the factors controlling the vacuum boiling of water in direct-contact evaporators for water vapour refrigeration systems. The compression device used for testing was a 2 kW three-stage steam jet ejector system with direct-contact interstage condensers with barometric legs. Three evaporators were used in the experimental programme. These were a through-flow evaporator where heat and mass transfer rates were derived at various points; a vertical cylinder where the rapid decompression of small contained quantities of water was investigated; and a narrow flow channel designed for photographic studies. The nature of boiling in direct-contact vacuum systems is described and the contributions of the various boiling regimes to the total heat transfer are discussed. Various forms of heat and mass transfer coefficients are presented, together with their applicability to evaporator design. The vacuum boiling process is governed by a combination of the water surface temperature and the hydrostatic pressure gradient. These in turn are determined by the flow geometry above the water surface and convection heat transfer below the surface.

INTRODUCTION

The South African gold mining industry faces an enormous challenge with regard to the development of new, more economical systems for removing heat from ultra-deep underground working areas and discharging it to the atmosphere. The phasing out of CFC-based refrigerants has introduced an additional factor in the development of more cost-effective mine refrigeration alternatives. Most established mines will opt for the conversion of R-12 systems to R-134a refrigerant. New mines are likely to use ammonia to a greater extent in installations located on the surface level, while R-134a could be used for underground plants. Strong interest has also been shown in using water vapour refrigeration systems, both on surface and underground (Shone, 1981; Shone and Sheer, 1988). The attractions of water as a refrigerant are that it is inherently non-polluting, it is non-toxic and non-flammable, and it is far cheaper than any conventional refrigerant. Water vapour systems have the particular advantage, as far as thermal efficiency is concerned, that they can utilize direct contact evaporators. The main disadvantage of such systems is that they operate at a very low evaporating pressure, equal to the saturation pressure at the evaporating temperature. At these pressures the water vapour volumetric flow rates are extremely high (Shone, 1981) and specialized compression devices are required. Compression devices in use include centrifugal compressors with large diameter blades (Ophir et al, 1996) and steam jet ejector systems, for applications where low-cost steam is available (Paul et al, 1996). Large plants based on each of these methods are in operation on mines in Southern Africa for the purpose of producing ice at the triple point in slurry form. Ice, produced above ground and used as the primary mine coolant to the underground levels, has the benefit of being able to absorb a large quantity of heat per unit mass flow rate, thereby reducing the costs of pumping the return water up the mine shafts (Sheer, 1995).

At the University of the Witwatersrand research is in progress, in collaboration with the mining industry, into various aspects of the use of natural refrigerants, particularly water. The purpose of the research described in this paper is to investigate the basic factors influencing the rate of evaporation in direct-contact evaporators in water vapour refrigeration systems.

1 EXPERIMENTAL EQUIPMENT AND TESTING

For the experiments conducted, a three-stage steam jet ejector system with barometric condensers was utilised to compress the water vapour. The layout of the laboratory system is shown in Fig. 1.

Steam at a pressure of 500 kPa provides the motive energy for the ejectors. Water vapour produced in the evaporator is compressed by the first stage ejector and the steam and vapour are condensed using a direct contact condenser with a barometric leg. Non-condensable gases and uncondensed vapour and steam are removed by the next two stages of compression.

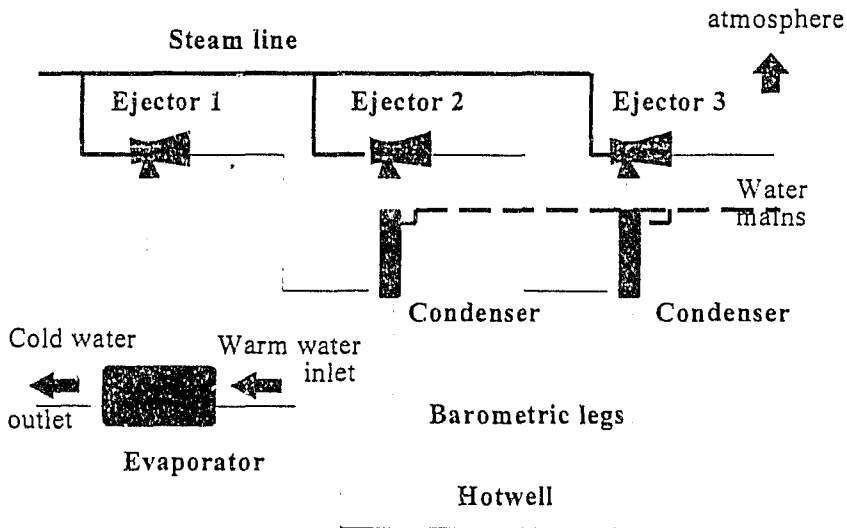
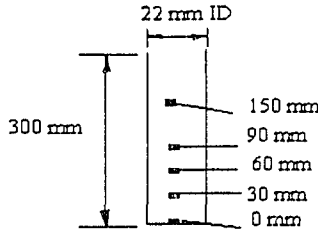
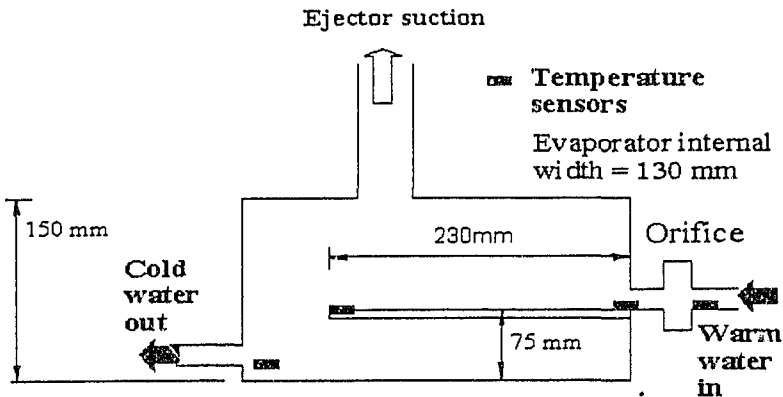


Figure 1- Schematic diagram of experimental installation

Three types of experiments were performed, requiring three types of evaporators. First, in order to visualise the vacuum boiling of water undergoing decompression, a photographic study was conducted. A simple evaporator comprising two 150 x 150 mm perspex sheets separated by 10 mm PVC strips was constructed and fitted to the steam jet refrigeration system via an isolation valve. Secondly, in order to understand the mechanisms involved in the vacuum boiling of a pool of water, a vertical cylinder filled with measured quantities of water was decompressed and the temperature of the water was measured over its depth. Thirdly, temperature profiles were measured in a through-flow evaporator under varying load conditions to investigate the processes involved and establish mass transfer coefficients for the evaporator. Fig. 2 shows the evaporators used for the latter two experiments.



Vertical Cylinder



Through-flow evaporator

Figure 2 - Evaporators used for vertical cylinder and through-flow testing

2 THE VACUUM BOILING PROCESS

In the photographic study, vacuum boiling of water was seen to consist of two distinct regimes: violent bulk boiling, and sporadic surface boiling and evaporation controlled by convection heat transfer. As can be seen from Fig. 3, as the water is decompressed it flashes and violent bulk boiling occurs. (Photograph at 4.5s. Note - the droplets seen above the water surface are due to condensation on the walls of the vessel.) Due to this process the bulk of the water cools. Because of the resulting cooling, the water at greater depth is no longer superheated. Boiling then ceases in the lower regions of the body of water because the hydrostatic pressures at those depths exceed the saturation pressure corresponding to the local temperature (photograph at 10.3s).

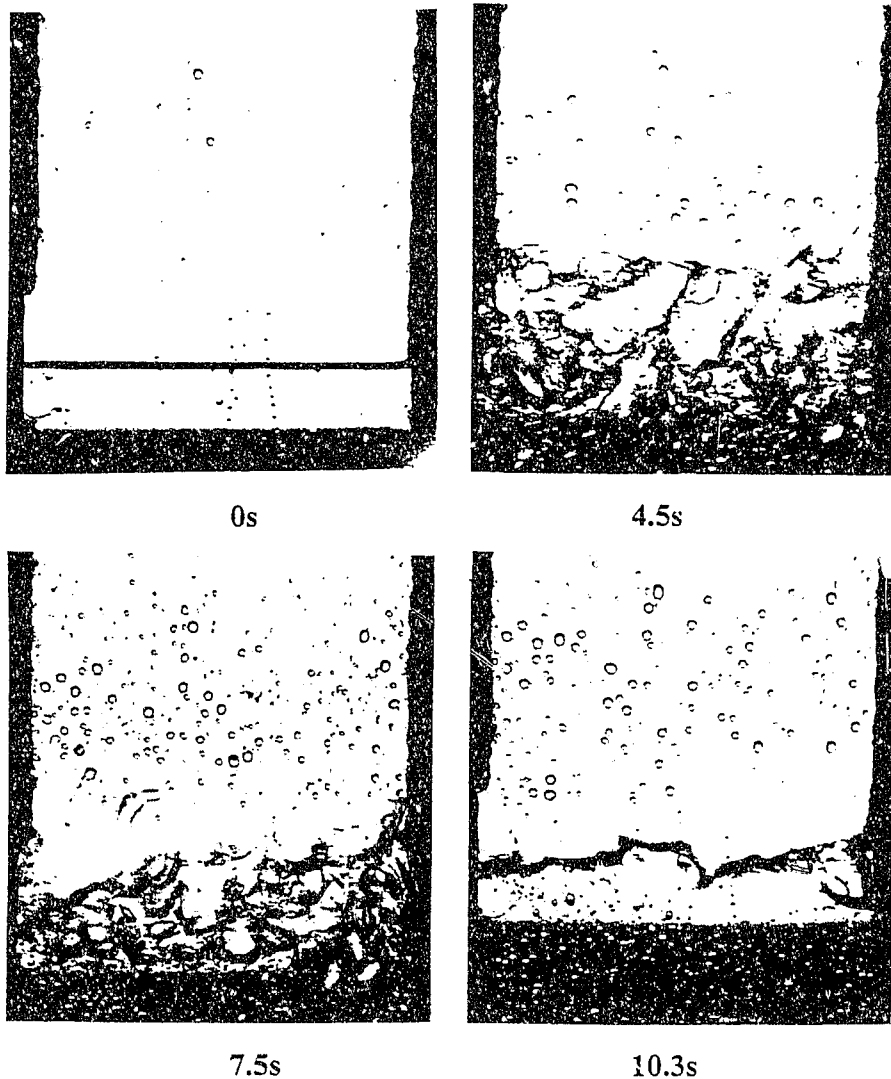


Figure 3 - Initial boiling in decompressed water

The driving potential for continued boiling at the surface of the water is provided by the convection heat transfer from the lower regions. Sporadic boiling just below the liquid surface occurred as bubbles detached from the sides of the evaporator and broke the liquid surface. The slow bubble formation and explosive bursting into the liquid surface is typical of sub-atmospheric boiling. This is shown in the photographs in Fig. 4.

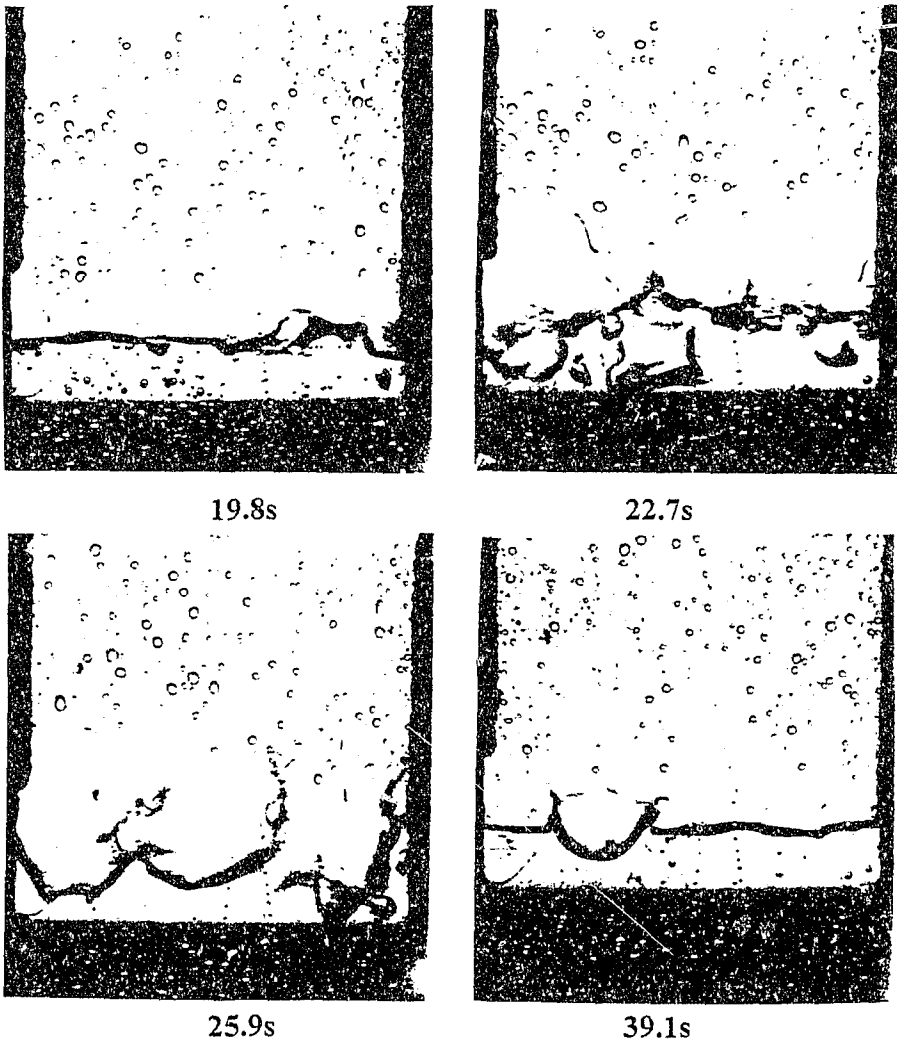


Figure 4 - Sporadic boiling at liquid surface

These two phases of boiling were verified by the vertical cylinder tests. Previous research (Miyatake et al, 1973; Miyatake et al, 1977) had identified these two phases. The bulk temperature of the pool of water in the cylinder decreased rapidly as flash evaporation occurred after the quick opening of the valve connecting the cylinder to the vacuum system. An increase in evaporator pressure from its initial low value accompanied this decrease (because of the rapid generation of vapour). The initial rapid decrease in bulk temperature was then followed by a slower, steady further decrease in both temperature and evaporator pressure. It was noted that although the liquid temperature was superheated relative to the saturation temperature corresponding to the cylinder vacuum, boiling rarely penetrated into the entire liquid depth. By measuring temperatures over the liquid column height, the local rate of change

of temperature could be measured. As can be seen in Fig. 5, definite temperature gradients were created within the bulk of the liquid. This means that the cooling of the bulk of the water is limited by the convection heat transfer rate once these temperature gradients have been established.

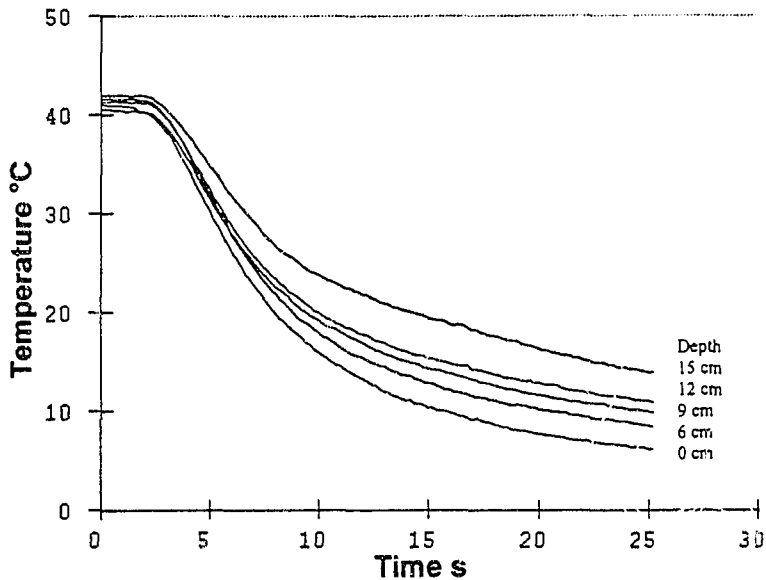


Figure 5 - Typical temperature gradients over the height of a column of water undergoing depressurization (initial temperature 40°C, 15 cm liquid height)

The initial rapid change in bulk temperature followed by a slower rate of change of the temperature indicate the difference in magnitude of heat transfer between bulk boiling and boiling restricted by convective transport. The initial rapid cooling is also aided by the violent boiling which exposes water within the column to the evaporator pressure. It can thus be stated that for efficient evaporator performance the flashing or violent bulk boiling regime must be maintained. By plotting the saturation pressures corresponding to local measured temperatures over the column height, it was found that the rate of cooling of the water surface controls the cooling of lower regions. The evaporator pressure was seen to rise rapidly during the violent bulk boiling phase. This would also have an effect in restricting the rate of heat transfer by reducing the superheat of the liquid. Boiling penetration depth was found to be greater with higher superheat.

Testing of the direct-contact through-flow evaporator further confirmed these results. It was found that the water cooled rapidly upon entering the evaporator. Thereafter, some cooling took place as the water flowed through the evaporator. Figure 6 shows the contribution of the flashing boiling regime to the overall rate of heat transfer in the evaporator.

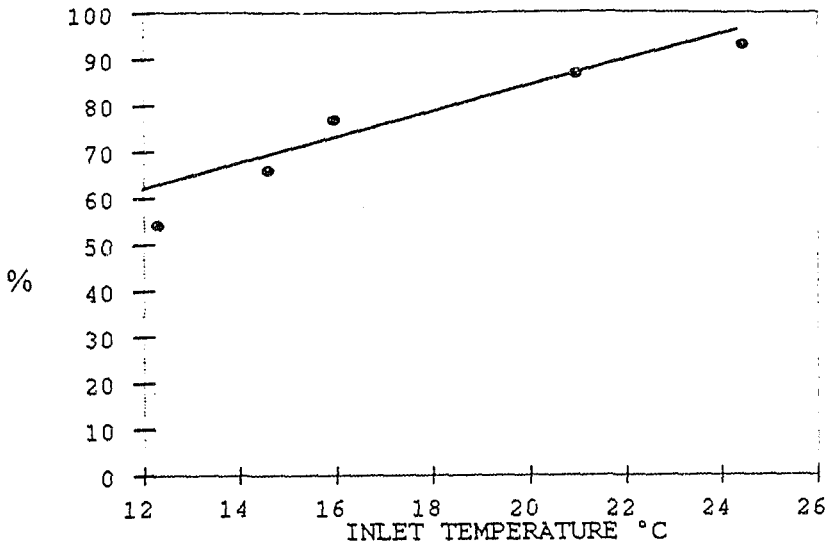


Figure 6 - Relative contribution of the flashing boiling regime to the cooling process in a direct contact through-flow evaporator

Different temperatures were measured at the inlet of the evaporator, within the evaporator and at the exit of the evaporator. This indicates that pressure gradients were present within the evaporator. Evaporators should therefore be of adequate size to accommodate high vapour flow rates without having high pressure drops. The high contribution of the flashing component of the boiling process indicates that flashing needs to be maintained and temperature gradients due to liquid height avoided. The general trends of the direct contact evaporator were that flashing increased with increasing driving potential and with increasing flow rate.

3 HEAT AND MASS TRANSFER COEFFICIENTS

An attempt was made to establish heat and mass transfer coefficients for design purposes. The results of the tests showed that a mass transfer coefficient could be defined for the direct contact evaporator thus:

$$K = \frac{m_{\text{vapour}}}{m_{\text{liquid}} \cdot (T_{\text{inlet}} - T_{\text{evap}})} \quad (1)$$

A typical result is shown in Fig. 7, where non-dimensional mass transfer is plotted against superheat. The slope of the graph is the mass transfer coefficient K .

Mass transfer as a function of Superheat

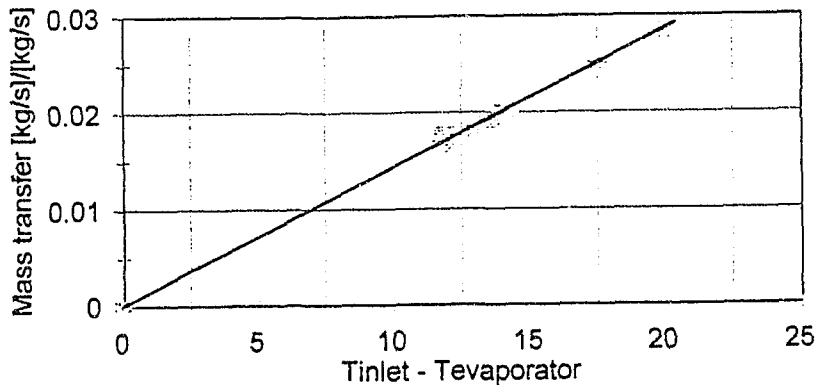


Figure 7 - Bulk mass transfer, mean water flow rate 0.0671 kg/s

Fair agreement for bulk mass transfer coefficients was found for the flow rates tested. The coefficients calculated for three water flow rates are listed below:

$K = 0.001616 \text{ (kg/s / kg/s) / K}$	for flow rate = 0,0245 kg/s
$K = 0.001667 \text{ (kg/s / kg/s) / K}$	for flow rate = 0,0588 kg/s
$K = 0.001429 \text{ (kg/s / kg/s) / K}$	for flow rate = 0,0671 kg/s

It is doubtful that coefficients of this sort would have any real design application, however, as they are specific to the prevailing system geometry and boiling conditions.

4 EVAPORATOR DESIGN

Experimental results from this project show that the two most important factors affecting the sizing of a direct-contact evaporator are whether flashing (violent boiling) can be maintained and the magnitude of the pressure difference between the inlet to the compressor and the surface of the water. If flashing is not maintained throughout the bulk of the water then the heat transfer rate is limited by convective heat transfer within the liquid body. This means that to maintain a given rate of heat transfer, the evaporator needs to contain a larger volume of water than if flashing were to be maintained. It is therefore important to avoid temperature stratification within the liquid. Two methods of preventing this are to employ mechanical agitation to expose the bulk of the water to the surface pressure, or to decrease the evaporator pressure to ensure that the lower regions of the water will always be boiling.

The second method has obvious costs associated with it, requiring compressors able to deliver greater pressure ratios. If flashing can be maintained throughout the liquid then the remaining design requirement for the evaporator is to ensure that the flow of vapour from the liquid surface to the compressor inlet does not involve too great a pressure loss. Having done this the operating performance of the evaporator will be solely dependent on the performance characteristics of the compressor, the inlet conditions of the water, the condensing pressure and the amount of leakage of non-condensables into the evaporator. The vacuum boiling process would be such that the evaporator pressure would approximately correspond to the bulk water saturation temperature.

5 CONCLUSIONS

The experimental work conducted describes the vacuum boiling of water in water vapour refrigeration systems as a combination of heat transfer mechanisms. It is shown that hydrostatic pressure plays a large role in determining the performance of evaporators. The design of evaporators depends not so much on a general mass transfer coefficient but rather on flow considerations and means of maintaining high rates of heat transfer through violent bulk boiling.

ACKNOWLEDGEMENTS

The authors gratefully acknowledge the financial support received from the Eskom through its Tertiary Education Support Programme in carrying out this work.

NOMENCLATURE

K	mass transfer coefficient	[kg/s]/[kg/s/K]
m_{vapour}	vapour mass flow rate	[kg/s]
m_{liquid}	liquid mass flow rate	[kg/s]
T_{inlet}	liquid inlet temperature	[°C]
T_{evap}	saturation temperature corresponding to the evaporator pressure	[°C]

REFERENCES

1. Miyatake, O., Murakami, K., Kawata, Y. and Fujii, T., 1973, Fundamental experiments with flash evaporation, *Heat Transfer - Japanese Research*, vol. 2, part 4: p. 89-100.
2. Miyatake, O., Fujii, T., Tanaka, T. and Nakaoka, T., 1977, Flash evaporation phenomena of pool water, *Heat Transfer - Japanese Research*, vol. 6, part 2: p. 13-24.
3. Ophir, A., Olomutski, D. and Koren, A., 1996, Mechanical vapour compression cycle using water vapour as refrigerant for mine cooling, *Proceedings of the FRIGAIR '96 Conference*, SAIRAC/ASHRAE, Johannesburg, South Africa.
4. Paul, J., Jahn, E. and Lausen, D., 1996, Cooling of mines with vacuum ice, *Proceedings of the FRIGAIR '96 Conference*, SAIRAC/ASHRAE, Johannesburg, South Africa.
5. Sheer, T. J., 1995, Pneumatic conveying of ice particles through mine-shaft pipelines, *Powder Technology*, vol. 85: p. 203-219.
6. Shone, R.D.C., 1981, An investigation into the use of water vapour refrigeration for cooling mine service water, *Journal of the Mine Ventilation Society of SA*, vol. 34, no. 7: p. 121-144.

7. Shone, R.D.C. and Sheer, T.J., 1988, An overview of research into the use of ice for cooling deep mines, *Proceedings of the Fourth International Mine Ventilation Congress*, Brisbane, Australian Inst. of Mining and Metallurgy: p. 407-413.
-

EBULLITION PAR LE VIDE DANS UN SYSTEME FRIGORIFIQUE A VAPEUR D'EAU

RESUME: Le but du projet expérimental était de décrire les facteurs qui influencent l'ébullition sous vide de l'eau dans des évaporateurs à contact direct conçus pour des systèmes de réfrigération à eau. Le compresseur utilisé était un éjecteur trois étages de vapeur d'eau d'une puissance de 2kW, avec des condenseurs à pieds barométriques. Trois évaporateurs ont été utilisés dans le programme expérimental. Un écoulement a pu être observé à travers l'évaporateur où les débits massique et thermique ont été mesurés différents endroits. La rapide décompression de petites quantités d'eau contenue dans un cylindre vertical a fait l'objet d'investigation. Un étroit canal a été conçu pour des études photographiques. La nature de l'ébullition dans les systèmes sous vide à contact direct est décrite, et la contribution des divers régimes d'ébullition dans l'apport totale de chaleur est discutée. Différents coefficients de transfert thermique et massique sont présentés, avec leur application dans la conception de l'évaporateur. Il s'avère que l'ébullition sous vide est régie par la combinaison de la température de la surface de l'eau et le gradient de la pression hydrostatique. Ceux-ci sont, à leur tour, déterminés par la géométrie de l'écoulement, au dessus de la surface, et par l'échange de chaleur par convection sous la surface.

REFERENCES

- [1] **Carpenter, N.E.** Keynote Address, *Frigair '96 Conference Proceedings*
- [2] **Spencer, E.** Steam Jet Refrigeration Equipment, ASHRAE Equipment Handbook Chapter 13, 1979, pp. 13.1-13.6.
- [3] **Havemeyer, H.R.** Do You Know Enough About Steam Jet Refrigeration?, *Chemical Engineering*, Sept. 1948, pp. 102-106.
- [4] **Spencer, E.** New development in Steam Vacuum Refrigeration, ASHRAE Transactions, Vol 67, 1961, pp. 339-353.
- [5] **Tyrer, M. & Meyer, S.** Final Year Mechanical Engineering Project, 1992.
- [6] **Abdel-Aal et al.** Other options of mass and energy input for steam jet refrigeration systems, *The Chemical Engineering Journal*, Vol 45, 1990, pp. 99-110.
- [7] ASHRAE Equipment Handbook, 1979.
- [8] **Munday et al.** Design and performance of a steam jet refrigeration system, *Conference on Thermal Inst. Eng. Australia*, Aug. 1974, pp. 55-61.
- [9] **Fraser et al.** Liquid atomization in chemical engineering Part 1, *British Chemical Engineering*, Aug. 1979, pp. 414-417.
- [10] **Spencer, E.** Steam Jet Refrigeration Equipment, *ASHREA Equipment Handbook*, Chapter 13, 1979, pp. 13.1-13.6.
- [11] **Munday** 1974.
- [12] **Munday, J.T. & Bagster, D.F.** A new ejector theory applied to steam jet refrigeration, *Ind. Eng. Chem, Process Des. Dev.*, vol.16, no.4, 1977, pp.442-449.
- [13] **Shone, R.** An investigation into the use of water-vapour refrigeration for cooling mine service water, *Journal of the Mine Ventilation Society of SA*, vol.34, no.7, July 1981, pp.121-127.
- [14] **Huang, B.J. et al** Ejector performance characteristics and design analysis of jet refrigeration systems, *Transactions of the ASME*, vol 107 July 1985, pp 792-802.
- [15] **Abdel-Aal et al.** 1990.
- [16] **Vil'der, S.I.** A simplified method of calculating steam-jet ejector vacuum pumps, *International Chemical Engineering*, vol.4, no.1, January 1964, pp.88-92.

- [17] **Griffith, P.** Nucleation and bubble formation in boiling, *Boiling Heat Transfer in Steam-Generating Units and Heat Exchangers*, Institution of Mechanical Engineers, Proceedings 1965-66, vol.180, Part 3C, pp.93-99.
- [18] **Gaertner, R.F.** Photographic Study of nucleate pool boiling on a horizontal surface, *Journal of Heat Transfer*, Transactions of the ASME, February 1965, pp.17-29.
- [19] **Madejski, J.** Improved "three-component" theory of nucleate pool boiling, *International Journal of Heat and Mass Transfer*, vol.15, pp.503-512.
- [20] **Van Stralen, S. et al**, The mechanisms of nucleate boiling in pure liquids and in binary mixtures - Part 1, *International Journal of Heat and Mass Transfer*, vol.9, pp. 995-1020.
- [21] **Van Stralen, S.** The mechanisms of nucleate boiling in pure liquids and binary mixtures - Part 2, *International Journal of Heat and Mass Transfer*, vol.9, pp.1021-1046.
- [22] **Han et al** The mechanism of heat transfer in nucleate pool boiling - Part 1, *Int. J. Heat Mass Transfer*, vol.8, pp.887-904.
- [23] **Han et al** The mechanism of heat transfer in nucleate pool boiling - Part 2, *Int. J. Heat Mass Transfer*, vol.8, pp.905-914.
- [24] **Tong, L.S.** Boiling Heat Transfer and Two Phase Flow, R.E. Krieger Publishing Co., 1975, pp 6-8.
- [25] **Westwater, J.W.** The Boiling of Liquids, *Advances in Chemical Engineering*, vol.1, Academic Press, 1956, pp.1-71.
- [26] **Mickic, B.B. et al** On bubble growth rates, *Int. J. Heat Mass Transfer*, vol.13, 1970, pp. 657-666.
- [27] **Mc Fadden et al** Relationship between bubble frequency and diameter during nucleate pool boiling, *Int. J. Heat Mass Transfer*, vol.5, 1962, pp.169-173.
- [28] **Akiyama, M.** Dynamics of an isolated vapour bubble in saturated nucleate boiling, *Bulletin of JSME*, vol.12, no.50, 1969, pp.273-282.
- [29] **Cooper, M.G.** The microlayer in nucleate pool boiling, *Int. J. Heat Mass Transfer*, vol.12, 1969, pp.895-913.
- [30] **Cooper, M.G.** The microlayer and bubble growth in nucleate pool boiling, *Int. J. Heat Mass Transfer*, vol.12, 1969, pp.915-933.
- [31] **Kiper, A.M.** Minimum bubble departure diameter in nucleate pool boiling, *Int. J. Heat Mass Transfer*, vol.14, 1971, pp.931-937.
- [32] **Van Ouwwerkerk, H.J.** The rapid growth of a vapour bubble at a liquid- solid interface, *Int. J. Heat Mass Transfer*, vol.14, 1971, pp.1415-1431.
- [33] **Saini, J.S. et al** Evaluation of microlayer contribution to bubble growth in nucleate pool boiling using a new bubble growth model, *Int. J. Heat Mass Transfer*, vol.18, 1975,

pp.469-472.

- [34] **Van Stralen, S. et al** Bubble growth rates in pure and binary systems : combined effect of relaxation and evaporation microlayers, *Int. J. Heat Mass Transfer*, vol.18, 1975, pp.453-467.
- [35] **Toikai, K.** Heat transfer in a contact area of a boiling bubble on a heating surface, *Bulletin of JSME*, vol.10, no.38, 1967, pp.338-348.
- [36] **Raben, I.A. et al**, A study of heat transfer in nucleate pool boiling of water at low pressure, *Chem. Eng. Progress Symposium Series : Heat Transfer - Boston*, vol.61, no.57, pp.249-257.
- [37] **Akiyama, M. et al**, Effect of pressure on bubble growth in pool boiling, *Bulletin of JSME*, vol.12, no.53, 1969, pp.1121-1129.
- [38] **Van Stralen, S. et al** Bubble growth rates in nucleate boiling of water at subatmospheric pressures, *Int. J. Heat Mass Transfer*, vol.18, 1975, pp.655-669.
- [39] **Dobzhanskiy, V.G. et al** Nucleate boiling of water under vacuum on horizontal tubes, *Heat Transfer - Soviet Research*, vol.14, no.2, March-April 1980, pp.109-110
- [40] **Miyatake, O.,Fuji, T., Kawata, Y. and Murakami, K.** Fundamental experiments with flash evaporation, *Heat Transfer - Japanese Research*, vol.2, Part 4, Oct.-Dec. 1973, pp.89-100
- [41] **Belyayev, N.M. and Artemenko Yu, G.** Experimental study of heat and mass transfer during evaporation of water under vacuum, *Heat Transfer - Soviet Research*, vol.2, no.2, March 1970, pp 88-91.
- [42] **Alamgir Md. and Lienhard J.H.** An experimental study of the rapid depressurization of hot water, *Journal of Heat Transfer*, vol.102, August 1980, pp.433-438.
- [43] **Alamgir, M.D. and Lienhard , J.H.** Correlation of pressure undershoot during hot-water depressurization, *Journal of Heat Transfer*, vol.103, February 1981, pp.52-55.
- [44] **Yefimochkin, G.I.** Investigation of the flashing of water upon sudden decompression in vacuum-type contact (mixing) preheaters, *Heat Transfer - Soviet Research*, vol.14, no.2, March-April 1982.
- [45] **Kendoush, A.A.** The delay time during depressurization of saturated water, *International Journal of Heat and Mass Transfer*, vol.32, no.11, 1989, pp.2149-2154.
- [46] **Owen, I. and Jalil, J.M.** Heterogeneous flashing in water drops, *International Journal of Multiphase Flow*, vol.17, no.5, 1991, pp.653-660.
- [47] **Miyatake O. et al** 1973.
- [48] **Miyatake, O., Fujii, T., Nakaoka, T. and Tanaka, T.** Flash evaporation phenomena of pool water, *Heat Transfer - Japanese Research*, vol.6, Part 2, April-June. 1977. pp 13-24.

- [49] **Nishikawa, S.** Nucleate boiling at low liquid levels, *Bulletin of JSME*, vol.10, no.38, 1967, pp.328-338.
- [50] **Forest, T.W. and Ward, C.A.** The effect of a dissolved gas on the homogeneous nucleation pressure of a liquid. *The Journal of Chemical Physics*, vol.66, no.6, March 1977, pp.2322-2330.
- [51] **Vil'der, S.I.** A simplified method of calculating steam-jet ejector vacuum pumps, *International Chemical Engineering*, vol.4 no.1, January 1964.
- [52] **How, H.** How to design barometric condensers, *Chemical Engineering*, Feb. 1956, pp.174-182.
- [53] **Collier, J.G.** Convective Boiling and Condensation- 2nd ed., *McGraw-Hill Book Company*, England, 1981.
- [54] **Fenner, R.T.** Mechanics of solids, *Blackwell Scientific Publications*, London, 1989.

Author Mitchley, Stephen Ronald.

Name of thesis Vacuum boiling of water in a steam refrigeration system. 1998

PUBLISHER:

University of the Witwatersrand, Johannesburg

©2013

LEGAL NOTICES:

Copyright Notice: All materials on the University of the Witwatersrand, Johannesburg Library website are protected by South African copyright law and may not be distributed, transmitted, displayed, or otherwise published in any format, without the prior written permission of the copyright owner.

Disclaimer and Terms of Use: Provided that you maintain all copyright and other notices contained therein, you may download material (one machine readable copy and one print copy per page) for your personal and/or educational non-commercial use only.

The University of the Witwatersrand, Johannesburg, is not responsible for any errors or omissions and excludes any and all liability for any errors in or omissions from the information on the Library website.